Thèse
de doctorat
de l'UTT

**Zhimao WANG**

# Experimental Study and Modelling of Thermomechanical Features and Heterogeneity of the Cr203-NiCr Systems

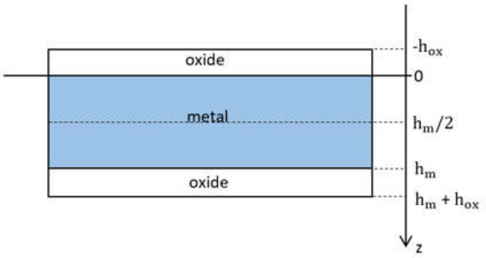

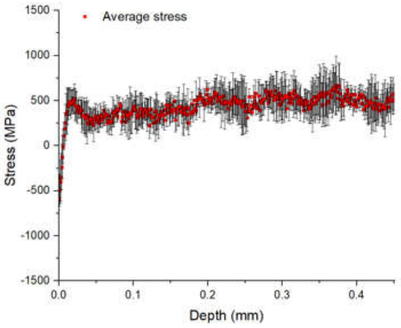

**Champ disciplinaire :**
Sciences pour l'Ingénieur

**2021TROY0020**

**Année 2021**

utt
UNIVERSITÉ DE TECHNOLOGIE
TROYES

# THESE

*pour l'obtention du grade de*

## DOCTEUR
## de l'UNIVERSITE DE TECHNOLOGIE DE TROYES

## en SCIENCES POUR L'INGENIEUR

**Spécialité : MATERIAUX, MECANIQUE, OPTIQUE, NANOTECHNOLOGIE**

*présentée et soutenue par*

**Zhimao WANG**

*le 30 juin 2021*

# Experimental Study and Modelling of Thermomechanical Features and Heterogeneity of the Cr203-NiCr Systems

## JURY

| | | |
|---|---|---|
| M. J. FAVERGEON | PROFESSEUR DES UNIVERSITES | Président |
| Mme C. BERDIN-MÉRIC | PROFESSEURE DES UNIVERSITES | Rapporteure |
| Mme I. POPA | MAITRE DE CONFERENCES - HDR | Rapporteur |
| M. G. GEANDIER | CHARGE DE RECHERCHE CNRS | Examinateur |
| M. D. MACIAS GUZMAN | MAITRE DE CONFERENCES | Examinateur |
| M. V. MAUREL | CHARGE DE RECHERCHE MINES PARISTECH | Examinateur |
| M. J.-L. GROSSEAU-POUSSARD | PROFESSEUR DES UNIVERSITES | Directeur de thèse |
| M. B. PANICAUD | PROFESSEUR DES UNIVERSITES | Directeur de thèse |

# Tables

# Acknowledgements

This thesis and all the work related to it were carried out in the LASMIS laboratory (Systèmes Mécaniques et d'Ingénierie Simultanée ) at the Université de Technologie de Troyes (UTT) and LaSIE laboratory (Laboratoire des Sciences de l'Ingénieur pour l'Environnement) at Université de La Rochelle from October 2017 to present.

First of all, I would like to give my very huge thanks for the encouragement and support from my supervisors Prof. Benoît PANICAUD and Prof. Jean-Luc GROSSEAU-POUSSARD. They have guided me throughout my thesis with their great patience, dedication, and knowledge. Their personality and expertise provided me with a very pleasant environment for research. Their perfect collaborative guidance was necessary for the success of this thesis.

I would like to thank Guillaume GEANDIER, with his involvement the experiments have been realized at Deutsches Elektronen-Synchrotron (DESY).

I would like to express my thanks to Jérôme FAVERGEON for helping me realize the experiments at Université de Technologie de Compiègne.

I would like to give many thanks to all the researchers in LASMIS laboratory. A great thanks should be given to Bruno GUELORGET, who training me on X-ray diffraction and other experiments machines. I would also thank Laurent DANIEL for his help with the software and server problems. Thanks should also be given to Carl LABERGÈRE and Zhidan SUN, who taught me to use software ABAQUS with UMAT.

Thanks should also go to Xusheng, Lan, Yangchan, Yuchen, Kai, and those mentioned above, who shared a very enjoyable and memorable time in my PhD life. It was great to have them as my colleagues.

Just before going to the financial supports, I would like to give my deepest appreciation to my family, especially my parents and my girlfriend, who have always supported me. Your love, comprehension and encouragement power my improvement.

Last but not least, I am most grateful to my beloved China and its Scholarship Committee (CSC), who supported my scholarship for 42 months.

# Introduction

When a metal or metallic alloy is oxidized at high temperature, an oxide film is usually formed and the stress caused by the growth of the oxide may affect the structure and properties of the metal. However, the durability of metallic materials is a major concern. For applications to high temperature, chromium-based alloys have been developed in order to form, in oxidizing atmospheres, chromia films providing in general a good protection against further oxidation. During oxidation, a compressive growth stress generally arises in the thermally grown oxide (TGO) from oxide formation within the layer, as the diffusing cations and anions meet and react, particularly along the vertical grain boundaries. The problem is that such growth stresses, when combined with thermal stresses that develop during cooling, may initiate and drive layer failure in the oxide layer (i.e., by cracking or spallation) with mechanical and chemical consequences, in turn limiting the alloys lifetime in such a severe environment.

The plastic or viscoplastic strain (such as creep mechanism) of the substrate and the oxide contributes to the relaxation of the stress. Concerning stress relaxation, an oxide creep is generally concerned rather than delamination, for chromia stressed at sufficiently high temperatures and fine-grained oxide according to Ashby map. From previous works concerning NiCr alloys, it was shown that the growth stresses are released by creep phenomena in the fine grain chromia film (grain size usually ranging from 0.2 to 0.8 μm) for temperatures between 800°C and 1000°C. Strain relaxation studies in the chromia layers were carried out in-situ, after imposing a sudden temperature change introducing a supplementary stress due to the mismatch of thermal expansion coefficients of the oxide and the alloy.

To improve the protective properties of the thermally grown chromia layer under high temperature oxidation, reactive elements are often introduced into the bulk or on the top surface of a metallic alloy, such as yttrium oxide ($Y_2O_3$ known as yttria) or zirconium (Zr). These kinds of reactive elements have been shown to decrease the oxidation kinetics and significantly increase the adhesion of chromia layer to the metallic substrate. However, the influence of the addition of reactive elements on the creep or oxide growth parameters has been insufficiently investigated, which will be discussed in this work.

Analytical models have been established to predict the stresses evolution, but as far as we know, most of them generally consider the thermomechanical features in the oxide layer and substrate as homogeneous. However, in real situations, the stress spatial distribution is more complex than so simple modelling that may be related to heterogeneity effects of the materials, especially for the metallic substrate. In previous works, models have been successfully applied, for example, to optimize the thermomechanical parameters. However, the existing analytical models are not fully adapted to analyze the results obtained from experiments providing stress spatial distributions, as obtained by high-energy synchrotron X-rays. Indeed, to improve our understanding of the stress spatial distribution in the substrate for a duplex oxide-metallic substrate system, we expect to use a specific method in transmission mode using high-energy synchrotron X-rays. It should be therefore possible to compare with modelling provided to enrich it by adapted components to model this stress spatial distribution.

The main objective of this work is thus the study of the mechanics in metal + thermal oxide systems in a high temperature environment (typically above 600°C) and make it possible to study the heterogeneity of the mechanical state. For this purpose, both experimental and numerical approaches have been developed. Moreover, in this thesis, a list of specific questions will be answered:

1. How to setup the thermomechanical model to describe the mechanics behavior of the {metal + thermal oxide} systems at high temperature?

2. How to determine the stress during the high temperature oxidation and at the room temperature using different modes of high-energy XRD equipment?

3. How to optimize the mechanical parameters of samples with reactive elements and explain the related mechanisms?

4. How to establish a model to explain the stress spatial distribution that is related to the heterogeneity of the mechanical properties?

5. How to develop a numerical model and implement it in Abaqus to simulate the mechanical state of these systems?

This PhD thesis manuscript then consists in 5 chapters:

The first chapter provides an establishment of thermomechanical models with a general review of bibliography, which presents the phenomena occurring during high temperature oxidation and the cooling process. It includes the growth and oxidation kinetics, the sources of stress and the stress relaxation terms. In addition, as a bibliographic chapter, several methods are reviewed in order to determine residual stresses and to optimize the thermomechanical parameters.

The second chapter contains experimental procedure and preliminary results. The material substrates studied in this thesis are also introduced. Two specific methods are proposed to treat the results obtained by different modes of high-energy XRD equipment (ESRF and DESY synchrotrons). Moreover, two possibilities for the stresses correction are also proposed under different hypotheses.

The third chapter presents the optimization of the mechanical parameters of samples with and without reactive elements. The data is obtain by reflection XRD mode by use of the procedure for the determination of stress as presented in chapter two. By applying the thermomechanical model proposed in chapter one, the mechanical parameters are thus obtained and the related possible mechanisms are discussed.

The fourth chapter discuss the heterogeneity of the mechanical state of the system and the stress spatial distribution. The experimental data is obtained by transmission XRD mode by use of the procedure for the determination of stress as shown in chapter two. As the oxidation proceeds, the depletion of chromium in the substrate cannot be ignored, which may introduce voids for example in the near interface zone in substrate. These voids may cause what we further call a chemical strain. Considering the mechanical balance, this chemical strain could be an important stresses source in the substrate at the vicinity of the oxide layer. The concentration of chromium profile provides therefore a possible source for stress, and may thus explain the spatial distribution of stress especially at the vicinity of the oxide layer.

The fifth chapter presents a numerical model performed with Abaqus software, which is used to simulate the mechanical state of these systems. The procedure of the numerical model establishment is introduced in details. Comparing the simulation results and experimental results, the mechanical parameters can be verified and it helps us to better understand the associated phenomena of the proposed model.

# Chapter 1: State of art

# 1.1 General information about high temperature oxidation

## 1.1.1 Thermodynamics of oxidation at high temperature

Metal alloys are increasingly used in industrial systems operating at high temperatures [1], such as thermal power stations, gas turbines, nuclear power stations, fuel cells, etc. When a metal or metallic alloy is oxidized at high temperature, an oxide film is usually formed [2-4]. In order to analyze energetically the influence of oxidation in the metal layer and the oxide layer, thermodynamics is generally used. The oxidation reaction can be written as follows:

$$2\frac{a}{b}M + O_2 = \frac{2}{b}M_aO_b \tag{1.1}$$

where M represents the metal, a and b are respectively the stoichiometric coefficients of metal and oxygen.

The oxide-forming reaction is very favorable in terms of thermodynamics, since the corresponding standard free energy, $\Delta_r G$, is generally negative ($\Delta_r G$ is about -550 kJ per mole of $O_2$ for chromium oxide at 800°C, and about -800 kJ per mole for alumina at 1100°C [5]). The driving force for oxidation is defined by:

$$\Delta_r G = \Delta_r G^0 + RTln\left(\frac{a_{M_aO_b}^{\frac{2}{b}}}{a_M^{\frac{2a}{b}} P_{O_2}}\right) \tag{1.2}$$

Where $\Delta_r G^0$ is the standard free enthalpy of oxide formation $M_aO_b$, $a_{M_aO_b}^{\frac{2}{b}}$ and $a_M^{\frac{2a}{b}} P_{O_2}$ represent the chemical activities of oxide and metal, R is the molar gas constant, T is the temperature and a the metal activities and $P_{O_2}$ is the partial pressure of oxygen (to the reference pressure $P_{O_2}^0$ taken equal to 1 bar). When the oxide layer formed does not deviate from stoichiometry and when the metal and the oxide are not mixable, these activities of oxide and metal are 1. Thus, the Eq.1.2 becomes:

$$\Delta_r G = \Delta_r G^0 - RTln(P_{O_2}) \tag{1.3}$$

Since the spontaneous formation of the oxide is only possible if $\Delta_r G < 0$. From the Eq.1.3, this gives us:

$$\Delta_r G^0 < RTln(P_{O_2}) \tag{1.4}$$

Oxide stability maps in variable environments are used to predict the main oxide phase that will develop, which are called Ellingham-Richardson diagrams (Fig.1.1).

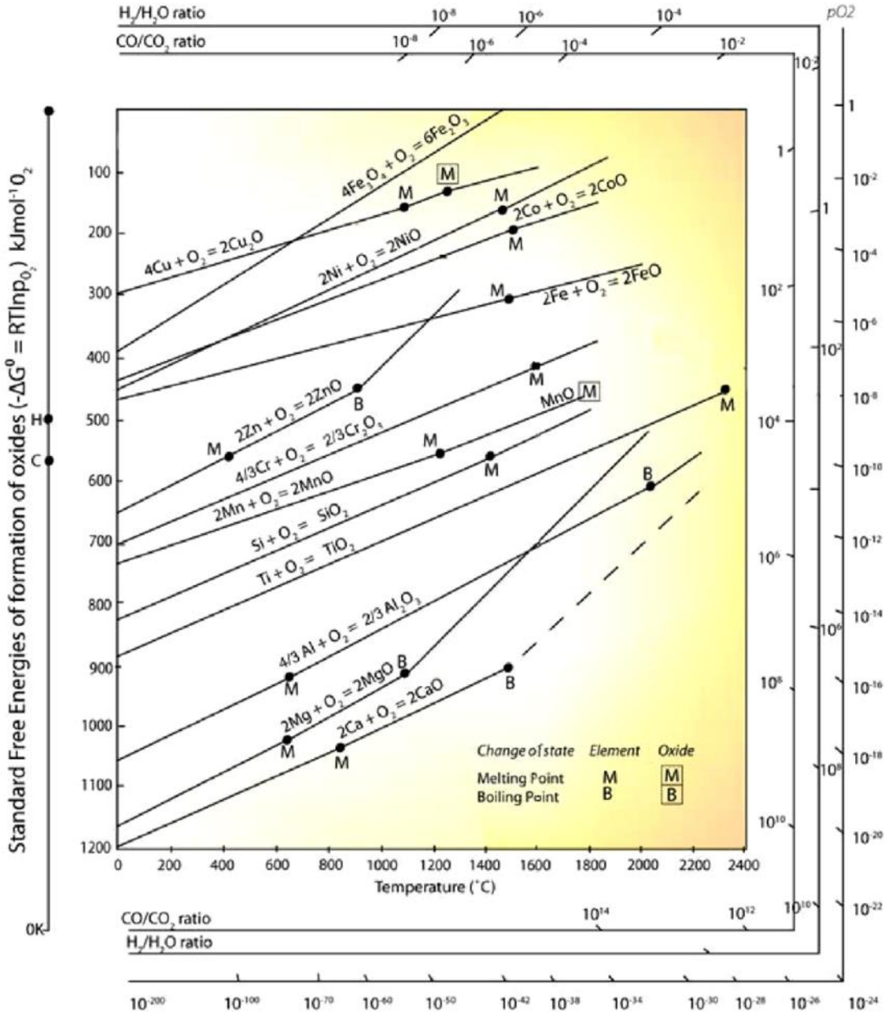

Figure 1.1: Ellingham-Richardson diagrams [6]

The Ellingham-Richardson diagram provides the standard formation free energy ($\Delta_r G^0$) of a certain type of compound (e.g., oxides, sulfides, carbides) as a function of temperature. The Ellingham-Richardson diagram is based on many assumptions, such as:

- Thermodynamic balance
- Pure metallic phase (without reactive alloying elements).
- Equality of the chemical activity of one mole of oxygen with its chemical potential and is directly related to the partial pressure of a perfect gas.
- Standard Gibbs free enthalpy linearity with temperature (Ellingham-Richardson hypothesis)

Although some of these assumptions are not always strictly met, Ellingham-Richardson diagrams are commonly used to predict the oxide phase at a given temperature and under oxygen partial pressure.

In addition, at a given temperature, the standard free enthalpy variation of a reaction is expressed by the expression:

$$\Delta_r G^0 = \Delta_r H^0 - T\Delta_r S^0 \quad (1.5)$$

Where $\Delta_r H^0$ is the molar enthalpy and $\Delta_r S^0$ is the molar entropy of reaction. Assuming $\Delta_r H^0$ and $\Delta_r S^0$ independent of temperature in Ellingham-Richardson approximation, $\Delta_r G^0$ becomes a linear function of temperature, whose slope corresponds to (-$\Delta_r S^0$) and the intercept to $\Delta_r H^0$. Ellingham-Richardson diagrams make it easy to compare the stability of different $M_a O_b$ oxides corresponding to different metals.

## 1.1.2 Growth and oxidation kinetics

### 1.1.2.1 Growth mechanisms of oxide layer

The growth of an oxide layer on the surface of a metallic substrate requires a material transport mechanism of chemical species [2-4], which is a process that is generally activated at high temperature. This kind of transport is achieved by the fact that different types of defects are involved: punctate (voids), linear and planar (grain boundaries and dislocations), which are present in both the oxide and the underlying metal. The oxidation kinetics are therefore controlled by the concentration of these defects and their mobility. The growth of oxide layer can be determined by studying the motion of these defects.

The oxidation process of a given material can be described as adsorption, dissociation and reaction.

At adsorption step, the oxygen molecules are absorbed on the surface of the metal. Then, the oxygen molecules may dissociate into anionic $O^{2-}$, which will react with the cationic ion of metal to generate a more stable compound ($M_a O_b$). After these steps, a thin layer of oxide is formed on the surface of the metal. Once this oxide layer is continuous, metal layer and oxide layer can be clearly distinguished, but still remains adherent. In addition, the growth will continue through anionic and/or cationic diffusion in the metal layer and oxide layer, as shown in Fig.1.2.

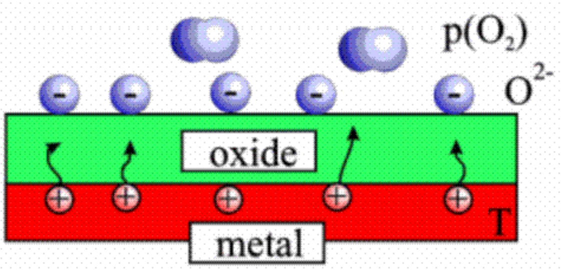

Figure 1.2 Schematic illustration of an oxide/metal system

Depending on the majority species involved and their motion, two main growth modes are introduced:

- Internal or anionic growth: the oxygen molecules dissociate into anionic $O^{2-}$ at oxide/gas interface. These ions diffuse through the oxide layer to the metal/oxide interface and incorporate into the oxide lattice.
- External or cationic growth: the oxygen molecules dissociate into anionic $O^{2-}$ at oxide/gas interface. The cationic metallic ion is generated in the metal layer near metal/oxide interface zone, which transports across the growing oxide layer and reacts with the anionic $O^{2-}$. In this case, an accumulation of cationic voids in the metal layer near metal/oxide interface zone is often observed [7].

As the oxide layer continues to grow, other processes may occur: cavities or pores, resulting from the coalescence of the voids [2, 3]. Their presence is often considered critical for the system (metal/oxide) because they can lead to the delamination of the layer from its substrate. In addition, when the stresses generated are high, cracking and buckling phenomena may occur.

Here, in this thesis, the alloys studied are Ni28Cr and Ni35Cr, where 28 and 35 are the weight percentage of chromium in the alloys. For the alloys NiCr that has a good behavior to oxidation at high temperature, both NiO and $Cr_2O_3$ are stable oxides at 1 atm oxygen. In addition, Fig.1.1 indicates that it has lower free enthalpy for forming $Cr_2O_3$ than NiO, which means that chromium has a higher affinity for oxygen than nickel. Although, the Ellingham-Richardson diagrams predicts the thermodynamically preferred oxide at final state, they do not completely determine the nature of the transient oxide formation or the kinetics quasi steady state of oxide layer.

The chromium percentage of the alloy mainly determines whether $Cr_20_3$ develops as external oxide layer or internal oxide in the alloy lattice. As discussed in [8, 9], if the alloy contains less than about 10% chromium by weight, there is usually not enough chromium for external oxide layer formation and the internal oxide will form. Thus, in this thesis, a type of external or cationic growth is analyzed.

#### 1.1.2.2 Oxidation kinetics

Kinetic laws are observed to describe the evolution of an oxidation reaction over time [10]. They aim at relating the oxidation rate of a given material, by measuring the variations of mass during oxidation at temperature.

Wagner has developed his well-known theory for the high-temperature oxidation of metals (parabolic rate law) [11]. The rate of oxidation decreases over time as the layer thickens. The growth of the oxide layers is controlled by diffusion mechanisms (anionic and/or cationic), which is described as Eq.1.6:

$$h_{ox}{}^2 = k_c(t - t_0) + h_{ox_0}{}^2 \tag{1.6}$$

$$k_c = 2\Omega\widetilde{D_L}\Delta C \tag{1.7}$$

where $h_{ox}$ is oxide layer thickness at time $t$, $h_{ox_0}$ corresponds to oxide thickness at initial time $t_0$, $k_c$ is the parabolic kinetics constant of the oxide layer growth in case of diffusion through lattice that has units of $m^2s^{-1}$, $\Omega$ corresponds to volume of oxide per oxide site, $\widetilde{D_L}$ is chemical diffusion coefficient in oxide lattice, $\Delta C$ is the difference in defect concentration between the oxide/gas interface and the metal/oxide interface [12].

If we considered the mass difference, Eq.16 can also be expressed as:

$$\left(\frac{\Delta m - \Delta m_0}{S}\right)^2 = k_p(t - t_0) \tag{1.8}$$

where $k_p$ is the parabolic mass constant and has units of $kg^2m^{-4}s^{-1}$, S is the surface area, $\Delta m$ is the difference of mass after oxidation and $\Delta m_0$ corresponds to initial mass difference.

As known in Eq.1.1, the general oxide form is expressed as $M_aO_b$. The relationship between $k_c$ and $k_p$ is:

$$k_c = \left(\frac{M_{M_aO_b}}{bM_O\rho_{M_aO_b}}\right)^2 k_p \tag{1.9}$$

where $M_{M_aO_b}$ and $M_O$ are the molar masses of oxide and oxygen, b is the number of oxidant atoms and $\rho_{M_aO_b}$ is the density of the oxide.

In addition, the oxide layer thickness can also be expressed as:

$$h_{ox} = Ap\sqrt{t} \tag{1.10}$$

#### 1.1.2.3 Other kinds of kinetic laws

With some conditions, the oxidation follows other types of rate laws, such as the linear law, the logarithmic law, cubic law etc.

a. Linear law

The oxidation rate remains constant over time. The growth of oxide layer is mainly ensured by gas-phase diffusion of oxygen and is controlled by rapid reactions at the interfaces, such as adsorption, dissociation, and ionization of oxygen [5].

$$\frac{\Delta m - \Delta m_0}{S} = k_1(t - t_0) \tag{1.11}$$

where $\Delta m$ is the difference of mass after oxidation, $\Delta m_0$ corresponds to initial mass difference, S is the surface area and $k_1$ is the linear kinetics constant whose units $m.s^{-1}$, which is also called interfacial reaction constant.

b. Logarithmic law

If metals are oxidized under certain conditions, usually at low temperatures, the initial oxide formation is characterized by a rapid initial reaction that is quickly reduced to a very low reaction rate. Such behavior follows the law of rate described by logarithmic function:

$$\left(\frac{\Delta m - \Delta m_0}{S}\right)^m = k_{log}(t) \tag{1.12}$$

where $\Delta m$ is the difference of mass after oxidation, $\Delta m_0$ corresponds to initial mass difference, m is exponent used for the power law kinetics of oxide layer growth (Logarithmic law), S is the surface area and $k_{log}$ is the logarithmic kinetics constant. Several interpretations of this type of behavior have been given [3, 13].

c. Cubic law

If the grain volume is assumed to be a cube of the grain size, a cubic growth law is applied to grain size. In the work of Rhines et al. [14, 15], a model with a grain volume proportional to time is proposed and the oxidation kinetics of Ni was in good accordance with a cubic law.

$$g^3(t) = k_h(t - t_0) + g_0^3 \tag{1.13}$$

where $g$ is grain size, $g_0$ corresponds to grain size at initial time and $k_h$ is cubic coefficient for the grain growth law. However, the analytical expression of oxidation kinetics of the cubic grain growth law is not given by Rhines, which is proposed in the work [12].

#### 1.1.2.4 Analysis of experimental oxidation kinetics

In order to interpret the experimental oxidation kinetics, a purely parabolic law is not sufficient, which is only applied in specific cases where a single type of oxide grows, with the same diffusion properties throughout all the experiment. However, the initial oxide grown during the transient period is also important. Thus, it is needed to modify the parabolic law in order to describe the system correctly. Two oxidation period are considered, which are the transient oxidation period and the oxide growing period. The transient period is usually considered as the first few minutes of oxidation [16] and the oxide growing period is the oxidation time after the transient period. In the works of Pieraggi and Monceau [17, 18], several parabolic laws designed for different experimental hypotheses were proposed.

a. Case 1

In this case, the oxidation kinetics is purely controlled by diffusion and the initial oxide grown during the transient period $(t < t_i)$ has the same protective properties as during the oxide growing period $(t > t_i)$.

$$\frac{d\Delta m}{dt}\frac{1}{S} = \frac{k_p S}{2\Delta m} \tag{1.14}$$

$$\left(\frac{\Delta m}{s}\right)^2 - \left(\frac{\Delta m_i}{s}\right)^2 = k_p(t - t_i) \tag{1.15}$$

b. Case 2

In this case, the oxidation kinetics is purely controlled by diffusion and the initial oxide grown during the transient period $(t < t_i)$ has less protective properties as during the oxide growing period $(t > t_i)$.

$$\frac{d\Delta m}{dt}\frac{1}{S} = \frac{k_p S}{2(\Delta m - \Delta m_i)} \tag{1.16}$$

$$\left(\frac{\Delta m - \Delta m_i}{s}\right)^2 = k_p(t - t_i) \tag{1.17}$$

c. Case 3

In this case, the oxidation kinetics is simultaneously controlled by diffusion step and interfacial reaction step and the initial oxide grown during the transient period $(t < t_i)$ has the same protective properties as the oxide growing period $(t > t_i)$.

$$\frac{d\Delta m}{dt}\frac{1}{S} = \frac{1}{\frac{1}{k_1} + \frac{2\Delta m}{k_p S}} \tag{1.18}$$

$$t - t_i = \left(\left(\frac{\Delta m}{s}\right)^2 - \left(\frac{\Delta m_i}{s}\right)^2\right)\frac{1}{k_p} + \frac{\Delta m - \Delta m_i}{k_1} \tag{1.19}$$

d. Case 4

In this case, the oxidation kinetics is controlled by diffusion step and interfacial reaction step and the initial oxide grown during the transient period $(t < t_i)$ has less protective properties as the oxide growing period $(t > t_i)$.

$$\frac{d\Delta m}{dt}\frac{1}{S} = \frac{1}{\frac{1}{k_1} + \frac{2(\Delta m - \Delta m_i)}{k_p S}} \tag{1.20}$$

$$t - t_i = \left(\frac{\Delta m - \Delta m_i}{s}\right)^2 \frac{1}{k_p} + \frac{\Delta m - \Delta m_i}{k_1} \tag{1.21}$$

In these cases, $\Delta m$ is the difference of mass after oxidation, $\Delta m_i$ corresponds to initial mass difference, S is the surface area, t is time, $t_i$ corresponds to the time of initial oxide grown during the transient period, $k_1$ is linear constant of the oxide layer growth and $k_p$ corresponds to parabolic constant of the oxide layer growth.

The case 4 is the most general case. If none of the cases matches with the experimental results, it should be considered that $k_p$ is a parameter that evolves with time rather than a constant.

### 1.1.3 Reactive elements

The performance of thermal oxide layers is characterized by their ability to resist to oxidation at high temperature and is strongly related to their ability to remain adherent to the substrate. It has been shown that the addition of certain reactive elements improves the performance of oxide layers [19, 20]. Reactive elements are elements with a higher oxygen reactivity. They are rare earth elements such as zirconium, yttrium, etc. These elements can be introduced into metallic materials by different ways: in the mass, as an alloying element which is added at the time of elaboration, by ion implantation, or by surface deposition [17]. Whatever the mode of introduction, the reactive elements are found at the grain boundaries of the oxide layer and at the metal/oxide interface [21]. Irrespective of their chemical nature, the most important effect of the addition of these elements is that the adhesion of the oxide layer to the metal substrate is greatly improved [22]. Moreover, it has been shown that a small amount of these elements (0.01 to 0.5% by weight) is sufficient to achieve considerable positive effects [23].

In this thesis, the studied alloy is nickel based NiCr alloy. The influence of reactive elements for NiCr alloy mainly includes the following aspects.

a. Decreasing spaces

It has been proposed that rare earth element oxide particles are preferential sites for nucleation of the first chromium oxide nuclei. These preferential sites reduced the space between the nuclei of this oxide so that the time required to form a continuous oxide layer is shorter [24-26]. This accelerates the formation of the protective film, and also makes it possible to eliminate the oxidation of the basic elements of the alloys (nickel). Therefore, the minimum quantity of chromium needed to form a continuous and protective layer is reduced.

b. Decreasing growth rates

Numerous studies carried out on different chromium alloys have shown that in the presence of reactive elements such as yttrium [27-30], cerium [22, 31, 32], neodymium [33,34], lanthanum [35, 36], zirconium [22, 31] or thorium, the growth kinetics of the chromium oxide layer are 10 to 100 times lower than those of based alloys. The mass increase are considerably reduced, mainly above 900°C.

Pint's theory of "dynamic segregation" is one of the principal theories that explain this effect [18]. In general, oxides of reactive elements segregate at the grain boundaries of chromium oxide. Since the reactive element ions are larger than chromium ions, they diffuse very slowly, through the grain boundaries, towards the external interface, which strongly slows down the diffusion of chromium ions. The growth of the layer is then controlled by the internal diffusion of oxygen anions, which leads to a decrease in oxidation kinetics. These phenomena of segregation at grain boundaries have been demonstrated by transmission electron microscopy (TEM) [37, 38].

c. Modifying microstructure

Due to the segregation of the reactive elements at the grain boundaries and their role as preferential sites for the nucleation of the oxide grains, the microstructure of the oxide film is modified because the growth of the grains is limited by the mobility of their boundaries. As a result, the oxide layer formed with reactive elements has an equiaxed microstructure, which makes the grain size 2 to 5 times smaller than that of the based alloys.

d. Improving adhesion

Generally speaking, an oxide layer is adherent while it is not delaminated from its substrate, which means that the metal/oxide interface remains adherent. It has been shown that the addition of reactive elements increases the adhesion of the oxide layer to the substrate. Because of the segregation of reactive elements at the grain boundaries, the outward transport of cation is blocked. Therefore, the formation of voids or pores at the metal/oxide interface is eliminated [39]. In addition, the high affinity of the reactive elements for sulfur allows them to trap or bind such impurities, which prevent their interaction with other elements in the alloy [39]. Furthermore, the presence of a reactive element could reduce the level of stress that may be the reason for the loss of adhesion of the oxide layers.

## 1.2 Stress development and relaxation in the oxide layer and metal layer

It has been known for many years that stress exists in both metal and oxide layers after high temperature oxidation. However, the origin of stress generation and relaxation still needs to be better understood. There are two main sources among many of driven stresses in the oxide layer: growth stress due to the growth of the oxide; thermal stress due to mismatch between the different thermal expansion coefficients between the oxide and the metal substrate when the temperature changes. For the metal layer, except the balance with the stress in the oxide layer, another stress source can be considered: the diffusion stress due to the depletion of chromium in the metal layer, for which very few work has been devoted [40] and it will be mainly discussed in chapter 4.

## 1.2.1 Stress sources

### 1.2.1.1 Elastic part

Elasticity behaviour is the cornerstone of all discussions both at the macro scale and at the micro scale, which provides a relationship between elastic strain and stresses. The classical Hooke model is used for the elastic strain $\varepsilon^{\mathrm{elastic}}$ in the metal and in the oxide [41], for an in-plane stress:

$$\varepsilon^{elastic} = \left(\frac{1-\nu}{E}\right)\sigma \tag{1.22}$$

In a rate formalism [42], by use of the time derivative of Eq.1.22, it leads to:

$$\frac{d\varepsilon^{elastic}}{dt} = \frac{d}{dT}\left(\frac{1-\nu}{E}\right)\frac{dT}{dt}\sigma + \left(\frac{1-\nu}{E}\right)\frac{d\sigma}{dt} \tag{1.23}$$

To obtain this equation, Poisson's ratio ν is supposed to be temperature independent and Young's modulus E is supposed to be temperature dependent, according to a polynomial function [3]:

$$E(T) = a_0 - a_1 T - a_2 T^2 \tag{1.24}$$

where $\mathrm{a_i}$ are constant and temperature independent.

### 1.2.1.2 Thermomechanical part

Thermal stresses are generated during the temperature variations due to the difference of thermal expansion coefficients between the oxide and the metal substrate, especially during the cooling period after oxidation. In general, the thermal expansion coefficient of the metal is higher than that of the oxide, which means $\alpha_m > \alpha_{ox}$. Therefore, during cooling, the oxide layer is in compression and the metal in tension. The greater the difference between these coefficients, the more significant are the generated thermal stresses.

For thermal strain $\varepsilon^{\mathrm{thermal}}$ in the metal and in the oxide, classical thermal expansion is considered [41]:

$$\frac{d\varepsilon^{thermal}}{dt} = \alpha(T)\frac{dT}{dt} \tag{1.25}$$

A rate formalism has been applied. The thermal expansion coefficient α may vary with temperature T [41] with a polynomial function:

$$\alpha(T) = b_0 - b_1 T - b_2 T^2 \tag{1.26}$$

where $\mathrm{b_i}$ are constants and temperature independent.

### 1.2.1.3 Growth strain part for oxide

a. Pilling and Bedworth model

Pilling and Bedworth first proposed a growth strain model [43]. The model is based on the molar volume difference between the oxide and the metal and the relation (Eq.1.27) has been established to describe the ratio (known as Pilling and Bedworth ratio) between these volumes:

$$PBR = \frac{V_M(oxide)}{V_M(metal)} \tag{1.27}$$

$$\varepsilon^{growth} = \sqrt[3]{PBR} - 1 = \varepsilon_{xx} = \varepsilon_{yy} = \varepsilon_{zz}(isotropic\ strain) \tag{1.28}$$

where $V_M(oxide)$ is the molar volume of oxide, $V_M(metal)$ is the molar volume of metal and $\varepsilon^{growth}$ is the growth strain. The following Table 1.1 shows some Pilling-Bedworth ratios (PBR) for some common metals:

Table 1.1 Pilling-Bedworth ratios (PBR) for some common metals [5]

| Oxide | Pilling-Bedworth ratios |
|---|---|
| MgO | 0.81 |
| $Al_2O_3$ | 1.28 |
| NiO | 1.65 |
| FeO (on α-Fe) | 1.68 |
| $Fe_2O_3$ (on α-Fe) | 2.14 |
| $Fe_3O_4$ (on α-Fe) | 2.10 |
| $TiO_2$ | 1.70-1.78 |
| CoO | 1.86 |
| $Cr_2O_3$ | 2.07 |

Table 1.1 compares Pilling-Bedworth ratios (PBR) for some common metals. The table shows that for most of those metals the PBR ratio is greater than 1, which means that the oxide has a larger molar volume than that of the substrate. For a purely elastic problem, the stress may be calculated as:

$$\sigma_{ox} = -\frac{E_{ox}}{1-\upsilon_{ox}}\left(\omega\left(\sqrt[3]{PBR} - 1\right)\right) \tag{1.29}$$

where $\sigma_{ox}$ is the stress in the oxide layer, $E_{ox}$ corresponds to Young's modulus of the oxide, $\upsilon_{ox}$ is Poisson's ratio of the oxide, $\omega$ corresponds to a corrective factor and $\left(\sqrt[3]{PBR} - 1\right)$ is the growth strain. As the Eq.1.28 shows, a PBR ratio greater than 1 leads to a positive $\varepsilon^{growth}$ at the oxide/metal interface and therefore introduces a compressive stress in the oxide layer.

However, there are some weak points that must be mentioned. The model supposes isotropic growth of the oxide film and the associated strain occurs only at the metal/oxide interface. According to the model, the oxide layer grows only because of anionic diffusion. However, oxide layers can also grow by external diffusion or a mixed mechanism. In addition, the oxide is formed both at the external surface (oxide/air surface) and at the internal oxide/metal interface [4, 42]. As for the magnitude of the associated stresses, the stress values obtained are largely overestimated, because the stress relaxation mechanisms that may occur during growth are not taken into account by use of Eq.1.29.

### b. Epitaxy mechanism

The growth stresses can be related to the difference in crystallographic parameters between the metal and the oxide film (epitaxy). The strain resulting from lattice incompatibility between the oxide layer and the metallic substrate at the metal/oxide interface [45] is shown in Fig.1.3.

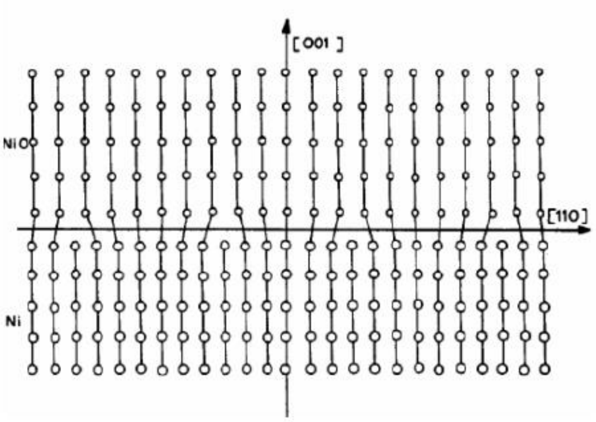

Figure 1.3: Lattices epitaxial arrangement for NiO/Ni system [45]

The difference in lattice parameters at the interface leads to a mismatch strain. The determination of the patterns of the oxide and metal lattices allows localizing these stresses around the interface. The stresses can be either compressive or tensile according to the epitaxy relationship.

This mechanism is important for thin layers and negligible when the oxide films become thick (thickness greater than 1µm). For $Cr_2O_3$/NiCr system, such epitaxy relationships have been observed between metal and oxide for the Ni20Cr/$Cr_2O_3$/$NiCr_2O_4$ system between 600°C and 900°C [46]. However, for some materials, such as pure nickel, epitaxy persists even when the NiO layer becomes thicker [4].

### c. Oxide developing with diffusion phenomena

Clarke et al [47, 48] have proposed an approach based on geometric microstructural considerations. They assumed that a mixed flow of anionic and cationic diffusion occurs to form the oxide in the grain boundaries. As a result, a significant in-plane growth strain is generated because of the cations and anions trapped inside these joints.

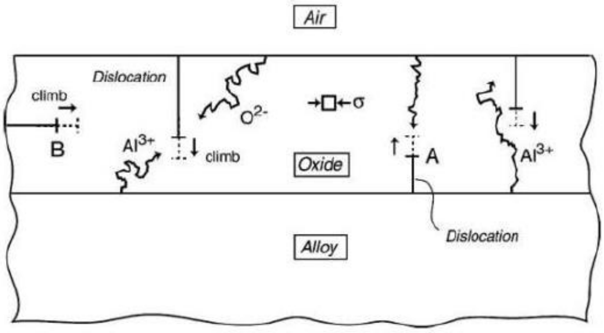

Figure 1.4 Illustration of Clarke's mechanism [48]

Fig.1.4 shows that the climb of edge dislocation is due to the reaction of metal ions and oxygen in the grain boundaries. An in-plane strain is generated when the dislocations show a Burgers vector parallel to the interface. The growth strain proposed by Clarke is:

$$\frac{d\varepsilon^{growth}}{dt} = \frac{Ar\theta}{ab2(\Delta x)}\frac{dh_{ox}}{dt} \tag{1.30}$$

where $\varepsilon^{growth}$ is the growth strain, A is the cross-section for a diffusing cation to attach to the dislocation core, r is the ratio of the outward cationic flux to the inward oxygen flux, θ is the disorientation angle between grain boundary and surface, *a* is the average distance between traps, *b* is the Burgers vector of the dislocation, 2(Δx) is the average thickness of grain boundaries and $h_{ox}$ is the thickness of the oxide layer.

The identification of these different coefficients is difficult. Therefore, a more general explanation is expected. The Clarke approaches has been verified and generalized by Panicaud et al. [49]. The growth strain rate is proportional to the oxide layer kinetics:

$$\frac{d\varepsilon^{growth}}{dt} = D_{ox}(T)\frac{dh_{ox}}{dt} \tag{1.31}$$

For the growth strain parameter $\mathrm{D_{ox}}$, it is more difficult to explicit the expression because the mechanisms depend on the considered system. We know that the $\mathrm{D_{ox}(T)}$ parameter depends on microstructural features and may also depend on temperature [50]. The temperature dependence $\mathrm{D_{ox}(T)}$ adapted to the present material may be:

$$D_{ox}^{-1} = D_{ox0}^{-1}\,exp\left(-\frac{Q_D}{RT}\right) \tag{1.32}$$

where $\mathrm{D_{ox0}}$ is an initial parameter for the present oxide, as proposed in [50]. $\mathrm{Q_D}$ corresponds to an activation energy for the growth strain parameter. The $\mathrm{D_{ox}}$ parameter may be also related to the ratio of the cationic/anionic flux occurring within the grain boundaries as the oxide layer grows [48]. Since both flows follow an Arrhenius dependence, the current activation energy in Eq.1.32 may be interpreted as the difference between the values associated to the anionic and cationic flows.

The oxide thickness $\mathrm{h_{ox}}$ often follows a parabolic evolution with oxidation time t that has already been experimentally evidenced for the present material with experimental characterization by Thermal Gravimetric Analysis [50, 51]. This aspect is discussed In chapter 2. $\mathrm{h_{ox}}$ is the thickness of the oxide layer evolving with time according to:

$$\frac{dh_{ox}}{dt} = \frac{Ap}{2\sqrt{t}} + \frac{dAp}{dT}\frac{dT}{dt}\sqrt{t} \tag{1.33}$$

with Ap the parabolic kinetics parameter that varies with temperature T in the range of studied temperature.

## 1.2.2 Stress relaxation

Stress relaxation phenomena are important phenomena that reduce the level of stresses both during oxidation and during cooling. First, the stresses can be relaxed by non-destructive relaxation mechanisms. The layers remain adherent. This type of relaxation is the result of high-temperature viscoplastic (creep) strains of the metal/oxide system. Destructive relaxation mechanisms may also occur and lead to the loss of integrity of the oxide layer: cracking, buckling, spalling, etc. [52, 53]. In principle, these delamination phenomena become active when the stresses exceed a certain critical limit for which viscoplastic strains are no longer sufficient to relax the system.

### 1.2.2.1 Non-destructive relaxation phenomena

The viscoplastic strain (creep) of the metal and the oxide contribute to the relaxation of the stress of the system [54]. Viscoplastic strain is defined as an irreversible and permanent strain, with time delay, for mechanical loading at a given temperature [55]. The measurement of the associated strain rate as a function of time allows to describe the viscoplastic behavior of the material. The viscoplastic relaxation depends on the nature of the material, its microstructure, the temperature and the stress level [55].

Generally speaking, at the approximately 35% of the melting temperature, the viscoplastic strain occurs to relax the stresses in these materials [54]. For a given stress, the curve obtained from a creep test is characterized by three main stages: first stage in which the strain rate decreases, second stage in which this rate is assumed to be constant, and last stage in which the strain rate increases continuously until failure (Fig.1.5) [56].

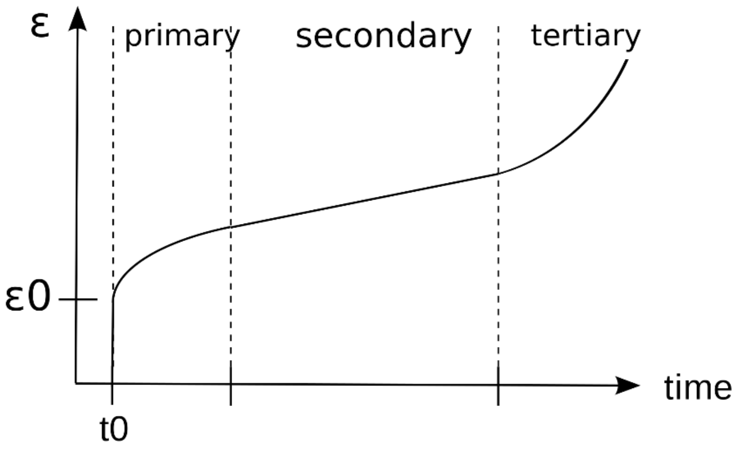

Figure 1.5 Strain as a function of time in a creep test with different stages

As shown in Fig.1.5, a primary creep stage, also called transient creep, is the initial stage during which the hardening of the material causes a decrease in strain rate. The secondary creep stage, also known as the steady state, is when the strain rate is constant. In the third stage, the strain rate increases because of necking phenomena until the failure point.

At high temperature, the viscoplastic behavior of a material is determined by the evolution of the strain rate corresponding to the second stage [57, 58]. A Norton-Hoff power law is often used to simulate the corresponding viscoplastic strain $\varepsilon^{viscoplastic}$, as usually considered in the metal and in the oxide [41], for an in-plane stress:

$$\frac{d\varepsilon^{viscoplastic}}{dt} = sign(\sigma)J|\sigma|^N = \frac{1}{2}sign(\sigma)\left(\frac{|\sigma|}{K}\right)^N \text{ and } N \in R \tag{1.34}$$

where J and K are the creep parameters ($\mathrm{J} = \frac{1}{2}\left(\frac{1}{\mathrm{K}}\right)^{\mathrm{N}}$) and N is the Norton exponent. It is already a rate form. We assume that stress release is caused mostly by creep diffusion in the oxide layer, which is regulated by the transport of chemical species along grain boundaries. The same approach as described in Refs. [57-59] has been applied. The Norton coefficient J for the oxide is given by:

$$J_{ox} = \frac{AD_0\delta\Omega}{k_BT}\left(\frac{1}{L}\right)^3 exp\left(-\frac{Q}{RT}\right) \tag{1.35}$$

where A is Coble constant without dimension, $\mathrm{D_0}$ is diffusion coefficient, $\delta$ is the grain boundary average thickness, $\Omega$ is the molar volume, $\mathrm{k_B}$ is Boltzmann constant, L is the grain size and Q is the activation energy of the mechanism.

### 1.2.2.2 Destructive relaxation phenomena

In general, any phenomenon leading to the delamination of oxide layers from their substrates is a destructive relaxation mechanism. These destructive relaxation mechanisms can have different ways such as buckling, peeling and cracking of the layers. When the stresses generated in the oxide films are too high, these destructive phenomena occur to relax the stresses. Therefore, the service lifetime of thermal oxide layers depends on their ability to resist these delamination phenomena [60, 61].

- Buckling : delamination between substrate and oxide layer as shown in Fig.1.6

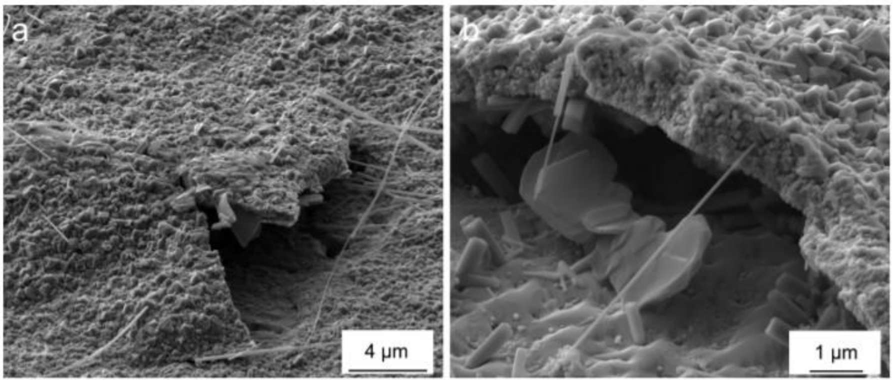

Figure 1.6 SEM images showing two cases of local buckling and spallation of the oxide layer [62]

The existence of voids at the metal/oxide interface decreases the contact surface between the metal and the oxide, which will progressively lead to the delamination of the layer from its substrate. These voids are considered as areas of high stress concentration, which causes the initial cracking at the metal/oxide interface. According to the buckling mechanics described by Evans and Schütze [60, 61, 63], the existence of these voids can lead to a local delamination of the layer. In addition, they may cause buckling of the oxide layer when the stress exceeds a critical limit. However, these limits depend on the temperature, the thickness and structure of the oxide layer, the cooling rate etc. [60, 64-66]. Moreover, it has been shown that the viscoplastic strain in the oxide layer above a certain temperature can slow down these buckling phenomena.

- Peeling : local spalling for oxide layer on a substrate

When these stresses exceed the elastic limit of the layer, cracks may appear and the stress will release from the oxide layer peeling from the substrate. The appearance of these cracks is often related to the existence of physical defects in the metal/oxide system, such as voids and microcracks. Some work has shown that the cooling rate has a significant impact on spalling by cracking for alloys such as FeCrAl alloy and NiCrAl alloy [60, 65, 66]. When these stresses are too high, buckling of the oxide layer can lead directly to peeling. The substrate is then exposed and re-oxidation occurs [67] as shown in Fig.1.7.

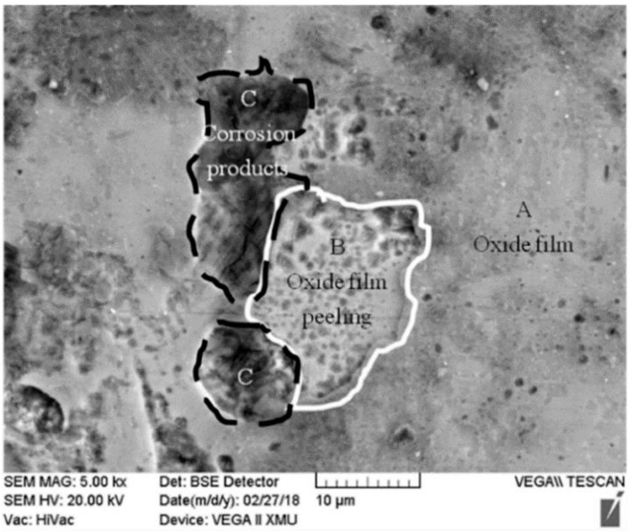

Figure 1.7 SEM morphology of Ti-6Al-4V titanium alloy after hot corrosion for 4 h [68]

### 1.2.3 Thermomechanical modeling

In this part, a methodology for developing thermomechanical model is presented. Based on some assumptions of the model, the different material behaviors such as elasticity, viscoplasticity, growth stress and thermal expansion are considered. In addition, the temperature influence on the material performances is also considered. After that, the strain continuity and mechanical balance equation are discussed. Finally, to agree with our cases, the analytical solution for isothermal case is obtained.

To obtain an accurate thermomechanical modelling, general hypotheses are considered:

- In each material, the system is isotropic and homogeneous; in other words, it has the same material properties in all directions and for all positions.
- For all the materials, the system is under in-plane stress condition. The average stress can ideally be calculated by considering the influence of a stress gradient. However, only an in-plane stress is here taken into account. The stress gradient will be discussed in chapter 4.
- For all the materials, the system has neither elastic limit nor hardening behavior; its behavior is directly elasto-viscoplastic.
- For oxide layer, the oxidation kinetics are assumed to be mainly parabolic [49, 69, 70].

### 1.2.3.1 Continuity condition

To systematically ensure the continuity condition during all the oxidation time of the metal, the additional most important assumptions are:

- The two-dimensional effects such as rumpling are not considered.
- For all the materials, non-linear mechanical phenomena (buckling, cracking, spalling) are not considered, which agrees with the observations on our systems.
- For metal layer, the chemical strain due to the diffusion of chromium is not considered.

Moreover, temperature may evolve with time, but no space gradient of temperature is considered. Because of the adherence between oxide layer and metallic substrate, after calculations, the continuity equation can be expressed as, for all time:

$$\varepsilon_m = \varepsilon_{ox} \tag{1.36}$$

The indices "ox" and "m" refer to the oxide layer and the metal layer respectively. With the proposed strain decomposition, it leads to:

$$\left(\varepsilon^{elastic} + \varepsilon^{viscoplastic} + \varepsilon^{thermal}\right)_m = \left(\varepsilon^{elastic} + \varepsilon^{viscoplastic} + \varepsilon^{thermal} + \varepsilon^{growth}\right)_{ox} \tag{1.37}$$

where $\varepsilon^{elastic}$ represents the elastic strain in the layer or in the metal layer, $\varepsilon^{viscoplastic}$ represents the viscoplastic strain in the layer or in the metal layer, $\varepsilon^{thermal}$ represents the thermal strain in the layer or in the metal layer and $\varepsilon^{growth}$ represents the oxide growth strain only in the oxide layer. In a rate formalism, it corresponds to:

$$\left(\frac{d\varepsilon^{elastic}}{dt} + \frac{d\varepsilon^{viscoplastic}}{dt} + \frac{d\varepsilon^{thermal}}{dt}\right)_m = \\ \left(\frac{d\varepsilon^{elastic}}{dt} + \frac{d\varepsilon^{viscoplastic}}{dt} + \frac{d\varepsilon^{thermal}}{dt} + \frac{d\varepsilon^{growth}}{dt}\right)_{ox} \tag{1.38}$$

In order to solve this time-related stress equation, we have to take into account the behavior models for both materials. The discussion about the different strain compositions and the temperature influence on the material performances has been discussed before in section 1.2.1 and section 1.2.2, which is not repeated here.

### 1.2.3.2 Mechanical balance

To calculate the stresses evolution during the oxidation of a metal, the additional most important assumptions are:

- The system has an isotropic and biaxial behavior (stress state).
- Symmetrical oxidation of the two metallic sides is considered.

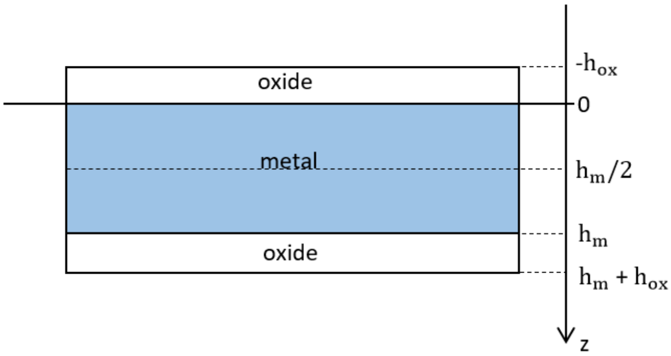

Figure 1.8 Geometry for the oxide growing on a metal

Fig.1.8 presents the geometry for the oxide growth on a metal. Thus, the equation of mechanical balance can be expressed as:

$$\int_0^{h_m} \sigma_m(z)dz + \int_{-h_{ox}}^{0} \sigma_{ox}\, dz + \int_{h_m}^{h_m+h_{ox}} \sigma_{ox}\, dz = 0 \tag{1.39}$$

Where $\sigma_{ox}$ is the stress in the oxide, $h_{ox}$ is the oxide thickness that depends on time t, $\sigma_m(z)$ is the stress in the substrate that depends on z, and $h_m$ is the thickness of the substrate [71]. The influence of the oxide on the top and bottom surfaces is the main effect, which causes the apparition of residual stresses parallel to the oxide-metal interface in the metal. By considering a homogeneous stress ($\sigma_m$) distribution in metal and oxide, the mechanical balance equation overall metal and oxide can be expressed as:

$$\sigma_m h_m + 2\sigma_{ox} h_{ox} = 0 \tag{1.40}$$

A symmetric oxidation is considered, thanks to the coefficient 2 in the mechanical balance in Eq.1.41. In rate form, it corresponds to:

$$\dot{\sigma}_m h_m + 2\dot{\sigma}_{ox} h_{ox} + 2\sigma_{ox}\dot{h}_{ox} = 0 \tag{1.41}$$

Moreover, because of $h_m$ and $h_{ox}$ are positive number, we necessarily have:

$$signe(\sigma_m) = -signe(\sigma_{ox}) \tag{1.42}$$

### 1.2.3.3 Analytical solutions

For further application, we propose to solve this problem under isothermal condition. Eq.1.22 – 1.42 are simplified to obtain the equation describing the oxide stress evolution with time. It leads to an ordinary differential equation:

$$\dot{\sigma}_{ox}=\frac{\frac{\sigma_{ox}}{t}\frac{1-\nu_m}{E_m}-signe(\sigma_{ox})\left(\frac{h_m}{Ap\sqrt{t}}\right)^{1-N_m}J_m|\sigma_{ox}|^{N_m}+signe(\sigma_{ox})J_{ox}|\sigma_{ox}|^{N_{ox}}\frac{h_m}{Ap\sqrt{t}}+\frac{D_{ox}h_m}{2t}}{\left(\frac{1-\nu_{ox}}{E_{ox}}\frac{h_m}{Ap\sqrt{t}}+2\frac{1-\nu_m}{E_m}\right)} \quad (1.43)$$

There are 1 geometrical parameter and 10 material parameters to be identified: $\mathrm{h_m}$, $\mathrm{\nu_m}$, $\mathrm{E_m}$, $\mathrm{\nu_{ox}}$, $\mathrm{E_{ox}}$, $\mathrm{Ap}$, $\mathrm{J_m}$, $\mathrm{N_m}$, $\mathrm{J_{ox}}$, $\mathrm{N_{ox}}$ and $\mathrm{D_{ox}}$.

$\mathrm{h_m}$ is the thickness of metal part, which can be easily measured and is supposed to be constant. Numerical values of Young's modulus of oxide $Cr_2O_3$ ($\mathrm{E_{ox}}$) and Poisson's ratio of oxide $Cr_2O_3$ ($\mathrm{\nu_{ox}}$) can be found in literature [72]. Numerical values of the others parameters can also be found in literature [69] for raw material and for different temperatures, such as the Young's modulus of metal ($\mathrm{E_m}$), Poisson's ratio of metal ($\mathrm{\nu_m}$), the parabolic kinetics parameter (Ap), the creep parameter of oxide $Cr_2O_3$ ($\mathrm{J_{ox}}$), the Norton exponent of oxide $Cr_2O_3$ ($\mathrm{N_{ox}}$), the creep parameter of metal ($\mathrm{J_m}$), the Norton exponent of metal ($\mathrm{N_m}$) and the growth strain parameter for oxide $Cr_2O_3$ ($\mathrm{D_{ox}}$).

From this equation, we can obtain simple analytical solutions for some asymptotic cases (short time or long time of oxidation) [42, 50, 51]. For general resolution of this equation, a numerical approach is more useful.

## 1.3 Determination of stresses

### 1.3.1 Determination of stresses by X-Ray Diffraction measurements

There are many works that explain the principle of X-ray diffraction (XRD) [73, 74]. XRD is widely used to measure the elastic strain in crystalline materials [75-77].

In order to introduce how to determine the stress in crystalline material, the basic information of X-ray diffraction should be known. X-rays are high-energy electromagnetic waves with a wavelength between $10^{-3}$ and $10^{1}$ nm. To generate stable X-rays, sealed tubes and rotating anodes is often used in university laboratory or synchrotron radiation sources is used in national or international institute like European Synchrotron Radiation Facility (ESRF).

The principle of measurement of the elastic strain in crystalline material is based on X-ray diffraction of the periodic atomic plane and detection of the angular or energy resolution of the diffraction signal as shown in Fig.1.9. The relationship between lattice spacing and the angle of the diffracted beam is given by W.L. Bragg [78].

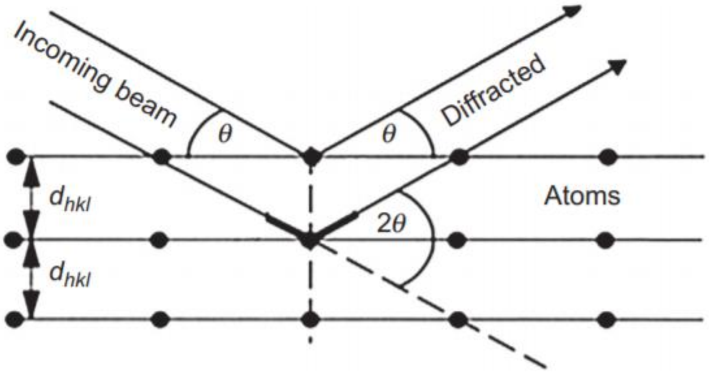

Figure 1.9 Geometrical condition for diffraction from lattice planes [79]

where θ is the angle of the diffracted beam and $d_{hkl}$ is the interreticular distance between two nearest planes of the lattice. The Bragg's law is:

$$n\lambda = 2d_{hkl}\sin(\theta) \tag{1.44}$$

where n is an integer number and $\lambda$ is the wavelength of the X-ray. The signal of diffused rays will be enhanced in phase only if the path difference is equal to an integer n of wavelengths and the diffraction data are often represented as intensity distribution versus the 2θ angle.

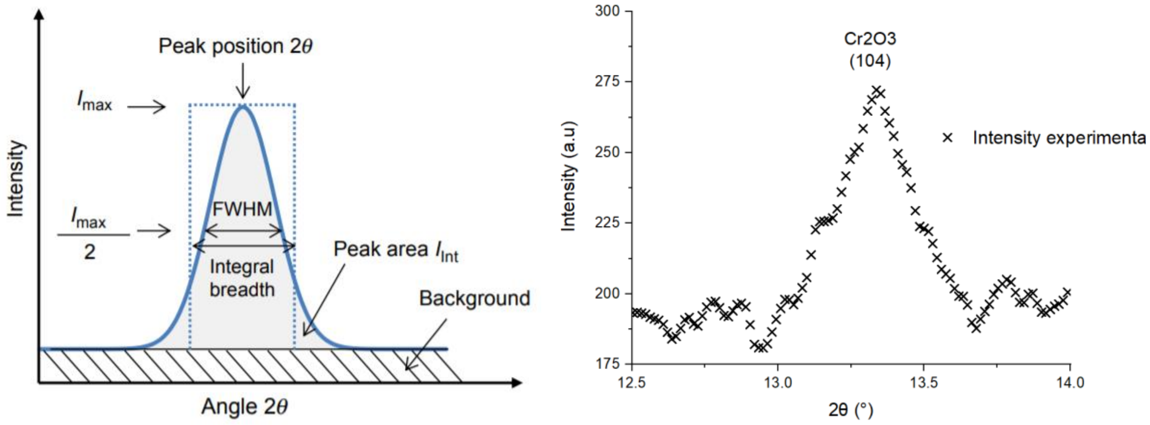

(a) (b)

Figure 1.10 Diffraction peak intensity distribution versus 2θ angle (a) in theory [75], (b) from experimental results

As shown in Fig.1.10, a lot of information can be obtained, such as the maximum peak intensity $I_{max}$, the peak position 2θ, the full width at half maximum FWHM etc. For us, the most interesting parameter is the peak position 2θ. As for the experimental results, peak is necessary to be fitted in order to extract the information. Knowing the peak position 2θ, the interreticular distance $d_{hkl}$ between two nearest planes of the lattice can be calculated. Therefore, by the measurement, the change of the interreticular distance allows us to determine the strain in a given direction, as shown in Fig.1.11.

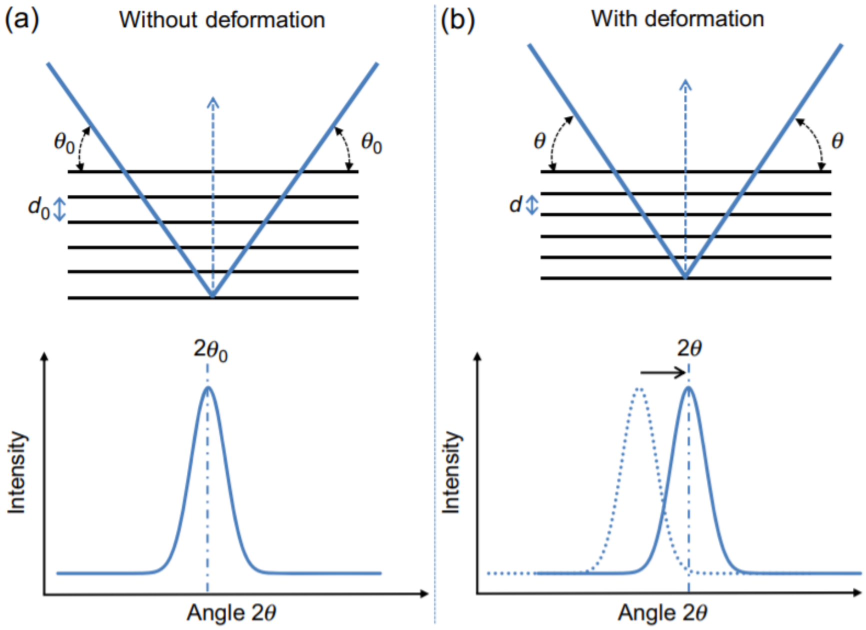

Figure 1.11 Illustration of the diffraction of a given hkl plane: (a) for a stress-free lattice; (b) for a lattice under compressive stresses [75]

After knowing the difference of the interreticular distance for a lattice under compressive stresses, the stresses can be obtained by several steps of calculation such as converting the difference of the interreticular distance into strain. The associated stress can be determined thanks to the $\sin^2\psi$ method, and using the radiocrystallographic elastic coefficients. These will be introduced in details in chapter 2.

The experimental geometry of the system is presented in Fig.1.12 for illustration. The mode used is in reflexion. The samples of plane geometry are at a fixed distance of an area detector. The energy of 20 keV (optimum for photons flux on BM02) is well adapted to optimize the film response. A XRD diagram has been recorded using an area detector (FReLoN, ESRF, Grenoble, France), which is large enough to extract the stresses evolution in both the film and the metal, and rapid enough to obtain data in real time, as in previous experiments [42].

Because the material consists of randomly oriented crystallites, Bragg's law is applied to evaluate the changes of distance between crystallographic planes and taking into account the diffraction geometry. Then, rings are obtained with the help of an area detector (Fig.1.12). From [19], a relation is given to transform ψ as a function of θ and γ.

$$\cos\psi = \sin(\theta)\sin(\omega) + \cos(\gamma)\cos(\omega)\cos(\theta) \qquad (1.45)$$

ψ is the angle between the normal to the surface and the normal to the diffracting planes, 2θ is the angle between the incident beam and the diffracted beam, ω is the incident angle, and γ is the angle between the vertical passing through the position of the direct beam and a given position on the diffraction ring.

Thus, each gamma value is related to ψ and the diffraction patterns are fitted for each ψ value, to obtain the corresponding d-spacing. In the present study, the measured strain corresponds to the average through a depth of a few microns below the surface of the metallic sample.

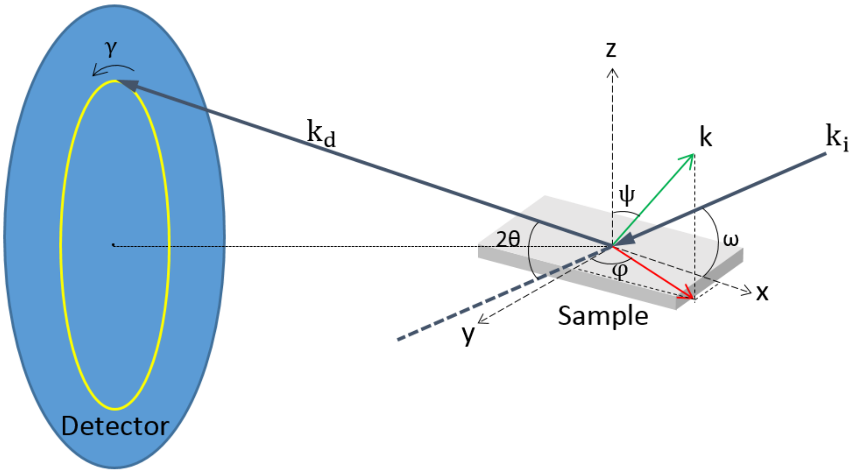

Figure 1.12 Geometrical configuration of the experiments performed at ESRF. Details on this configuration can be found in [76, 77].

### 1.3.2 Calculation of stress by Runge-Kutta numerical solutions

In numerical analysis, the Runge–Kutta methods are a family of implicit and explicit iterative methods [80, 81]. These methods were developed around 1900 by the German mathematicians Carl Runge and Wilhelm Kutta. The most widely known member of the Runge–Kutta family is generally referred to as "RK4", the "classic Runge–Kutta method" or simply as "the Runge–Kutta method". The problem given by Eq.1.43 can be solved by using the Runge–Kutta method, which can be expressed as:

$$\dot{\sigma}_{ox} = f(\sigma_{ox}(t), t),\ \sigma_{ox}(t_0) = \sigma_0 \tag{1.46}$$

where $\sigma_{ox}$ is an unknown function of time t; $\dot{\sigma}_{ox}$ is the derivative function of the stress depending on t and $\sigma_{ox}$ itself; at the initial time $t_0$, $\sigma_{ox}$ has the value $\sigma_0$ and the function f, $t_0$ and $\sigma_0$ are known. To solve this kind of problem, a classical Runge-Kutta resolution scheme is thus applied [80, 81].

$$\begin{cases} \sigma_{ox,n+1} = \sigma_{ox,n} + \frac{\Delta t}{6}(k_1 + 2k_2 + 2k_3 + k_4) \\ k_1 = f(t_n, \sigma_{ox,n}) \\ k_2 = f\left(t_n + \frac{\Delta t}{2}, \sigma_{ox,n} + \frac{\Delta t}{2} k_1\right) \\ k_3 = f\left(t_n + \frac{\Delta t}{2}, \sigma_{ox,n} + \frac{\Delta t}{2} k_2\right) \\ k_4 = f(t_n + \Delta t, \sigma_{ox,n} + \Delta t k_3) \\ t_{n+1} = t_n + \Delta t, n = 0,1,2,3 \ldots \end{cases} \tag{1.47}$$

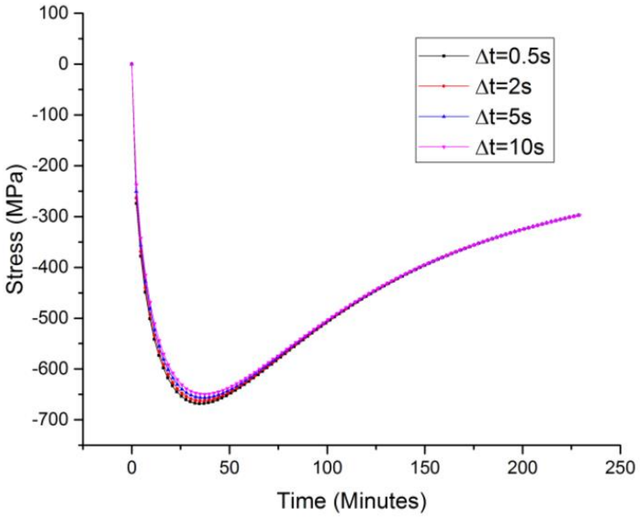

Figure 1.13 Time step influence on an external growth in the oxide for isothermal conditions

The influence of the time step has been tested. Fig.1.13 shows that by changing the time step Δt, the evolution of simulation is quite similar. It is known that a smaller time step leads to a more accurate numerical calculation, which is obviously a disadvantage to the total calculation time. The results indicate that the difference is only significant for the inflection zone. Moreover, the precision increases with the reduction of the time step, its choice has a very small influence, which enables a good compromise with the total calculation time. Therefore, we will now assume that the influence of the time step is negligible if it is chosen relatively small. We will choose a time step of 0.5 seconds for the further calculations for a total oxidation time of several hours. By using the previous Runge-Kutta method, the numerical solution of Eq.1.43 can systematically be obtained.

### 1.3.3 Calculation of stresses by finite element simulations

In order to determine the stress in oxide and metal layer, the finite element method can also be applied. The finite element method (FEM) is the most widely used method for solving problems of engineering and mathematical models. For realizing the numerical simulation, the software ABAQUS is chosen. In addition, a user subroutine that is called the user-defined material model (UMAT) is used, which allows us to modify the input parameters of material models.

The Finite Element Method (FEM) is an approximate numerical method to solve mechanics problems governed by a set of partial differential equations (PDE), which is developed based on the rapid development of computers. These partial differential equations are the foundation of the common problems of solid and fluid mechanics [80, 81].

The development of Finite Element Method (FEM) and computer forms the basis of computational mechanics. The main ideas of finite element method are "numerical approximation" and "discretization".

Before the invention of the finite element method, all mechanical and engineering problems could only be solved by analytical solutions for partial differential equations. This kind of solution is mathematically demanding and depends strongly on a number of idealized assumptions. Instead, the finite element method discretizes the complex whole structure to a finite number of elements, and then applies the material model equations to each elements within the structure. After that, the response of the structure is solved by assembling all elements analysis and considering the boundary conditions. The response of each element can be obtained by individual mapping with the response of the total structure, so that mechanical and mathematical models of the complex structure can be avoided. In the work of [82], the total process can be described as:

a. Discretize the solution domain into elements

Discretization and the characteristics of the corresponding elements are also an important area of finite element research. The finite elements discretization of the whole structure are mainly divided in:

- 1D element
  - bar element ------ truss
  - beam element ------ frame
  - plate element ------ shell
- 2D element ------ plain stress and plain strain
  - triangle element
  - quadrilateral element
  - polygonal element
- 3D element) ----- 3D problem
  - tetrahedrons element
  - hexahedrons element
  - polyhedrons element

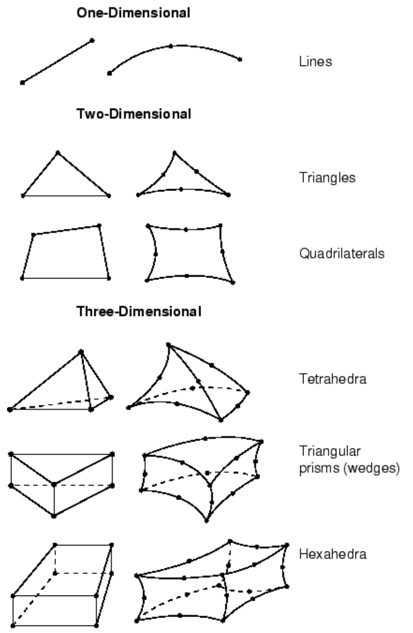

Figure1.14 Classification and element shape

The classification and element shape are shown in Fig.1.14. It can be seen that each element can increase the order of shape function (the number of nodes) to improve the accuracy.

b. Derive the element matrix equation

In each of those elements, an appropriate approximate function is selected. For example, a linear shape functions interpolation is applied in a triangular element [83] as shown in Fig.1.15.

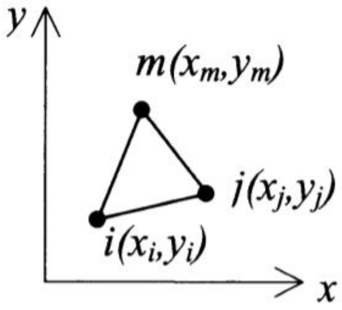

Figure 1.15 The linear triangular element [83]

For this kind of elements, the element stiffness matrix $[k]$ is given by:

$$[k] = \mathrm{A}[B]^T[D][B] \tag{1.48}$$

where A is the area of the element, which can be calculated by:

$$2A = x_i(y_j - y_m) + x_j(y_m - y_i) + x_m(y_i - y_j) \tag{1.49}$$

and matrix $[B]$ is :

$$[B]=\frac{1}{2A}\begin{bmatrix}\beta_i & 0 & \beta_j & 0 & \beta_m & 0\\ 0 & \gamma_i & 0 & \gamma_j & 0 & \gamma_m\\ \gamma_i & \beta_i & \gamma_j & \beta_j & \gamma_m & \beta_m\end{bmatrix} \tag{1.50}$$

with:

$$\begin{cases}\beta_i = y_j - y_m\\ \beta_j = y_m - y_i\\ \beta_m = y_i - y_j\\ \gamma_i = x_m - x_j\\ \gamma_j = x_i - x_m\\ \gamma_m = x_j - x_i\end{cases} \tag{1.51}$$

For cases of plane stress the matrix [D] is:

$$[\mathrm{D}]=\frac{E}{1-\upsilon^2}\begin{bmatrix}1 & \upsilon & 0\\ \upsilon & 1 & 0\\ 0 & 0 & \frac{1-\upsilon}{2}\end{bmatrix} \tag{1.52}$$

So that for a no charge element, the element matrix equation is presented as:

$$[k]\{u\}=0 \tag{1.53}$$

where $[k]$ is the element stiffness matrix, $\{u\}$ is node displacement vector.

c. Assemble the element matrix equation at every node

Once the global stiffness matrix $[K]$ is determined, we can assemble the element matrix equation at every node. For example, for a linear triangular element [83] with n nodes, there are two degrees of freedom at each node. Thus, the global stiffness matrix $[K]$ should be a matrix of size 2n*2n. In addition, the global element matrix is:

$$[K]\{U\}=\{B\} \tag{1.54}$$

where $[K]$ is the global stiffness matrix, $\{U\}$ corresponds to the global nodal displacement vector and $\{B\}$ is the global nodal boundary condition vector.

d. Solve the equations

The matrix equation Eq.1.54 is solved by methods such as Gaussian elimination [84, 85] and Gaussian quadrature [86], which is usually under the help of computer. Generally, the higher the order of the shape function is, the higher the approximation accuracy is. However, the number of control points and Gaussian integral points are also more numerous. In addition, the more precise the mesh of the elements is, the more accurate the approximate results are. Moreover, the computational time will increase as the shape function interpolation improving the accuracy of the finite element method.

Finally, once the unknown displacements and reactions are found, the stresses can be obtained and under the help of the FEM software, the results can be visualized.

Theoretically, there can be infinite possibilities in this field, because the pursuit of accuracy and numerical stability is infinite.

**References of chapter 1**

[1] C. Duhamel et al., Corrosion et protection des matériaux à haute température. Presses des Mines, 2011.
[2] M. Schütze, Protective Oxide Scales and Their Breakdown, NJ, 1991.
[3] P. Kofstadt, High Temperature Corrosion, London, 1998.
[4] A.M. Huntz, B. Pieraggi, Oxydation des matériaux métalliques, Hermès Science, Paris, 2003.
[5] N. Birks, G. H. Meier, and F. S. Pettit, Introduction to the High Temperature Oxidation of Metals. 2006.
[6] H. J. T. Ellingham, Reducibility of oxides and sulphides in metallurgical processes, London, 1944
[7] H. Svensson, P. Knutsson, K. Stiller, Oxidation of Metals 2009, 71, 143.
[8] F. H. Stott, Materials Science and Technology 1989, 5, 734.
[9] A. RAPP Robert, Corrosion 1965, 21, 382
[10] C. Wagner, Journal of the Electrochemical Society 1952, 99, 369.
[11] C. Wagner, Zeitshrift für Physik B21 1933, 25.
[12] L. Bataillou, C. Desgranges, L. Martinelli, D. Monceau, Corrosion Science 2018, 136, 148.
[13] K. Hauffe, Oxidation of Metals, 1995, 79.
[14] F.N. Rhines, R.G. Connell Jr., Journal of the Electrochemical Society 1977, 124, 93.
[15] F.N. Rhines, R.G. Connell Jr., M.S. Choi, Journal of the Electrochemical Society 1979, 126 1061.
[16] B. Roy, J. Das, R. Mitra, Corrosion Science 2013, 68, 231.
[17] S. Chevalier, Traitements de surface et nouveaux matériaux : quelles solutions pour lutter contre la dégradation des matériaux à haute température Dijon: Ed. Universitaires de Dijon, 2007.
[18] B. A. Pint, Oxidation of Metals 1996, 45, 1.
[19] J. Stringer, Materials Science and Engineering 1989, 120–121, 129.
[20] E. Lang, The role of active elements the oxidation behaviour of high temperature metals and alloys, London and New York, 1989.
[21] G. Bonnet, G. Aguilar, J. C. Colson, J. P. Larpin, Corrosion Science 1993, 35, 893.
[22] K. N. Straffordt and J. M. Harrison, Oxidation of Metals 1976, 10, 347.
[23] P. Y. Hou, Material Science 2011, 39, 696.
[24] M. J. Bennett and D. P. Moon, The role of active element on the oxidation behaviour of high temperature metals and alloys, Brussel and Luxembourg, 1989.
[25] D. P. Whittle, M. E. El-Dahshan, and J. Stringer, Corrosion Science 1977, 17, 879.
[26] P. Y. Hou and J. Stringer, Materials Science and Engineering 1995, 202, 1.
[27] P. Y. Hou and J. Stringer, Oxidation of Metals 1988, 29, 45.
[28] K. Przybylski and G. J. Yurek, Journal of the Electrochemical Society 1988, 517.
[29] H. Yedong and F. H. Stott, Corrosion Science 1994, 36, 1869.
[30] T. A. Ramanarayanan, R. Ayer, R. Petkovic-Luton, and D. P. Leta, Oxidation of Metals 1988, 29, 446.
[31] R. J. Hussey and M. J. Graham, Oxidation of Metals 1996, 45, 349.
[32] M. F. Stroosnijder, J. F. Norton, V. Guttmann, and M. J. Bennett, Materials Science and Engineering 1989, 116, 103.
[33] S. Chevalier, G. Bonnet and J. P. Larpin, Applied Surface Science 2000, 167, 125.
[34] S. Chevalier, G. Bonnet, K. Przybylski, and J. C. Colson, Oxidation of Metals 2000, 54, 527.
[35] A. Gil, S. Mrowec, J. Jedlinski, and G. Borchardt, Solid State Ionics 1922, 58, 13.

[36] M. J. Bennett, H. E. Bishop, P. R. Chalker, and A. T. Tuson, Materials Science and Engineering 1987, 90, 177.
[37] X. Peng, Y. Guan, Z. Dong, C. Xu, and F. Wang, Corrosion Science 2011, 53, 1954.
[38] K. Przybylski, A. J. Garratt, and G. J. Yurek, Journal of the Electrochemical Society: Solid -State Science and Technology, 1988.
[39] B. Pieraggi and R. A. Rapp, Journal of the Electrochemical Society 140 (1993) 2844.
[40] A. M. Huntz, J. G. Zhao, Reactivity of Solids, 1987, 3, 21-31.
[41] J. Lemaitre, J. l. Chaboche, Mécanique des matériaux solides, Paris, 2001.
[42] B. Panicaud, J.-L. Grosseau-Poussard, Z. Tao, F. Rakotovao, G. Geandier, P.-O. Renault, P. Goudeau, N. Boudet, N. Blanc, Acta Mechanica 2017, 228, 3595.
[43] N. B. Pilling and R. E. Bedworth, Journal of the Institute of Metals 1923, 29.
[44] F. Balbaud, C. Desgranges, C. Duhamel, L. Marchetti, L. Martelli, R. Mols, S. Perr, and F. Rouillard, Corrosion et protection des matériaux à haute température, Presse des mines, Paris 2011.
[45] B. Pieraggi and R. A. Rapp, Acta Materialia 1988, 36.
[46] G. Calvarin, R. Molins, and A. M. Huntz, Oxidation of Metals 2000, 53, 25.
[47] D. R. Clarke, Current Opinion in Solid State & Materials Science 2002, 6, 237.
[48] D. R. Clarke, Acta Materialia 2003, 51, 1393.
[49] B. Panicaud, J. L. Grosseau-Poussard, J. F. Dinhut, Computational Materials Science 2008, 42, 286.
[50] B. Panicaud, J.-L. Grosseau-Poussard, M. Kemdehoundja, J.-F. Dinhut, Computational Materials Science 2009, 46, 42.
[51] Z. J. Tao, F. Rakotovao, J. L. Grosseau-Poussard, B. Panicaud, Advanced Materials Research 2014, 996, 896.
[52] W. R. Cannon and T. G. Langdon, Journal of Materials Science 1983, 18, 1.
[53] A. H. Hüer, R. M. Cannon, and N. J. Tighe, Ultrafine-Grain Ceramics, Springer US, 1970, 15, 339.
[54] D. R. H. Michael Schutze, Protective Oxide Scales and Their Breakdown. 1997.
[55] R. M. Cannon and R. L. Coble, Plenum press, New Work, 1975, 100.
[56] D. Francois, A. Peau, and A. Zaoui, Comportement mécanique des matériaux, Elasticité et Plasticité, ED Hermès, 1993.
[57] D. J. Baxter and K. Natesan, Reviews on high temperature materials, 1983, 5, 149.
[58] J. P. Poirier, Creep of crystals: high-temperature deformation processes metals, ceramics, and minerals, Cambridge University Press, New York, 1985.
[59] F. Rakotovao, B. Panicaud, J. L. Grosseau-Poussard, Z. Tao, G. Geandier, P. O. Renault, P. Girault, P. Goudeau, N. Blanc, N. Boudet, G. Bonnet, Acta Materialia 2018, 159, 276.
[60] H. E. Evans and M. P. Tatlock, Surface and Coatings Technology 1997, 27, 9.
[61] M. Schütze, P. F. Tortorelli, and I. G. Wright, Oxidation of Metals 2010, 73, 389.
[62] J. Everaerts, E. Salvati, H. Li, W. Li, A.M. Korsunsky, Corrosion Science 2020, 165.
[63] H. E. Evans, Oxidation of Metals 2013, 79, 1.
[64] H. E. Evans, A. T. Donaldson, and T. C. Gilmour, Oxidation of Metals 1999, 52, 379.
[65] P. Lours, J. Sniezewski, Y. Le Maoult, B. Pieraggi, Materials Science and Engineering 2008, 480, 40.
[66] J. Sniezewski, P. Lours, Y. Le Maoult, Materials at High Temperatures 2011, 28, 17.
[67] V. K. Tolpygo and D. R. Clarke, Materials Science and Engineering 2000, 278, 142.
[68] M. Geng, G. He, Z. Sun, J. Chen, Z. Yang, Y. Li, Coatings 2018, 8, 400.
[69] J.-L. Grosseau-Poussard, B. Panicaud, S. Ben Afia, Computational Materials Science 2013, 71, 47.
[70] B. Panicaud, J. L. Grosseau-poussard, And J. F. Dinhut, Applied Surface Science 2006, 252.
[71] Z. Wang, J.-L. Grosseau-Poussard, B. Panicaud, G. Geandier, P.-O. Renault, P. Goudeau, N. Boudet, N. Blanc, F. Rakotovao, Z. Tao, Metals 2018, 8, 913.
[72] Y. Wang, H. Fang, C.l. Zacherl, Z. Mei, S. Shang, L.-q. Chen, P.d. Jablonski, Z.-k. Liu, Surface Science 2012, 606.
[73] M. Birkholz, Thin Film Analysis by X-Ray Scattering, 2006
[74] P.P. Ewald, Fifty Years of X-Ray Diffraction, 1962
[75] G. Huebschen, I. Altpeter, R. Tschuncky, H.-G. Herrmann, Materials Characterization Using Nondestructive Evaluation (NDE) Methods, 2016

[76] D.faurie, G.geandier, P.-O. Renault, E. Le Bourhis, D.thiaudière, Thin Solid Films 2013, 530.
[77] M. François, Journal of Applied Crystallography 2008, 41, 44.
[78] W.L. Bragg, Mathematical Proceedings of the Cambridge Philosophical Society 1913, 17, 43.
[79] Spieß, L., Teichert, G., Schwarzer, R., Behnken, H., Genzel, C., 2009. Moderne R€ontgenbeugung, second ed. Teubner Verlag, Wiesbaden
[80] P. L. Devries , J. E. Hasbun, A First Course in Computational Physics, 2 edition, 2011.
[81] E. Hairer, C. Lubich, M. Roche, The numerical solution of differential-algebraic systems by Runge-Kutta methods, 1989.
[82] G.R. Liu, S. S. Quek, Finite Element Method: A Practical Course, 1975
[83] Pei-bai Zhou, Numerical Analysis of Electromagnetic Fields (Electric Energy Systems and Engineering Series), 1993
[84] Peter I. Kattan, MATLAB Guide to Finite Elements, 2003.
[85] J.F. Grcar, Mathematicians of Gaussian Elimination 2011, 58, 11.
[86] T. Sasaki, H. Murao. ACM Transactions on Mathematical Software 1982, 8, 277.

# Chapter 2: Experimental procedure and preliminaries results

## 2.1 Materials, preliminary analyses and pretreatments

### 2.1.1 Metal alloys under investigation

The material substrate studied in this thesis is a Ni-based alloy with different weight percentages of Cr. The NiCr alloy contains a weight percentage of 28.28% Cr, symbolized by Ni28Cr, another kind of sample with a weight percentage of 34.5% Cr is marked as Ni35Cr. These materials are alloys that are resistant to oxidation and their behaviors after different oxidation conditions have been studied extensively [1-4]. Their chemical composition (weight percentages) is shown in Table 2.1.

Table 2.1. Chemical composition (weight percentages)

| | | | | |
|---|---|---|---|---|
| Ni28Cr alloy | Ni | Cr | Si | Mn |
| | 71.2 | 28.28 | < 0.01 | < 0.01 |
| Ni35Cr alloy | Ni | Cr | C | Al |
| | 63.5 | 34.5 | 1.025 | 0.95 |

The oxide formed at the surface of substrate is mainly $Cr_2O_3$, which has been studied in [1-4]. However, other oxides $NiO/NiCr_2O_4$ can be formed under the experimental conditions such as oxidation at 1000°C for 20h [5]. In the high temperature oxidation, there is also a phenomena of evaporation of chromia, which occurs at 1000°C, as shown by [6].

### 2.1.2 Determination of oxidation experimental conditions

In order to choose the appropriate oxidation conditions, the following criteria have been considered:

- Prevention of crack and maintenance of adhesion between oxide layer and substrate in order to limit delamination phenomena
- Sufficient thickness of oxide layer to generate residual stress as further detailed

#### 2.1.2.1 Theoretical calculation of oxide thickness

It has been previously evidenced for nickel-based alloy with experimental characterization by Thermal Gravimetric Analysis [7] that the oxide thickness $h_{ox}$ follows a parabolic evolution with oxidation time t as shown in Eq.2.1. However, it should be noticed that all values of Ap in Table 2.2 are for the system $Ni30Cr/Cr_2O_3$, which does not perfectly coincide with our alloy.

$$h_{ox} = Ap\sqrt{t} \qquad (2.1)$$

where Ap is the parabolic kinetics parameter that varies with temperature T. The parabolic kinetics parameter Ap given in [4,5-8] is shown in Table 2.2.

Table 2.2. Values of the parabolic oxidation constants

| Temperature (°C) | Ap (ms$^{-0.5}$) in [4] | Ap (ms$^{-0.5}$) in [7] | Ap (ms$^{-0.5}$) in [8] | Ap (ms$^{-0.5}$) in [9] |
|---|---|---|---|---|
| 1200 | - | - | $9.20*10^{-8}$ | - |
| 1100 | - | - | $5.43*10^{-8}$ | - |
| 1000 | - | $1.43*10^{-8}$ | - | - |
| 900 | $1.76*10^{-7}$ | $4.73*10^{-9}$ | $1.02*10^{-8}$ | $2.98*10^{-9}$ |
| 800 | $4.85*10^{-8}$ | $2.83*10^{-9}$ | - | $1.82*10^{-9}$ |
| 700 | $1.03*10^{-8}$ | - | - | - |

Knowing the values of Ap, the thickness of oxide layer can be calculated. For example, using the given parabolic kinetics parameter Ap [7], Table 2.3 is obtained, which shows the predicted thickness of oxide layer for different temperatures and different oxidation times.

Table 2.3. Predicted thickness of oxide layer

| 1000 °C | | | | | | | |
|---|---|---|---|---|---|---|---|
| Time (h) | 1 | 2 | 3 | 4 | 5 | 10 | 20 |
| Thickness (µm) | 0.86 | 1.22 | 1.50 | 1.73 | 1.93 | 2.73 | 3.86 |
| 900°C | | | | | | | |
| Thickness (µm) | 0.29 | 0.40 | 0.50 | 0.57 | 0.64 | 0.91 | 1.28 |
| 800°C | | | | | | | |
| Thickness (µm) | 0.17 | 0.24 | 0.30 | 0.34 | 0.38 | 0.54 | 0.77 |

Table 2.3 indicates that for 1000 °C the oxide layer grows faster than at 900 °C and 800 °C, as expected. Considering the thickness of the oxide layer, in order to prevent cracking and maintain adhesion between the oxide layer and the substrate, it is not advisable to be too thick. It should also not be too thin so that it does not generate residual stress. Previous works [3,10] show that 1h oxidation under 1000 °C is sufficient for generating residual stress of about -400 MPa in the oxide layer, which means that the thickness around 1 µm is well adapted.

However, it is shown in Table 2.2 that even for the same system Ni30Cr/$Cr_2O_3$ and the same oxidation temperature, the results of Ap are very different. Therefore, to determine more precisely the experimental conditions that agree with our systems, several complementary experiments are required.

### 2.1.2.2 Experimental verifications

a. Comparison of surface quality for different oxidation times

The material of the sample is Ni28Cr, whose diameter is 12 mm and thickness is 1.5 mm. The surface quality has been compared after oxidation at 1000 °C for 1 h, 5 h and 20 h. For each oxidation time, three samples are oxidized at the same time.

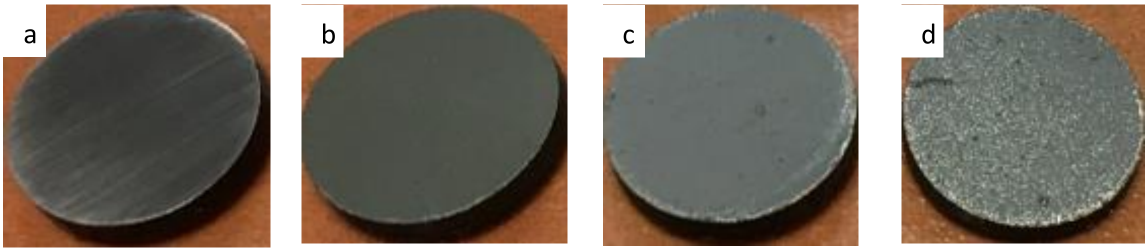

Figure 2.1 Samples before oxidation (a), after oxidation at 1000 °C for 1 h (b), 5 h (c) and 20 h (d)

As shown in Fig.2.1, some cracks and spalls can be clearly observed in the sample oxidized at 1000 °C for 20 h. Instead, the surface of the sample oxidized at 1000 °C for 1 h and 5 h are more homogeneous and smooth.

We assume that:

- The mass variation is due to oxygen reaction, which forms oxide.
- The oxide layer is made of $Cr_2O_3$, as confirmed by XRD measurements.
- Top surface, bottom surface and side surface are considered,

The average of mass variation is measured by a precision electronic balance with an accuracy of $10^{-6}$g. The calculation for oxide layer thickness is expressed as:

$$h_{ox} = \frac{\Delta \mathrm{m}}{M_O}\frac{M_{Cr_2O_3}}{3\rho_{Cr_2O_3}S} \tag{2.2}$$

where $\Delta \mathrm{m}$ is mass variation, $M_O$ corresponds to the molar masses of oxygen, $M_{Cr_2O_3}$ is the molar masses of oxide $Cr_2O_3$, $\rho_{Cr_2O_3}$ corresponds to the density of $Cr_2O_3$ and S is the area surface.

As discussed in section 1.1.2, we assumed that the oxide growth at high temperature follows parabolic rate law:

$$h_{ox} = Ap\sqrt{t} \tag{2.3}$$

The mass before and after oxidation are measured by using a balance with a precision of $10^{-6}$ g. The average of mass variation, the oxide layer thickness and parabolic kinetics parameter Ap are shown in Table 2.4.

Table 2.4. Quantitative comparison for different oxidation times at 1000°C

| Oxidation time (h) | Δ mass (g) | $h_{ox}$ (μm) | Ap ($ms^{-0.5}$) |
|---|---|---|---|
| 1 | 0.000293 | 0.63 | $1.05*10^{-8}$ |
| 5 | 0.000463 | 0.99 | $7.41*10^{-9}$ |
| 20 | -0.000327 | - | - |

As shown in Table 2.4, the mass variation of the sample oxidized at 1000 °C for 20 h is negative, which means that there are too much cracks and peelings when the oxidation time is too long. For the values of Ap at 1 and 5 hours, it is close to the values obtained in [7-9]. Overall, these results indicate that for a high temperature, such as 1000 °C, the oxidation time should not be too long. As previous works [3,10] shows, the oxidation for 1h under 1000 °C is sufficient for generating residual stress. In addition, as in the experience verification, the surface of 5h oxidation under 1000 °C does not have too much cracks and peelings. Therefore, when determining the oxidation conditions of the experiment, we decided that the predicted oxide thickness should not be thicker than 2 μm as shown in Table 2.3.

b. Microstructure of samples surface

In order to get the grain size and the surface quality for the oxide layer, the Atomic Force Microscope and high quality video microscope are used.

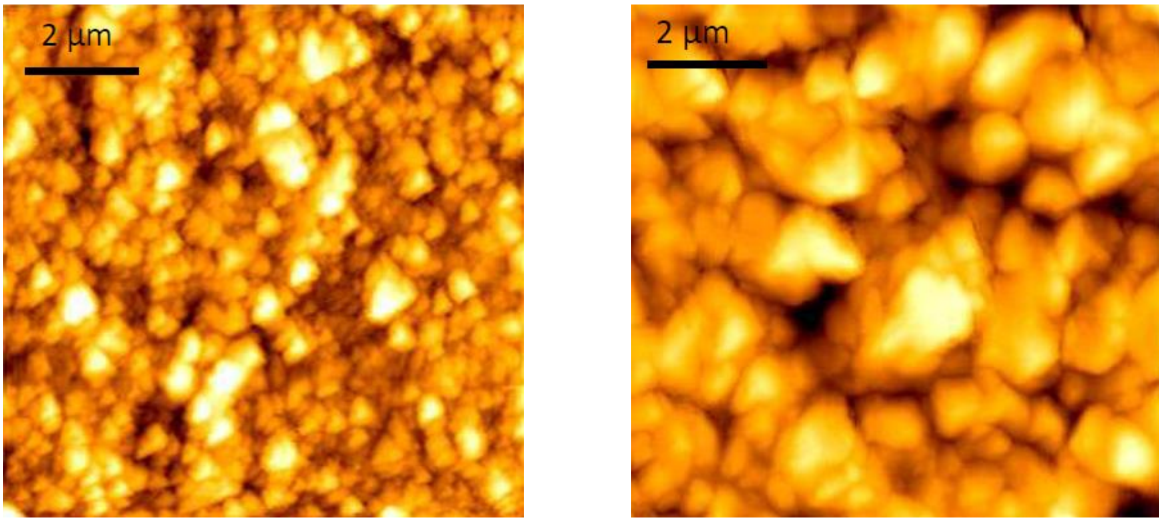

(a) (b)

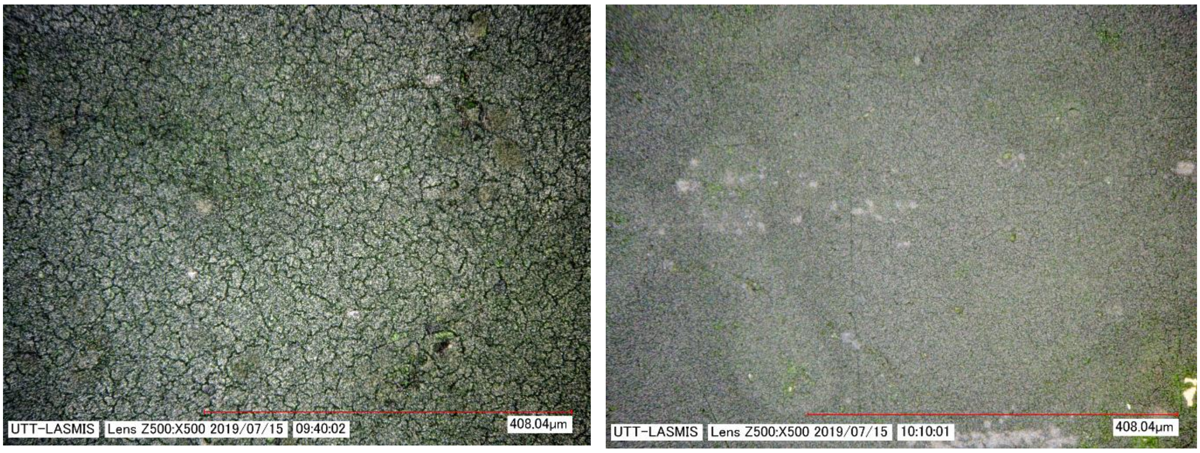

(c) (d)

Figure 2.2 Observation by AFM of the oxide layer after 3 hours of oxidation at 800°C (a) [7], 3 hours of oxidation at 1000°C (b) [7]. Observation by high quality video microscope after 3 hours of oxidation at 1000°C (c) and 10 hours of oxidation at 900°C (d)

The comparison between Fig.2.2 (a) and Fig.2.2 (b) shows that for the same oxidation time, the lower oxidation temperature will generate smaller grain size. As shown in Fig.2.2 (c) and Fig.2.2 (d), even for a longer oxidation time, the sample surface has better quality at low temperature. The better surface quality of the sample means that there are fewer cracks and peels and the adhesion between the oxide layer and the substrate is better.

### c. Verification for the effect of pre-oxidation

For NiCr/$Cr_2O_3$ system, several works indicate that the oxide layer formed at high temperature prevents the formation of oxide layer at lower temperatures. This phenomenon has been discussed in previous works [3, 11, 12, 13]. In addition, deflection tests will be carried out and they require an earlier study of the effects of pre-oxidation. For the deflection tests, a thin plate sample is used. There is only one surface that is oxidized, which produces the deflection. The other surface is protected by pre-oxidation.

To ensure the protection of the pre-oxidation, two tests are made with a thermogravimetric analysis machine at Nogent laboratory of University of Technology of Troyes.

The thermogravimetric analysis machine is SETSYS EVO ATG 1600, SETARAM. The system mainly includes a microbalance, a graphite resistor furnace and alumina analysis tube and three gas providing tubes. The capacity of microbalance is 35 g with a measuring range ± 200 mg and electronic resolution 0.002 µg. The graphite resistor furnace and alumina analysis tube is cooled by water circulation. The temperature range is from ambient to 1600°C and the temperature change rate is from 0.01 to

99.99°C/min. The three gas providing tubes is regulated by mass flow rate sensor, which can mix auxiliary and reactive gas.

The first test (a) is oxidation at 950°C for 10 hours, then oxidation at 900°C for 10 hours. The second test (b) is oxidation at 950°C for 10 hours, followed by oxidation at 800°C for 10 hours. The mass variations with time are plotted in Fig.2.3 (a) and (b).

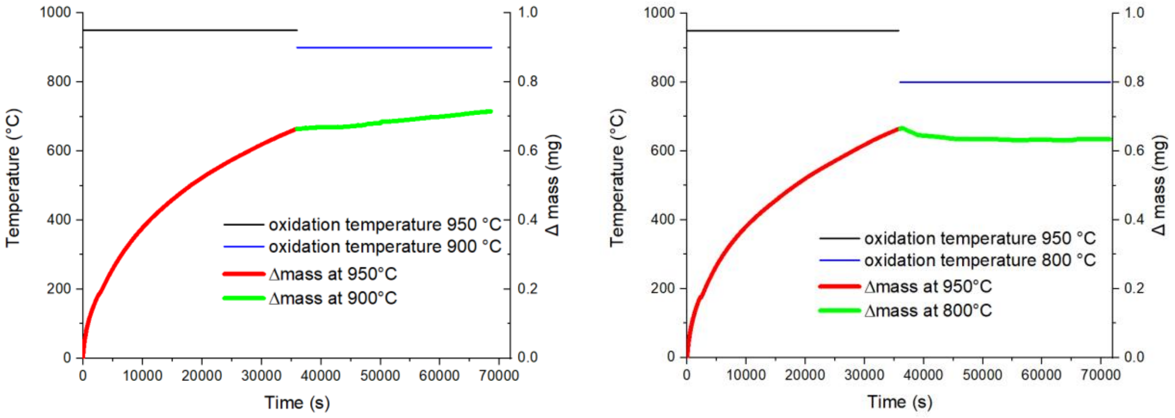

(a) (b)

Figure 2.3 Mass variation with time for two tests: pre-oxidation at 950 °C for 10h, followed by oxidation at 900°C for 10 hours (a), or followed by oxidation at 800°C for 10 hours (b)

Fig. 2.3 verifies that the oxide layer previously formed at high temperature prevents the formation of the oxide layer at lower temperatures, especially for a bigger difference between pre-oxidation temperature and oxidation temperature.

In conclusion, to prevent the cracks and maintain the adhesion, the oxidation temperature and time should be chosen carefully. When we determine the oxidation conditions of the experiment, the predicted oxide thickness should not be thicker than 2 µm as shown in Table 2.3. In addition, in order to achieve the same state of oxidation, a lower temperature should be chosen.

## 2.1.3 Deposition and implantation techniques

In order to find out the influence of reactive elements on the mechanical properties of the chromia layers, we have also performed some groups of experiments using the reactive elements $Y_2O_3$ or Zr.

### 2.1.3.1 Deposition of $Y_2O_3$

For the series with $Y_2O_3$, the samples were treated by the technique of physical vapor deposition (PVD) [12], and were exposed in a chamber for different exposure times in order to vary the quantity of $Y_2O_3$ in the alloy. The principle consists in sputtering a target of yttrium oxide with a beam of ions (Ar+) produced by using a radiofrequency source. The atoms of the $Y_2O_3$ target are then sputtered and deposited on the surface of the substrate with an energy varying from a few electron volts to a hundred electron volts.

The machine used is NORDIKO-3000. During the experiment, the gun releasing a beam of ions (Ar+) was kept at very low pressure, which ranges from 0.1 Pa to 1 Pa. In addition, because the atoms extract off from the target are very energetic, the chamber is maintained at extremely low pressure (0.01 Pa) to avoid their self-collision.

In order to compare the influence of different quantities of $Y_2O_3$ in the alloy, we have exposed the samples Ni28Cr with different exposure times corresponding respectively to 10s, 50s and 100s.

#### 2.1.3.2 Implantation of Zr

For the series of Zr, the metallic substrates have been subjected to ionic implantation of zirconium. Three doping fluences have been applied: $1*10^{15}$, $5*10^{15}$ and $1*10^{16}$ ions.cm$^{-2}$. The implanter is EATON$^{TM}$NV3206 [12]. The implanter consists of an ion source, an electro-magnet, an accelerator, a beam shaping system and a chamber where the sample is implanted. The $Zr^+$ ions were obtained by sputtering a source of zirconium with $Xe^+$ ions that was ionized from the atoms of a neutral gas (xenon). The electro-magnet chamber allowed selecting $Zr^+$ ions for implantation. After the acceleration system and beam shaping system, the $Zr^+$ ions are implanted on the sample surface.

The fluence measurement (ions/cm$^2$) corresponds to the integration of the current measured by an ammeter, for a given surface and during the implantation period. The experiment was performed at room temperature.

## 2.2 Deflection Method

### 2.2.1 Experimental setup

The principle of this test is to observe the deflection of a thin plate of the metal during oxidation at high temperature and by analyzing the deflection, the stress in the oxide layer is obtained. The experimental equipment is set up by Professor Jérôme Favergeon of University of Technology of Compiègne, which was used in thesis of David, F. [14], Kurpaska, L. [15] etc.

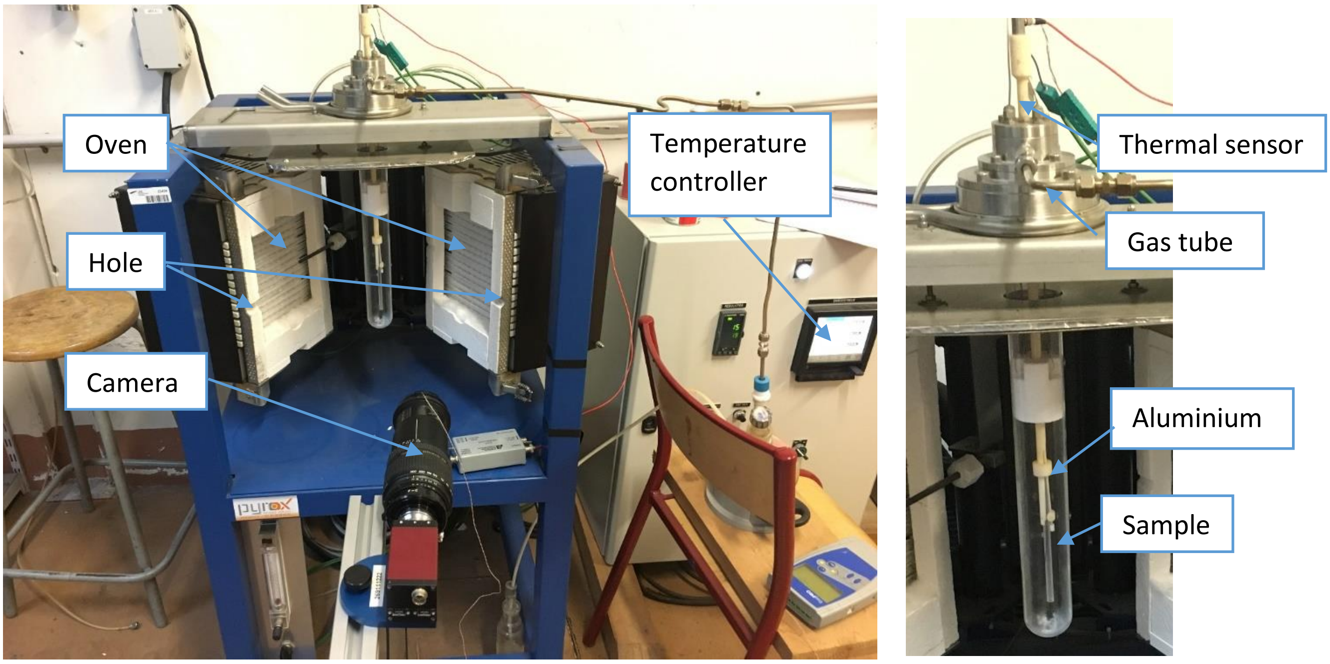

(a) (b)

Figure 2.4 Illustration for the deflection experimental equipment

As shown in Fig.2.4, the experimental equipment is generally divided into two parts: the control part (a) and reaction part (b). In the control part (a), the oven heats up the sample. The hole allows us to see the sample during the thermal application and record the pictures with the camera. The computer linked with the camera is set to record the images every 2 minutes. The temperature controller allows us to set the experiment temperature. In the reaction part (b), the thermal sensor is linked with the temperature controller. The gas tube allows us to change the oxidation environments by giving different gas. The aluminum parts help us to hold the sample.

The materiel used in this experiment is alloy Ni35Cr. The shape of sample is 5*50*0.28 mm. The preparation of sample is mainly divided into three steps. First step, the top surface and bottom surface is polished to a roughness of 1 µm using a polisher with different polish paper. In the second step, the polished sample is oxidized at 950 °C for 10 h in an oven. After the oxidation, one of the sample surface is polished again to a roughness of 1 µm, during which the sample is protected in resin that can be dissolved in alcohol. Thus, a sample with one surface protected is obtained.

### 2.2.2 Models of Literature

Several authors have modeled the metal oxidation process to predict the stresses in the metal/oxide system by deflection method. The deflection illustration is shown in Fig.2.5:

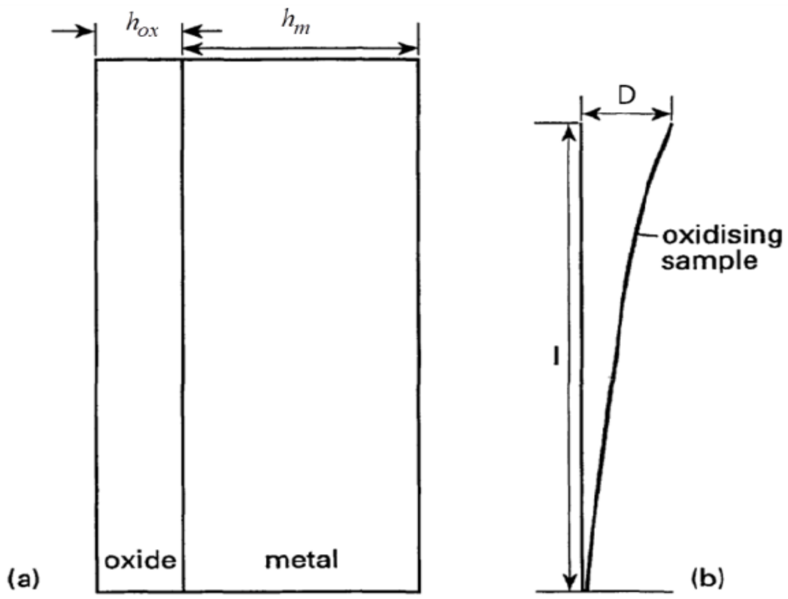

Figure 2.5 Illustration of sample deflection

As shown in Fig2.5 (a), the metal layer thickness is symbolized as $h_m$ and $h_{ox}$ for the oxide layer. The metal sample has a thin plate shape. The specimen length is $l$ and the deflection of the specimen is D.

The expression of the curvature κ is expressed by the following relationship:

$$\kappa = \frac{2D}{l^2} \tag{2.4}$$

Evans [16], Brenner and Senderoff [17] and Przybilla [18] have proposed expressions of the $\sigma_{ox}$ (MPa) constraints in the oxide, which is an average stress in the oxide. With the Young's modules of oxide layer $E_{ox}$, Poisson's ratio of oxide layer $\nu_{ox}$, oxide layer thickness $h_{ox}$, Young's modules of metal layer $E_m$, Poisson's ratio of metal layer $\nu_m$, metal layer thickness $h_m$ and the curvature κ, the expressions of the $\sigma_{ox}$ (MPa) are:

Proposition of Evans [16]:

$$\sigma_{ox} = -\frac{E_m h_m (h_m + h_{ox})\kappa}{6h_{ox}} \tag{2.5}$$

Proposition of Brenner and Senderoff [17]:

$$\sigma_{ox} = -\frac{E_m h_m (h_m + h_{ox})\kappa}{6h_{ox}} + \frac{(E_{ox} - E_m)\kappa}{6h_{ox}} \frac{{h_m}^3}{h_m + h_{ox}} \tag{2.6}$$

Proposition of Przybilla [18]:

$$\sigma_{ox} = -\frac{E_m {h_m}^3 \kappa}{6(1-\nu_m)h_{ox}(h_m + h_{ox})} - \frac{E_{ox} {h_{ox}}^2 \kappa}{6(1-\nu_{ox})(h_m + h_{ox})} \tag{2.7}$$

The oxide layer thickness $h_{ox}$ can be calculated by:

$$h_{ox} = A_p\sqrt{t} \tag{2.8}$$

where $A_p$ is the kinetics coefficient of the global chemical oxidation reaction and t is the oxidation time.

### 2.2.3 Preliminary findings

The tested sample is 5*50*0.28 mm with alloy Ni35Cr. The protected surface is oxidized at 950 °C for 10 h. The whole experimental process is a temperature rising by 30°C/min up to 900 °C, then oxidation at 900 °C for 10 h and a temperature decreasing by 15°C/min until room temperature. The beginning picture and final picture are shown in Fig. 2.6.

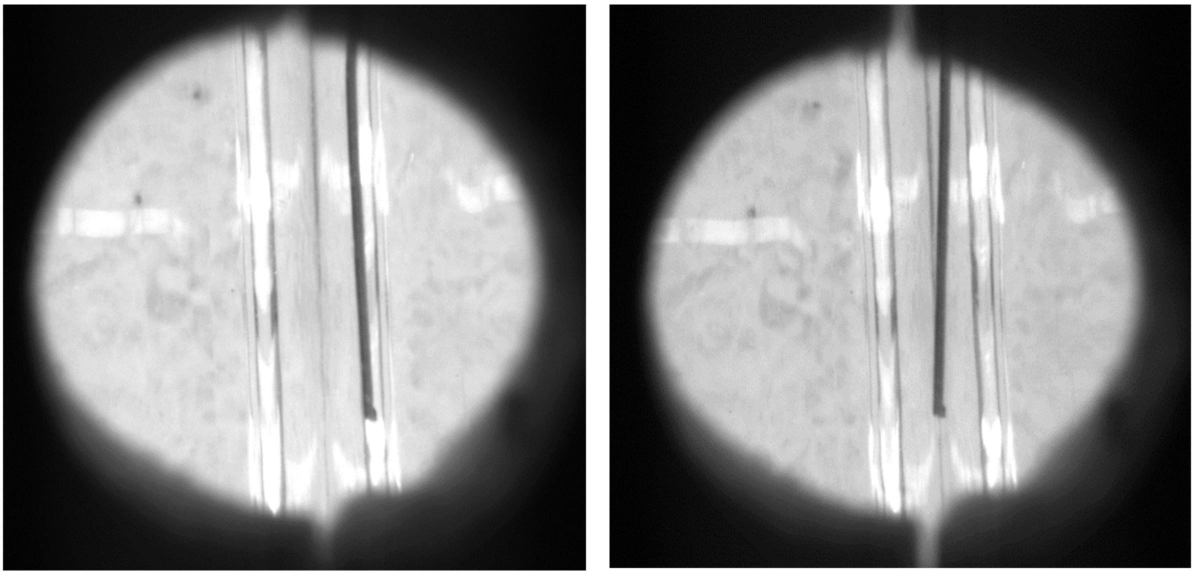

(a) (b)

Figure 2.6 Deflection of sample at beginning 900°C (a) at the end 900°C (b)

The deflection can be plotted as a function of time.

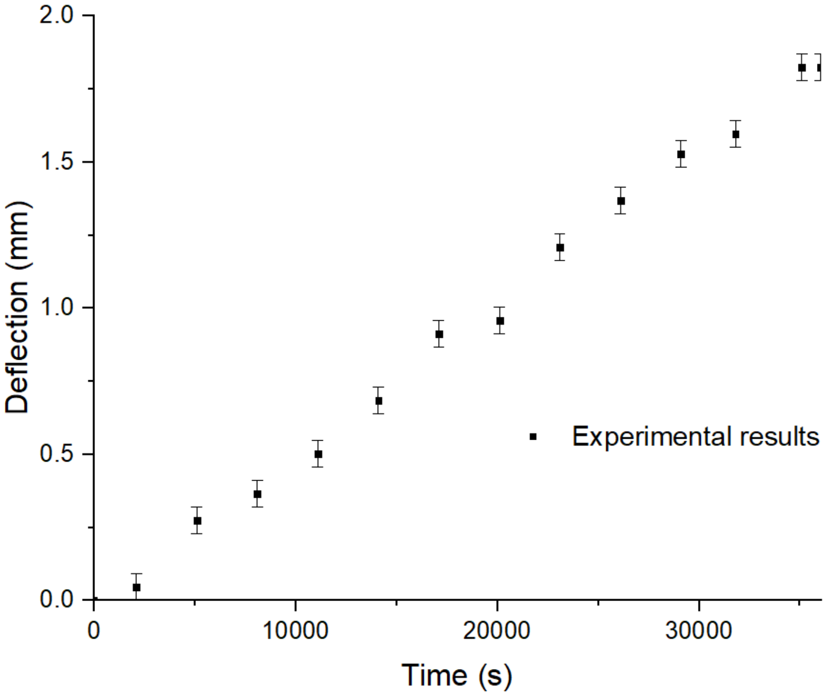

Figure 2.7. Deflection as a function of time

Figure 2.7 shows that the deflection is almost linear with time. The error bar comes from the error during the measurement of deflection. The deflection maximum is 1.82 ± 0.04 mm at the end of 900 °C (Fig. 2.6(b)). By using the parameters given in Table 2.5, the stress in the oxide layer is calculated (Table 2.6).

Table 2.5 Input parameters at 900°C

| $E_m$(GPa) | $\nu_m$ | $E_{ox}$(GPa) | $\nu_{ox}$ | $A_p\ (mm/s^{0.5})$ |
|---|---|---|---|---|
| 165 | 0.3 | 215 | 0.29 | 4.73E-6 |

Table 2.6 The stress in the oxide layer by use of the different models at final time

| | $\sigma_{ox}$ (GPa) |
|---|---|
| Evans | -3.52 |
| Brenner and Senderoff | -4.58 |
| Przybilla | -4.99 |

The calculated stresses have the same magnitude, which is around 4.5GPa. These values are much larger than those of our recent studies [1-4, 7]. In fact, our system is a three layers system, pre-oxidation layer (protected surface) – metal layer – oxidation layer. The protected surface is oxidized at 950 °C for 10 h. Because of the different expansion coefficient between the pre-oxidation layer ($Cr_2O_3$) and metal layer (Ni35Cr), there is a thermal stress as the temperature rising up to 900 °C. For such a three layers, a proposition for calculating the stress in the oxide layer has been mentioned in [19].

$$\sigma_{ox2}h_{ox2} - \sigma_{ox1}h_{ox1} = -\frac{E_m {h_m}^2 \kappa}{6(1-\nu_m)} \tag{2.9}$$

where $\sigma_{ox1}$ is the stress in the oxide layer, $h_{ox1}$ corresponds to the thickness of oxide layer, $\sigma_{ox2}$ is the stress in pre-oxide layer, $h_{ox2}$ corresponds to the thickness of pre-oxide layer, $E_m$ is Young's modules of metal layer, $\nu_m$ corresponds to Poisson's ratio of metal layer, $h_m$ is the thickness of metal layer and κ is the curvature. Moreover $h_{ox1}$ and $h_{ox2}$ both can be calculated by Eq.2.8.

We assumed that $\sigma_{ox2}$ is the thermal stress and the stress relaxation during the oxidation period. In order to provide a simple representation of the relaxation, the stress in the pre-oxide layer is taken as the thermal stress multiplied by a factor β. Although the hypothesis is strong and the stress relaxation is not calculated, in order to have a preliminary estimation for the stress in the oxide layer, it is acceptable.

$$\sigma_{ox2} = \sigma_{thermal}\beta = -\frac{E_{ox}(\alpha_{ox}-\alpha_m)\Delta T}{1-\nu_{ox}}\beta \tag{2.10}$$

where $E_{ox}$ is Young's modules of pre-oxide layer, $\nu_{ox}$ corresponds to Poisson's ratio of pre-oxide layer, $\alpha_{ox}$ is the expansion coefficient of pre-oxide layer, $\alpha_m$ is the expansion coefficient of metal layer and $\Delta T$ is the difference of temperature.

Table 2.7 Input parameters at 900°C

| $E_m$(GPa) | $\nu_m$ | $E_{ox}$(GPa) | $\nu_{ox}$ | $\alpha_{ox}$ $(K^{-1})$ | $\alpha_m$ $(K^{-1})$ |
|---|---|---|---|---|---|
| 165 | 0.3 | 215 | 0.29 | 7.2E-6 | 1.96E-5 |
| $A_p$ $(mm/s^{0.5})$ 900 °C | $A_p$ $(mm/s^{0.5})$ 950 °C | $\Delta T$ $(K)$ | | | |
| 4.73E-6 | 7.66E-6 | 873 | | | |

With these parameters, the stress in the oxide layer is obtained.

Table 2.8. Calculation results for $\sigma_{ox1}$ with different β

| Relaxation factor β | Stress $\sigma_{ox1}$ (GPa) |
|---|---|
| 0 | -5,00 |
| 0,2 | -3,94 |
| 0,4 | -2,88 |
| 0,6 | -1,82 |
| 0,8 | -0,75 |
| 1 | 0,31 |

The results in Table 2.8 indicate that the stress $\sigma_{ox1}$ has a strong relationship with the relaxation factor β. When the relaxation factor β is 0, with no stress in the pre-oxidation layer, the stress $\sigma_{ox1}$ is -5.00 GPa, which is quite close to the results of Przybilla proposition -4.99 GPa. The simplification of Eq.2.7 is Eq.2.9, when the relaxation factor β is 0.

Table 2.8 also shows that as the relaxation factor β increases, the absolute value of stress $\sigma_{ox1}$ decreases. In addition, when the relaxation factor β is 1, with no relaxation in the pre-oxidation layer, the stress $\sigma_{ox1}$ is positive, which means that the stress in the oxide layer is tension. As the known results in [3, 10], the stress in the oxide layer is compression. Therefore, considering the relaxation of stress is necessary.

Comparing the two layers system, the three layers system adapts better to our system. Because the relaxation of stress has not been calculated, the stress $\sigma_{ox2}$ used for Eq.2.9 is not the real stress in the pre-oxidation layer, which may introduce an error. However, the results give us a perspective for the relationship between $\sigma_{ox1}$ and $\sigma_{ox2}$. This model could be studied further, but it is not the main focus of this thesis.

## 2.3 Introduction of X-Ray Diffraction

### 2.3.1 Mode reflection

#### 2.3.1.1 Experimental setup

X-ray diffraction (XRD) is extensively applied to determine the elastic strain of crystalline materials. The associated stress can be determined thanks to the $\sin^2 \psi$ method, and using the radiocrystallographic elastic coefficients.

The experiments, using the reflection mode, have been realized in-situ at high temperature on the beamline BM02 of the ESRF (European Synchrotron Radiation Facility) in Grenoble. The X-ray beam arriving on the sample is monochromatic, with a wavelength of 0.062 nm (energy of 20 keV).

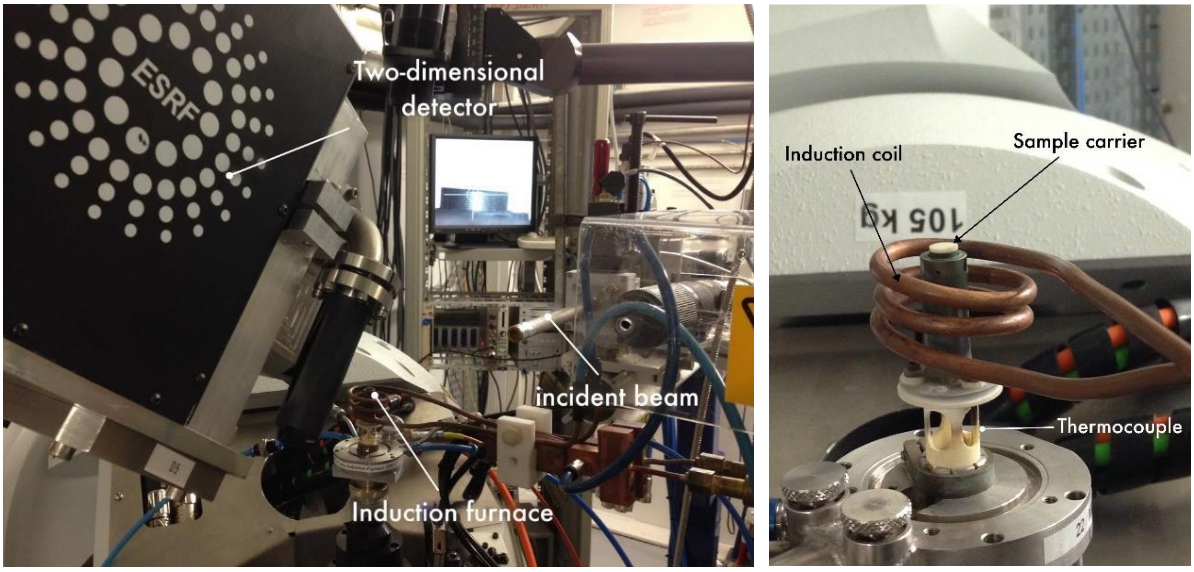

(a) (b)

Figure 2.8 The equipment of beamline BM02 of the ESRF (a) and the furnace (b) [13]

The experiments includes a goniometer, a sample carrier, a two-dimensional detector and two photodiodes. The goniometer allows us to know the angles used in the following calculations. The sample carrier is surrounded by induction coil of 7 mm diameter and 4 mm depth with a high-power generator (maximum 3kW). The maximum temperature that can be reached is 1600 °C. The two-dimensional detector receives the reflection signal of X-ray, which will be analyzed.

#### 2.3.1.2 Data processing

Bragg's law is applied to evaluate the changes of distance between crystallographic planes and taking into account the diffraction geometry (Fig. 2.9). Then, rings are obtained with the help of a two-dimensional detector. From [20], a relation is given to transform ψ as a function of θ and γ.

$$\cos\psi = \sin(\theta)\sin(\omega) + \cos(\gamma)\cos(\omega)\cos(\theta) \tag{2.11}$$

where ψ is the angle between the normal to the surface and the normal to the diffracting planes, 2θ is the angle between the incident beam and the diffracted beam, ω is the incident angle and γ is the angle between the vertical, passing through the position of the direct beam, and a given position on the diffraction ring (see in Fig. 2.9).

As a result, for each gamma value, it is linked to ψ and the diffraction models are fitted for each ψ value. After that, the $\sin^2\psi$ method is used to determine the associated stress.

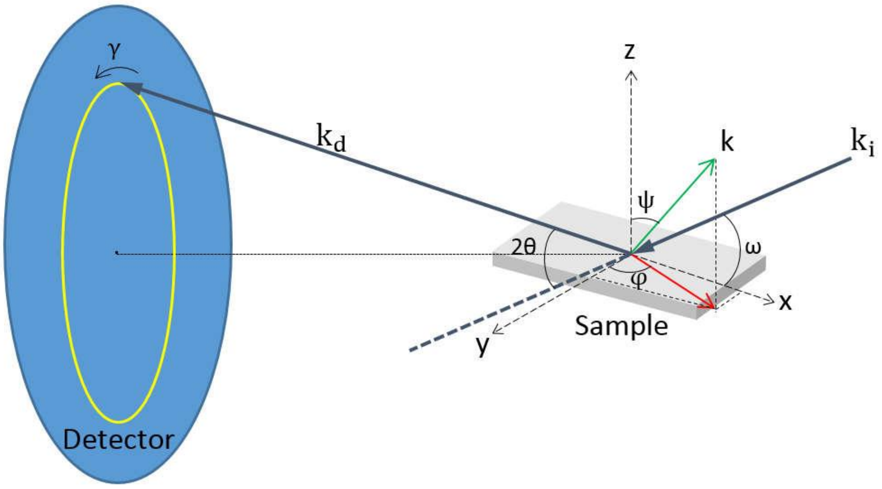

Figure 2.9 Geometrical configuration of the experiments performed at ESRF. Details on this configuration can be found in [20] and [21]

The untreated data (see an example in Fig. 2.10) are images of the diffracted rings. It requires further analysis to obtain the stress in the oxide layers. For a stress-free material, the data should draw perfect circles. Fig. 2.10 shows an example recorded for the NiCr + $\mathrm{Cr_2O_3}$system.

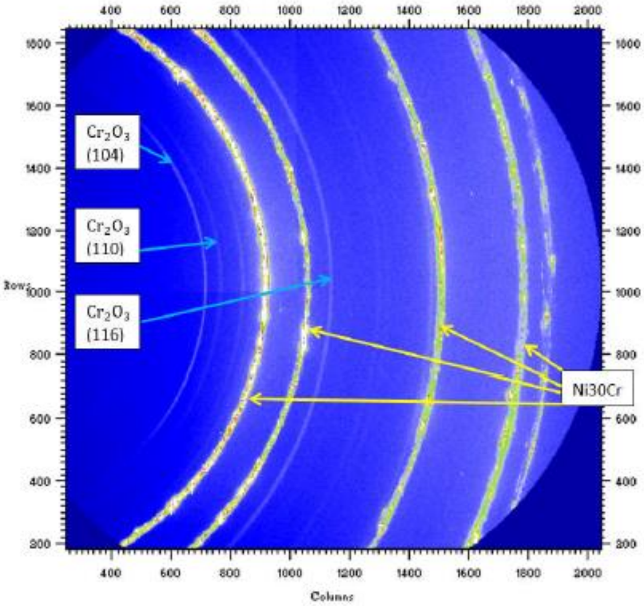

Figure 2.10 Diffracted rings for the Ni28Cr + $Cr_2O_3$ system

In order to analyze the untreated data, the rings were subdivided into 128 sectors γ whose values are between {-61.5 ° and + 65.5 °} with a step of 1° (Fig. 2.11).

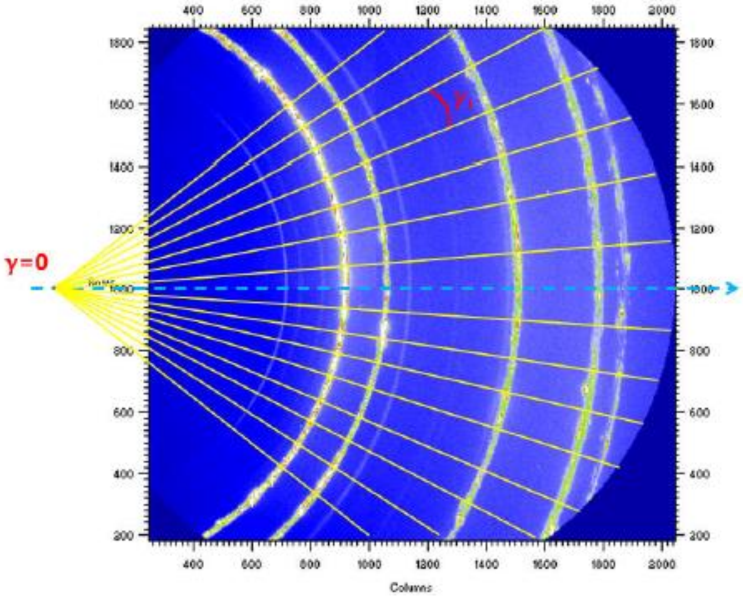

Figure 2.11 Subdivision of the rings of the Ni28Cr + $Cr_2O_3$ system

From these data, it is possible to plot the intensities of each sector γ as a function of 2θ, giving a 1D diffraction diagram. The peaks to be studied for the chromium oxide are (104), (110), (116), which are the most intense and best defined. The 2θ free of stress reference positions are summarized in Table 2.9. The theoretical position of 2θ is related to the X-ray energy, where E=20 keV in the reflection mode.

Table 2.9. Reference positions for the free of stress diffraction peaks [22] with E=20 keV

| Plan (hkl) $Cr_2O_3$ | (104) | (110) | (116) |
|---|---|---|---|
| 2θ Theoretical (°) | 13,25 | 14,30 | 21,20 |

To choose the best simulation for each diffraction diagram, four main distribution functions have been tested to simulate the peaks profile, which are Gauss, Lorentz, Pearson 7 and Pseudo-Voigt. In addition, it is necessary to minimize the influence of the background. The polynomial relationship for the background is tested. We can simulate the peak distribution and the background noise either simultaneously or separately.

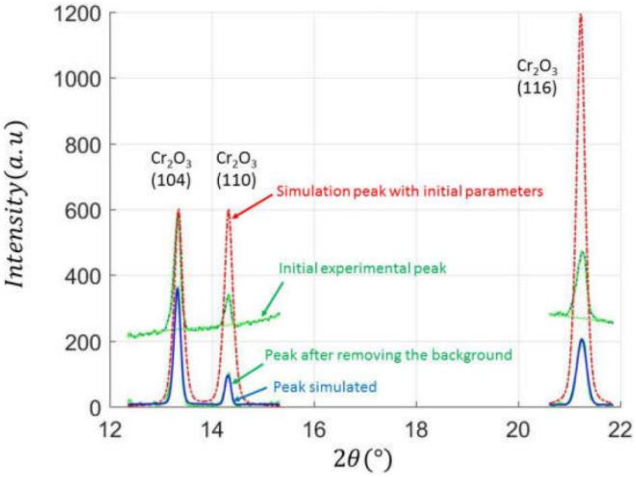

Figure 2.12. Fitting of the peak profiles with or without background

Fig. 2.12 shows an example, which simulates the peak forms and the background separately. Given the initial experimental peak, the background is considered as a polynomial relationship. After removing it, the different distribution functions are used to simulate the peak profile.

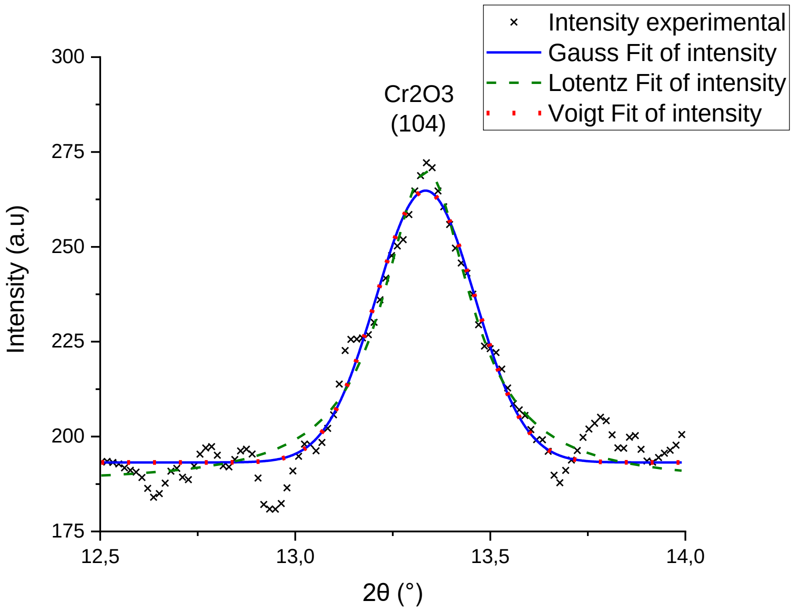

Figure 2.13 Different peak profiles modelling

Fig. 2.13 shows the results obtained for the different distribution functions. In that case, the simulation results are quite similar for the parameters obtained such as the intensity, the position, and the width of the peak. In order to choose the best function, we need to test systematically this procedure by considering a big number of experimental data. All this procedure has been automatized in a Matlab handmade software with the implementation of validity criteria on the fitting quality.

To simulate the background noise, a polynomial function is chosen whose order need to be tested. In the test, the peak and the background noise can be simulated together or separately.

Several quality indicators are considered, such as:

- Slope Indicator :

Given that the data tested corresponds to 5min of oxidation, which is short time with respect to the total duration of the experiment, the stress can be considered as a constant or linear with a very small slope over this period.

- Mean value Indicator

Mean value Indicator is an indicator on the average stress value, which is calculated from the stresses obtained of the different methods. The mean value indicator is an indicator that represents a comparison of the mean stresses of the different methods.

- Variance Indicator

Variance indicator is an indicator that represent the difference between the results and average stress value. It is the most important parameter for smoothing the curve. When the variance indicator value is smaller, the curve is more convergent and smoother, which is exactly what we expected.

- Difference between maximum and minimum indicator

Difference between maximum and minimum indicator is an indicator of the difference between the maximum and minimum value. The difference between maximum and minimum indicator is also an important parameter for smoothing the curve and for controlling the stress interval. However, it is less important than variance indicator.

By applying this procedure for 100 pictures and after comparing these quality indicators, we consider that a Pearson 7 distribution function simultaneously with a background simulated by an order 3 polynomial leads to a correct minimization satisfying all the quality indicators. Therefore, this distribution has been considered for the simulation of all the data.

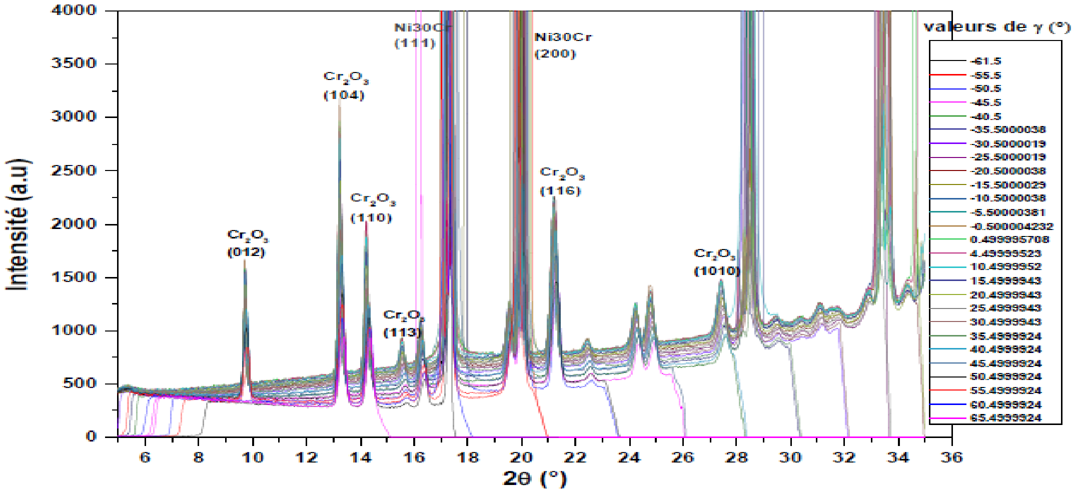

Figure 2.14 diffractogramme I(ϒ) =) f(2θ) corresponding to the Ni30Cr/Cr2O3 system [12]

The complete diffractogramme was done by F. N. RAKOTOVAO [12], which is under the help with G. GEANDIER. The data processing could be done using three types of software: PYFAI (for the transformation of pixels into degrees), Fit2D (for subdivision and integration) and Matlab (for fitting the peaks).

### 2.3.1.3 Sin²ψ method

When a material is deformed, the distance between crystallographic planes $d_{hkl}$ will extend or contract, which will cause a shift in the rings position in the diffraction pattern. In turn, the changes of distance between crystallographic planes can be evaluated by measurement of this angular shift, so that the elastic strain can be determined.

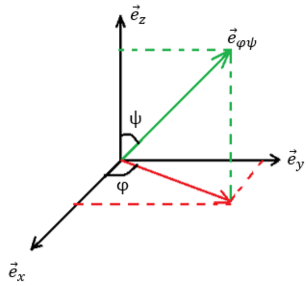

Figure 2.15 Directions and axes of measurement

The reference (x, y, z) is an orthonormal coordinate system linked to the sample. The direction $\vec{\mathrm{e}}_{\varphi\psi}$ is the normal to the diffracting planes as shown in Fig. 2.15. The strain on the direction $\vec{\mathrm{e}}_{\varphi\psi}$ is:

$$\varepsilon_{\psi\varphi} = \vec{\mathrm{e}}_{\varphi\psi}\bar{\bar{\varepsilon}}\vec{\mathrm{e}}_{\varphi\psi} \tag{2.12}$$

with

$$\vec{\mathrm{e}}_{\varphi\psi} = \sin\psi\cos\varphi\vec{\mathrm{e}}_{\mathrm{x}} + \sin\psi\sin\varphi\vec{\mathrm{e}}_{\mathrm{y}} + \cos\psi\vec{\mathrm{e}}_{\mathrm{z}} \tag{2.13}$$

and $\bar{\bar{\varepsilon}}$ is the elastic strain tensor:

$$\bar{\bar{\varepsilon}} = \begin{pmatrix} \varepsilon_{\mathrm{xx}} & \varepsilon_{\mathrm{xy}} & \varepsilon_{\mathrm{xz}} \\ \varepsilon_{\mathrm{xy}} & \varepsilon_{\mathrm{yy}} & \varepsilon_{\mathrm{yz}} \\ \varepsilon_{\mathrm{xz}} & \varepsilon_{\mathrm{yz}} & \varepsilon_{\mathrm{zz}} \end{pmatrix} \tag{2.14}$$

The strain along the direction $\vec{\mathrm{e}}_{\varphi\psi}$ is developed:

$$\varepsilon_{\psi\varphi} = \left(\varepsilon_{\mathrm{xx}}\cos^2\varphi + \varepsilon_{\mathrm{yy}}\sin^2\varphi + \varepsilon_{\mathrm{xy}}\sin2\varphi - \varepsilon_{\mathrm{zz}}\right)\sin^2\psi + \left(\varepsilon_{\mathrm{xz}}\cos\varphi + \varepsilon_{\mathrm{yz}}\sin\varphi\right)\sin(2\psi) + \varepsilon_{\mathrm{zz}}, \tag{2.15}$$

The true strain along the direction $\vec{\mathrm{e}}_{\varphi\psi}$ can also be obtained by comparing the unstrained distance $\mathrm{d}_0$ between crystallographic planes with the strained distance $\mathrm{d}$.

$$\varepsilon_{\psi\varphi} = \ln\left(\frac{\mathrm{d}}{\mathrm{d}_0}\right) = \ln\left(\frac{\sin\theta_0}{\sin\theta}\right) \tag{2.16}$$

By combining Eq. 2.15 and Eq. 2.16, it provides a relationship between the angular shift (from $\theta_0$ to $\theta$) and the elastic strain that corresponds to the expected $\sin^2\psi$ strain relationship.

$$\ln\left(\frac{\sin\theta_0}{\sin\theta}\right) = \left(\varepsilon_{\mathrm{xx}}\cos^2\varphi + \varepsilon_{\mathrm{yy}}\sin^2\varphi + \varepsilon_{\mathrm{xy}}\sin2\varphi - \varepsilon_{\mathrm{zz}}\right)\sin^2\psi + \left(\varepsilon_{\mathrm{xz}}\cos\varphi + \varepsilon_{\mathrm{yz}}\sin\varphi\right)\sin(2\psi) + \varepsilon_{\mathrm{zz}} \tag{2.17}$$

If we assume that elasticity of the material is linear, homogeneous and isotropic, the conversion of elastic strain into stress can be done by using Hooke’s model according to:

$$\bar{\bar{\varepsilon}} = \frac{1+\nu}{\mathrm{E}}\bar{\bar{\sigma}} - \frac{\nu}{\mathrm{E}}\mathrm{trace}(\bar{\bar{\sigma}})\bar{\bar{\mathrm{I}}} \tag{2.18}$$

with trace $\overline{\overline{\sigma}}$ is the first invariant of the stress tensor and $\overline{\overline{\mathrm{I}}}$ is the three-dimensional (3D) identity tensor. With the assumption of transverse isotropy for an in-plane stress state as expected in oxide, we have:

$$\overline{\overline{\sigma}} = \begin{pmatrix} \sigma_{xx} & \sigma_{xy} & 0 \\ \sigma_{xy} & \sigma_{yy} & 0 \\ 0 & 0 & 0 \end{pmatrix} \tag{2.19}$$

Moreover, we consider that there is no shear stress and we suppose the absence of stress gradient.

$$\overline{\overline{\sigma}} = \begin{pmatrix} \sigma & 0 & 0 \\ 0 & \sigma & 0 \\ 0 & 0 & 0 \end{pmatrix} \tag{2.20}$$

The $\sin^2\psi$ stress relationship is obtained by simplifying Eq. 2.17 – 2.20, which indicates the connection between the angular offset, corresponding to the difference between $\theta_0$ and $\theta$, and the stress.

$$\ln\left(\frac{\sin\theta_0}{\sin\theta}\right) = \frac{1+\nu}{E}\sigma \sin^2\psi - \frac{\nu}{E}2\sigma \tag{2.21}$$

By using the radiocrystallographic elastic coefficients Sij, the $\sin^2\psi$ relation becomes:

$$\ln\left(\frac{1}{\sin\theta}\right) = \frac{1}{2}S_{2(hkl)}\sigma \sin^2\psi + 2S_{1(hkl)}\sigma - \ln(\sin\theta_0) \tag{2.22}$$

The slope of this straight line corresponds to $\frac{1}{2}S_{2(hkl)}\sigma$ and the intercept corresponds to $2S_{1(hkl)}\sigma - \ln(\sin\theta_0)$. Since we already have the radiocrystallographic elastic coefficients (Table 2.10) for different families of planes (hkl), we can then calculate the stress in the oxide for these different families (104), (110), (116).

Table 2.10. Radiocrystallographic elastic coefficients for $Cr_2O_3$ for different families of (hkl) planes at 1073K, 1173K and 1273K [13]

| | 1073K | | |
|---|---|---|---|
| Plane (hkl) $Cr_2O_3$ | (104) | (110) | (116) |
| $S_1$(TPa$^{-1}$) | -0.824 | -1.018 | -0.805 |
| 0.5*$S_2$ (TPa$^{-1}$) | 3.987 | 4.557 | 3.927 |
| | 1173K | | |
| Plane (hkl) $Cr_2O_3$ | (104) | (110) | (116) |
| $S_1$(TPa$^{-1}$) | -0.821 | -1.014 | -0.802 |

| | | | |
|---|---|---|---|
| 0.5*$S_2$ (TPa$^{-1}$) | 3.993 | 4.559 | 3.934 |
| | 1273K | | |
| Plane (hkl) $Cr_2O_3$ | (104) | (110) | (116) |
| $S_1$(TPa$^{-1}$) | -0.817 | -1.010 | -0.800 |
| 0.5*$S_2$ (TPa$^{-1}$) | 3.999 | 4.561 | 3.941 |

After that, to fit the sin²ψ curves, different quality criteria have also been defined in the computing procedure. For example, there is a criterion corresponding to the confidence interval around the linear fit, which can control the removal of abnormal points. In addition, the intensity coefficient of the fit and the difference between the first point and the last point of the linear fit are also used to assess the quality of the fit. If all these criteria are satisfied, we can consider that the fitted curves are correct and the corresponding slopes then stress are satisfying from a data processing point of view. Fig. 2.16 gives an example of result obtained for ψ<0. The trend for ψ>0 is similar (not shown).

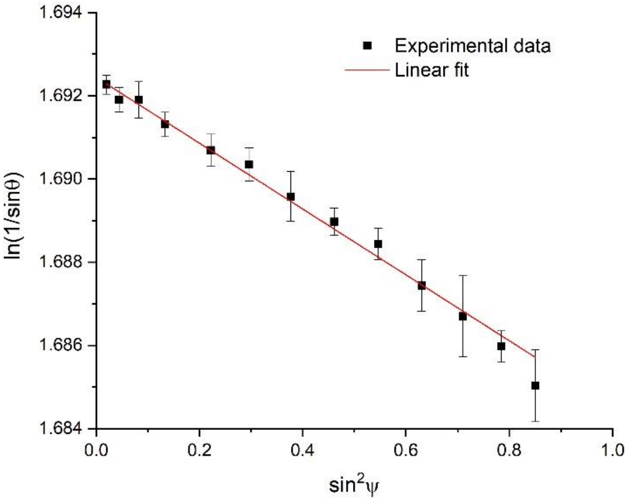

Figure 2.16 $\ln\left(\frac{1}{\sin\theta}\right)$ versus $\sin^2\psi$ for the oxide peak (116)

It corresponds to the (116) peak of the chromium oxide. The slope of this line corresponds to $\frac{1}{2}S_{2(116)}\sigma$ and the intercept to $2S_{1(116)}\sigma - \ln(\sin\theta_0)$. The range of variation of the values $\ln\left(\frac{1}{\sin\theta}\right)$ is 7.2*10$^{-3}$. The error bar is in the range 2.3*10$^{-4}$ to 9.8*10$^{-4}$, which is small compared to the variation of the values for $\ln\left(\frac{1}{\sin\theta}\right)$. The relationship between $\ln\left(\frac{1}{\sin\theta}\right)$ and $\sin^2\psi$ is well linear as described by Eq. 2.22. The stress value, which can be deduced in that case, corresponds to only one time point in the stress-time curve evolution. After repeating this procedure for all the experimental pictures, we can finally get the stress-time curve for the oxide peak (116).

By using the same procedure, we can get the stress-time curves for the different (hkl) oxide families in the oxide and for all the systems. Only the results for one peak are further presented for our system.

## 2.3.2 Mode transmission

### 2.3.2.1 Experimental setup

Basically, X-ray in transmission mode and X-ray in reflection mode (XRD) share the same principles. X-rays in transmission can be used to determine the residual stress distribution in substrate as a function of depth. The X-rays in transmission mode was used to determine the lattice parameters as a function of depth for Thermal Barrier Coatings, which is related to the depth-dependence of strain [23]. Transmission XRD or reflection XRD shares the same principles to detect the crystalline peaks [24, 25]. A comparison between the conventional Bragg-Brentano diffractometer and the two-dimensional XRD shows that the two-dimensional diffraction provides more information than conventional diffractometer and can be used to determine stress [24].

The experiments was done under the help with G. GEANDIER.

Experiments has been performed at PETRA P07-EH2 beamline (DESY-Petra III, Hamburg, Germany). A high energy beam (E=103.4 keV) with a rectangular shape and a small dimension along the vertical axis (300x2 microns$^2$) has been used coupled with a vertical translation at 10 microns/s and a fast 2D Perkin-Elemer detector with a frame rate of 10 Hz. This allows to obtain a 2D images (2048x2048 pixels) containing full Debye-Scherrer rings, every micron step corresponding to a diffraction volume of 300x(sample size)x3 microns$^3$. Detector was placed at 1.5 m from the sample. Sample top surface was aligned with the beam using rocking curves and absorption scans for different orientations around the vertical axis.

Absorption has been recorded using a photo-diode placed in the direct beam. Setup was calibrated using a $CeO_2$ powder (NIST standard). Sample to detector distance and detector misalignment have been determined using pyFAI software [26]. Calibrating powder and sample has been placed at the same position using a camera looking on sample top surface and performing absorption scans along x and y directions. Motor resolution for rocking curves was set to 0.005°, meaning that the final alignment is better due to the high number of points in the scan (30 above Full Width at Half Maximum typically), so the required resolution can be easily reached with the setup for 1 µm resolution along z direction. As mentioned, all sources of misalignment will cause a change in strain/stress gradient determination, but the resolution of the setup is largely sufficient for our experiment. Samples was glued on an aluminum holder. The top sample surface was aligned using the direct beam and a photo-diode placed behind the sample. Several absorption and rocking curve scans have been performed to place the surface as flat as possible with respect to the beam.

#### 2.3.2.2 Data processing

Bragg's law is applied to evaluate the changes in distance between crystallographic planes, taking into account the diffraction geometry (Fig. 2.17).

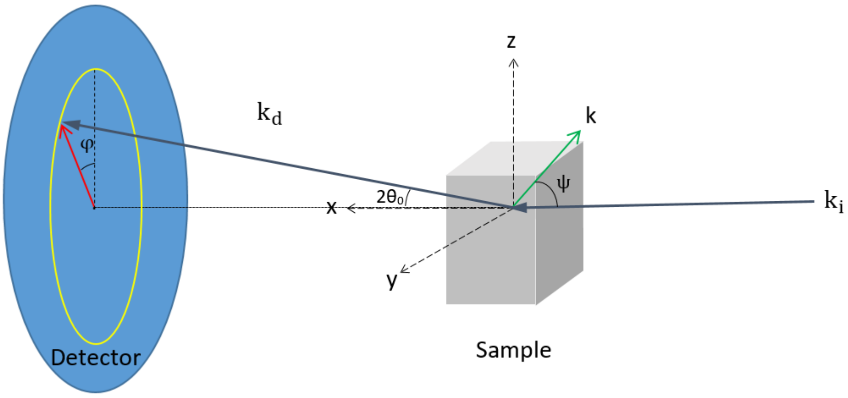

Figure 2.17 Geometrical configuration of the experiments

The direction $\vec{e}_{\varphi\psi}$ is the normal to the diffracting planes, where ψ is the angle between the normal to the surface and the normal to the diffracting planes and $\varphi = \gamma$ is the angle between the vertical passing through the position of the direct beam and a given position on the diffraction ring. $2\theta_0$ is the angle between the incident beam and the diffracted beam.

The raw data (see an example in Fig. 2.18) is an image of the diffraction ring. Further treatments are required to obtain the stress.

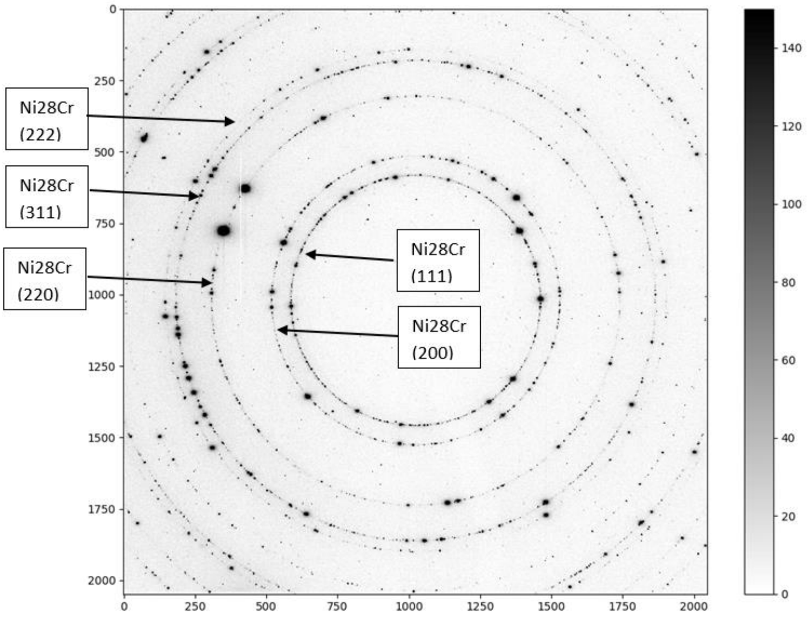

Figure 2.18 Diffracted rings for Ni28Cr substrate

The process of data treatment is quite similar as the XRD in reflection mode, which has been discussed in section 2.2.1.2. As can be seen from Fig.2.18, the quality of different rings varies considerably. The diffraction rings have been divided into several sectors. For each sector, the integration of intensity as a function of $2\theta$ was calculated. By choosing the best method to fit the peaks, the values $2\theta$ can be obtained, which have a shift from the values $2\theta_0$.

### 2.3.2.3 Sin²$\varphi$ method

When a material is deformed, the distance between the crystallographic planes $d_{hkl}$ expands or contracts, causing a shift in the position of the rings in the diffraction pattern. Changes in the distance between the crystallographic planes can be evaluated as a result by measuring this angular shift, which can then determine the elastic strain.

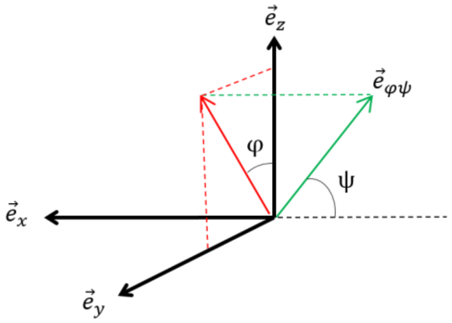

Figure 2.19 Directions and axes of measurement

As shown in Fig. 2.17 and Fig. 2.19, the reference (x, y, z) is an orthonormal coordinate system linked to the sample. The strain on the direction $\vec{e}_{\varphi\psi}$ is:

$$\varepsilon_{\psi\varphi} = \vec{e}_{\varphi\psi}\bar{\bar{\varepsilon}}\vec{e}_{\varphi\psi} \tag{2.23}$$

with

$$\vec{e}_{\varphi\psi} = -cos\psi\vec{e}_x + sin\psi sin\varphi\vec{e}_y + sin\psi cos\varphi\vec{e}_z \tag{2.24}$$

and $\bar{\bar{\varepsilon}}$ is the elastic strain tensor with the assumption that there is no shear strain:

$$\bar{\bar{\varepsilon}} = \begin{pmatrix} \varepsilon_{xx} & 0 & 0 \\ 0 & \varepsilon_{yy} & 0 \\ 0 & 0 & \varepsilon_{zz} \end{pmatrix} \tag{2.25}$$

The strain along the direction $\vec{e}_{\varphi\psi}$ can be developed as:

$$\varepsilon_{\psi\varphi} = cos^2\psi\varepsilon_{xx} + sin^2\psi sin^2\varphi\varepsilon_{yy} + sin^2\psi cos^2\varphi\varepsilon_{zz} \tag{2.26}$$

The actual strain along the direction $\vec{e}_{\varphi\psi}$ can also be calculated by comparing the undeformed distance $d_0$ between the crystallographic planes with the deformed distance d.

$$\varepsilon_{\psi\varphi} = ln\left(\frac{d}{d_0}\right) = ln\left(\frac{sin\theta_0}{sin\theta}\right) \tag{2.27}$$

It provides, through the combination of Eq.2.26 and Eq.2.27, a linear relationship between the angular shift (from $\theta_0$ to $\theta$) and the elastic strain.

$$ln\left(\frac{sin\theta_0}{sin\theta}\right) = cos^2\psi\varepsilon_{xx} + sin^2\psi sin^2\varphi\varepsilon_{yy} + sin^2\psi cos^2\varphi\varepsilon_{zz} \tag{2.28}$$

Because of the geometry configuration, the direction of measurement is the bisector between the incident beam and the diffracted beam.

$$\psi = \frac{\pi}{2} - \theta_0 \tag{2.29}$$

The normal $\sin^2\psi$ strain relationship is modified into $\sin^2\varphi$ strain relationship.

$$ln\left(\frac{1}{sin\theta}\right) = sin^2\theta_0\varepsilon_{xx} + cos^2\theta_0 sin^2\varphi\varepsilon_{yy} + cos^2\theta_0 cos^2\varphi\varepsilon_{zz} - ln(sin\theta_0) \tag{2.30}$$

Under the assumption that the elasticity of the material is linear, homogeneous and isotropic, the conversion of elastic strain to stress can be performed using Hooke's model according to:

$$\bar{\bar{\varepsilon}} = \frac{1+\nu}{E}\bar{\bar{\sigma}} - \frac{\nu}{E}\mathrm{trace}(\bar{\bar{\sigma}})\bar{\bar{I}} \tag{2.31}$$

where trace ($\bar{\bar{\sigma}}$) is the first invariant of the stress tensor and $\bar{\bar{I}}$ is the three-dimensional (3D) identity tensor.

The shear stress is not considered as done in previous works [3, 10]. In addition, a stress gradient along axis z is considered as normal stress $\sigma_N$. The tensor $\bar{\bar{\sigma}}$ should be:

$$\bar{\bar{\sigma}} = \begin{pmatrix} \sigma & 0 & 0 \\ 0 & \sigma & 0 \\ 0 & 0 & \sigma_N \end{pmatrix} \tag{2.32}$$

By applying the radiocrystallographic elastic coefficients $S_{ij}$, the $\sin^2\varphi$ relation becomes:

$$\begin{aligned} ln\left(\frac{1}{sin\theta}\right) = \frac{1}{2}S_{2(hkl)}(\sigma-\sigma_N)cos^2\theta_0 sin^2\varphi + \frac{1}{2}S_{2(hkl)}\sigma + S_{1(hkl)}(2\sigma+\sigma_N) \\ +\frac{1}{2}S_{2(hkl)}(\sigma_N-\sigma)cos^2\theta_0 - ln(sin\theta_0) \end{aligned} \tag{2.33}$$

Plotting the curve $ln\left(\frac{1}{sin\theta}\right)$ as a function of $sin^2\varphi$ gives us:

$$\begin{cases} Slope: A = \frac{1}{2}S_{2(hkl)}(\sigma-\sigma_N)cos^2\theta_0 \\ Intercept: B = \frac{1}{2}S_{2(hkl)}\sigma + S_{1(hkl)}(2\sigma+\sigma_N) + \frac{1}{2}S_{2(hkl)}(\sigma_N-\sigma)cos^2\theta_0 - ln(sin\theta_0) \end{cases} \tag{2.34}$$

By solving this two variable linear equations, the stresses $\sigma$ and $\sigma_N$ can be obtained:

$$\begin{cases} \sigma_N = \dfrac{B + ln(sin\theta_0) - \dfrac{\beta_2 A}{\beta_1}}{\beta_2+\beta_3} \\ \sigma = \sigma_N + \dfrac{A}{\beta_1} \\ \beta_1 = \frac{1}{2}S_{2(hkl)}cos^2\theta_0 \\ \beta_2 = 2S_{1(hkl)} + \frac{1}{2}S_{2(hkl)}(1-cos^2\theta_0) \\ \beta_3 = S_{1(hkl)} + \frac{1}{2}S_{2(hkl)}cos^2\theta_0 \end{cases} \tag{2.35}$$

The radiocrystallographic elastic coefficients (Table 2.11) for the different families of planes (hkl) have been considered and the initial position of $2\theta_0$ (Table 2.11) can be calculated by the values given in [26, 27].

Table 2.11. Radiocrystallographic elastic coefficients and position initial $2\theta_0$ for different families of planes (hkl) for E=103.4 keV

| Plan (hkl) NiCr | $S_1$ (hkl) ($TPa^{-1}$) | $0.5S_2$ (hkl) ($TPa^{-1}$) | $2\theta_0$(°) |
|---|---|---|---|

| | | | |
|---|---|---|---|
| (311) | -17.693 | 54.472 | 6.496 |
| (222) | -1.122 | 4.760 | 6.785 |

To summarize, it has been shown that there is a relationship between the diffraction pattern observed ( $2\theta$ ) when X-rays are diffracted through the crystal lattices and the distance between the crystallographic planes d within the material. The interplanar spacing $d_0$ of a stress-free material will produce a characteristic diffraction pattern ($2\theta_0$) for this material. By changing the interplanar spacing, different diffraction patterns can be obtained. This induced change in crystallographic planes will cause a shift in the diffraction pattern. Precise measurements of this angular shift allow evaluating the changes in interplanar spacing and thus enable to deduce the stress in the material.

## 2.4 Stress corrections for uncertainties

### 2.4.1 Uncertainty sources

The uncertainty of stresses is mainly generated during the experimental steps. In order to make the sample surface parallel to the beam, adjustment steps are required before each experiment to have a better accuracy. The procedure for adjustment of the flatness of the sample is as follows.

- Note the detected intensity of the uncut incident beam
- Adjust the sample to partially cut off the incident beam, detected intensity is then less than the previous intensity
- Rotate the sample around the axis to find the ideal position, for which the detected intensity is maximum. After this adjustment, the surface of the sample is then parallel to the incident beam
- Adjust precisely the height of the sample so that the detected intensity is equal to the ideal position

Because of all these complex steps and even with all calibration and adjustment processes, it is necessary, to obtain a correct stress value, to propose a correction method for possible errors or systematic bias such as beam deviation.

Different causes may explain the systematic errors and bias during the measurement. It includes, without completeness:

- Dilatation correction: at the beginning of each temperature plateau, a procedure is applied to adjust the position of the sample; its height is corrected from the dilation effect. Therefore, the X-ray should irradiate the same place, whatever the temperature is. However, an uncertainty is associated to this correction step.

- Calibration procedure: to get the angular positions of the diffracted rings, it is necessary to establish a correspondence between the rings and pixels positions on the area images. To achieve such a goal, the obtained raw data have been systematically corrected by using references standard positions (NIST Silicon or $Cr_2O_3$) analyzed in the same diffraction conditions. However, an uncertainty of magnitude 10 MPa is also associated to this procedure.

## 2.4.2 Stress correction by use of mechanical balance

The geometry for the oxide growth on a metal is shown in Fig.2.20.

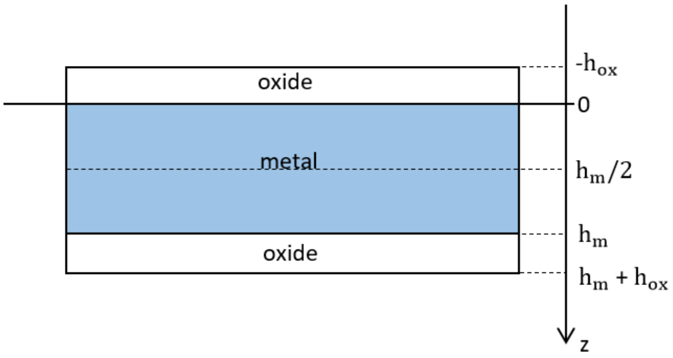

Figure 2.20 Geometry for the oxide growing on a metal

The mechanical balance equation overall metal and oxide can be expressed as:

$$\int_0^{h_m} \sigma_m(z)dz + \int_{-h_{ox}}^{0} \sigma_{ox}\, dz + \int_{h_m}^{h_m+h_{ox}} \sigma_{ox}\, dz = 0 \tag{2.36}$$

where $\sigma_{ox}$ is the stress in the oxide, $h_{ox}$ is the oxide thickness that depends on time t, $\sigma_m(z)$ is the stress in the substrate that depends on z, and $h_m$ is the thickness of the substrate. The influence of the oxide on the top and bottom surfaces is the main effect, which causes the apparition of residual stresses parallel to the oxide-metal interface in the metal.

### 2.4.2.1 Stress correction for reflection mode in XRD

For the reflection mode in XRD, we considered that the stress in metal may be divided into two parts. One part is the stress detected by XRD and that can be obtained with the $\sin^2\psi$ method. Due to the absorption of X-rays by the metal layer, X-rays can only detect a part of the metal. The depth of detect part is noted as $\mathrm{h(detected)}$ and the corresponding stress is noted as $\sigma_{\mathrm{met}}(\mathrm{detected})$. The rest part is the remaining part, noted as $\mathrm{h(rem)}$ and the corresponding stress is $\sigma_{\mathrm{met}}(\mathrm{rem})$. A symmetric oxidation is taken into account, thanks to the coefficient 2 in the mechanical balance equation in Eq.2.37.

$$\mathrm{\sigma_{met}(detected)h(detected) + \sigma_{met}(rem)h(rem) = -2\sigma_{ox}h_{ox}} \tag{2.37}$$

where $\mathrm{\sigma_{met}(detected)}$ is the stress in the detected part, $\mathrm{h(detected)}$ is the corresponding detected thickness, $\mathrm{\sigma_{met}(rem)}$ is the stress in the remaining part, and $\mathrm{h(rem)}$ is the remaining thickness.

According to bibliography [28-30], it is assumed that the detected stress is larger than the remaining stress in the metal layer.

$$\mathrm{\sigma_{met}(rem)} = \beta\mathrm{\sigma_{met}(detected)}, \qquad \beta \leq 1 \tag{2.38}$$

We have then:

$$\mathrm{\sigma_{met}(detected)h(detected)} + \beta\mathrm{\sigma_{met}(detected)h(rem) = -2\sigma_{ox}h_{ox}} \tag{2.39}$$

$$\mathrm{\sigma_{met}(detected)} = -\frac{\mathrm{2\sigma_{ox}h_{ox}}}{\mathrm{h(detected)} + \beta\mathrm{h(rem)}} \tag{2.40}$$

with:

$$\mathrm{h(detected)} + \beta\mathrm{h(rem)} \leq \mathrm{h_{met}} \tag{2.41}$$

It implies that:

$$\mathrm{|\sigma_{met}(detected)|} = \left|\frac{\mathrm{2\sigma_{ox}h_{ox}}}{\mathrm{h(detected) + \beta h(rest)}}\right| \geq \left|\frac{\mathrm{2\sigma_{ox}h_{ox}}}{\mathrm{h_{met}}}\right| \tag{2.42}$$

By giving a homogeneous stress distribution in metal and oxide, we consider at first approximation the measured stress as equal to the global averaged stress in all of the metal part. That is to say, the absolute value of the detected stress under this hypothesis is a maximum value of the stress in metal. When considering this assumption, the mechanical balance equation overall metal and oxide can be expressed as:

$$\mathrm{2\sigma_{ox}h_{ox} + \sigma_{met}(detected)h_{met} = 0} \tag{2.43}$$

a. Correction with Method 1

Hypothesis 1: the correction of stress is different in oxide and in metal.

$$\mathrm{2(\sigma_{ox} + C_{ox})h_{ox} + (\sigma_{met} + C_{met})h_{met} = 0} \tag{2.44}$$

$$\Rightarrow \ \mathrm{\sigma_{ox}\frac{2h_{ox}}{h_{met}} + \sigma_{met} = -C_{ox}\frac{2h_{ox}}{h_{met}} - C_{met}} \tag{2.45}$$

By figuring the relationship $\mathrm{\sigma_{ox}}\frac{2\mathrm{h_{ox}}}{\mathrm{h_{met}}} + \mathrm{\sigma_{met}}$ in terms of $\frac{2\mathrm{h_{ox}}}{\mathrm{h_{met}}}$, the slope of this line corresponds to $-\mathrm{C_{ox}}$, which is the correction of the stress in oxide, whereas the intercept corresponds to $-\mathrm{C_{met}}$ which is the correction of the stress in metal.

b. Correction with Method 2

Hypothesis 2: the correction values of stress in oxide and metal are identical.

$$2(\mathrm{\sigma_{ox}} + \mathrm{C})\mathrm{h_{ox}} + (\mathrm{\sigma_{met}} + \mathrm{C})\mathrm{h_{met}} = 0 \tag{2.46}$$

$$\Rightarrow \ \mathrm{\sigma_{ox}}\frac{2\mathrm{h_{ox}}}{\mathrm{h_{met}}} + \mathrm{\sigma_{met}} = -\mathrm{C}\left(\frac{2\mathrm{h_{ox}}}{\mathrm{h_{met}}} + 1\right) \tag{2.47}$$

By figuring the relationship $\mathrm{\sigma_{ox}}\frac{2\mathrm{h_{ox}}}{\mathrm{h_{met}}} + \mathrm{\sigma_{met}}$ in terms of $\frac{2\mathrm{h_{ox}}}{\mathrm{h_{met}}} + 1$, the slope of this line corresponds to – C, which is the correction for the stress in both oxide and substrate. According to Eq. 2.47, the linear fitting should intercept the origin point.

### 2.4.2.2 Stress correction for transmission mode in XRD

For the transmission mode in XRD, a symmetric oxidation is taken into account:

$$\int_0^{h_m} \sigma_m(z)dz + 2 * \int_{-h_{ox}}^{0} \sigma_{ox}\, dz = 0 \tag{2.48}$$

$\sigma_m(z)$ is obtained by transmission mode of XRD related to depth. $\sigma_{ox}$ is obtained by reflection mode as a constant value. Therefore, Eq. 2.48 can be transformed into:

$$\sum_{i=1}^{n} \sigma_m(z)_i\, \Delta z + 2\sigma_{ox}\mathrm{h_{ox}} = 0 \tag{2.49}$$

where n is the number of experimental points, $\sigma_m(z)_i$ corresponds to the stress in the metal layer at point i and $\Delta z$ is the distance between two nearest points. In addition, because the experimental points is linearly distributed along the depth, $\Delta z$ is a constant value.

a. Correction with Method 1

Hypothesis 1: the correction of stress is different in oxide and in metal.

$$2(\mathrm{\sigma_{ox}} + \mathrm{C_{ox}})\mathrm{h_{ox}} + \sum_{i=1}^{n} (\sigma_m(z)_i + \mathrm{C_{met}})\, \Delta z = 0 \tag{2.50}$$

$$\Rightarrow \ \sigma_{\mathrm{ox}}\frac{2\mathrm{h}_{\mathrm{ox}}}{\Delta z}+\sum_{i=1}^{n}(\sigma_m(z)_i) = -\mathrm{C}_{\mathrm{ox}}\frac{2\mathrm{h}_{\mathrm{ox}}}{\Delta z} - \mathrm{nC}_{\mathrm{met}} \tag{2.51}$$

By figuring the relationship $\sigma_{\mathrm{ox}}\frac{2\mathrm{h}_{\mathrm{ox}}}{\Delta z}+\sum_{i=1}^{n}(\sigma_m(z)_i)$ in terms of $\frac{2\mathrm{h}_{\mathrm{ox}}}{\Delta z}$ , the slope of this line corresponds to $-\mathrm{C}_{\mathrm{ox}}$, which is the correction of the stress in oxide, whereas the intercept corresponds to $-\mathrm{nC}_{\mathrm{met}}$ which is the correction of the stress in metal.

b. Correction with Method 2

Hypothesis 2: the correction values of stress in oxide and metal are identical.

$$2(\sigma_{\mathrm{ox}}+\mathrm{C})\mathrm{h}_{\mathrm{ox}}+\sum_{i=1}^{n}(\sigma_m(z)_i+\mathrm{C}_{\mathrm{met}})\,\Delta z = 0 \tag{2.52}$$

$$\Rightarrow \ \sigma_{\mathrm{ox}}\frac{2\mathrm{h}_{\mathrm{ox}}}{\Delta z}+\sum_{i=1}^{n}(\sigma_m(z)_i) = -\mathrm{C}\left(\frac{2\mathrm{h}_{\mathrm{ox}}}{\Delta z}+\mathrm{n}\right) \tag{2.53}$$

By figuring the relationship $\sigma_{\mathrm{ox}}\frac{2\mathrm{h}_{\mathrm{ox}}}{\Delta z}+\sigma_{\mathrm{met}}$ in terms of $\frac{2\mathrm{h}_{\mathrm{ox}}}{\Delta z}+1$, the slope of this line corresponds to – C, which is the correction for the stress in both oxide and substrate. According to Eq. 2.53, the linear fitting should intercept the origin point.

## References of chapter 2

[1] B. Panicaud, J.-L. Grosseau-Poussard, Z. Tao, F. Rakotovao, G. Geandier, P.-O. Renault, P. Goudeau, N. Boudet, N. Blanc, Acta Mechanicah 2017, 228, 3595.
[2] Z. J. Tao, F. Rakotovao, J. L. Grosseau-Poussard, B. Panicaud, Advanced Materials Research 2014, 996, 896.
[3] Z. Wang, J.-L. Grosseau-Poussard, B. Panicaud, G. Geandier, P.-O. Renault, P. Goudeau, N. Boudet, N. Blanc, F. Rakotovao, Z. Tao, Computational Materials Science 2020, 180, 109689.
[4] B. Panicaud, J.-L. Grosseau-Poussard, M. Kemdehoundja, J.-F. Dinhut, Computational Materials Science 2009, 46, 42.
[5] I. G. Wright, B. A. Wilcox, R. I. Jaffee, Oxid Met 1975, 9, 275.
[6] P. Berthod, Oxid Met 2005, 64, 235.
[7] M. Guerain, Contribution à l'étude des mécanismes de relaxation de contraintes dans les films de chromine formés sur Ni-30Cr et Fe-47Cr : approche multi-échelle par spectroscopie Raman et microdiffraction Synchrotron, PhD Thesis, Université de La Rochelle, La Rochelle, France, 2012.
[8] P. Moulin, A. M. Huntz, G. Beranger, and P. Lacombe, Scripta METALLURGICA 1977, 11, 533.
[9] S. C. Tsai, A. M. Huntz, and C. Dolin, Materials Science and Engineering 1996, 212, 6.
[10] Z. Wang, J.-L. Grosseau-Poussard, B. Panicaud, G. Geandier, P.-O. Renault, P. Goudeau, N. Boudet, N. Blanc, F. Rakotovao, Z. Tao, Metals 2018, 8, 913.

[11] F. Rakotovao, B. Panicaud, J.L. Grosseau-Poussard, Z. Tao, G. Geandier, P.O. Renault, P. Girault, P. Goudeau, N. Blanc, N, Acta Materialia 2018, 159, 276–285.

[12] F. Rakotovao, Relaxation des contraintes dans les couches de chromine développées sur alliages modèles (NiCr et Fe47Cr): apport de la diffraction in-situ à haute température sur rayonnement Synchrotron à l'étude du comportement viscoplastique: effets d'éléments réactifs, PhD Thesis, Université de La Rochelle, La Rochelle, France, 2016.

[13] Z.J. Tao, Experimental study and modelling of mechanical features in an oxide layer under thermal loadings, PhD Thesis, Université de technologie de Troyes, Troyes, France, 2018.

[14] F. David, Aspects mécaniques de l'oxydation haute température du zirconium: modélisation des champs de contrainte et suivi expérimental multi technique des endommagements, PhD Thesis, Université de technologie de Compiègne, Compiègne, France, 2017.

[15] L. Kurpaska, Analyse des contraintes mécaniques à haute température dans les films d'oxyde: application au système Zr/ZrO2, PhD Thesis, Université de technologie de Compiègne, Compiègne, France, 2012.

[16] U.R. Evans, and A.B. Winterbottom, Metallic corrosion, passivity and protection, 1948.

[17] A. Brenner, S. Senderoff, Journal of Research of the National Bureau of Standards 1949, 42, 105.

[18] W. Przybilla, M. Schutze, Oxidation of Metals 2002, 58.

[19] Li, M., Li, T., Gao, W., Liu, Z., n.d. Determination of Oxide Growth Stress by a Novel Deflection Method, Oxidation of Metals, 1999, 51, 516.

[20] M. François, Journal of Applied Crystallography 2008. 41, 44–55.

[21] J. Liu, R.E. Saw, Y.-H. Kiang, Journal of Pharmaceutical Sciences 2010. 99, 3807–3814.

[22] M. M. Abdullah, F. M. Rajab, S. M. Al-Abbas, AIP Advances 2014, 4, 027121.

[23] C. Li, S.D.M. Jacques, Y. Chen, P. Xiao, A.M. Beale, M. di Michiel, N. Markossan, P. Nylen, R.J. Cernik, Scripta Materialia 2016. 113, 122–126.

[24] B. B. He, U. Preckwinkel, K. L. Smith, International Centre for Diffraction Data 2003, 46, 6.

[25] L. Le, D. W. Ming, B. Sutter, 46th Lunar and Planetary Science Conference 2015, 2.

[26] S. Petrovic, N. Bundaleski, M. Radovic, Z. Ristic, G. Gligoric, D. Perusko, S. Zec, Sci Sintering 2006. 38, 155–160.

[27] B. Panicaud, Contraintes « de croissance » et cinétiques d'oxydation dans des couches d'oxides thermiques de Fer et de Nickel ; Etude in-situ par Diffraction des Rayons X et modélisation, PhD Thesis, Université de La Rochelle, La Rochelle, France, 2004.

[28] Schütze, M. Protective Oxide Scales and Their Breakdown; Wiley: Hoboken, NJ, USA, 1991.

[29] Kofstadt, P. High Temperature Corrosion; Elsevier: London, UK, 1998.

[30] Huntz, A.M.; Pieraggi, B. Oxydation des matériaux métalliques; Hermès Science: Paris, France, 2003.

# Chapter 3: Optimization of thermomechanical parameters

# 3.1 Experimental results from ESRF

## 3.1.1 Experimental conditions

### 3.1.1.1 Materials

As mentioned in chapter 2, the studied material substrate is a NiCr alloy. The alloy that was used in these experiments performed at ERSF and presented in this chapter, contains a weight percentage of 28.28% Cr, symbolized by Ni28Cr. The work in this chapter is the continuity of works of F. Rakotovao [1] and Z.J. Tao [2]. In their works, they have used the method $\sin^2\psi$ to treat the data obtained thanks to synchrotron x-ray diffraction and they have begun the study of the thermal activation of creep deformation.

With the objective of investigating the influence of the reactive elements on the mechanical properties of the chromia layers, several groups of experiments were realized with the reactive elements $Y_2O_3$ or Zr. In order to call the sample more easily, we have given code names for the samples Ni28Cr with different exposure times corresponding to different quantities of $Y_2O_3$ in the alloy, as shown in Table 3.1, and for the samples Ni28Cr with different doping fluences corresponding to different quantities of Zr in the alloy, as shown in Table 3.2:

Table 3.1. Code names for the sample Ni28Cr with different exposure times

| Code name | Reactive element $Y_2O_3$ exposure time |
|---|---|
| $Y_2O_3$_t10 | t = 10s |
| $Y_2O_3$_t50 | t = 50s |
| $Y_2O_3$_t100 | t = 100s |

Table 3.2. Code names for the sample Ni28Cr with different doping fluences

| Code name | Reactive elements Zr fluence |
|---|---|
| Zr_1E15 | $1*10^{15}$ ions.cm$^{-2}$ |
| Zr_5E15 | $5*10^{15}$ ions.cm$^{-2}$ |
| Zr_1E16 | $1*10^{16}$ ions.cm$^{-2}$ |

### 3.1.1.2 Experimental setup

The XRD reflection mode is used, which has been performed as in-situ at high temperature. The energy of X-ray is 20 keV. The equipment has been introduced in section 2.2.1.1. The associated stress can be determined thanks to the $\sin^2\psi$ method, and using the radiocrystallographic elastic coefficients. The development of the $\sin^2\psi$ method is also presented in section 2.2.1. The experiments were done by F.

Rakotovao [1] and Z.J. Tao [2] during their PhD and have required complementary investigations, because it was not data treated or partially or with simpler data processing.

### 3.1.2 Results for stresses

The thermal solicitation applied to the sample Ni28Cr without pre-treatment is shown in Fig. 3.1:

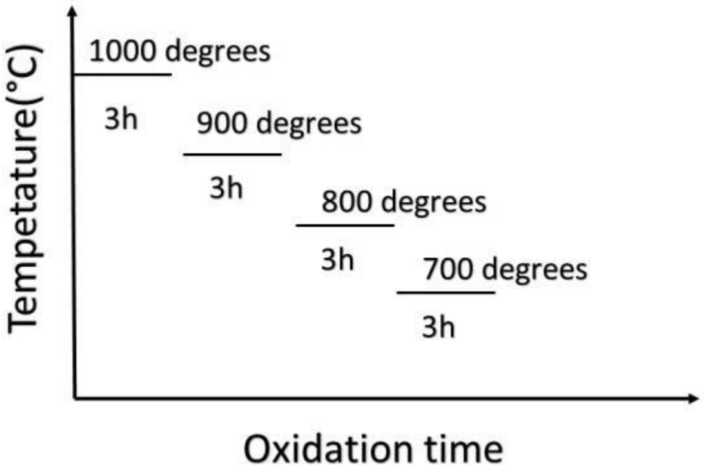

Figure 3.1. Thermal solicitation for the sample Ni28Cr

By using the $\sin^2\psi$ method on the experimental experiments, the stress-time curves in oxide are obtained. Fig. 3.2 shows the obtained results.

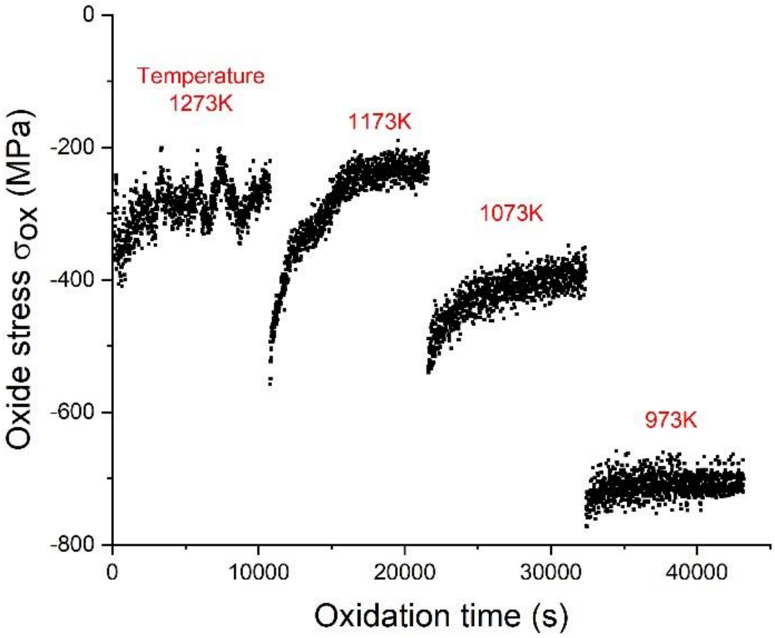

Figure 3.2. Stress evolution in the oxide versus time

Fig. 3.2 evidences that the stress in oxide is compressive. When the temperature changes, the jump of the oxide stress between plateaus is clearly visible. During the plateaus, when the temperature is isothermal, the evolution of stress is mainly related to the growth of the oxide and the viscoplastic relaxation.

The results of two samples Ni28Cr with pre-treatment are shown in Fig. 3.3 and Fig. 3.4, corresponding to $Y_2O_3$_t100 and $\mathrm{Zr1E16}$:

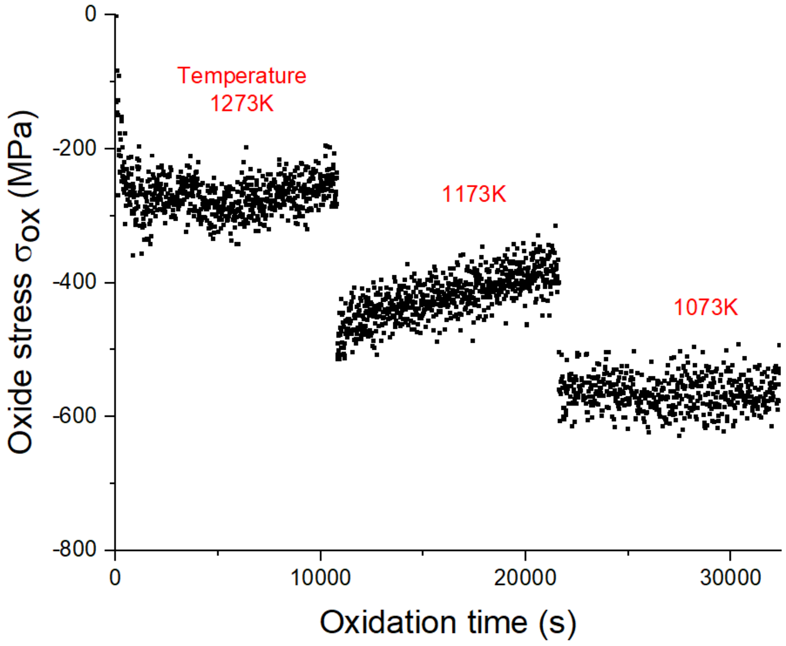

Figure 3.3. Stress evolution in the oxide versus time for sample $\mathrm{Y_2O_3\_t100}$

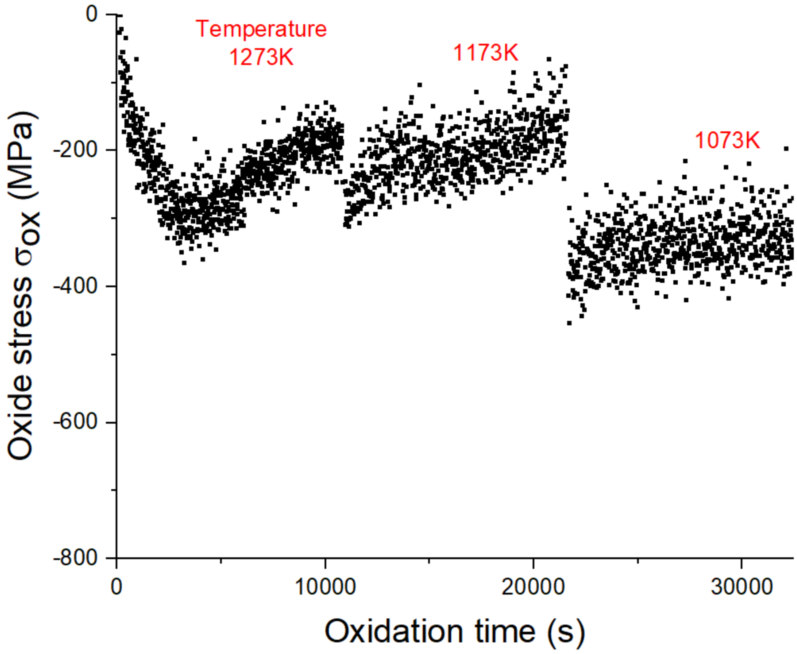

Figure 3.4. Stress evolution in the oxide versus time for sample $\mathrm{Zr1E16}$

There is no thermal load at 973K for the samples with pre-treatment. Comparing Fig. 3.2-4, we can see that after the pre-treatment, the jump between plateaus still exist. However, the stress evolution for each plateau changes a lot, especially for the low temperature plateaus at 1173 K and 1073 K. The increase and relaxation of absolute stress is clearly shown in Fig.3.3 and Fig.3.4, for the first plateau at 1273K. For the two low temperature plateaus at 1173 K and 1073 K, there is mainly the relaxation of stress. Moreover, for plateau at 1073 K, the change of stress is very small, which may be ignored. In order to investigate this phenomenon, an optimization process is proposed for identification of thermomechanical parameters.

## 3.2 Optimization process

### 3.2.1 Principle for optimization

The method for optimizing the parameters is based on the comparison of the time–dependent stresses (shown in section 3.1.2) and the numerical solution (related to section 1.2.3.3). By varying the parameters (the growth strain parameter for oxide ($\mathrm{D_{ox}}$) and the creep parameter for oxide ($\mathrm{J_{ox}}$)), the numerical solution can be made as similar as possible to the experimental time-dependent stresses. The way to find the best numerical solution compared to the time-dependent stresses is called optimization of parameters and corresponds to a fitting plateau per plateau.

Firstly, a full modelling of all the plateaus by taking into account all the experimental points as well as the modelling with thermal strain has been tested and proved to be not satisfying for the present study. As known in [3], the difference of thermal expansion coefficients α between oxide layer and metal substrate lead to a stress jump between plateaus. Using such a modelling to analyze the whole results for all the plateaus is more difficult and gives more uncertainty on the optimized parameters, which are $\mathrm{D_{ox}}$ and $\mathrm{J_{ox}}$. Thus, from a physical point of view, we chose to optimize the parameters plateau by plateau, which avoids introducing the influence of the thermal expansion coefficients α and the stress jump between plateaus within the parameter's identification process.

Secondly, because of the protection induced by the chromia layer formed at 1273K, no more significant growth of the oxide layer occurs at lower temperature plateau. This has been verified through ATG by mass evolution in the oxide phase (as shown in section 2.1.2). Moreover, it is shown in [1] that the evolution of the diffraction intensities does not change any more after the highest temperature plateau. Therefore, $\mathrm{D_{ox}}$ can be chosen equal to zero at 973K, 1073K and 1173K with a good confidence, when a previous plateau at a higher temperature is performed [4]. Additionally, the parabolic kinetics parameter (Ap) is equal to zero, because of no significant growth of oxide at lower temperature plateaus. Thus, the only parameter to be identified for these lower temperature plateaus is $\mathrm{J_{ox}}$.

Moreover, one condition for a correct fitting is that $\mathrm{J_{ox}(T)}$ should also have a physical meaning. As seen in Eq. (1.35), the parameter $\mathrm{J_{ox}(T)}$ can be described as:

$$\mathrm{J_{ox}} = \frac{\mathrm{Cste}}{\mathrm{k_B T}} \exp\left(-\frac{\mathrm{Q}}{\mathrm{RT}}\right) \tag{3.1}$$

where Cste is a constant, $\mathrm{k_B}$ is the Boltzmann constant and Q is the activation energy associated to the considered creep mechanism. This equation can be transformed into:

$$\mathrm{Ln(J_{ox} k_B T)} = \mathrm{Ln(Cste)} - \frac{\mathrm{Q}}{\mathrm{R}} \times \frac{1}{\mathrm{T}} \tag{3.2}$$

If we draw the curve of $\mathrm{Ln(J_{ox}k_BT)}$ versus $\frac{1}{\mathrm{T}}$ for different temperatures, we should get a straight line and the activation energy Q can be deduced from the slope of this line. By drawing the curve $\mathrm{Ln(J_{ox}k_BT)}$ versus 1/T using $\mathrm{J_{ox}}$ for temperature plateaus at 973K, 1073K and 1173K, the theoretical value of $\mathrm{J_{ox}}$ for 1273K can be extrapolated. By using this theoretical value of $\mathrm{J_{ox}}$ for 1273K at first iteration, we can fit the first temperature plateau at 1273K and optimize the values of both $\mathrm{J_{ox}}$ and $\mathrm{D_{ox}}$ at the same time.

### 3.2.2 Optimization of Jox for the lower temperature plateaus with Dox = 0

The simulation results have been obtained for the 973K, 1073K and 1173K temperature plateaus, except for the first temperature plateau at 1273K [2]. The sample is raw material Ni28Cr alloy and the thermal solicitation is shown in Fig. 3.1.

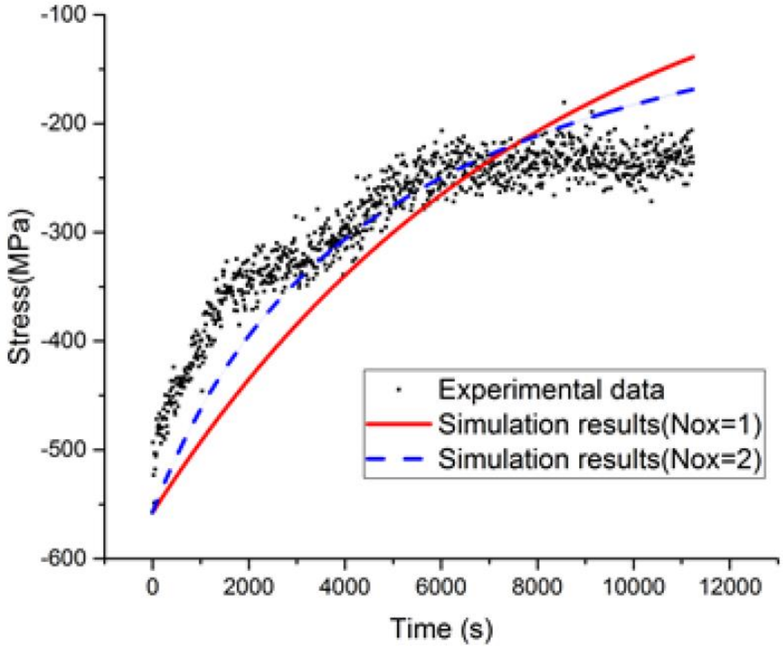

Figure 3.3.a Fitting for parameter $J_{ox}$ at 1173K using different Nox [2]

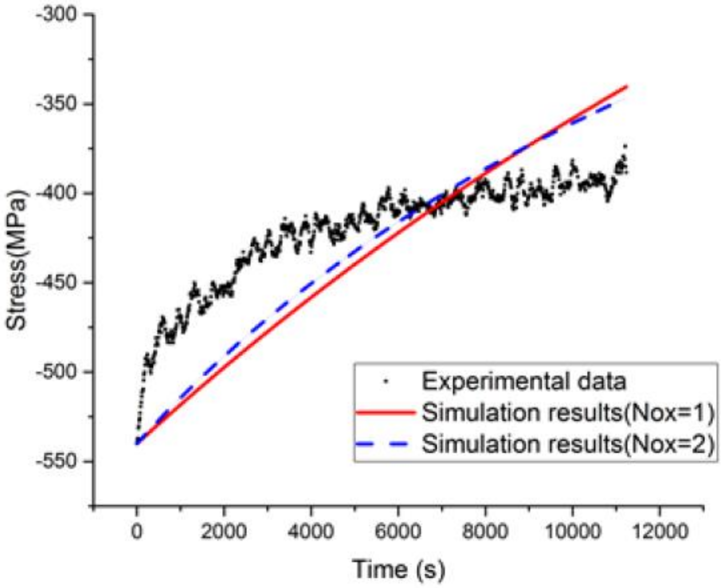

Figure 3.3.b Fitting for parameter $J_{ox}$ at 1073K using different Nox [2]

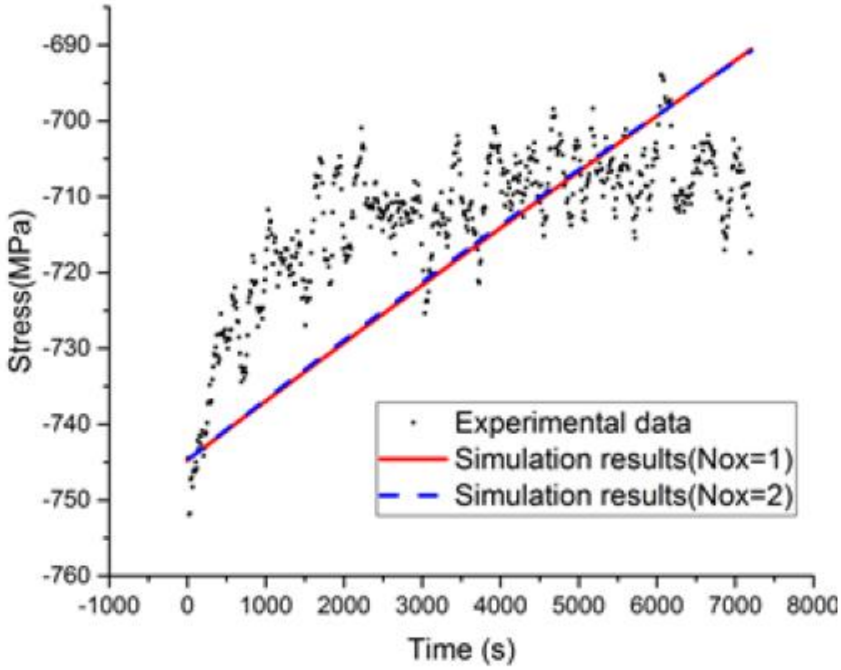

Figure 3.3.c Fitting for parameter $J_{ox}$ at 973K using different Nox [2]

Figs 3.3.a.b.c show that the simulations are not as good as expected. Maybe it is because the $D_{ox}$ value has been fixed for all these temperature plateaus. If $D_{ox}$ was remained as variable and if the fitting procedures have considered for both $J_{ox}$ and $D_{ox}$ at the same time, then the fit quality could be better from a mathematical point of view. However, Rakotovao [1] has showed that the microstructure was constructed only during the first temperature plateau and the thickness and grain size do not change any more for the lower temperature plateau. Thus, it is quite reasonable to assume $D_{ox}$ = 0 for the lower temperature plateaus, even if the simulation quality does not appear as so good for some plateaus. We require mainly physical consistence of the identification process. There may also be other possible physical explanations. For example, the creep parameter of metal ($J_m$) and the Norton exponent of metal ($N_m$), which are very sensitive and difficult to identify.

The test in Fig. 3.3 shows that the Norton exponent Nox tested as 1 and 2, which have not significant difference for low temperature plateaus. Moreover, the Norton exponent Nox can be extracted by the asymptotic approach for a long time and often leads to a unit exponent. This behavior is generally interpreted as boundary creep mechanisms [5]. Indeed, the Nabarro-Herring and Coble creep mechanisms lead to a Norton exponent that equals to 1. The value for Nox can be chosen very confidently [6]. Therefore, for layer oxide, the Nox value is assumed systematically equal to 1 for the considered oxides. In addition, it is possible to check once again that Nox is close to the unit. This was achieved successfully, as presented in Panicaud et al [7].

### 3.2.3 Optimization of Jox and Dox for the first plateau

From Figs 3.3.a.b.c, the different creep parameters $\mathrm{J_{ox}}$ have been identified for the temperature plateaus at 973K, 1073K and 1173K. Therefore, by plotting the curve $\mathrm{Ln(J_{ox}k_BT)}$ versus 1/T, a theoretical and numerical value of $\mathrm{J_{ox}}$ for 1273K can be extrapolated. The sample is raw material Ni28Cr alloy.

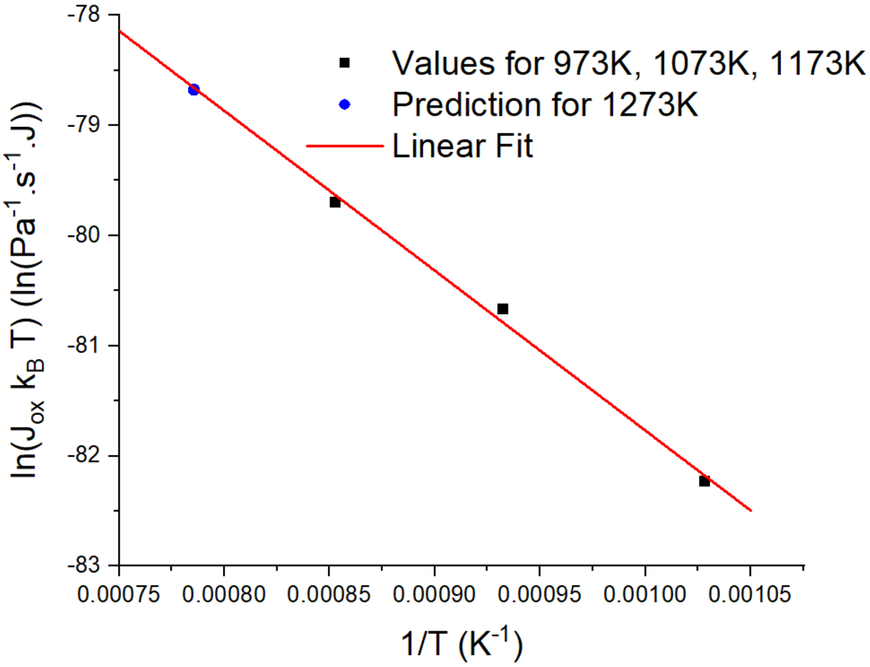

Figure 3.4. Linear fit of $\mathrm{Ln(J_{ox}k_BT)}$ versus $\frac{1}{\mathrm{T}}$ and extrapolation of $\mathrm{J_{ox}}$ at 1273K

Fig. 3.4 shows that the creep parameter $\mathrm{J_{ox}}$ for temperature plateaus at 973K, 1073K and 1173K have a perfect linear fit. From this linear fit, the $\mathrm{J_{ox}}$ value for 1273K can be predicted.

Finally, with this theoretical value of $\mathrm{J_{ox}}$ for 1273K, we can fit the first temperature plateau at 1273K and optimize then simultaneously the values of $\mathrm{J_{ox}}$ and $\mathrm{D_{ox}}$.

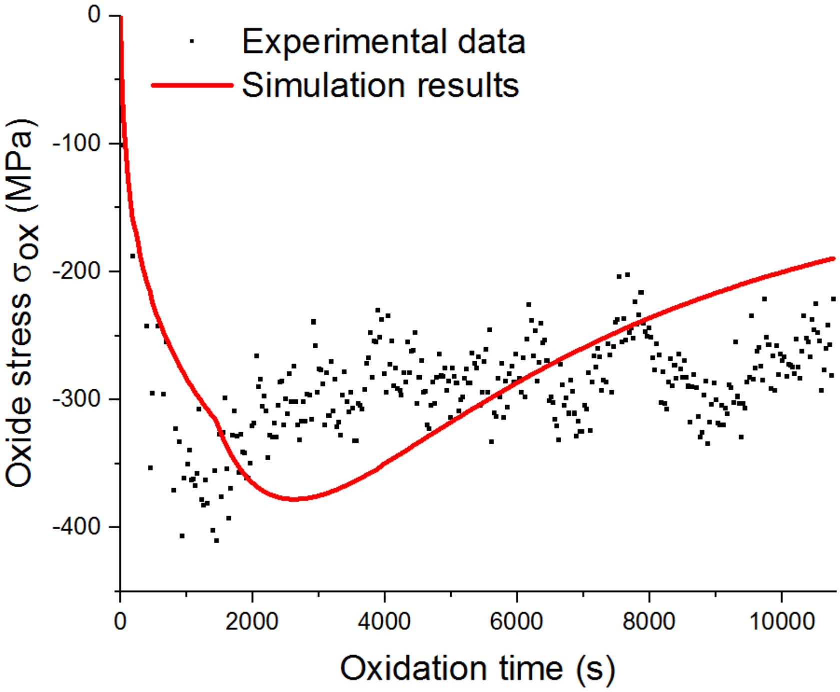

Figure 3.5. Fitting for parameter $J_{ox}$ and $D_{ox}$ at 1273K with Nox=1

Fig. 3.5 fits the parameter $J_{ox}$ and $D_{ox}$. Since this is the first plateau, we assume that the stress is 0MPa at the very beginning of our experiment. This assumption can be well verified by the experience data in many samples.

## 3.3 Results for the different materials

### 3.3.1 Results for the raw material Ni28Cr alloy

In section 3.2, the process of optimization of raw material Ni28Cr alloy has been presented. The thermal solicitation of sample Ni28Cr includes 4 plateaus: 1273K, 1173K, 1073K and 973K, as shown in Fig. 3.1. The results concerning $J_{ox}$ ($Pa^{-1}s^{-1}$) and $D_{ox}$ ($m^{-1}$) obtained from the optimization procedure for the raw material Ni28Cr alloy are presented in Table 3.3.

Table 3.3. Results for raw material Ni28Cr alloy

| Temperature (K) | 1273 | 1173 | 1073 | 973 |
|---|---|---|---|---|
| $J_{ox}$ ($Pa^{-1}s^{-1}$) | $4.68*10^{-15}$ | $1.48*10^{-15}$ | $6.20*10^{-16}$ | $1.45*10^{-16}$ |

| | | | | |
|---|---|---|---|---|
| $D_{ox}$ ($m^{-1}$) | 2513.5 | 0 | 0 | 0 |

We can draw the linear fit of $Ln(J_{ox}k_BT)$ versus $\frac{1}{T}$ for Ni28Cr, as shown in Fig. 3.6:

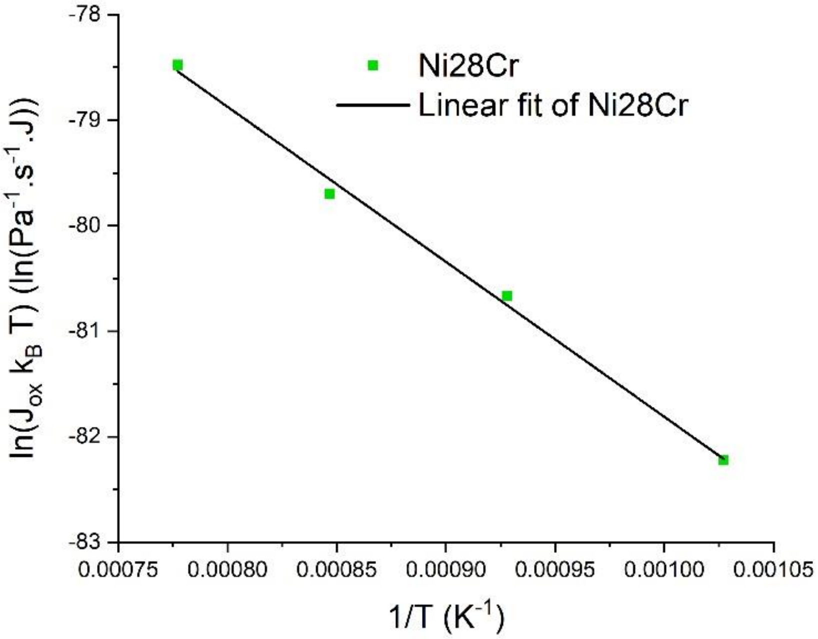

Figure 3.6. Linear fit of $Ln(J_{ox}k_BT)$ versus $\frac{1}{T}$

The activation energy Q can be calculated from the slope of this line that is 1.22 keV. Fig. 3.6 indicates that the creep parameter $J_{ox}$ decreases with a lower temperature, which is consistent with the thermal activation of the creep mechanism

## 3.3.2 Results for the yttria-coated materials

### 3.2.2.1 Sample $Y_2O_3$_t10

For the yttria-coated samples, there is no thermal load plateau at 973K. The simulation of experimental data of the sample $Y_2O_3\_t10$ and optimization procedure for plateaus 1073K, 1173K and 1273K are shown in Figs 3. 3.7.a.b.c.

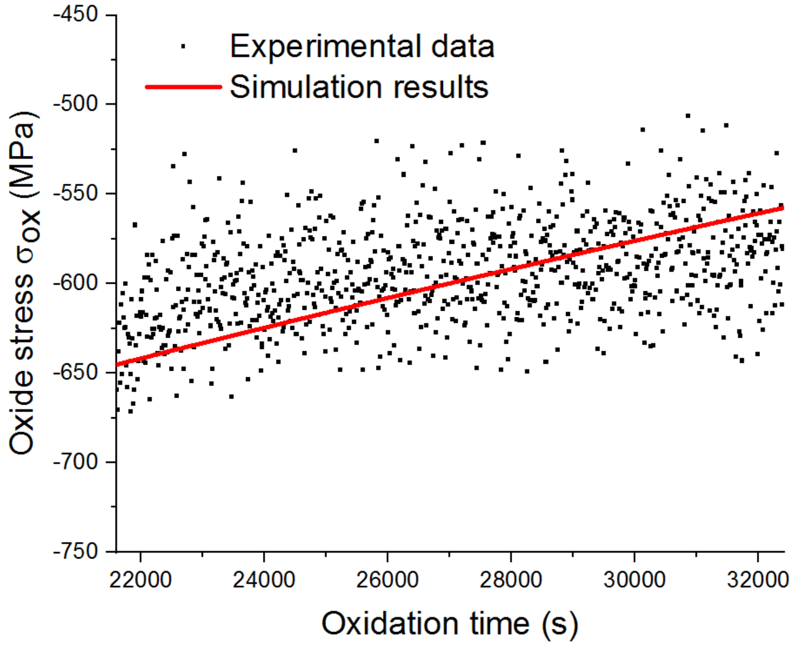

Figure 3.7.a Fitting for parameter $J_{ox}$ at 1073K

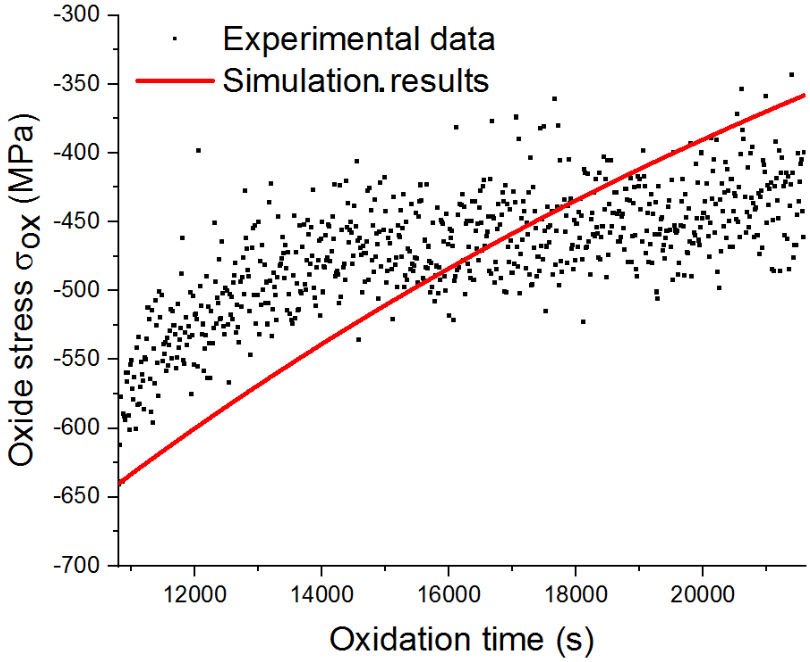

Figure 3.7.b Fitting for parameter $J_{ox}$ at 1173K

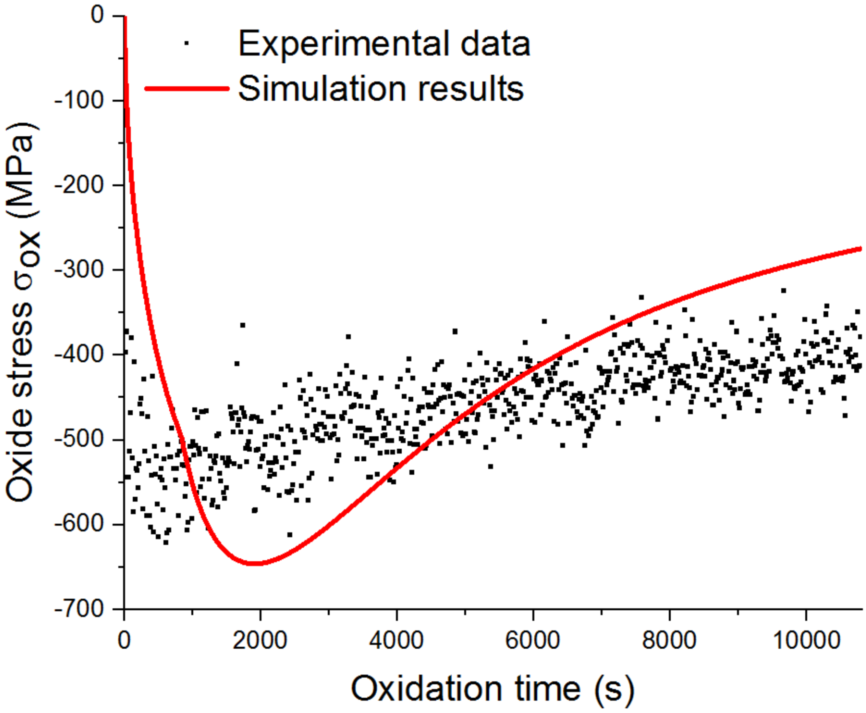

Figure 3.7.c Fitting for parameter $J_{ox}$ and $D_{ox}$ at 1273K

Figs 3.7.a.b.c show the simulations of $J_{ox}$ for sample $Y_2O_3\_t10$ with $N_{ox}$=1, which is the lowest deposited yttria amount. Fig 3.7.c indicates that the evolution of stress is clearly the result of a balance between two phenomena, which are the increase of stress in absolute value mainly caused by the growth of oxide layer and the relaxation of stress mainly caused by creep behavior. At the beginning of the plateau 1273K, the increase of stress holds a dominant position, until around 714s when the stress reaches -646MPa. After that, the relaxation of stress mainly holds the leading position in mechanical balance.

Fig 3.7.a and Fig 3.7.b indicate that there is no increase of stress, in relation to the protection of oxide layer formed at 1273K. The latter also indicates that the oxide layer formed at high temperature prevents the formation of oxide layer at lower temperatures. This phenomenon has been discussed in previous works with a simple model [2]. In the present work, a full thermomechanical model is applied that obtains the same conclusion, which also confirms that the oxide layer thickness does not increase when temperature jumps were applied towards lower values. The stress was released along two isothermal periods for 6h (3h for 1173K and 3h for 1073K). The stress release along the temperature plateaus is 280 MPa at 1173 K and 90 MPa at 1073 K.

The results concerning $J_{ox}$ ($Pa^{-1}s^{-1}$) and $D_{ox}$ ($m^{-1}$) obtained from the optimization procedure for the yttria-coated material $Y_2O_3\_t10$ are presented in Table 3.4.

Table 3.4. Results for the yttria-coated material $Y_2O_3$_t10

| Temperature(K) | 1273 | 1173 | 1073 |
|---|---|---|---|
| $J_{ox}$ ($Pa^{-1}s^{-1}$) | $1.19*10^{-15}$ | $1.09*10^{-16}$ | $2.96*10^{-17}$ |
| $D_{ox}$ ($m^{-1}$) | 4633.1 | 0 | 0 |

As discussed before, $D_{ox}$ equals to zero for plateaus at 1073K and 1173K. In addition, the creep parameter $J_{ox}$ decreases as temperature decreases.

### 3.2.2.2 Sample $Y_2O_3$_t50

The simulation of experimental data of sample $Y_2O_3\_t50$ and optimization procedure for plateau 1073K, 1173K and 1273K are shown in Figs 3.8.a.b.c.

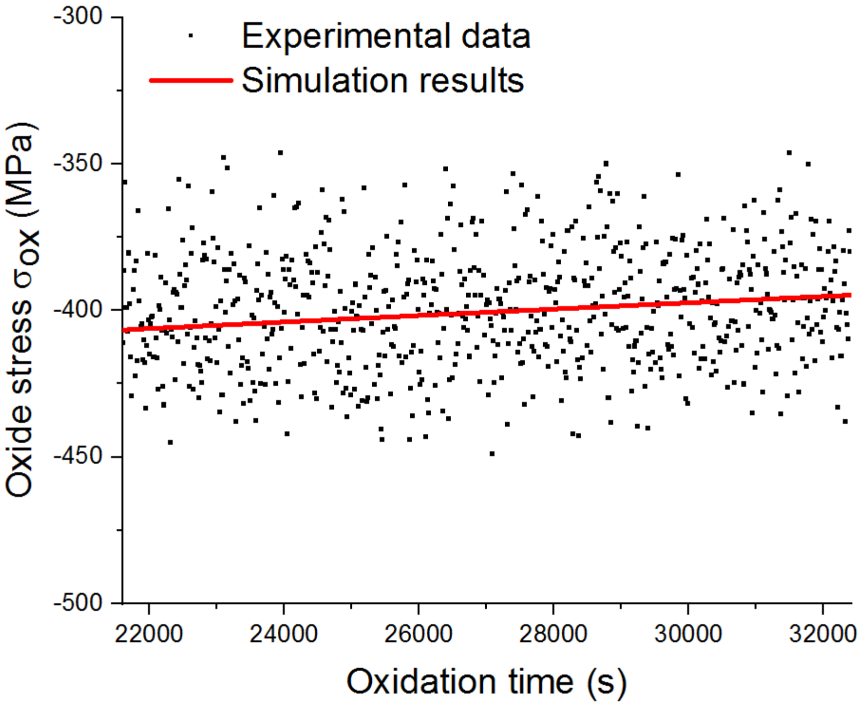

Figure 3.8.a Fitting for parameter $J_{ox}$ at 1073K

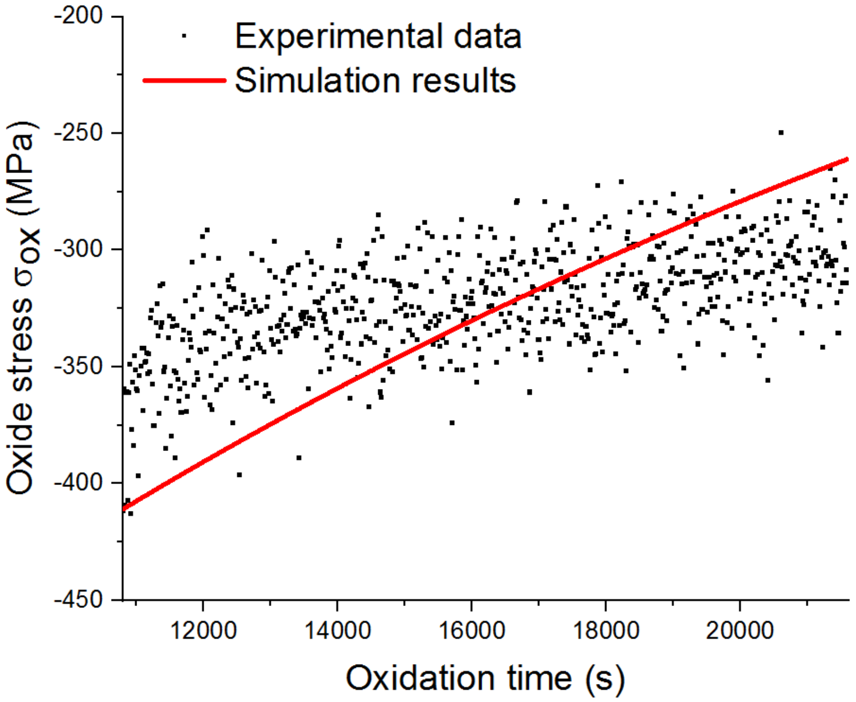

Figure 3.8.b Fitting for parameter $J_{ox}$ at 1173K

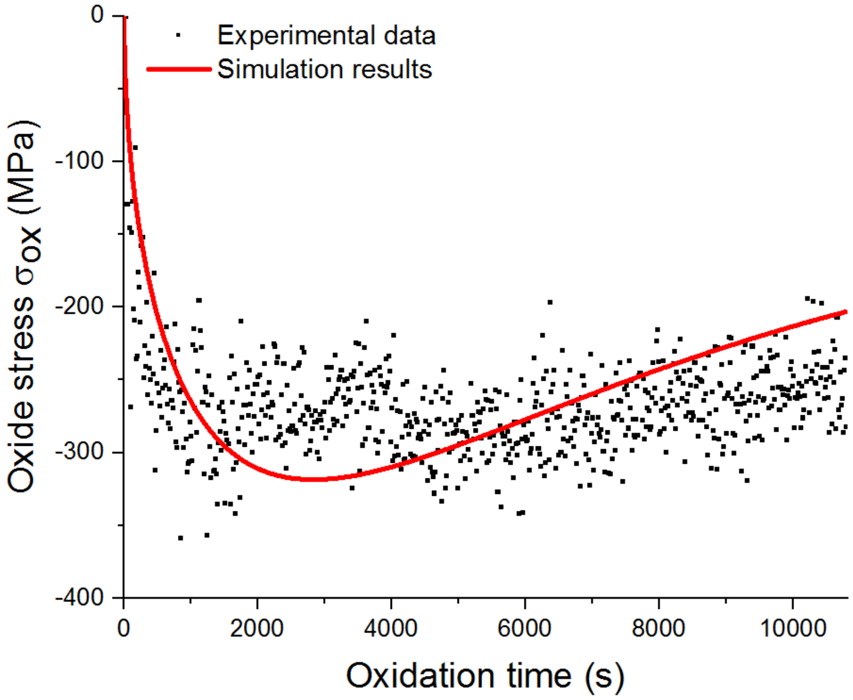

Figure 3.8.c Fitting for parameter $J_{ox}$ and $D_{ox}$ at 1273K

Figs 3.8.a.b.c show the simulation of $J_{ox}$ for sample $Y_2O_3\_t50$ with Nox=1, which leads to the same conclusions as for Figs 3.7.a.b.c. For the plateau at 1273K, the evolution of stress is the result of a balance between two phenomena. Until 1470s when stress reaches -319MPa, the increase of stress holds a dominant position. After that, the relaxation of stress holds the leading position.

Fig 3.8.a and Fig 3.8.b indicate that there is no increase of stress. The stress was released along two isothermal periods for 6h (3h for 1173K and 3h for 1073K). After temperature jumps, stress relaxation is always considered with a decreasing amplitude with the isothermal temperature plateau (150MPa at 1173K and 10MPa at 1073K). Particularly, for the plateau at 1073K, the change of stress is very low, compared to the stress change at 1173K and 1273K, which means that during the isothermal periods at 1073K, there is almost no relaxation of stress, which means that creep behavior is relatively weak compared to the plateaus with high temperature.

The results concerning $J_{ox}$ ($Pa^{-1}s^{-1}$) and $D_{ox}$ ($m^{-1}$) obtained from the optimization procedure for the yttria-coated material $Y_2O_3\_t50$ are presented in Table 3.5.

Table 3.5. Results for the yttria-coated material $Y_2O_3\_t50$

| Temperature(K) | 1273 | 1173 | 1073 |
|---|---|---|---|
| $J_{ox}$ ($Pa^{-1}s^{-1}$) | $7.50*10^{-16}$ | $8.62*10^{-17}$ | $5.51*10^{-18}$ |
| $D_{ox}$ ($m^{-1}$) | 3660.5 | 0 | 0 |

The same kind of results can be extracted as for sample $Y_2O_3\_t10$. $D_{ox}$ equals to zero for plateau at 1073K and 1173K. For plateau at 1273K, $D_{ox}$ of $Y_2O_3\_t50$ is smaller than $D_{ox}$ of $Y_2O_3\_t10$. In addition, the creep parameter $J_{ox}$ decreases as the temperature decreases.

### 3.2.2.3 Sample $Y_2O_3\_t100$

The simulation of experimental data of sample $Y_2O_3\_t100$ and optimization procedure for plateau at 1073K, 1173K and 1273K are shown in Figs 3.9.a.b.c.

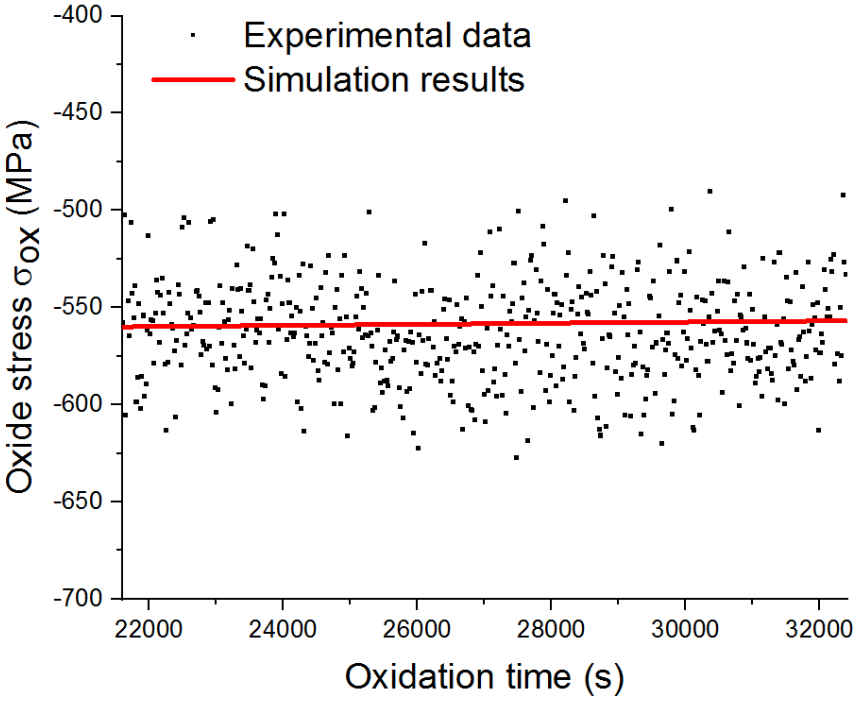

Figure 3.9.a Fitting for parameter $J_{ox}$ at 1073K

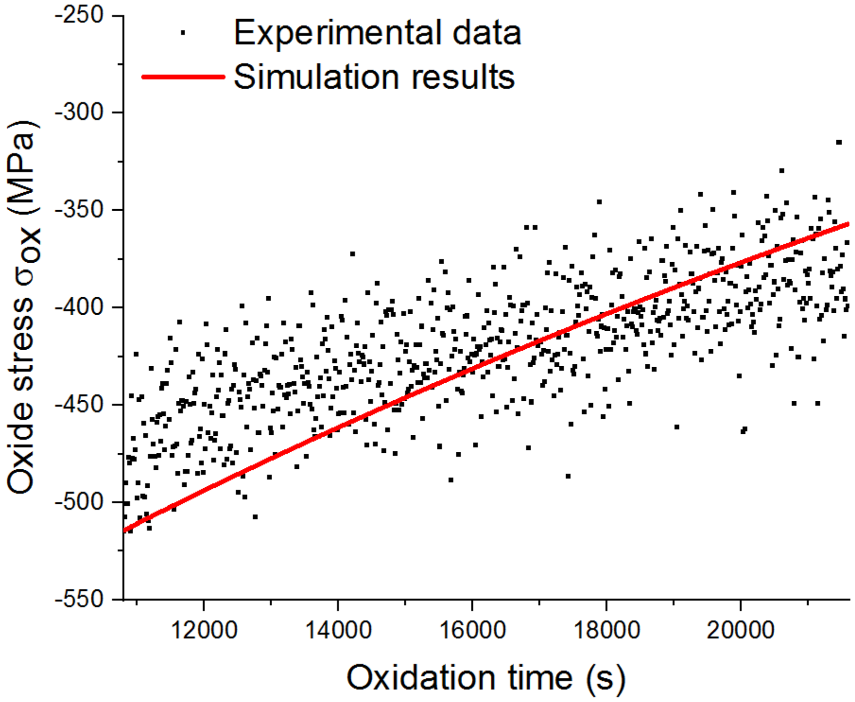

Figure 3.9.b Fitting for parameter $J_{ox}$ at 1173K

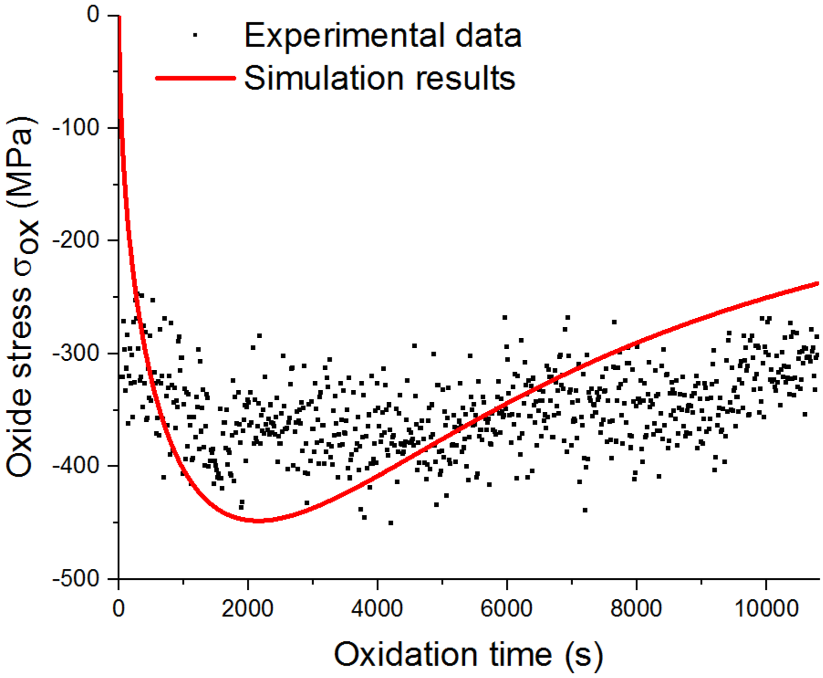

Figure 3.9.c Fitting for parameter $J_{ox}$ and $D_{ox}$ at 1273K

Figs 3.9.a.b.c show the simulation of $J_{ox}$ for sample $Y_2O_3\_t100$ with Nox=1, which leads to the same conclusions as Figs 3.8.a.b.c. For the plateau 1273K, untill 2454s when stress reaches -448MPa, the increase of stress holds a dominant position. After that, the relaxation of stress holds the leading position. Fig 3.9.a and Fig. 3.9.b indicate that there is no increase of stress. The stress relaxation amplitude is 60 MPa at 1173K and 0 MPa at 1073K. For the plateau at 1073K, the change of stress is very small, compared to the stress change at 1173K and 1273K, which means that the creep amplitude is lower.

The results concerning $J_{ox}$ (Pa$^{-1}$s$^{-1}$) and $D_{ox}$ (m$^{-1}$) obtained from the optimization procedure for the yttria-coated material $Y_2O_3\_t100$ are presented in Table 3.6.

Table 3.6. Results for the yttria-coated material $\mathrm{Y_2O_3\_t100}$

| Temperature(K) | 1273 | 1173 | 1073 |
|---|---|---|---|
| $J_{ox}$ (Pa$^{-1}$s$^{-1}$) | 8.21*10$^{-16}$ | 6.85*10$^{-17}$ | 1.35*10$^{-18}$ |
| $D_{ox}$ (m$^{-1}$) | 2666.8 | 0 | 0 |

The same kind of results can be extracted as for sample $Y_2O_3\_t10$. $D_{ox}$ equals to zero for plateau at 1073K and 1173K. For the plateau at 1273K, $D_{ox}$ for $Y_2O_3\_t100$ is smaller than $D_{ox}$ for $Y_2O_3\_t50$ and $D_{ox}$ for $Y_2O_3\_t10$. The growth strain parameter $D_{ox}$ decreases with the exposure time, thus with the increase of the quantity of reactive elements. In addition, the creep parameter $J_{ox}$ decreases as the temperature decreases.

## 3.3.3 Results for the zirconium-doped materials

### 3.3.3.1 Sample Zr_1E15

For the zirconium-doped samples, there is no thermal load plateau at 973K. The simulation of experimental data of sample Zr_1E15 and optimization procedure for plateau 1073K, 1173K and 1273K are shown in Figs 3.10.a.b.c.

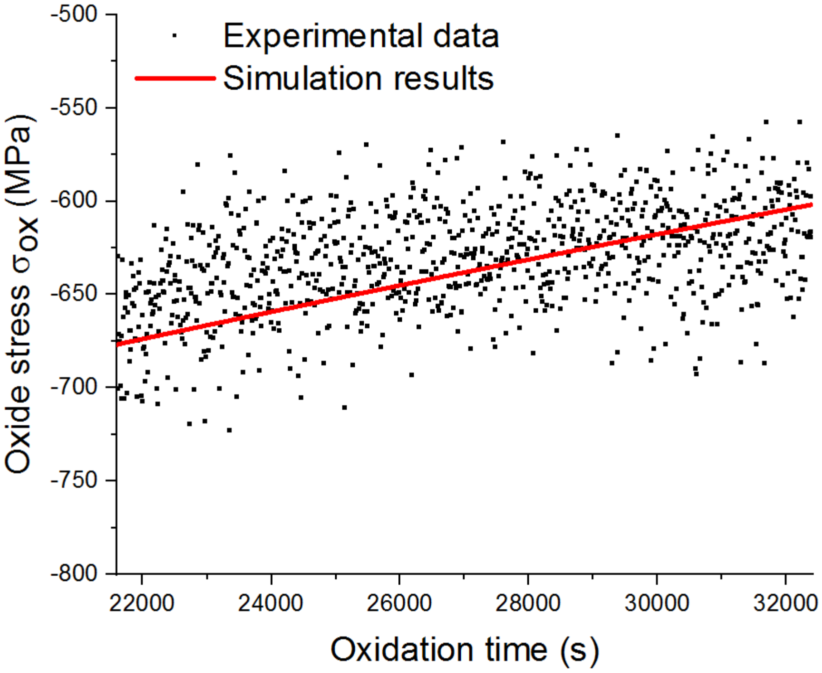

Figure 3.10.a Fitting for parameter $J_{ox}$ at 1073K

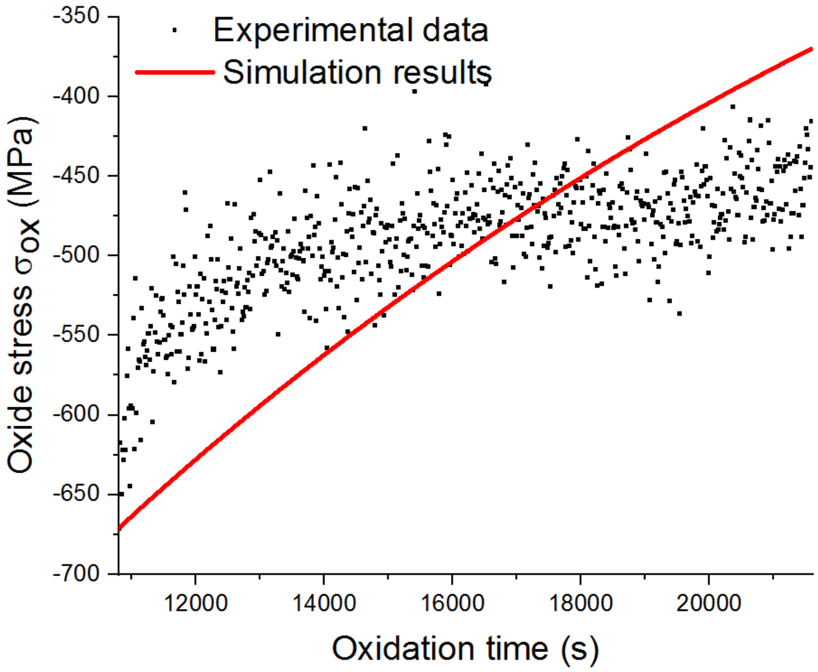

Figure 3.10.b Fitting for parameter $J_{ox}$ at 1173K

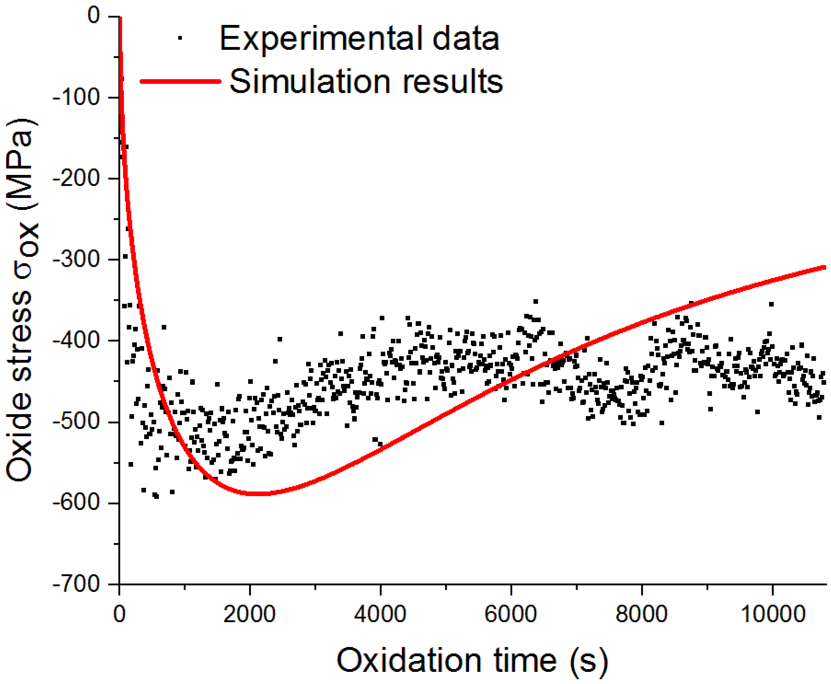

Figure 3.10.c Fitting for parameter $J_{ox}$ and $D_{ox}$ at 1273K

Figs 3.10.a.b.c show the simulation of $J_{ox}$ for sample Zr_1E15 with Nox=1, which is the smallest deposited zirconium amount. Fig. 3.10.c indicates that the evolution of stress is the result of a balance between two phenomena, which are the increase of stress mainly caused by the growth of oxide layer and the relaxation of stress mainly caused by creep behavior. At the beginning of the plateau 1273K, the increase of stress holds a dominant position, until 1014s when the stress reaches -588MPa. After that, the relaxation of stress holds the leading position.

Fig. 3.10.a and Fig. 3.10.b indicate that there is no increase of stress, due to the protection of oxide layer formed at 1273K, which proves that the oxide layer formed at high temperature prevents the formation of oxide layer at low temperature. This phenomenon has been discussed in previous works with simple model [2]. In the present work, a full model is applied that leads to the same conclusions, which confirms that the oxide layer did not increase when temperature jumps were applied towards lower values. The stress was released along two isothermal periods for 6h (3h for 1173K and 3h for 1073K). The stress release amplitude along the temperature plateaus is 300 MPa at 1173 K and 75 MPa at 1073 K.

The results concerning $J_{ox}$ (Pa$^{-1}$s$^{-1}$) and $D_{ox}$ (m$^{-1}$) obtained from the optimization procedure for the zirconium-doped material Zr_1E15 are presented in Table 3.7.

Table 3.7. Results for the zirconium-doped material Zr_1E15

| Temperature(K) | 1273 | 1173 | 1073 |
|---|---|---|---|
| $J_{ox}$ ($Pa^{-1}s^{-1}$) | $8.33*10^{-16}$ | $1.47*10^{-16}$ | $4.68*10^{-17}$ |
| $D_{ox}$ ($m^{-1}$) | 3528.4 | 0 | 0 |

As we discussed before, $D_{ox}$ equals to zero for plateau 1073K and 1173K. In addition, the creep parameter $J_{ox}$ decreases as the temperature decreases.

### 3.3.3.2 Sample Zr_5E15

The simulation of experimental data of sample Zr_5E15 and optimization procedure for plateau 1073K, 1173K and 1273K are shown in Figs 3.11.a.b.c.

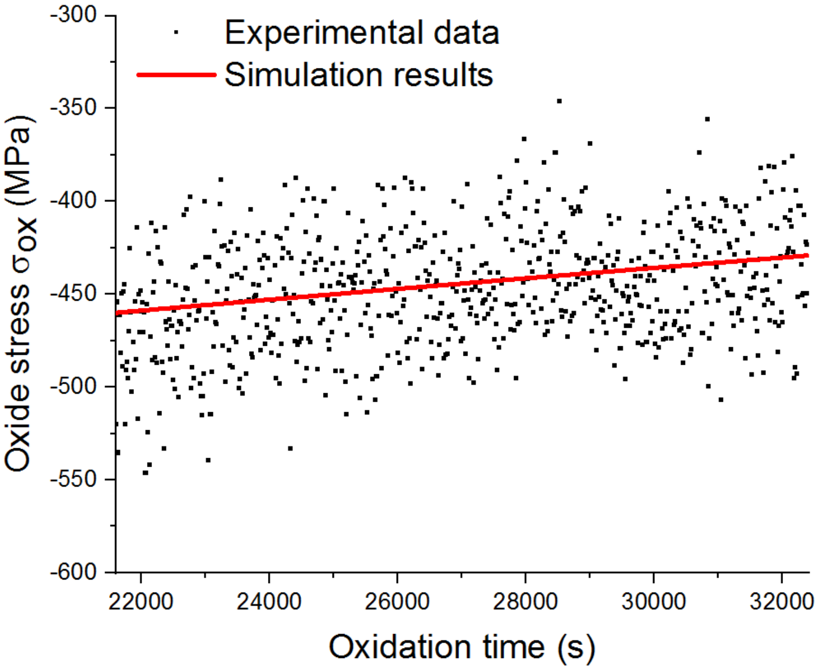

Figure 3.11.a Fitting for parameter $J_{ox}$ at 1073K

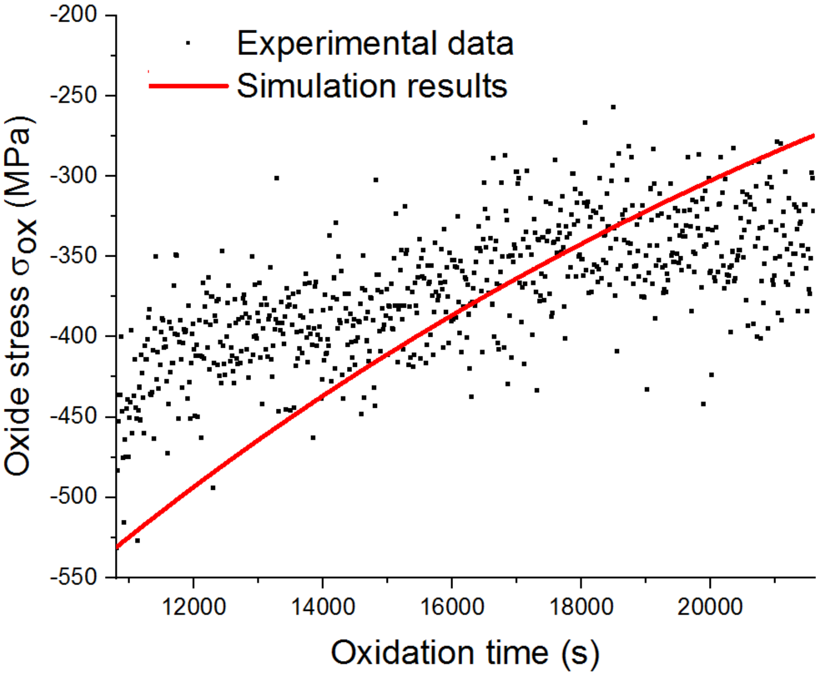

Figure 3.11.b Fitting for parameter $J_{ox}$ at 1173K

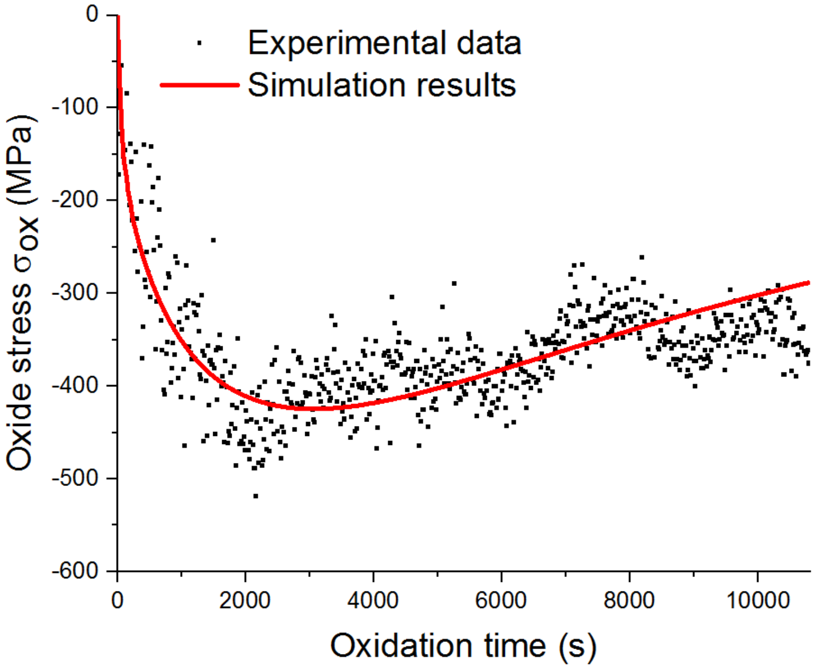

Figure 3.11.c Fitting for parameter $J_{ox}$ and $D_{ox}$ at 1273K

Figs 3.11.a.b.c show the simulation of $J_{ox}$ for sample Zr_5E15 with Nox=1, which leads to the same conclusions as for sample Zr_1E15. For the plateau 1273K, the evolution of stress is the result of a balance between two phenomena. Until 2388s when stress reaches -425MPa, the increase of stress holds a dominant position. After that, the relaxation of stress holds the leading position.

Figs 3.11.a and 11.b indicate that there is no increase of stress. The stress was released along two isothermal periods for 6h (3h for 1173K and 3h for 1073K). After temperature jumps, stress relaxation is always considered with a decreasing amplitude with the isothermal temperature plateau (250MPa at 1173K and 50MPa at 1073K).

The results concerning $J_{ox}$ (Pa$^{-1}$s$^{-1}$) and $D_{ox}$ (m$^{-1}$) obtained from the optimization procedure for the zirconium-doped material Zr_1E15 are presented in Table 3.8.

Table 3.8. Results for the zirconium-doped material Zr_5E15

| Temperature(K) | 1273 | 1173 | 1073 |
|---|---|---|---|
| $J_{ox}$ (Pa$^{-1}$s$^{-1}$) | $5.99*10^{-16}$ | $1.24*10^{-16}$ | $2.41*10^{-17}$ |
| $D_{ox}$ (m$^{-1}$) | 2156.7 | 0 | 0 |

The same kind of results can be extracted as for sample Zr_1E15. $D_{ox}$ equals to 0 for plateau 1073K and 1173K. For plateau 1273K, $D_{ox}$ of Zr_5E15 is smaller than $D_{ox}$ of Zr_1E15. In addition, the creep parameter $J_{ox}$ decreases as the temperature decreases.

### 3.3.3.3 Sample Zr_1E16

The simulation of experimental data of sample Zr_1E16 and optimization procedure for plateau 1073K, 1173K and 1273K are shown in Figs 3.12.a.b.c.

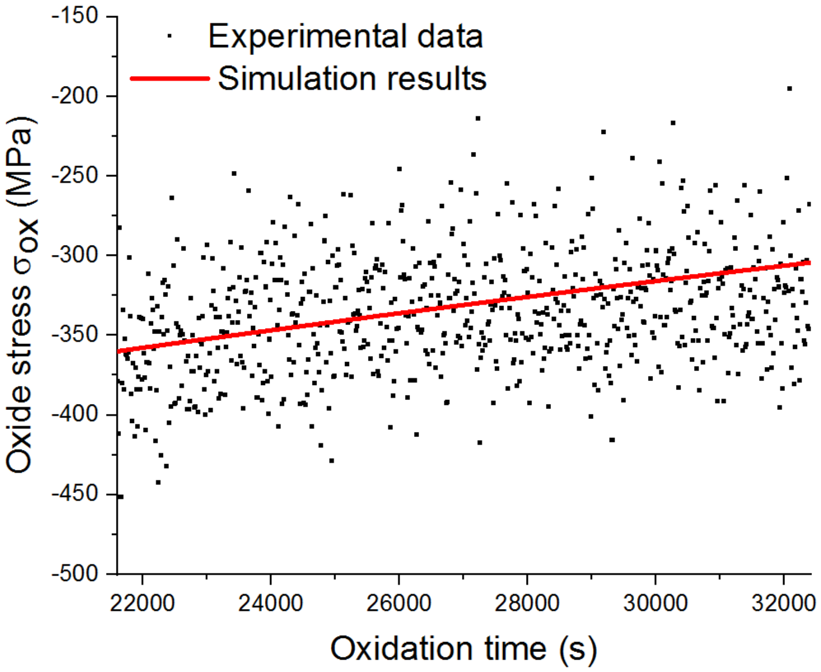

Figure 3.12.a Fitting for parameter $J_{ox}$ at 1073K

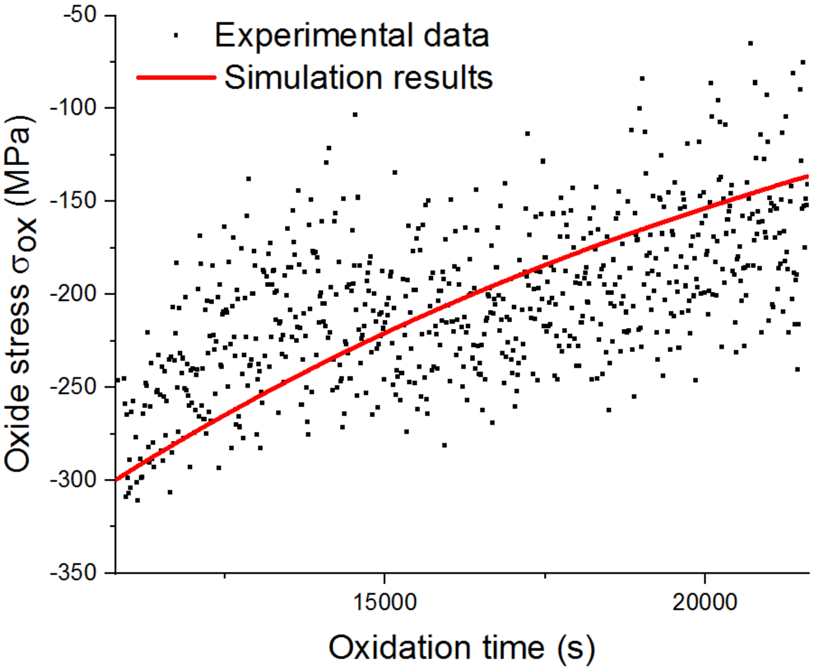

Figure 3.12.b Fitting for parameter $J_{ox}$ at 1173K

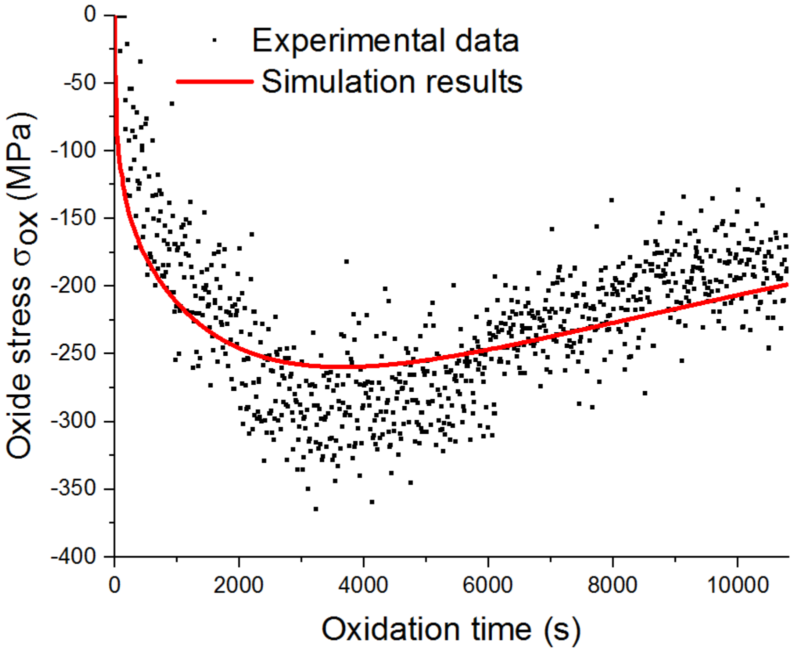

Figure 3.12.c Fitting for parameter $J_{ox}$ and $D_{ox}$ at 1273K

Figs 3.12.a.b.c show the simulation of $J_{ox}$ for sample Zr_1E16 with Nox=1, which leads to the same conclusions as for sample Zr_1E15. For the plateau 1273K, until 3438s (3846s for the simulation results) when stress reaches -260MPa, the increase of stress holds a dominant position. After that, the relaxation of stress holds the leading position. Fig. 3.12.a and Fig. 3.12.b indicate that there is no increase of stress. The stress relaxation is 164MPa at 1173K and 30MPa at 1073K.

The results concerning $J_{ox}$ ($Pa^{-1}s^{-1}$) and $D_{ox}$ ($m^{-1}$) obtained from the optimization procedure for the zirconium-doped material Zr_1E16 are presented in Table 3.9.

Table 3.9. Results for the zirconium-doped material Zr_1E16

| Temperature(K) | 1273 | 1173 | 1073 |
|---|---|---|---|
| $J_{ox}$ ($Pa^{-1}s^{-1}$) | $5.37*10^{-16}$ | $8.82*10^{-17}$ | $5.35*10^{-18}$ |
| $D_{ox}$ ($m^{-1}$) | 1249.1 | 0 | 0 |

The same kind of results can be extracted as for sample Zr_1E15. $D_{ox}$ equals to 0 for plateau 1073K and 1173K. For plateau 1273K, $D_{ox}$ of Zr_1E16 is smaller than $D_{ox}$ of Zr_5E15 and $D_{ox}$ of Zr_1E15. The growth strain parameter $D_{ox}$ decreases with the exposure time, which means with the increasing quantity of reactive elements. In addition, the creep parameter $J_{ox}$ decreases as the temperature decreases.

## 3.4 Discussion about the parameters Jox, Dox and the activation energies

### 3.4.1 Analysis for the yttria-coated materials

#### 3.4.1.1 The results for creep parameter Jox

The values of $J_{ox}$ as a function of temperature are shown in Fig. 3.13:

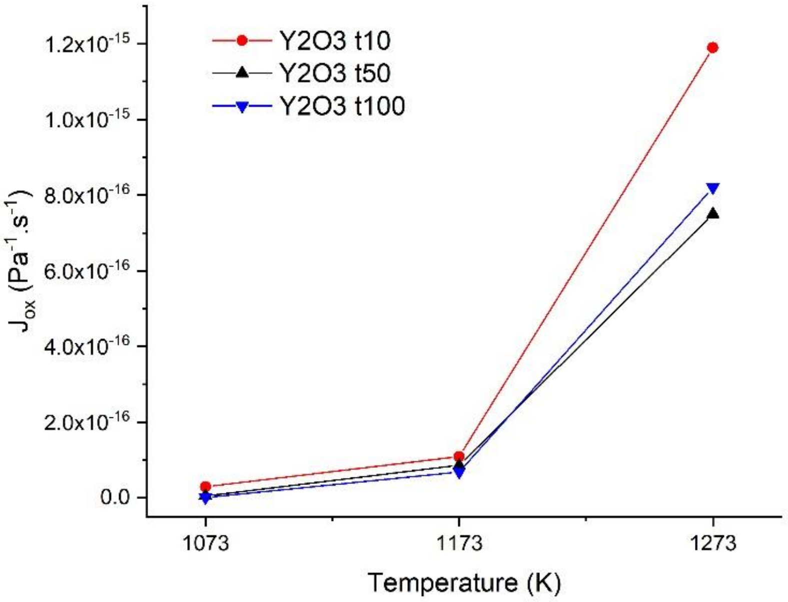

Figure 3.13. $J_{ox}$ versus temperature for the different yttria-coated samples.

Fig. 3.13 indicates that the creep parameter $J_{ox}$ increases as the temperature increases, whatever the quantity of yttria introduced is, which confirms the thermal activation of this relaxation mode. The aims of introducing reactive elements is generally to improve the protective properties of the thermally grown chromia layer under high temperature oxidation and to decrease the oxidation kinetics. By increasing the quantity of yttria coated, the creep parameter $J_{ox}$ decreases at plateau 1073K and 1173K. In other words, the viscoplastic strain rate is smaller with a large quantity of coated yttria for a same temperature. However, at 1273K, the $J_{ox}$ value of the yttria-coated 50s sample is slightly lower than the yttria-coated 100s sample, while the $J_{ox}$ value of the yttria-coated 10s is much higher than the other two samples. The $J_{ox}$ value of the yttria-coated 50s and 100s are close at 1273K, relatively to the one for the yttria-coated 10s sample.

We can also draw the linear fit of $Ln(J_{ox} * k_B * T)$ versus $\frac{1}{T}$, as shown in Fig. 3.14:

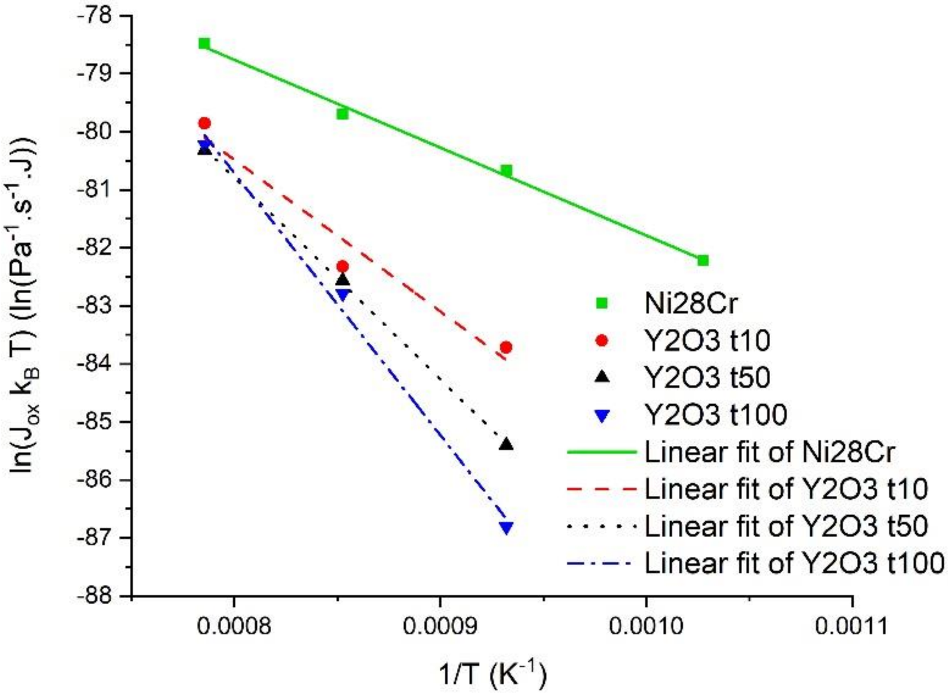

Figure 3.14. Linear fit of $Ln(J_{ox}k_BT)$ versus $\frac{1}{T}$ for yttria-coated materials and for the raw material (Ni28Cr in the legend)

Fig. 3.14 indicates that for the raw material and for all the yttria-coated materials, the creep parameter $J_{ox}$ decreases with a lower temperature as a proof of the thermal activation of the creep mechanism following an Arrhenius model. In addition, this behavior is observed independently of the amount of yttria introduced. For these {Ni28Cr + yttria-coated + $Cr_2O_3$} systems, when the yttria amount increases, the slope becomes higher which corresponds to an increase of the activation energy. The activation energies have been deduced for all the different materials. The activation energy for 10s and 50s yttria deposits are respectively 2.25eV and 2.99eV, which are much higher than the activation energy for the raw material 1.42eV. For the maximum yttria amount, the slope is the highest and the activation energy is then close to 3.89eV. The results are shown in Fig. 3.15:

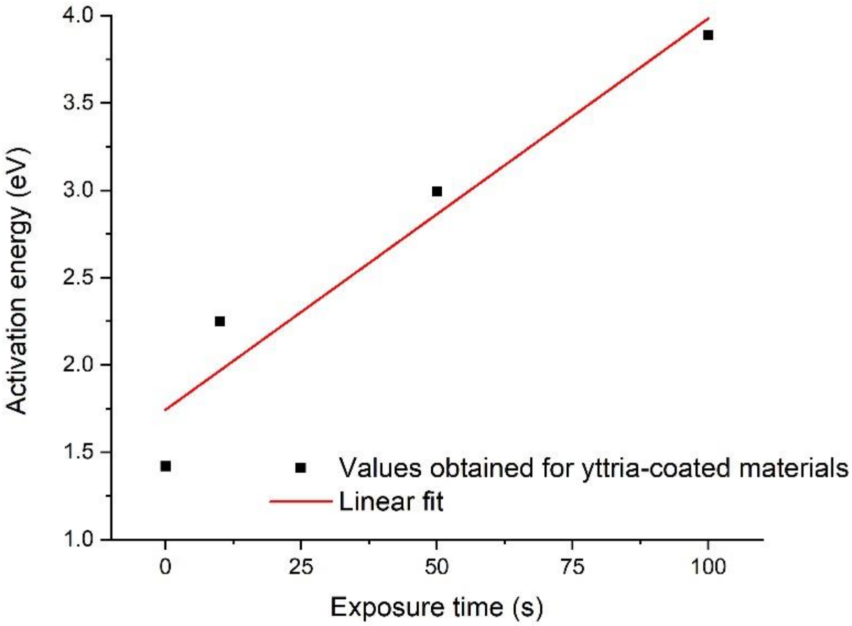

Figure 3.15. Activation energy $Q$ versus exposure time

As Fig. 3.15 shows, the activation energy increases with the exposure time, thus with the increase of the quantity of reactive element. This evolution is roughly linear.

To determine the elementary mechanisms that govern the viscoplastic behavior of the oxide layer as a function of the amount of yttria deposited, the growth mechanism of the thin the oxide layer should be considered at the same time [2]. The influence of reactive elements for NiCr alloy mainly is discussed in section 1.1.3. Moreover, it is known that the growth mechanism of the thin chromia oxide layers becomes anionic when a sufficient quantity of a reactive element is introduced; the formation of the oxide layer is thus controlled by the internal diffusion of oxygen along the diffusion short-circuits, i.e. the grain boundaries [8]. On the other hand, the relaxation of stresses due to diffusion creep in chromia oxide films containing reactive elements is governed by the diffusion of chromium at the grain boundaries. Moreover, the diffusion creep is controlled both by anionic and cationic mechanisms. According to these mechanisms, the energy around 1 eV would be attributed to the anionic mechanisms, while the energy around 2 eV would be attributed to the cationic mechanism [15]. Indeed, it is generally accepted that if the diffusion rate of the ions moving faster controls the oxidation process, then the creep rate is controlled by the motion of the ions moving more slowly [8-14].

Theoretically, a certain elementary mechanism is associated with an activation energy value. In the present case, the activation energy value of about 1eV is attributed to the anionic diffusion of oxygen $O^-$ while the value of about 2eV is attributed to the cationic diffusion of $Cr^+$ [15]. Fig. 3.15 indicates that the activation energy for the raw material is between 1eV and 2eV, which includes the mixing effect of the anionic and cationic diffusion. Fig. 3.15 also indicates an increase in energy with the exposure time, whose value is higher than 2eV, which means that the creep activation energy seems now to be mainly determined by the cationic diffusion of $Cr^+$. As the exposure time is longer, the activation energy of cationic is higher.

### 3.4.1.2 The results for the growth strain parameter Dox

The results concerning the $D_{ox}$ ($m^{-1}$) parameters for the yttria-coated material are presented in Fig. 3.16.

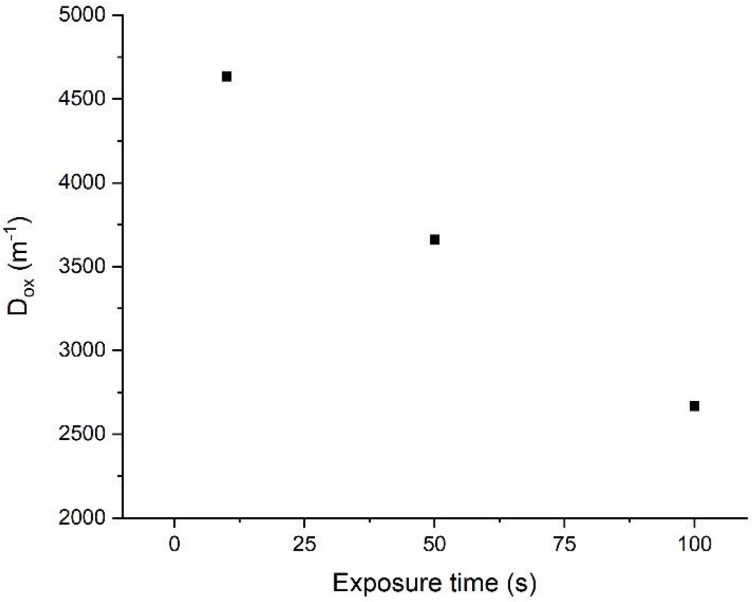

Figure 3.16. Growth strain parameter versus exposure time at 1273K

Fig. 3.16 gives the evolution of the $D_{ox}$ parameter as a function of the exposure time; so when the yttria content increases, the values of $D_{ox}$ decreases. As proposed in Eq.1.32, the activation energy for the growth strain parameter $Q_D$ can be calculated by:

$$Q_D = -ln\left(\frac{D_{ox0}}{D_{ox}}\right)RT \tag{3.3}$$

where $D_{ox0}$ is an parameter for the present oxide, as proposed in [16], which is equals to $0.122m^{-1}$. Thus, the activation energy for growth $Q_D$ versus exposure time has been plotted in Fig. 3.17:

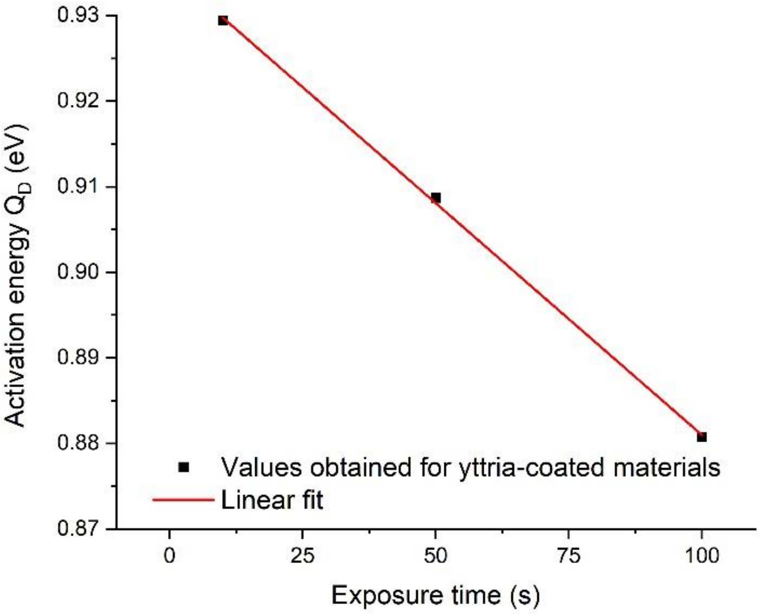

Figure 3.17. Activation energy $Q_D$ versus exposure time

Fig. 3.17 shows that the activation energy for growth strain $Q_D$ decreases as the exposure time increases. As discussed before in section 1.2.1.3 for the growth strain, the corresponding mechanisms are not yet fully established. The $D_{ox}(T)$ parameter depends on microstructural features and may also depend on temperature [16]. It is thus the driving "force" for stress generation in isothermal condition. The $D_{ox}$ parameter may also be related to the ratio of the cationic/anionic flux occurring within the grain boundaries as the oxide layer grows [17]. Hence, we propose that:

$$D_{ox} = D_{ox0}\, exp\left(\frac{Q_D}{RT}\right) = A\left(\frac{J_{anionic}}{J_{cationic}}\right)^{B} \tag{3.4}$$

where A is a parameter which represents the relevance between the growth strain parameter $D_{ox}$ and the ratio of the cationic/anionic flux, B is a coefficient related to the material. In our system, the value of B is considered as -1.

Since both flows follow an Arrhénius dependence, this leads to the fact that the current activation energy corresponds to the difference between the values associated with the anionic and cationic activation energies:

$$D_{ox0}\, exp\left(\frac{Q_D}{RT}\right) = A\left(\frac{J_{anionic\;0}\, exp\left(-\frac{Q_{anionic}}{RT}\right)}{J_{cationic\;0}\, exp\left(-\frac{Q_{cationic}}{RT}\right)}\right)^{B} \tag{3.5}$$

which gives us:

$$Q_D = RT(ln(A) - ln(D_{ox0})) + BRTln(\frac{J_{anionic\;0}}{J_{cationic\;0}}) + B(Q_{cationic} - Q_{anionic}) \tag{3.6}$$

where $Q_D$ is the activation energy for the growth strain, $Q_{anionic}$ is the activation energy for anionic diffusion and $Q_{cationic}$ is the activation energy for cationic diffusion.

According to the results presented in 3.4.1.1, the activation energy $Q$ for creep diffusion is higher when the yttria concentration increases, which indicates that the cationic flows is reduced. Therefore, we assumed that, when the yttria concentration increases, $Q_{cationic}$ is higher. However, these two activation energies are not necessarily the same.

We also assumed that the $Q_{anionic}$ does not change as the yttria concentration changes. At the same time, $Q_D$ decreases as the exposure time increases, which is proved in Fig. 3.17.

Thus, as the exposure time is longer, $Q_D$ decreases and $Q_{cationic}$ increases, which seems to be in good agreement with Eq.3.6 when B equals to a negative value.

## 3.4.2 Analysis for the zirconium-doped materials

### 3.4.2.1 The results for creep parameter Jox

The results concerning $J_{ox}$ (Pa$^{-1}$s$^{-1}$) of zirconium-doped material are presented in Fig. 3.18.

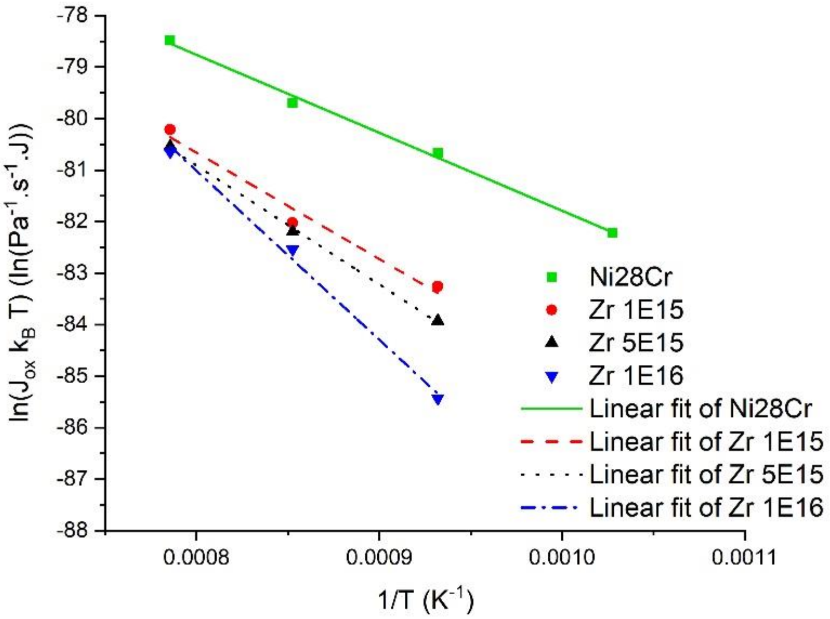

Figure 3.18. Linear fit of $Ln(J_{ox}k_BT)$ versus $\frac{1}{T}$ for zirconium-doped material

Fig. 3.18 shows the same trend as Fig. 3.14 for the creep parameter $J_{ox}$. The creep parameter $J_{ox}$ decreases as the temperature decreases, whatever is the quantity of zirconium introduced, which confirms the thermal activation of this relaxation mode. For all temperature, the values of $J_{ox}$ decrease with the increasing of the quantity of zirconium introduced, which means that the reactive element zirconium is able to significantly modify the mechanical properties.

Since it has been shown that the creep parameters depend on the temperature, it is possible to calculate the activation energies associated to the viscoplastic strain phenomena in the oxide layer. Such activation energies were determined for each added quantity of zirconium by applying Eq. 3.2. The activation energy Q is calculated and plotted in Fig. 3.19.

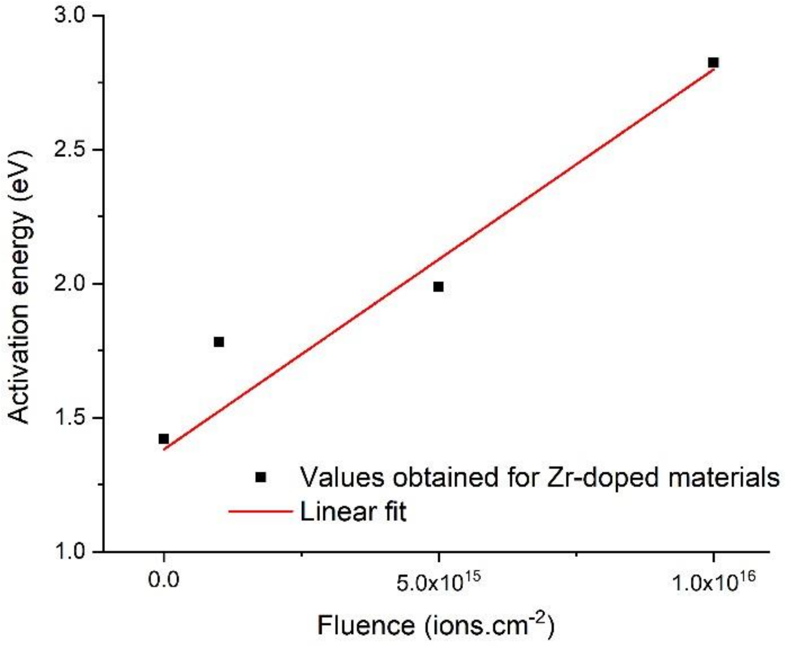

Figure 3.19. Activation energy Q versus fluence of zirconium

The activation energy increases with a higher fluence and it has a good linear fitting of activation energy versus fluence, which means that the surface treatment (doping reactive element $Zr$) is effective to delay the oxidation rate. For (Ni28Cr + Zr + $Cr_2O_3$) systems, the activation energies are very close for the raw material and the $1*10^{15}$ ions.cm$^{-2}$ zirconium fluence. It corresponds respectively to an activation energy of 1.42eV and 1.78eV. On the contrary, for the greater zirconium quantity of $5*10^{15}$ ions.cm$^{-2}$ zirconium-doped and $1*10^{16}$ ions.cm$^{-2}$ zirconium-doped, the activation energy is clearly higher as the values are respectively 1.99eV and 2.82eV.

As previously discussed for the reactive element $Y_2O_3$, we can determine the elementary mechanisms that should govern the viscoplastic behavior of the oxide layer as a function of the amount of zirconium implanted. It leads to the same conclusions for the reactive element zirconium as for yttria. In particular, the creep rate changes and the activation energy is much higher after this surface modification.

### 3.4.2.1 The results for the growth strain parameter Dox

The results concerning $D_{ox}$ for zirconium-doped materials are presented in Fig. 3.20.

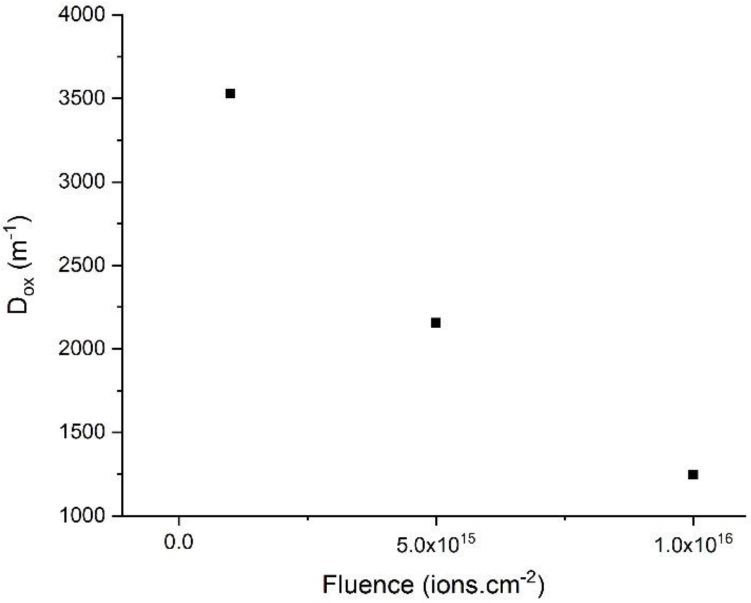

Figure 3.20. Growth strain parameter versus fluence of zirconium at 1273K

Fig. 3.20 indicates a decrease for $D_{ox}$ versus fluence for the zirconium-doped material. As proposed in Eq.3.3, the activation energy for growth $Q_D$ can also be calculated for such a case. The activation energy for growth $Q_D$ versus exposure time is plotted in Fig. 3.21.

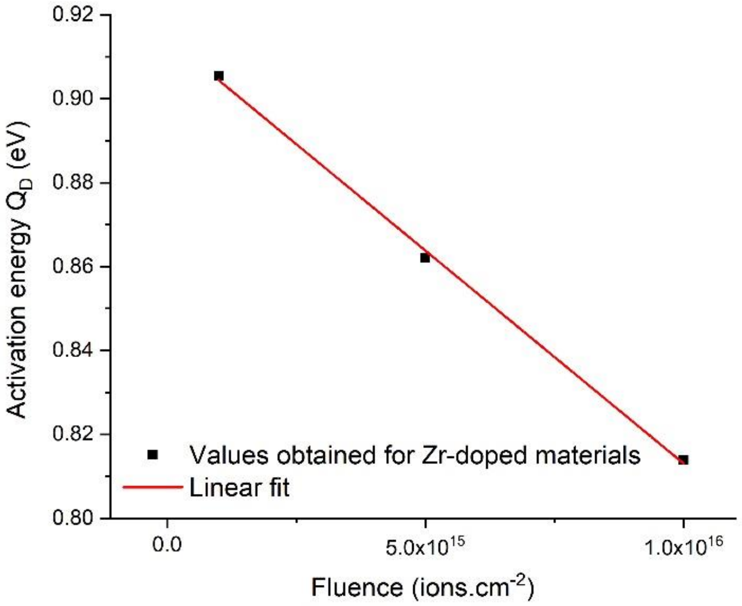

Figure 3.21. The activation energy for growth $\mathrm{Q_D}$ versus fluence of zirconium

Fig. 3.21 leads to the same conclusion as for yttria-coated samples: the activation energy for growth $Q_D$ decreases as the fluence of zirconium increases. However, as discussed before in section 1.2.1.3, the growth strain parameter $D_{ox}$ evolution is complicated because the mechanisms are not yet fully established. $Q_D$ corresponds to an activation energy for growth strain. Indeed, the $D_{ox}$ parameter is also determined by the ratio of the cationic/anionic flux occurring within the grain boundaries as the oxide layer grows, which is proposed in Eq.3.4 – Eq.3.6. The results lead to the fact that the current activation energy corresponds to the difference between the values associated with the anionic and cationic flows. As $Q_{cationic}$ increases, the activation energy for growth $Q_D$ decreases, which has good agreement with Eq.3.6.

## References of chapter 3

[1] F. Rakotovao, Relaxation des contraintes dans les couches de chromine développées sur alliages modèles (NiCr et Fe47Cr): apport de la diffraction in-situ à haute température sur rayonnement Synchrotron à l'étude du comportement viscoplastique: effets d'éléments réactifs, PhD Thesis, Université de La Rochelle, La Rochelle, France, 2016.

[2] Z.J. Tao, Experimental study and modelling of mechanical features in an oxide layer under thermal loadings, PhD Thesis, Université de technologie de Troyes, Troyes, France, 2018.

[3] J. Lemaitre, J.L. Chaboche, Mécanique des matériaux solides, Dunod, Paris, 2001.

[4] F. Rakotovao, B. Panicaud, J. L. Grosseau-Poussard, Z. Tao, G. Geandier, P. O. Renault, P. Girault, P. Goudeau, N. Blanc, N. Boudet, G. Bonnet, Acta Materialia 2018, 159, 276.

[5] W. R. Cannon, T. G. Langdon, Creep of ceramics, J. Mater. Sci., vol. 18, no. 1, pp. 1–50, 1983.

[6] J.-L. Grosseau-Poussard, B. Panicaud, S. Ben Afia, Computational Materials Science 2013, 71, 47.

[7] B. Panicaud, D. Retraint, J.-L. Grosseau-Poussard, L. Li, M. Guérain, P. Goudeau, N. Tamura, M. Kunz, Corrosion Science 2012, 60, 224.

[8] H. E. Evans, International Materials Reviews 1995, 40, 1.

[9] T.G. Lanydon, ructural ceramics, California 91360, USA, PROGRESS IN MATERIALS SCIENCE. (n.d.) 255.

[10] K. Przybylski, G. J. Yurek, MSF 1991, 43, 1.

[11] C.M. Cotell, G.J. Yurek, R.J. Hussey, D.F. Mitchell, M.J. Graham, The Influence of Implanted Yttrium on the Mechanism of Growth of Cr203 on Cr, (n.d.) 2.

[12] R. J. Hussey, P. Papaiacovou, J. Shen, D. F. Mitchell, M. J. Graham, Materials Science and Engineering: A 1989, 120–121, 147.

[13] S. Chevalier, G. Bonnet, P. Fielitz, G. Strehl, S. Weber, G. Borchardt, J. C. Colson, J. P. Larpin, Materials at High Temperatures 2000, 17, 247.

[14] S. Chevalier, G. Bonnet, G. Borchardt, J. C. Colson, J. P. Larpin, MSF 2001, 369–372, 327.

[15] A. F. Carley, P. R. Davies, M. W. Roberts, Philosophical Transactions of the Royal Society A: Mathematical, Physical and Engineering Sciences 2005, 363, 829.

[16] B. Panicaud, J.-L. Grosseau-Poussard, M. Kemdehoundja, J.-F. Dinhut, Computational Materials Science 2009, 46, 42.

[17] D. R. Clarke, Acta Materialia 2003, 51, 1393.

# Chapter 4: Stress spatial distribution

# 4.1 Experimental results

## 4.1.1 Experimental conditions

### 4.1.1.1 Materials

The studied materials are different NiCr alloys. With the purpose of better understanding the stress spatial distribution in the substrate, several samples were designed. First of all, there are two shapes: a rectangle with a geometry of 6x6x0.4 mm, and a cylinder with a geometry of Ø6x0.9 mm. In order to name the samples more easily, code names are given in Table 4.1 for the samples with different shapes and oxidation conditions and Table 4.2 for the samples with doping reactive elements zirconium on the surface.

Table 4.1. Code name for the samples with different shapes and oxidation conditions

| Code name | Shape | Size | Oxidation temperature | Oxidation time |
|---|---|---|---|---|
| Cyl_T1000_1h | cylinder | Ø6x0.9 mm | 1000 °C | 1 h |
| Cyl_T1000_5h | cylinder | Ø6x0.9 mm | 1000 °C | 5 h |
| Rec_T900_10h | rectangle | 6x6x0.4 mm | 900 °C | 10 h |
| Rec_T800_10h | rectangle | 6x6x0.4 mm | 800 °C | 10 h |

Table 4.2. Code name for the samples with doping reactive elements zirconium on surface

| Code name | Shape | Size | Oxidation temperature | Oxidation time | Fluence |
|---|---|---|---|---|---|
| Cyl_T900 | cylinder | Ø6x1.5 mm | 900 °C | 7.5 h | 0 |
| Cyl_T900_ZrE16 | cylinder | Ø6x1.5 mm | 900 °C | 7.5 h | $1*10^{16}$ ions.cm$^{-2}$ |
| Cyl_T1000 | cylinder | Ø6x1.5 mm | 1000 °C | 5 h | 0 |
| Cyl_T1000_ZrE15 | cylinder | Ø6x1.5 mm | 1000 °C | 5 h | $1*10^{15}$ ions.cm$^{-2}$ |
| Cyl_T1000_ZrE16 | cylinder | Ø6x1.5 mm | 1000 °C | 5 h | $1*10^{16}$ ions.cm$^{-2}$ |

In order to investigate the influence of reactive elements on the stress spatial distribution, different doping fluences are also tested. Besides, the non-doped reference materials are also measured for the second group of experiments in order to be able to compare more accurately.

For cylinder samples, the chemical composition is a Ni-based alloy with a weight percentage of 28.28% Cr marked as Ni28Cr. For rectangular samples, whose chemical composition has a weight percentage of 34.5% Cr marked as Ni35Cr. These two materials are alloys that are resistant to oxidation and their behaviors after different oxidation conditions have extensively been studied [1-3]. Their chemical composition (percentage by weight) is shown in Table 2.1.

### 4.1.1.2 Experimental setup

Basically, X-ray in transmission mode and X-ray in reflection mode share the same principles and are used to obtain information from materials. For example, XRD is widely applied to determine the elastic strain of crystalline materials [4-6]. X-rays in transmission mode can be used to determine the residual stress distribution in substrate as a function of depth. The X-rays in transmission mode was used to determine the lattice parameters as a function of depth for Thermal Barrier Coatings, which is related to the depth-dependence of strain [7]. Transmission XRD and reflection XRD share the same principles to detect the crystalline peaks [8, 9]. A comparison between the conventional Bragg-Brentano diffractometer and the two-dimensional XRD showed that the high-energy two-dimensional diffraction provides more information than conventional diffractometer and can be used to determine stress [10]. The detail has been already introduced in section 2.3.2.

## 4.1.2 Results for stresses

### 4.1.2.1 Comparison of in-plane stress σ and normal stress $\sigma_N$

First, by using the method described previously (Eq. 2.30 in section 2.3.2), the stress-depth curves in metal are obtained. The in-plane stress $\sigma$ and normal stress $\sigma_N$ can be clearly presented by overlapping them in the same figure (Fig. 4.2).

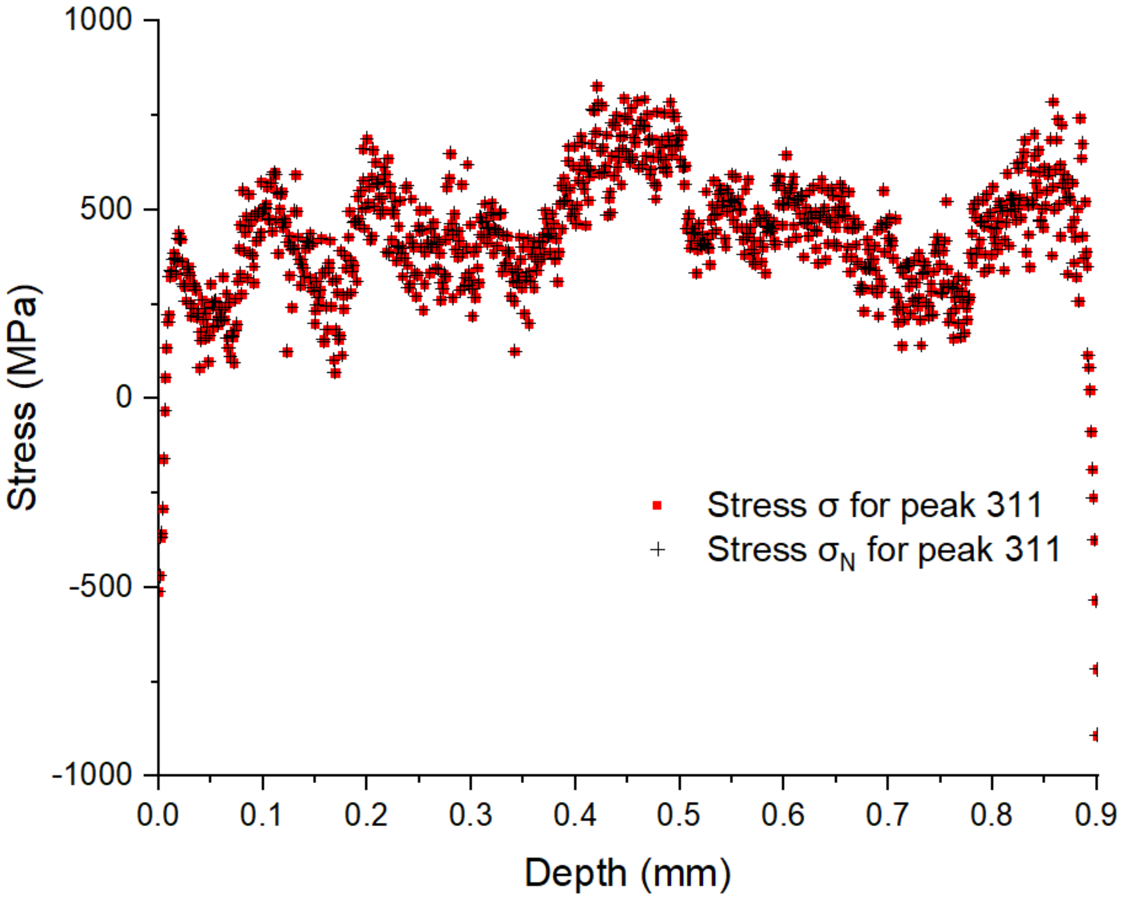

Figure 4.2. Stress $\sigma$ and $\sigma_N$ for peak (311) of sample Cyl_T1000_1h

Fig. 4.2 compares stress $\sigma$ and $\sigma_N$ for peak (311) of sample Cyl_T1000_1h at rotation direction 0°, where depth 0 mm is the top surface and depth 0.9 mm is the bottom surface. The overlap clearly indicates that the stress $\sigma$ and $\sigma_N$ are identical in the metal. From the data processing point of view, the term $\frac{A}{\beta_1}$ is very small (Eq. 2.32), where A is the slope of the curve $ln\left(\frac{1}{sin\theta}\right)$ as a function of $sin^2\varphi$ and $\beta_1$ can be considered as a constant related to the different peaks. The slope A is close to 0, which leads to the stress $\sigma$ and $\sigma_N$ to be similar in the metal. It does not contribute significantly to the value of the out-plane stress. It is worth noting that this distribution of stresses are measured only in the metal (under the measurement uncertainties). Similar results have been obtained for all the samples. According to these results, a relation between in-plane stress $\sigma$ and normal stress $\sigma_N$ in the metal is proposed for the investigated materials:

$$\sigma_{xx} = \sigma_{yy} \approx \sigma_{zz} \tag{4.1}$$

where $\sigma_{xx}$ and $\sigma_{yy}$ equals to in-plane stress $\sigma$, and $\sigma_{zz}$ equals to normal stress $\sigma_N$.

Because the system is not in general a priori isotropic, there is not only hydrostatic stress in such a system. There are in-plane and out-plane stresses, both in the metal and in the oxide, that a priori can depend on the z position especially for the metal, whereas for the oxide it can be considered as constant at first-order approximation. Indeed, from an experimental point of view, the oxide layer is too thin to consider a stress distribution along the axis z and is thus considered as homogeneous, because the beam size (2 µm) is bigger or equivalent to the oxide thickness (1 µm to 3 µm). For the determination of stress in the oxide layer, the reflection mode of XRD is regularly used. Mechanical balance is thus considered in such a system by means of these assumptions.

Previous modelling takes into account only in-plane stress (i.e. out-plane stress = 0), whereas in the present study we also consider the out-plane stress. However, an in-plane stress is assumed for the oxide layer because the thickness is too thin, of the order of 1 µm, as already performed in previous works [12, 13]. Such a hypothesis of in-plane stress for the oxide layer is not fully satisfying, which may bring a lack of continuity of the normal stress at the metal/oxide interface. Another consequence is that the thickness of the oxide layer is so thin that the stress gradient in the oxide is generally ignored. On the contrary, the substrate has a larger thickness. For sample Cyl_T1000_1h, the thickness is 0.9 mm, which is around 900 times thicker than the thickness of oxide layer. The equation of mechanical balance and recent work [12] confirm that the stress in the oxide layer is compression and the stress in the metal layer is tension, which are opposites ones, for the considered systems. Thus, the existence of stress gradient as a function of depth is possible, especially in the near interface zone. This is confirmed in Fig. 4.2 and has been observed for all the samples.

Ideally, the stress-depth curve should be a curve symmetrical with respect to the middle plan, because of the symmetrical geometry, the identical oxidation conditions, the same measurement process etc. As shown in Fig. 4.2, the stress distribution is observed roughly symmetric to the central plane, especially when focusing at the stress distribution near the top and bottom surfaces. However, due to the bonding between the sample and sample holder, we can observe signal differences at the bottom surface. In addition, at the bottom surface, the signal can be polluted by information providing by the sample holder. Nevertheless, only the top half part will be presented, including the top surface and the stress distribution down to the central plane. Assuming the symmetry of the system and considering only half of the information, the equation of mechanical balance should be now approximately considered as:

$$\int_{0}^{h_m/2} \sigma_m(z)dz + \int_{-h_{ox}}^{0} \sigma_{ox}\, dz = 0 \tag{4.2}$$

### 4.1.2.2 Results of the samples with different shapes and oxidation conditions

a. Comparison of stresses for three directions of penetration

For the samples with different shapes and oxidation conditions, three directions of penetration have been applied: 0°, 90° and -90°, which are related to the sample position rotation around the z axis (0° rotation direction is shown in Fig. 2.15). Normally, -90° and 90° should be equivalent because of the same X-ray beam path.

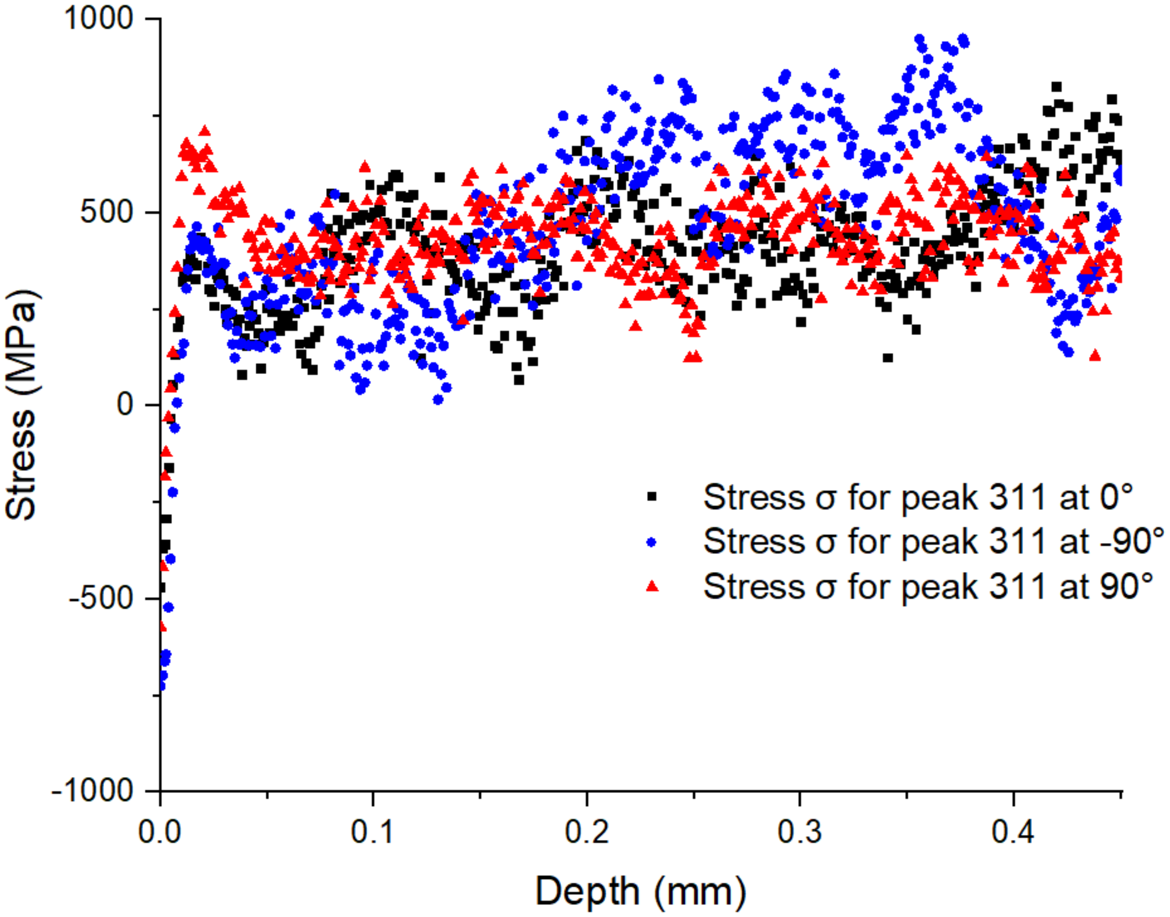

Figure 4.3. Stress $\sigma$ for three rotation directions for peak (311) of sample Cyl_T1000_1h

As shown in Fig. 4.3, the stresses between different rotation directions are quite similar. The response to a same X-ray path should be theoretically the same. However, there are slights differences between different rotation directions, even for -90° and 90°. This may be explained by instrumentation errors or beam variations when rotating the sample, as well as possible heterogeneities of the number and size of grains in the beam depending on the X-ray path (between 0° and 90°). No significant difference in the trends of the stress distribution was found between these three directions of rotation, especially at the near surface part where a stress gradient is systematically observed. So that we can consider that the stress state is isotropic but heterogeneous in the metallic substrate.

In order to investigate the stress distribution as a function of depth, the mean stress of these three rotation directions has been calculated. In the meantime, the sample standard deviation is also obtained. Since there are only three directions of rotation, to investigate the mean stress of all directions, the sample standard deviation is used, which is presented as error bars in the further figures. The mean standard deviation of the present sample in all the three directions is 153 MPa. This value can be considered as the maximum range of acceptable error. In fact, this error is not homogeneous all over the depth. Especially, in the gradient region, the error of the measurement is very small and it is indeed reproducible.

### b. Average stress as a function of depth

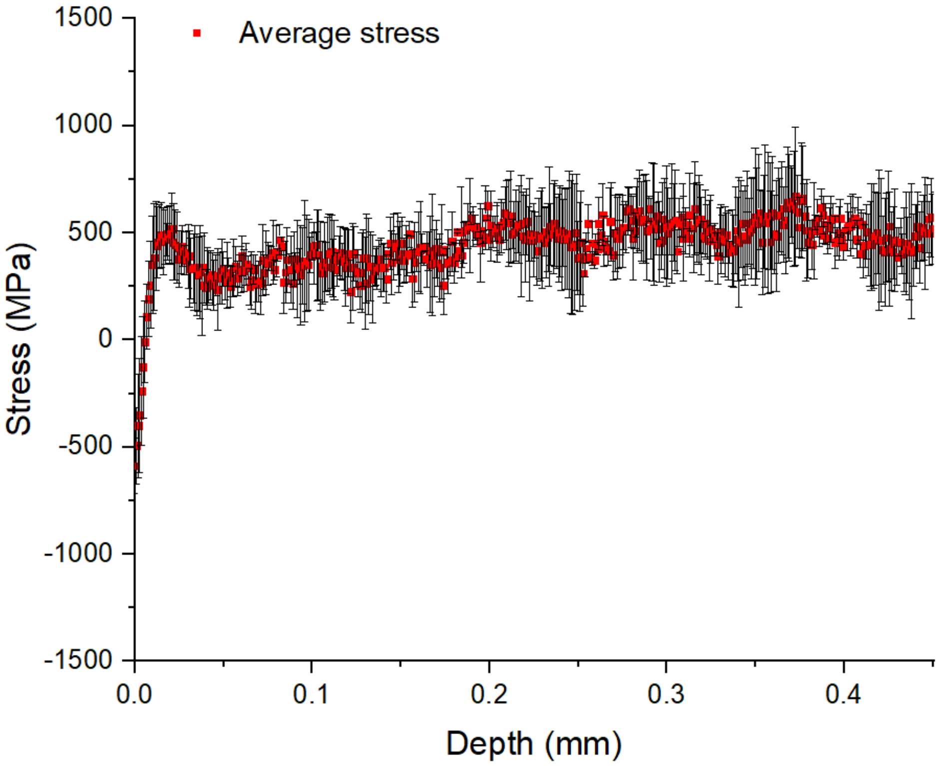

Figure 4.4. Average stress of three rotation directions for peak (311) as a function of depth of sample Cyl_T1000_1h.

Fig. 4.4 presents the results for Cyl_T1000_1h. As shown in Fig. 4.4, the distribution of stress $\sigma$ as a function of depth is non-linear and roughly constant far from the interface. The sample standard deviation is calculated by three different rotation directions, which is shown as error bars in Fig. 4.4. The minimum stress is at the top surface, which is -588 ± 128 MPa. Since the stress in the oxide layer is negative [12, 14] and expecting continuity of the normal stress (equal to the in-plane stress in the metal), it seems reasonable that the stress in the substrate has a negative value near the interface. At depth 7 µm, the stress exceed 0 MPa. Because of mechanical balance [12], the majority of stress in the metallic substrate should be positive. The stress indeed changes very fast between 0 and 10 µm, which changes from -588 ± 128 MPa to 384 ± 249 MPa. At this depth, the influence of the concentration of different elements is concerned, such as O, Cr and Ni [15-17]. For the system NiCr + $Cr_2O_3$, the $Cr^+$ diffusion is considered, which means cationic $Cr^+$ transport outward the surface to form $Cr_2O_3$. Therefore, the depletion of Cr causes crystallographic defects such as vacancy defects, edge dislocation, etc. The crystallographic defects may induce strain and stress, which can be called diffusion stress.

After 10 µm, the majority of stress distributes from 0 MPa to 500 MPa and the average stress in the metal is 452.3 MPa. The average of sample standard deviation is 153 MPa.

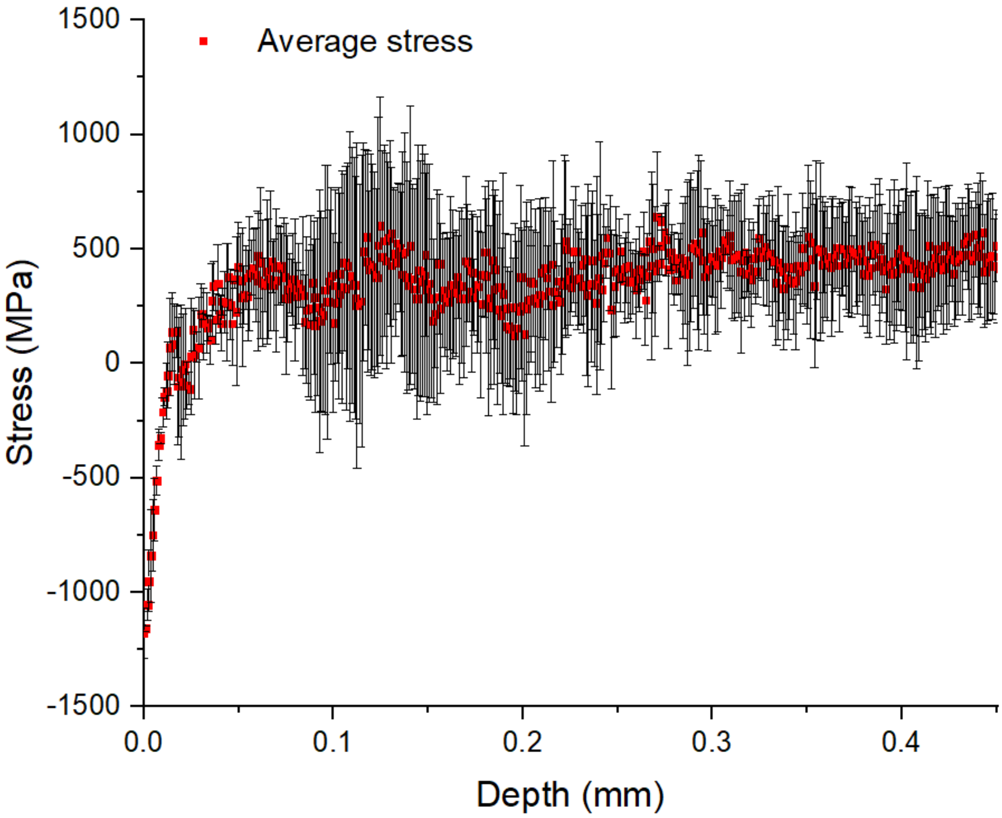

Figure 4.5. Average stress of three rotation directions for peak (311) as a function of depth of sample Cyl_T1000_5h.

Fig. 4.5 presents the results for Cyl_T1000_5h. It shows that the minimum stress is -1179 ± 108 MPa at top surface, which is lower than the stress at the same depth of sample Cyl_T1000_1h. Because of longer oxidation time, the oxide thickness of sample Cyl_T1000_5h is thicker than sample Cyl_T1000_1h, which causes a higher growth strain magnitude in the oxide layer. The stress in metal exceed 0 MPa at 14 µm, which is deeper compared to sample Cyl_T1000_1h. After 14 µm, the majority of stress then distributes from 0 MPa to 500 MPa and the average stress in the metal is 388.8 MPa;

the average of sample standard deviation is now 274 MPa, which is higher than for sample Cyl_T1000_1h.

The values of the experimental stress may also present uncertainties, because of the measurement process, the dilatation correction and calibration procedure [12], that are not presently detailed. It also strongly depends on the numerical value of the stress-free Bragg's angle ($2\theta_0$). However, if the present experimental results are considered in a relative way, for example by comparing ratio between different oxidation conditions, these results keep a significant interpretation. The same tendency of stress distribution is repeatable for different oxidation times and for different oxidation temperatures, meaning that the stress spatial evolution with non-linear variation is a significant and an important result of the present measurements.

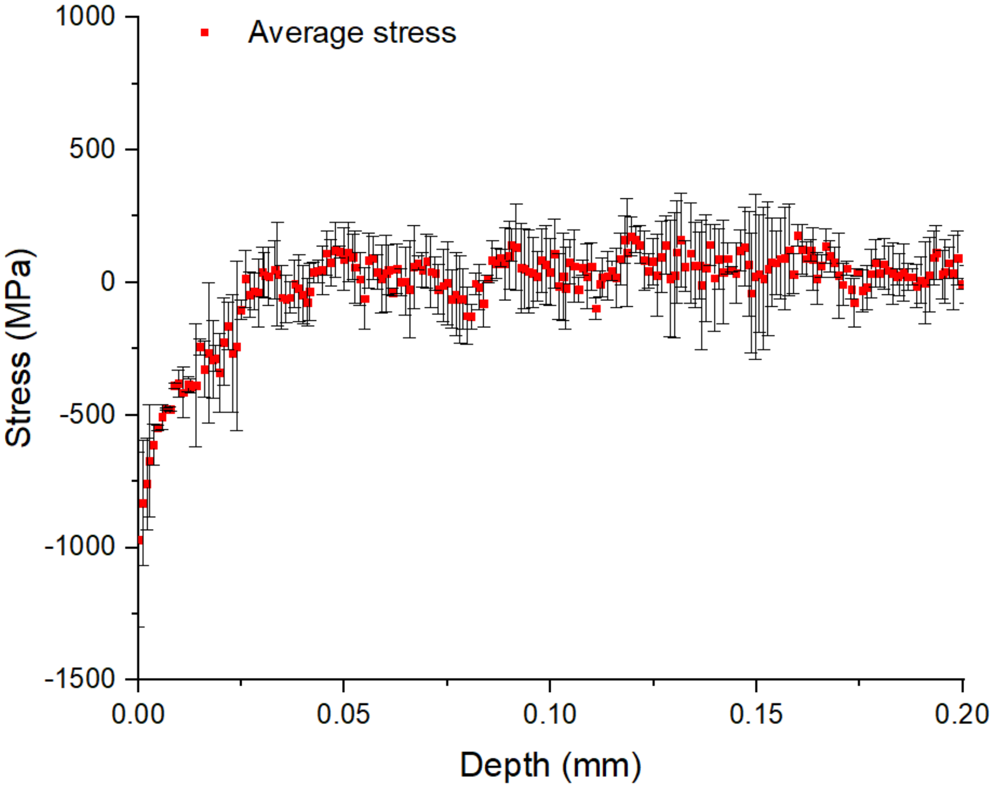

Figure 4.6. Average stress of three rotation directions for peak (222) as a function of depth of sample Rec_T900_10h.

Fig. 4.6 shows that the stress distribution of sample Rec_T900_10h is quite similar to that of oxidized samples at 1000 °C. The minimum stress is -970 ± 329 MPa at the top surface. It exceeds 0 MPa at 26 µm. The majority stress is distributed from 0 MPa to 250 MPa with an average stress at 41.7 MPa, and the average of sample standard deviation is 120 MPa.

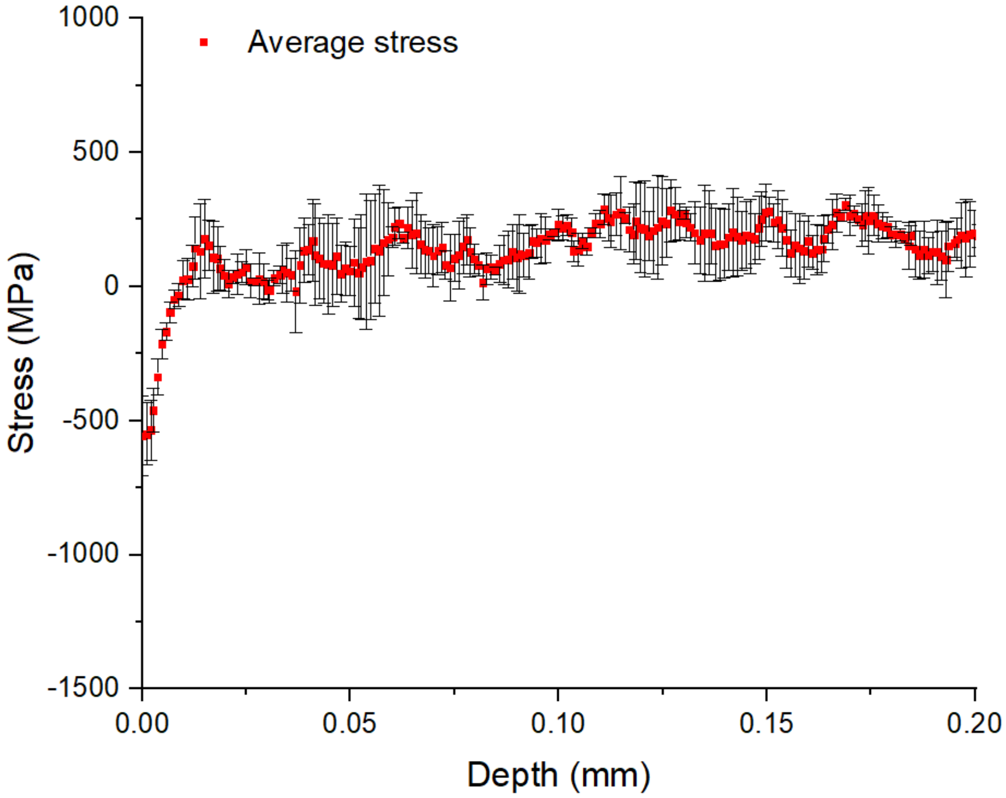

Figure 4.7. Average stress of three rotation directions for peak (222) as a function of depth of sample Rec_T800_10h.

As shown in Fig. 4.7, for sample Rec_T800_10h, the minimum stress is -557 ± 148 MPa at top surface. It exceeds 0 MPa at 10 μm. After that, the stress mainly distributes from 0 MPa to 250 MPa with an average stress 151.5 MPa. The average of sample standard deviation is 97 MPa.

Table 4.4. Comparison of parameters for the four samples

| | Minimum stress at interface | Depth for 0 MPa | Average stress after depth for 0 MPa | Average of sample standard deviation |
|---|---|---|---|---|
| Cyl_T1000_1h | -588 ± 128 MPa | 7 μm | 452.3 MPa | 153 MPa |
| Cyl_T1000_5h | -1179 ± 108 MPa | 14 μm | 388.8 MPa | 274 MPa |
| Rec_T800_10h | -557 ± 148 MPa | 10 μm | 151.5 MPa | 97 MPa |
| Rec_T900_10h | -970 ± 329 MPa | 26 μm | 41.7 MPa | 120 MPa |

The resume of Fig. 4.4 – Fig. 4.7 (in Table 4.4) indicates that the minimum stress appears at the oxide/metal interface. It shows with the same oxidation temperature, the longer oxide time, the lower minimum stress is reached; and with the same oxidation time, the higher oxidation temperature, the lower minimum stress is reached. For the depth for 0 MPa, the longer oxidation time or the higher oxidation temperature, the depth is deeper. The depth for 0 MPa is related to the stress at interface, which is connected to the stress in the oxide layer through the mechanical balance of the system, providing adhesion at the interface. It is shown clearly that there is a stress gradient at the near surface zone, which is related to the oxidation condition. Because of the oxidation, there is a gradient of concentration of Cr, which gives a chemical (diffusion) stress [19]. Therefore, we proposed that this stress gradient is related to the gradient of Cr.

The average stress after depth for 0 MPa in metal part presents difference for cylinder samples and rectangle samples. The expected results are the opposite of what are observed. Indeed, the rectangle samples are less thick, so this should give higher stresses in the metal layer because of the mechanical balance. However, it would be necessary to compare for identical oxidation conditions, which is not the case here. What we can conclude is that the oxidation conditions are the main influence of the stress gradient.

However, comparing the samples with the same shape shows that the average stress after depth for 0 MPa is smaller for longer oxidation time and higher oxidation temperature, which means that the relaxation of stress is more significant when the oxidation time is longer or the oxidation temperature is higher, at a given point in the metal.  This confirms that relaxation is driven by a thermally activated process, viscoplasticity or creep phenomena, as already shown in [1-3].

#### 4.1.2.3 Results for the samples with doping reactive elements zirconium on surface

For the samples with doping reactive elements zirconium on the surface, only one direction of penetration has been measured. Considering the different experimental conditions and the different results between these two groups of experiments, we decided to use different parameters to evaluate the results. For the results of the samples with doping reactive elements zirconium (for example Fig. 4.9), there stresses in the metal layer is mainly negative, which is compression. Thus, the depth of stress 0 MPa can not be found and compared. It need other parameters to evaluate the results.

First, the average stress from 0.1 mm to 0.5 mm is calculated, as an evaluation stress for the whole sample, which is called constant stress. The depth 0.1 mm exceeds the near surface zone, which means that the stress gradient is not included in the average stress.

Secondly, in order to evaluate the stress gradient, another stress is calculated, which is the average stress for near surface zone from 0 to 0.03mm. From the results for the samples without doping reactive elements, the maximum depth of stress gradient is 0.026 mm. Therefore, the depth from 0 to 0.03mm is considered to evaluate the stress gradient for the samples with doping reactive elements zirconium on surface.

Thirdly, the depth to calculate the spatial gradient evolution is from the surface to the point where the stress reaches the average stress for near surface zone.

In addition, the different stresses between the minimal stress, constant stress and the average stress for near surface zone are also evaluated.

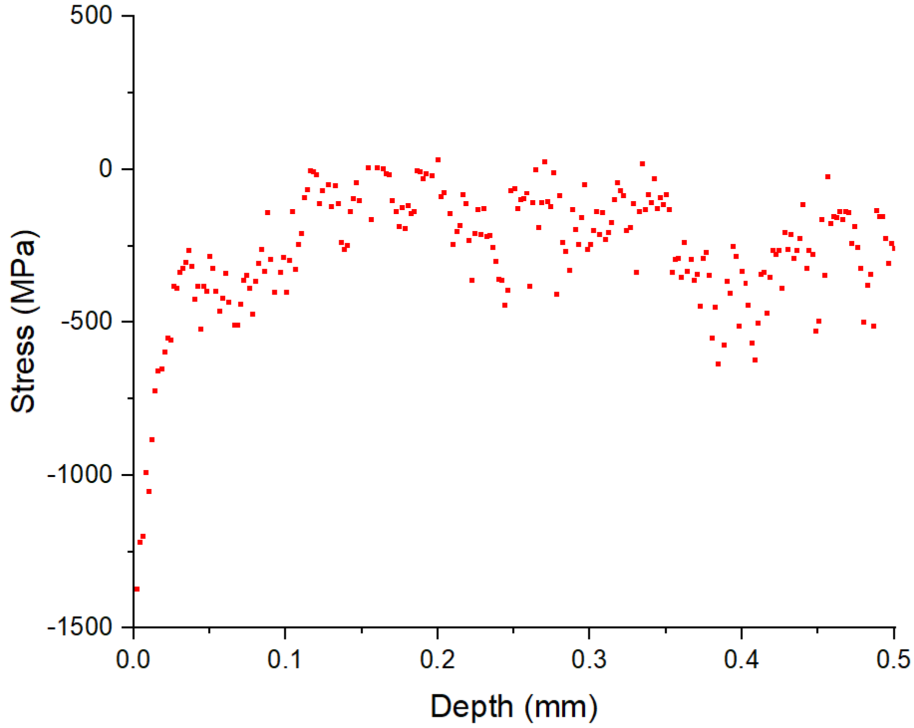

Figure 4.8. Stress of peak (311) as a function of depth of sample Cyl_T900

Fig. 4.8 presents the results of Cyl_T900. For this sample, the fluence of reactive elements is 0. However, the same parameters will be used for this group of experiments. As shown in Fig. 4.8, the distribution of stress $\sigma$ as a function of depth is non-linear. Comparing the results of stress for the first experiment group, it is not obvious that the stress far from the interface is roughly constant. However, the stress spatial gradient is evidenced, which will be evaluated.

The minimum stress is at the top surface, which is -1369 MPa. Since the stress in the oxide layer is negative [12, 14] and expecting continuity of the normal stress (equal to the in-plane stress in the metal), it seems reasonable that the stress in the substrate has a negative value near the interface. The average stress from 0.1 mm to 0.5 mm is -189± 184 MPa. The average stress for near surface zone from 0 to 0.03 mm is -769 MPa and the depth from the surface to this point is 0.013mm. The difference between the minimal stress and constant stress is 1180 MPa and between the minimal stress and the average stress for near surface zone is 600 MPa.

The stress indeed changes very fast from 0 to 13 µm, which changes from -1369 MPa to -769 MPa and gives a spatial gradient $4.6*10^4$ MPa/mm. As mentioned before, at this depth, the influence of the concentration of different elements is concerned, such as O, Cr and Ni.

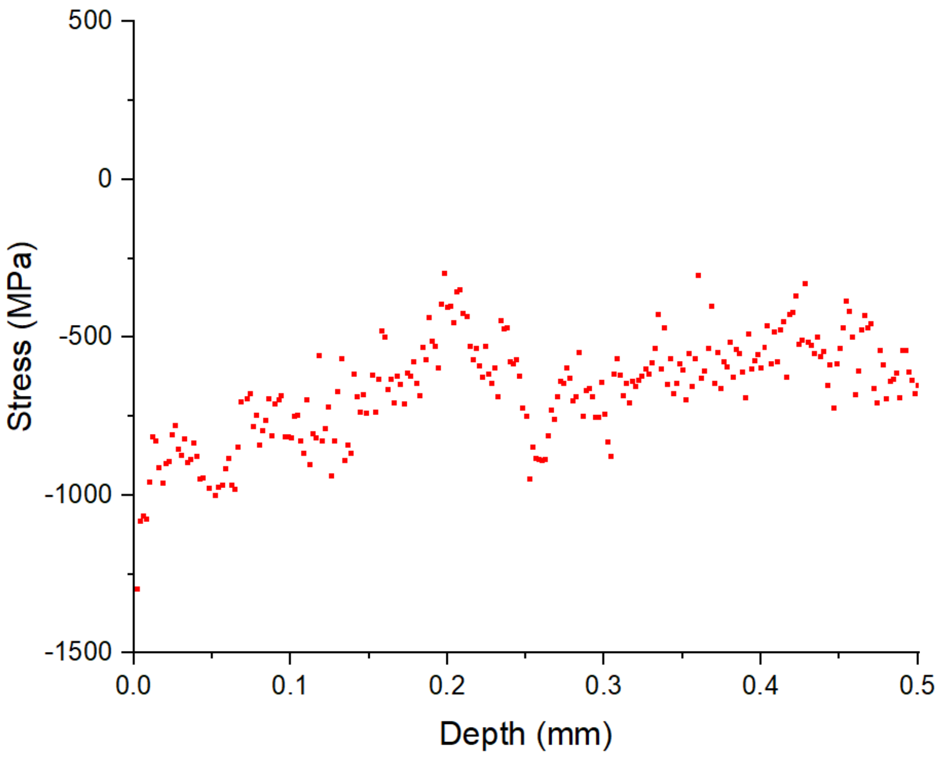

Figure 4.9. Stress of peak (311) as a function of depth of sample Cyl_T900_ZrE16

Fig. 4.9 shows the results of sample Cyl_T900_ZrE16, which indicates that the minimum stress is -1296 MPa at top surface, which is higher than the stress at the same position of sample Cyl_T900. The average stress from 0.1 mm to 0.5 mm is -613 ± 135 MPa. The average stress for near surface zone from 0 to 0.03 mm is -938 MPa corresponding to a depth of 0.011mm. The difference between the minimal stress and constant stress is 682 MPa and the one between the minimal stress and the average stress for near surface zone is 357 MPa, which gives a stress spatial gradient of $3.2*10^4$ MPa/mm.

By doping with the reactive element Zr on the surface, the outward cationic $Cr^+$ transport in the oxide scale is slowed down [3], which would consume less Cr on the metal side and therefore reduce the thickness of the Cr-depleted zone. Thus, for the same oxidation time, the depletion zone of Cr in the metal should be thinner, which could be related to a lower difference between the minimal stress and the average stress for near surface zone and a lower stress spatial gradient, due to a diffusion stress.

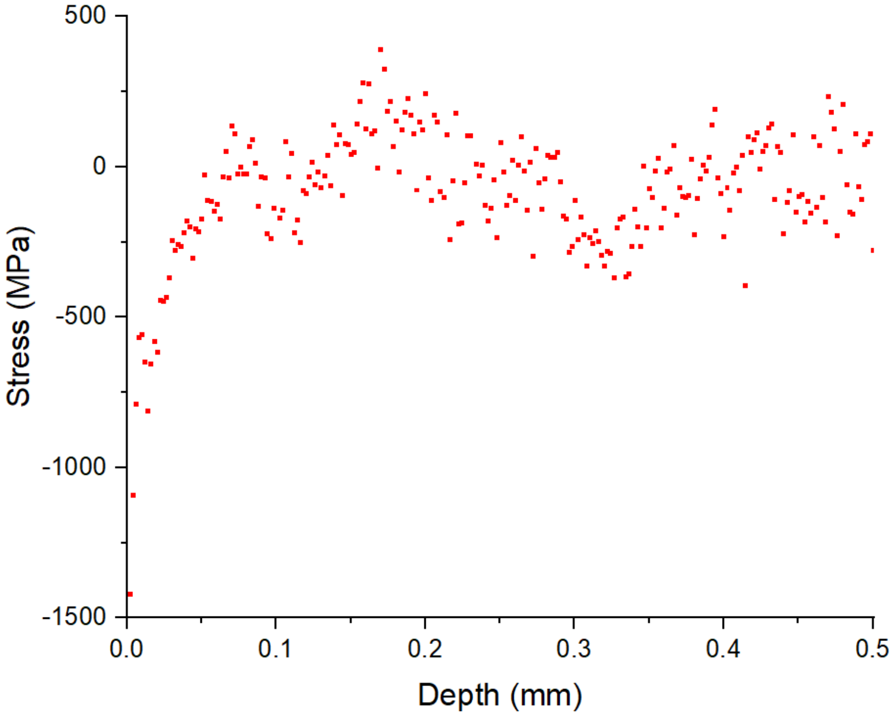

Figure 4.10. Stress of peak (311) as a function of depth of sample Cyl_T1000

Fig. 4.10 presents the results of sample Cyl_T1000, which is able to be compared with Fig. 4.5 for the sample Cyl_T1000_5h. We can see that the tendency is quite similar. The minimal stress is -1419MPa. The average stress from 0.1 mm to 0.5 mm is -40 ± 149 MPa. The average stress for near surface zone from 0 to 0.03 mm is -718 MPa corresponding to a depth of 0.011mm. The difference between the minimal stress and constant stress is 1379 MPa and between the minimal stress and the average stress for near surface zone is 702 MPa, which gives a stress spatial gradient $6.4*10^4$ MPa/mm.

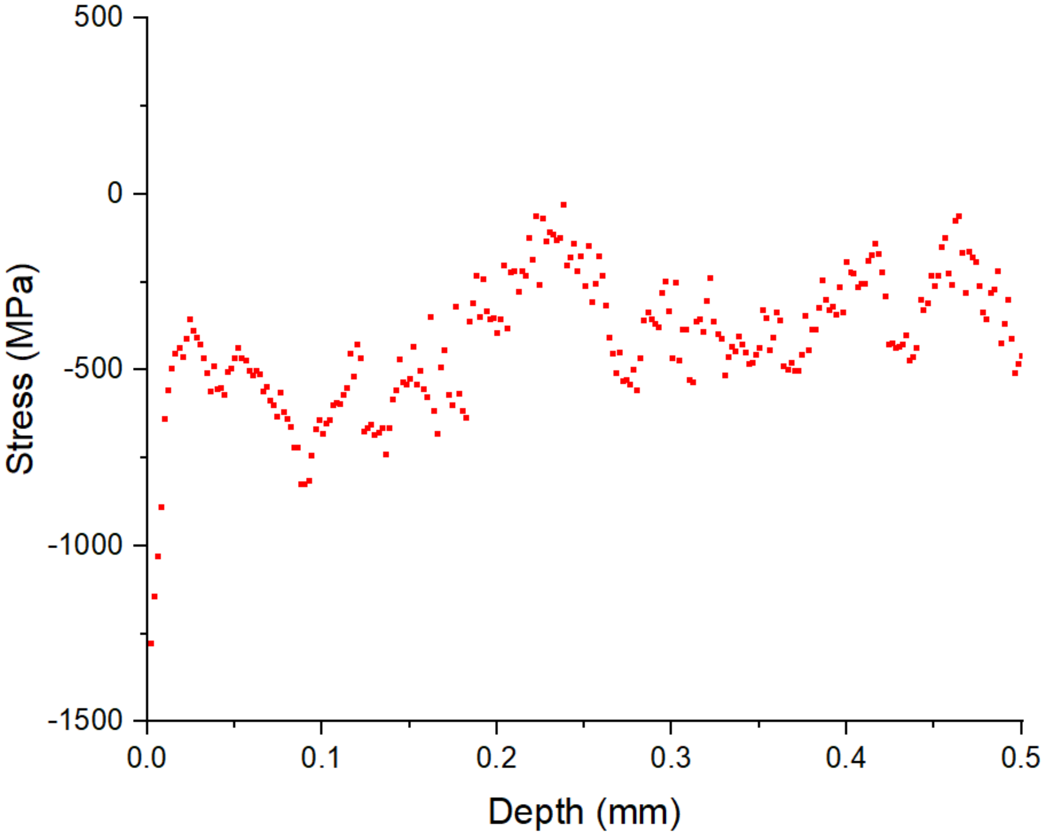

Figure 4.11. Stress of peak (311) as a function of depth of sample Cyl_T1000_ZrE15

As shown in Fig. 4.11, the minimal stress of sample Cyl_T1000_ZrE15 is -1276MPa. The average stress from 0.1 mm to 0.5 mm is -374 ± 139 MPa. The average stress for near surface zone from 0 to 0.03 mm is -656 MPa corresponding a depth of 0.011mm. The difference between the minimal stress and constant stress is 902 MPa and between the minimal stress and the average stress for near surface zone is 620 MPa, which gives a stress spatial gradient 5.6*$10^4$ MPa/mm.

Because of doping with the reactive element Zr at the surface, the differences are lower between the minimal stress and constant stress and between the minimal stress and the average stress for near surface zone. Moreover, the stress spatial gradient also decreases.

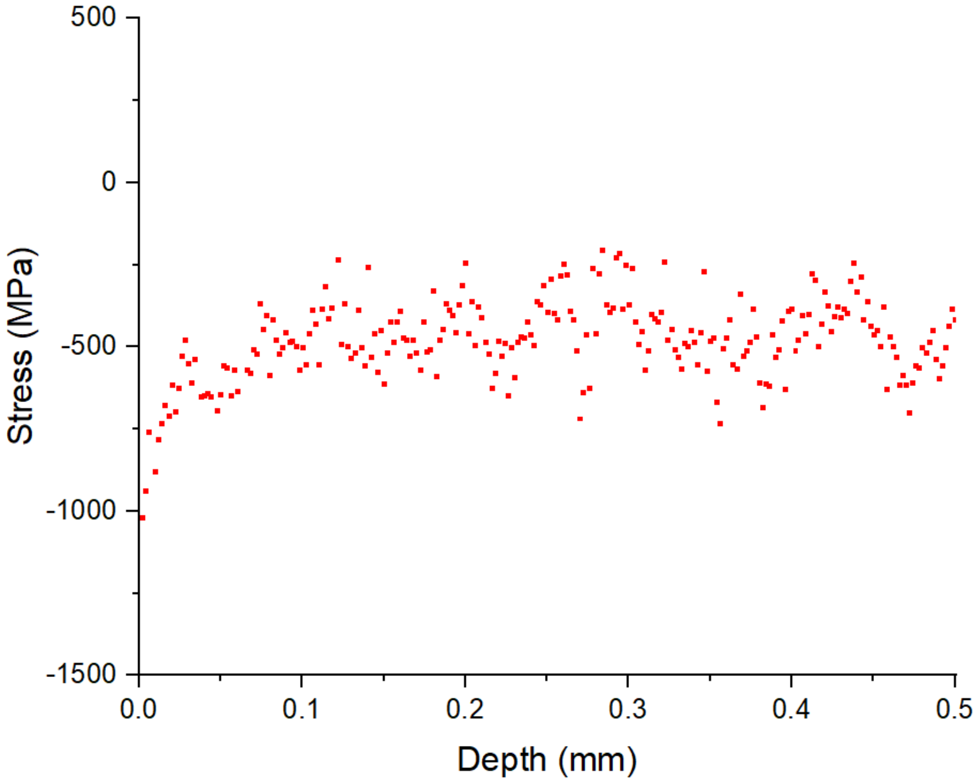

Figure 4.12. Stress of peak (311) as a function of depth of sample Cyl_T1000_ZrE16

Fig. 4.12 shows the results of sample Cyl_T1000_ZrE16. The minimal stress is -1019 MPa. The average stress from 0.1 mm to 0.5 mm is -455 ± 110 MPa. The average stress for near surface zone from 0 to 0.03 mm is -746 MPa corresponding a depth of 0.013mm. The difference between the minimal stress and constant stress is 564 MPa and between the minimal stress and the average stress for near surface zone is 273 MPa, which gives a stress spatial gradient $2.1*10^4$ MPa/mm.

Table 4.5. Comparison of the samples with the doping reactive element zirconium on the surface

| Name | Minimal stress (MPa) | The constant stress (MPa) | The average stress for near surface zone | Depth of average stress (mm) |
|---|---|---|---|---|
| Cyl_T900 | -1369 | -189 ± 184 | -769 | 0.013 |
| Cyl_T900_ZrE16 | -1296 | -613 ± 135 | -938 | 0.011 |
| Cyl_T1000 | -1419 | -40 ± 149 | -718 | 0.011 |
| Cyl_T1000_ZrE15 | -1276 | -374 ± 139 | -656 | 0.011 |
| Cyl_T1000_ZrE16 | -1019 | -455 ± 110 | -746 | 0.013 |

|  | Difference between minimal stress and the average stress for near surface zone (MPa) | Spatial gradient evolution for near surface zone (MPa/mm) | Difference between minimal stress and the constant stress (MPa) |  |
|---|---|---|---|---|

| | | | |
|---|---|---|---|
| Cyl_T900 | 600 | $4.6*10^4$ | 1180 |
| Cyl_T900_ZrE16 | 357 | $3.2*10^4$ | 682 |
| Cyl_T1000 | 702 | $6.4*10^4$ | 1379 |
| Cyl_T1000_ZrE15 | 620 | $5.6*10^4$ | 902 |
| Cyl_T1000_ZrE16 | 273 | $2.1*10^4$ | 563 |

The comparison in Table 4.5 indicates that the standard deviation of the average stress from 0.1 mm to 0.5 mm has the same magnitude whatever the samples are, which is around -150 MPa. The depths from the surface to the average stress point are very close.

The stress values for the second group experiment seem to have a calibration problem. Comparing the sample Cyl_T1000_5h of the first group and the sample Cyl_T1000 of the second group, they have the same oxidation temperature, oxidation time and the material, and the difference between them is the thickness of substrate. However, the results of these two sample has an offset about 450 MPa. This offset may be caused by the systematic errors and bias during the measurement, which has been discussed in section 2.4 and need to be studied in more details. However, concerning the spatial gradient evolution for near surface zone, it can also draw some conclusions.

For the same temperature, as the Zr doping fluence is increasing, the minimal stress increases and the constant stress decreases. Therefore, the difference between minimal stress and the constant stress decreases. Moreover, the difference between minimal stress and the average stress for near surface zone and the stress spatial gradient evolution for near surface zone decreases.

As discussed in section 1.1.3, by adding the reactive element Zr, the microstructure is modified and the growth rate of chromium oxide decreases, which may be because of the segregation of the reactive elements at the grain boundaries of chromium oxide. The cationic $Cr^+$ transport outward is slowed down. Therefore, the phenomena of $Cr^+$ depletion is reduced. We assume that the chromium depletion in the metal will cause a diffusion stress, which may explain the decreasing of the difference between minimal stress and the constant stress and the stress spatial gradient evolution for near surface zone. However, the influence of doping reactive elements on the diffusion stress requires further investigations.

## 4.2 Proposition of stress source

### 4.2.1 Chromium diffusion coefficient

In order to analyze the stress distribution in the metallic substrate, a chemical/diffusion strain is introduced and proposed in the modelling, as the experimental results shows that a stress gradient appears near the interface of metal and oxide layer. Indeed, in such materials, the concentration profile indicates that the concentration of chromium changes near the interface of metal and oxide layer in such a system [15-17], which has been proved to have an effect on the lattice spacing *d* between the crystallographic planes within the material. This variation in Cr concentration is strongly related with local variations in observed diffraction pattern ($2\theta$), which will cause a stress gradient in the metal layer. Thus, a chemical/diffusion strain is proposed to investigate the importance of this effect through the modelling.

To calculate the concentration profile of chromium, the 1D diffusion of Fick's law is used:

$$D\frac{\partial^2[Cr](z,t)}{\partial z^2}-\frac{\partial[Cr](z,t)}{\partial t}=0 \tag{4.3}$$

where *D* is the chromium diffusion coefficient in the alloy; $[Cr]$ is the weight percentages concentration of element Cr, and z is the depth. The diffusion coefficient *D* of element Cr in Nickel-Chromium alloys system has been studied in [16, 17]. In the work of Ruzickova, J et al. [16], the alloy used is Ni29.4Cr and the alloy is Ni30Cr in the work of Monma, K et al.[17], which are quite similar to the alloys studied in our present work. An Arrhenius law is proposed to describe the temperature dependence:

$$D = D_0 exp\left(\frac{-Q}{RT}\right) \tag{4.4}$$

where *D* is the diffusion coefficient, $D_0$ is the pre-exponential factor, Q the activation energy, R the ideal gas constant and T the temperature. With the expression of *D* (Eq. 4.4), the figure of *ln(D)* as function of 1/T has been plotted (Fig. 4.13).

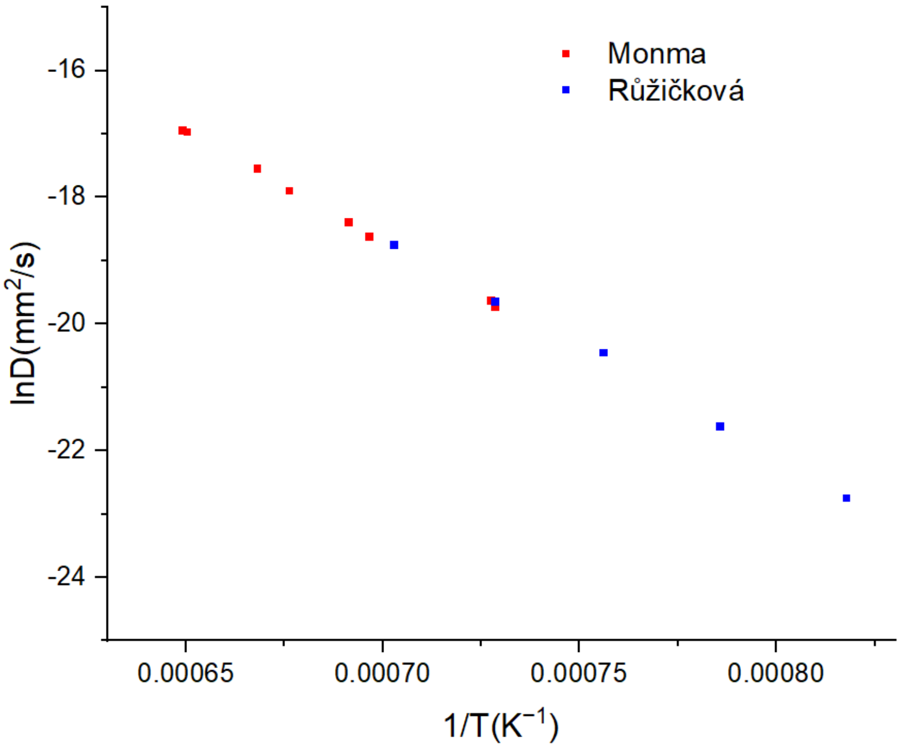

Figure 4.13. Diffusion data from the literature [16, 17]

Fig. 4.13 provides an overview of a linear relationship between ln(D) and 1/T. Therefore, the diffusion coefficient at 800°C, 900°C and 1000°C can be calculated (Table 4.6).

Table 4.6. Diffusion coefficient with $D_0$=297.5 mm2/s and Q=288.8kJ

(calculated from Eq. 4.4 by using data from the literature [16, 17])

| T (K) | D (mm$^2$/s) |
|---|---|
| 1073 | $2.59038*10^{-12}$ |
| 1173 | $4.09273*10^{-11}$ |
| 1273 | $4.19124*10^{-10}$ |

## 4.2.2 Chromium concentration profiles

To analyze the concentration of chromium in our system, the initial condition (IC) and boundary condition (BC) are considered as:

$$\begin{cases} IC: \quad [Cr]_i = [Cr](z,0) = 28.28\% \text{ or } 34.5\% \\ BC1: \quad \dfrac{\partial [Cr](z,t)}{\partial z} = 0, z = \dfrac{h_m}{2}, 0 < t < \infty \\ BC2: \quad [Cr](0,t) = \alpha [Cr]_i, 0 < t < \infty \end{cases} \tag{4.5}$$

The initial condition indicates that, at initial time, the weight concentration of chromium is 28.28% for all depth for cylinder samples and 34.5% for rectangle samples. The first boundary condition (BC1) indicates that at any time the rate of weight concentration for Cr at central plane is 0 due to the assumed symmetry of the system. On the contrary, in the near interface area, the depletion of Cr cannot be ignored. The second boundary condition (BC2) indicates that, at the interface oxide/metal, the concentration of chromium is related to the initial value 28.28% or 34.5%. The interfacial concentration of cation is studied in [15], which shows that during the later stages of oxidation, the interfacial concentration of cation increases to an almost constant value. To simplify the calculation, the ratio $\alpha$ is considered as a constant equal to 0.413 for the parabolic oxidation law, which is given by the calculation in work [15].

If considering the whole sample, from top surface to bottom surface, it would be a problem with Dirichlet boundary conditions. However, only the top half part are presented, from the top surface down to the central plane. At the central plan, the rate of weight concentration for Cr is 0 due to symmetry. Thus, conditions given in Eq. 4.5 are Neumann-Dirichlet boundary condition in our case. The Eq.4.3 can be solved considering the following general solution:

$$[Cr](z,t) = (1-\alpha)[Cr]_i erf(q) + \alpha[Cr]_i \tag{4.6}$$

where $[Cr]_i$ is the initial concentration of chromium; and $q = \frac{z}{2\sqrt{Dt}}$. The numerical approximations of function error erf are given in [18]. By combining the numerical approximation and Eq. 4.6, an analytical solution is obtained as:

$$[Cr](z,t) = (1-\alpha)[Cr]_i\left(1 - (a_1 n + a_2 n^2 + a_3 n^3 + a_4 n^4 + a_5 n^5)e^{-q^2}\right) + \alpha[Cr]_i \tag{4.7}$$

with

$$\left\{\begin{array}{c} q = \dfrac{z}{2\sqrt{Dt}} \\ n = \dfrac{1}{1+pq} \\ p = 0.3275911, a_1 = 0.254829592, a_2 = -0.284496736, \\ a_3 = 1.421413741, a_4 = -1.453152027, a_5 = 1.061405429 \\ \alpha = 0.413 \\ |error(z)| \leq 1.5 * 10^{-7} \end{array}\right. \tag{4.8}$$

The chromium concentration profiles can then be calculated for the different sample's conditions:

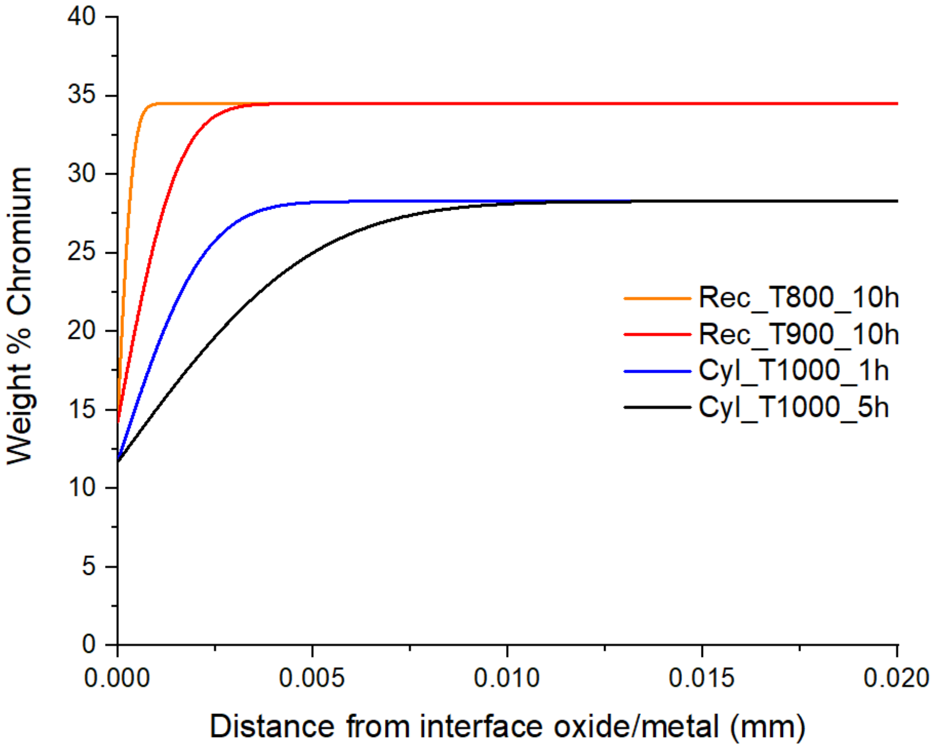

Figure 4.14. Chromium concentration profiles for different oxidation conditions

Fig. 4.14 shows the chromium concentration profiles in the first 20 µm from interface oxide/metal, which proves the chromium depletion near the interface far from the sample center where no depletion occurs, providing that the metal thickness is sufficient enough. Comparison of different oxidation conditions indicates that the depth of chromium-depleted zone increases with the time and temperature of oxidation. With longer oxidation time and higher oxidation temperature, the spatial concentration gradient changes faster. However, it also shows that the chromium concentration equals to the initial value after 10 µm for the four samples (Table 4.7). Furthermore, Scanning Electron Microscope and Energy-dispersive X-ray spectroscopy test for chromium concentration profiles have been performed at oxidation condition of 800 °C for 1 h, which has been done at Institut Jean Lamour of University of Lorraine. It shows a variation of weight concentration of chromium within 1 µm in near interface zone, which is consistent with the present calculations. At shorter oxidation time and lower oxidation temperature, the variation of weight concentration of chromium is very difficult to detect.

Table 4.7. Calculated weight concentration of chromium in the near interface zone

| Depth(µm) | 0 | 1 | 2 | 3 | 4 | 6 | 8 | 10 | 12 | 15 |
|---|---|---|---|---|---|---|---|---|---|---|
| Cyl_T1000_1h | 11.68 | 18.91 | 24.14 | 26.88 | 27.92 | 28.27 | 28.28 | 28.28 | 28.28 | 28.28 |
| Cyl_T1000_5h | 11.68 | 15.06 | 18.22 | 20.98 | 23.25 | 26.25 | 27.63 | 28.11 | 28.25 | 28.28 |
| Rec_T800_10h | 14.25 | 34.45 | 34.5 | 34.5 | 34.5 | 34.5 | 34.5 | 34.5 | 34.5 | 34.5 |
| Rec_T900_10h | 14.25 | 26.2 | 32.45 | 34.23 | 34.48 | 34.5 | 34.5 | 34.5 | 34.5 | 34.5 |

### 4.2.3 Proposition for diffusion stress

Due to the important variation of chromium concentration in the near-surface zone, we propose to associate a strain gradient related to the chromium concentration profiles [19].

$$\bar{\bar{\varepsilon}}^{diffusion}(z,t) = \eta([Cr](z,t) - [Cr]_i)\bar{\bar{I}} \tag{4.9}$$

where $\bar{\bar{\varepsilon}}^{diffusion}(z,t)$ is the strain caused by diffusion of chemical specie Cr, which is at least a function of z but also on time t ; $\eta$ is a constant coefficient coupling the chromium concentration profiles to the diffusion strain; $[Cr](z,t)$ is chromium concentration profiles as a function of z and time t ; $[Cr]_i$ is the initial concentration of chromium.

The relation between the stress and the elastic stain is given by Hooke's model (Eq. 4.10), which can also be written as, with Lamé's coefficients  and μ :

$$\bar{\bar{\sigma}} = \lambda trace\left(\bar{\bar{\varepsilon}}^{elastic}\right)\bar{\bar{I}} + 2\mu\bar{\bar{\varepsilon}}^{elastic} \tag{4.10}$$

The stress tensor $\bar{\bar{\sigma}}$ (Eq. 4.11) and elastic strain tensor $\bar{\bar{\varepsilon}}^{elastic}$ are considered as:

$$\bar{\bar{\sigma}} = \begin{pmatrix} \sigma & 0 & 0 \\ 0 & \sigma & 0 \\ 0 & 0 & \sigma_N \end{pmatrix} \text{ and } \bar{\bar{\varepsilon}}^{elastic} = \begin{pmatrix} \varepsilon^{elastic} & 0 & 0 \\ 0 & \varepsilon^{elastic} & 0 \\ 0 & 0 & {\varepsilon^{elastic}}_N \end{pmatrix} \tag{4.11}$$

A proportional relationship between in-plane stress $\sigma$ and normal stress $\sigma_N$ in the metal is assumed:

$$\sigma_N = \beta\sigma \tag{4.12}$$

As proposed in Eq. 4.1 from experimental observations, $\beta$ = 1. By combining Eq. 4.1, Eq. 4.10 and Eq. 4.11, the relation between elastic in-plane strain $\varepsilon^{elastic}$ and normal elastic strain ${\varepsilon^{elastic}}_N$ in the metal is obtained:

$${\varepsilon^{elastic}}_N = \frac{\beta - 2\nu_m}{1 - \nu_m - \beta\nu_m}\varepsilon^{elastic} \tag{4.13}$$

The in-plane stress $\sigma$ in metal can then be calculated:

$$\sigma = \frac{E_m}{1 - \nu_m - \beta\nu_m}\varepsilon^{elastic} \tag{4.14}$$

The strain in the metal layer includes different components. After modifying it by adding $\varepsilon^{diffusion}$, the strain in the metal layer is:

$$\varepsilon^{total} = \varepsilon^{elastic} + \varepsilon^{viscoplastic} + \varepsilon^{thermal} + \varepsilon^{diffusion} \tag{4.15}$$

Eq. 4.14 can be expressed as:

$$\sigma = \frac{E_m}{1 - \nu_m - \beta\nu_m}\left(\varepsilon^{total} - \varepsilon^{viscoplastic} - \varepsilon^{thermal} - \varepsilon^{diffusion}\right) \tag{4.16}$$

Eq. 4.16 can be split into 2 terms: the diffusion stress and another term:

$$\sigma^{diffusion} = \frac{-E_m}{1 - \nu_m - \beta\nu_m}\varepsilon^{diffusion} \tag{4.17}$$

$$\sigma^{else} = \frac{E_m}{1 - \nu_m - \beta\nu_m}\left(\varepsilon^{total} - \varepsilon^{viscoplastic} - \varepsilon^{thermal}\right) \tag{4.18}$$

Because $\varepsilon^{diffusion}$ is related to chromium concentration profiles varying with depth z, $\sigma^{diffusion}$ is a function of z. To find coefficient $\eta$, the boundary value of stress is considered, which can be related to the experimental results. For metal layer, when z=0,

$$\sigma(0) = \sigma^{diffusion}(0) + \sigma^{else} \Leftrightarrow \sigma^{else} = \sigma(0) - \sigma^{diffusion}(0) \qquad (4.19)$$

We assume for the sake of simplicity that $\sigma^{else}$ does not depend on z. By combining Eq. 4.9, Eq. 4.17 and Eq. 4.18, the equation of mechanical balance becomes:

$$\int_0^{h_m/2} \left( \sigma(0) + \frac{E_m}{1 - \nu_m - \beta\nu_m}\eta([Cr](0,t) - [Cr]_i) - \frac{E_m}{1 - \nu_m - \beta\nu_m}\eta([Cr](z,t) - [Cr]_i) \right) dz + \int_{-h_{ox}}^{0} \sigma_{ox}\, dz = 0 \qquad (4.20)$$

where $[Cr](0,t)$ is the concentration of chromium at the interface oxide/metal. To obtain the value of $\eta$, the unknown value of $\sigma_{ox}$ in Eq. 4.20 is required. However, $\sigma_{ox}$ is studied under oxidation temperature in [20]. On the contrary, $\sigma_{ox}$ in Eq. 4.20 should be considered at room temperature, which can be calculated by adding the thermal stress component, but neglecting the relaxation phenomena during the cooling procedure:

$$\sigma_{ox} = {\sigma_{ox}}^{T_{oxidation}} - \frac{E_{ox}}{1 - \nu_{ox}}(\alpha_{ox} - \alpha_{met})(T_{room} - T_{oxidation}) \qquad (4.21)$$

with thermal expansion coefficient of oxide layer $\alpha_{ox}$, which is 5.67E-6 K$^{-1}$ [21]; thermal expansion coefficient of metal layer $\alpha_{met}$, which is 12.93E-6 K$^{-1}$ [21]; room temperature $T_{room}$ is 298 K and oxidation temperature $T_{oxidation}$ that depends on the sample conditions. The other used parameters for the different samples are presented in Table 4.8:

Table 4.8: Input data and related parameters in Eq. 4.20 [20]

| | $E_m$ (MPa) | $\nu_m$ | $\frac{h_m}{2}$ (mm) | $\sigma(0)$ (MPa) | $E_{ox}$ (MPa) | $\nu_{ox}$ | $h_{ox}$ (mm) | ${\sigma_{ox}}^{T_{oxidation}}$ (MPa) |
|---|---|---|---|---|---|---|---|---|
| Cyl_T1000_1h | 160000 | 0.3 | 0.45 | -588.09 | 299700 | 0.270 | 0.00097 | -144.1±18.5 |
| Cyl_T1000_5h | 160000 | 0.3 | 0.45 | -1178.70 | 299700 | 0.270 | 0.00216 | -133.1±23.9 |
| Rec_T800_10h | 170000 | 0.3 | 0.2 | -556.68 | 301100 | 0.273 | 0.0006 | -277.8±11.4 |
| Rec_T900_10h | 165000 | 0.3 | 0.2 | -969.93 | 300400 | 0.271 | 0.00101 | -150.0±34.3 |

Because of the different oxidation temperatures, the values of $E_m$ , $E_{ox}$ and $\nu_{ox}$ are different. The residual stresses at room temperature can be calculated by using Eq. 4.21 and the parameters in Table 4.8, which can also be determined by use of Raman spectroscopy [22] or XRD [23]. The comparison of these results with our calculations is shown in Table 4.9.

Table 4.9: Comparison of residual stresses at room temperature

| Calculated results | | Measured results for system Ni30Cr/$Cr_2O_3$ [22, 23] | | | |
|---|---|---|---|---|---|
| Sample | $\sigma_{ox}$ (GPa) | Sample | $\sigma_{ox}$ (GPa) | Sample | $\sigma_{ox}$ (GPa) |
| Cyl_T1000_1h | -3.05 | 1000°C_3h | -2.60, -2.35, -3.05 | | |
| Cyl_T1000_5h | -3.04 | | | 1000°C_18h | -3.00 |
| Rec_T800_10h | -2.61 | 800°C_3h | -1.56 | 800°C_18h | -1.84 |
| Rec_T900_10h | -2.77 | 900°C_3h | -1.94 | 900°C_18h | -2.40, -2.10, -2.50 |

Table 4.9 shows that the calculated values of residual stresses at room temperature are smaller than the measured values, but the oxidation time are different. In addition, the relaxation is not taken into account in the calculation, whereas in the measurement there is relaxation of stress during the high temperature loading. However, they are at the same order of magnitude. The calculated results are chosen for the subsequent calculations.

As proposed in Eq. 4.1, $\beta$ = 1 and in Eq. 4.9, $\eta$ is a constant coefficient. Eq. 4.20 can be transformed into:

$$\eta = \frac{-\int_{-h_{ox}}^{0} \sigma_{ox}\, dz - \int_{0}^{h_m/2} \sigma(0) dz}{\int_{0}^{h_m/2} \frac{E_m}{1-2\nu_m}\big([Cr](0,t) - [Cr](z,t)\big) dz} \tag{4.22}$$

The coefficient $\eta$ coupling diffusion with strain is calculated:

Table 4.10. Values for the coefficient $\eta$

| Code name | coefficient $\eta$ |
|---|---|
| Cyl_T1000_1h | $-8.98*10^{-3}$ |
| Cyl_T1000_5h | $-1.80*10^{-2}$ |
| Rec_T800_10h | $-6.57*10^{-3}$ |
| Rec_T900_10h | $-1.18*10^{-2}$ |

$\eta$ is strongly related to $\sigma_{ox}$ and $\sigma(0)$. Table 4.10 shows that the order of magnitudes of coefficient $\eta$ is around -1E-02, from which the diffusion stress for four samples can in return be calculated.

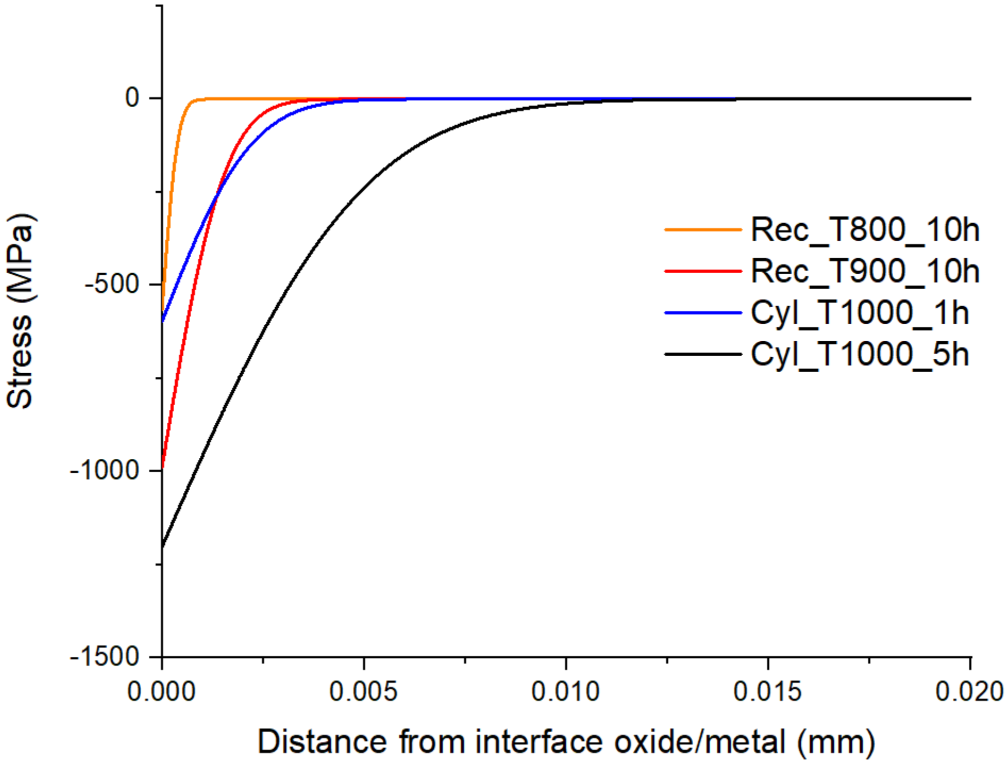

Figure 4.15 Diffusion stress calculated for the four samples

As shown in Fig. 4.15, the diffusion stress calculated for the four samples in the first 20 µm from interface oxide/metal is plotted, which gives a maximum diffusion stress of -1200 MPa for sample Cyl_T1000_5h. The important variation of chromium depletion leads to a diffusion stress with maximum magnitudes between -500 and -1500 MPa. Such a stress cannot be ignored.

### 4.2.4 Discussion about diffusion stress

By combining the Eq. 4.9 and Eq. 4.17, a diffusion stress equation is obtained:

$$\bar{\bar{\sigma}}^{diffusion} = \frac{-E_m}{1-\nu_m-\beta\nu_m}\eta([Cr](z,t)-[Cr]_i)\bar{\bar{I}} \tag{4.23}$$

From Eq. 4.23, we can see that the diffusion stress depends on parameters: $E_m, \nu_m, \beta, \eta, [Cr](z,t)\ and\ [Cr]_i$. For a given materiel, Young's modulus $E_m$, Poisson's ratio $\nu_m$, coefficient $\beta$ and the initial concentration of chromium $[Cr]_i$ are known as constants.

$\eta$ is a constant coefficient coupling the chromium concentration profiles to the diffusion strain, which needs to be investigated. $[Cr](z,t)$ is chromium concentration profiles as a function of z, which also depends on oxidation time t and diffusion coefficient D.

With our handmade program of Matlab, the diffusion stress can be calculated directly as shown in Fig. 4.15. Two tests are made to discuss the proposition of diffusion stress and the influence of different parameters.

The first test is for the influence of oxidation time, which uses the parameter for 1000°C, such as $E_m$=160000MPa, $\nu_m$=0.3, $\beta$=1, $[Cr]_i$=0.345 and $\eta$=-1.80E-02.

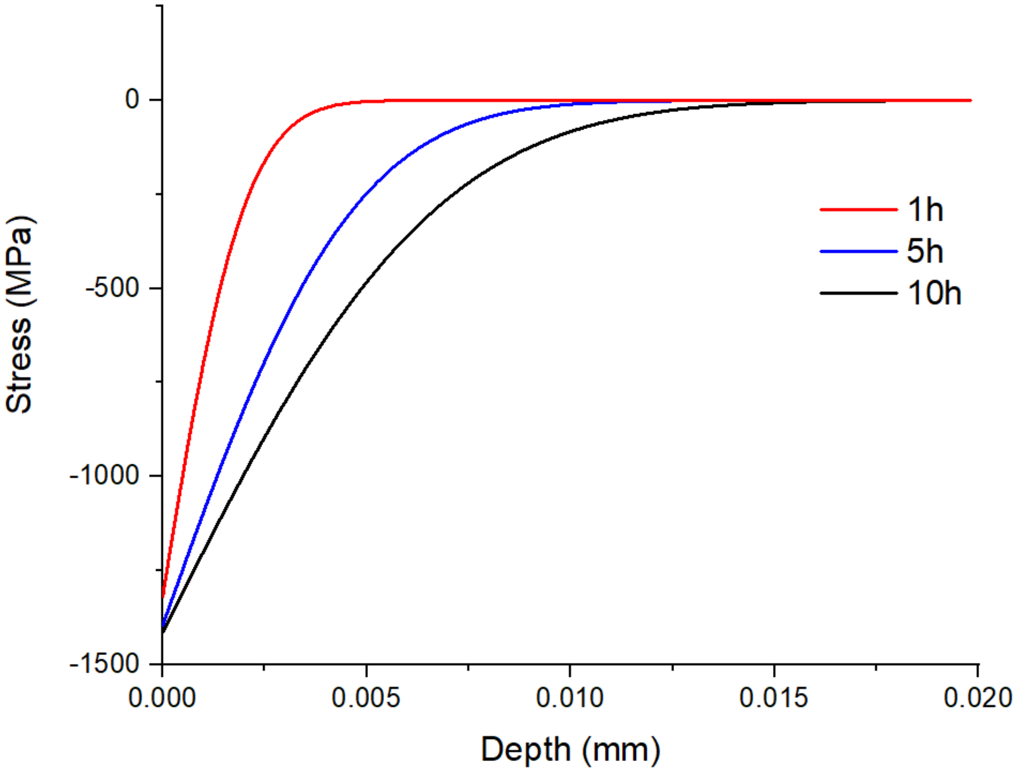

Figure 4.16. Test for different oxidation time

Fig. 4.16 shows that in this proposal, as the oxidation time is shorter, the depth of the stress gradient in the metal layer is smaller, which is reasonable. For a given temperature, the diffusion coefficient is a constant. When the oxidation time is short, the time of cationic $Cr^+$ transport outward is short. Therefore, the depth of depletion of Cr is small, which introduces a smaller stress gradient depth.

The second test is for the influence of coefficient $\eta$, which uses the parameter for 1000°C, such as $E_m$=160000MPa, $\nu_m$=0.3, $\beta$=1, $[Cr]_i$=0.345 and oxidation time 5h.

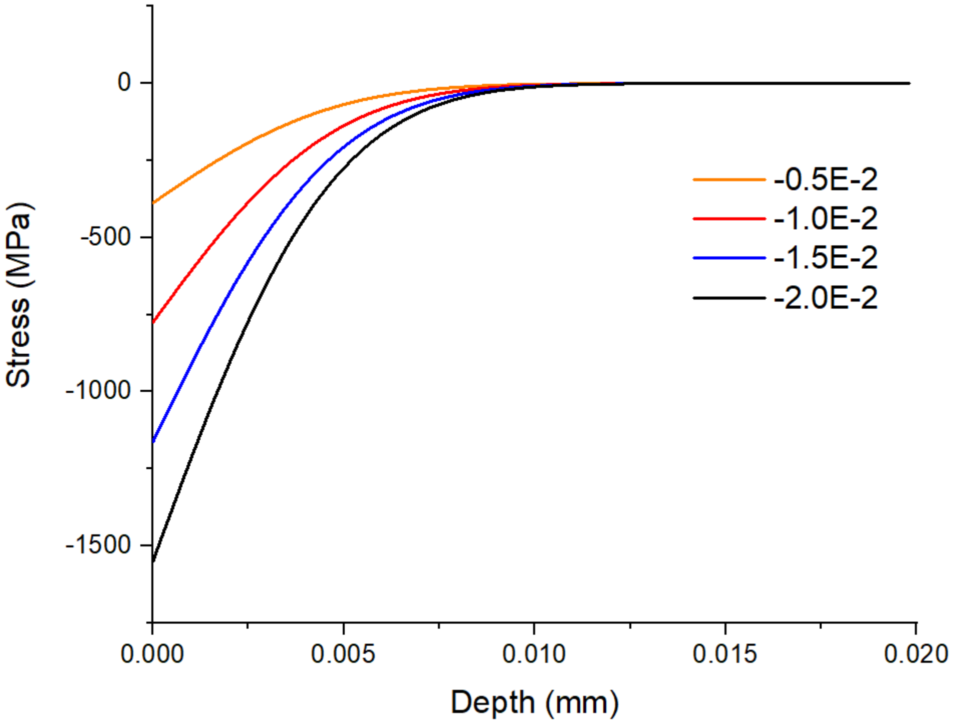

Figure 4.17. Test for different coefficient $\eta$

As sown in Fig. 4.17, the coefficient $\eta$ has a strong effect on the results, which relates the chromium concentration profiles to the diffusion strain. The Table 4.10 shows that the coefficient $\eta$ is a complicated coefficient and it seems hard to determine, because it is not only related to oxidation temperature and oxidation time. The stress increases when the coefficient $\eta$ increases. As far as the current study is concerned, the coefficient $\eta$ can be obtained by the experimental results and be optimized by a full thermomechanical modelling.

## 4.3 Thermomechanical modeling by adding diffusion stress

### 4.3.1 Thermomechanical + diffusion modeling

The thermomechanical modelling has been investigated in section 1.2.3. As shown in Eq.1.37:

$$\left(\varepsilon^{elastic} + \varepsilon^{viscoplastic} + \varepsilon^{thermal}\right)_m = \left(\varepsilon^{elastic} + \varepsilon^{viscoplastic} + \varepsilon^{thermal} + \varepsilon^{growth}\right)_{ox} \quad (1.37)$$

The indices "ox" and "m" refer to the oxide layer and the metal layer respectively. $\varepsilon^{elastic}$ represents the elastic strain in the oxide layer or in the metal layer, $\varepsilon^{viscoplastic}$ represents the viscoplastic strain in the oxide layer or in the metal layer, $\varepsilon^{thermal}$ represents the thermal strain in the oxide layer or in the metal layer and $\varepsilon^{growth}$ represents the oxide growth strain in the oxide layer.

After adding diffusion strain in Eq.1.37, it becomes:

$$\left(\varepsilon^{elastic}+\varepsilon^{viscoplastic}+\varepsilon^{thermal}+\varepsilon^{diffusion}\right)_m = \left(\varepsilon^{elastic}+\varepsilon^{viscoplastic}+\varepsilon^{thermal}+\varepsilon^{growth}\right)_{ox} \tag{4.24}$$

In a rate formalism, it corresponds to:

$$\left(\frac{d\varepsilon^{elastic}}{dt}+\frac{d\varepsilon^{viscoplastic}}{dt}+\frac{d\varepsilon^{thermal}}{dt}+\frac{d\varepsilon^{diffusion}}{dt}\right)_m = \left(\frac{d\varepsilon^{elastic}}{dt}+\frac{d\varepsilon^{viscoplastic}}{dt}+\frac{d\varepsilon^{thermal}}{dt}+\frac{d\varepsilon^{growth}}{dt}\right)_{ox} \tag{4.25}$$

Considering the mechanical balance, the analytical solutions becomes:

$$\dot{\sigma}_{ox} = \frac{\frac{\sigma_{ox}}{t}\frac{1-\nu_m}{E_m} - signe(\sigma_{ox})\left(\frac{h_m}{Ap\sqrt{t}}\right)^{1-N_m} J_m|\sigma_{ox}|^{N_m} + signe(\sigma_{ox})J_{ox}|\sigma_{ox}|^{N_{ox}}\frac{h_m}{Ap\sqrt{t}} + \frac{D_{ox}h_m}{2t} - \frac{\eta[\dot{C}r](z,t)h_m}{Ap\sqrt{t}}}{\left(\frac{1-\nu_{ox}}{E_{ox}}\frac{h_m}{Ap\sqrt{t}} + 2\frac{1-\nu_m}{E_m}\right)} \tag{4.26}$$

There are 1 geometrical parameter and 11 material parameters to be identified: $\mathrm{h_m}$, $\mathrm{\nu_m}$, $\mathrm{E_m}$, $\mathrm{\nu_{ox}}$, $\mathrm{E_{ox}}$, Ap, $\mathrm{J_m}$, $\mathrm{N_m}$, $\mathrm{J_{ox}}$, $\mathrm{N_{ox}}$, $\mathrm{D_{ox}}$ and $\eta$.

$\mathrm{h_m}$ is the thickness of metal part, which can be easily measured and is supposed to be a constant parameter, which is not related to the temperature and oxidation time. Numerical values of Young's modulus of oxide $Cr_2O_3$ ($\mathrm{E_{ox}}$) and Poisson's ratio of oxide $Cr_2O_3$ ($\mathrm{\nu_{ox}}$) can be found in literature [24]. Numerical values of the other parameters can also be found in literature [25] for raw material and for different temperatures, such as the Young's modulus of metal ($\mathrm{E_m}$), Poisson's ratio of metal ($\mathrm{\nu_m}$), the parabolic kinetics parameter (Ap), the creep parameter of oxide $Cr_2O_3$ ($\mathrm{J_{ox}}$), the Norton exponent of oxide $Cr_2O_3$ ($\mathrm{N_{ox}}$), the creep parameter of metal ($\mathrm{J_m}$), the Norton exponent of metal ($\mathrm{N_m}$), the growth strain parameter for oxide $Cr_2O_3$ ($\mathrm{D_{ox}}$) and the coefficient coupling the chromium concentration profiles to the diffusion strain $\eta$.

### 4.3.2 Comparison between modeling and experimental results

Therefore, to observe the effect of adding diffusion stress in the modelling, several results are plotted in the same figure, which includes the stress without the diffusion stress (corresponding to modelling that can be found in [12,26]), the stress in the metal layer with the diffusion stress (using the models of Equation 4.26 including the term calculated with the values of $\eta$ as given in Table 4.10) and the experimental results previously presented in Figs 4.4 - 4.7.

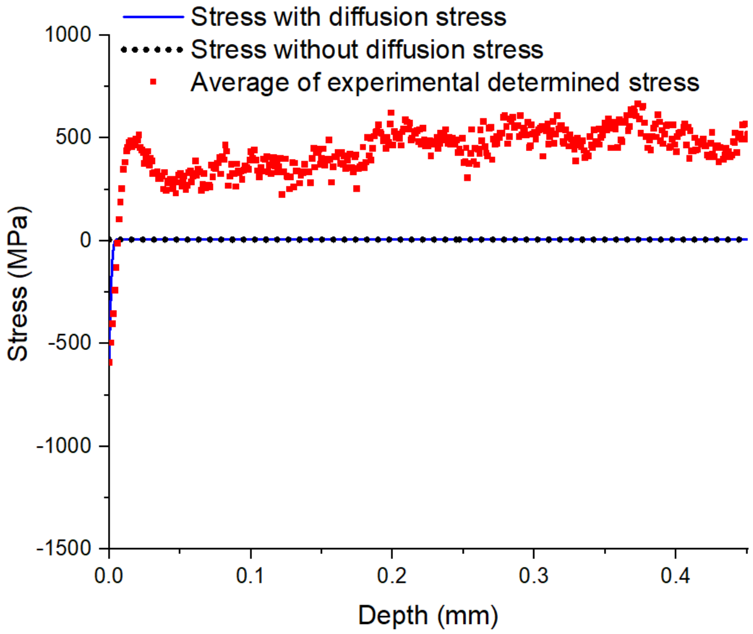

Figure 4.18.a Stress distribution in sample Cyl_T1000_1h

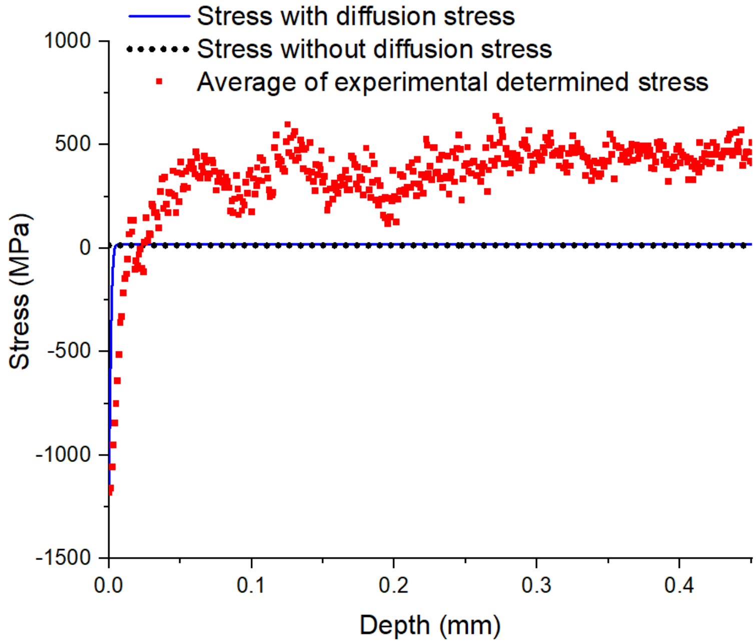

Figure 4.18.b Stress distribution in sample Cyl_T1000_5h

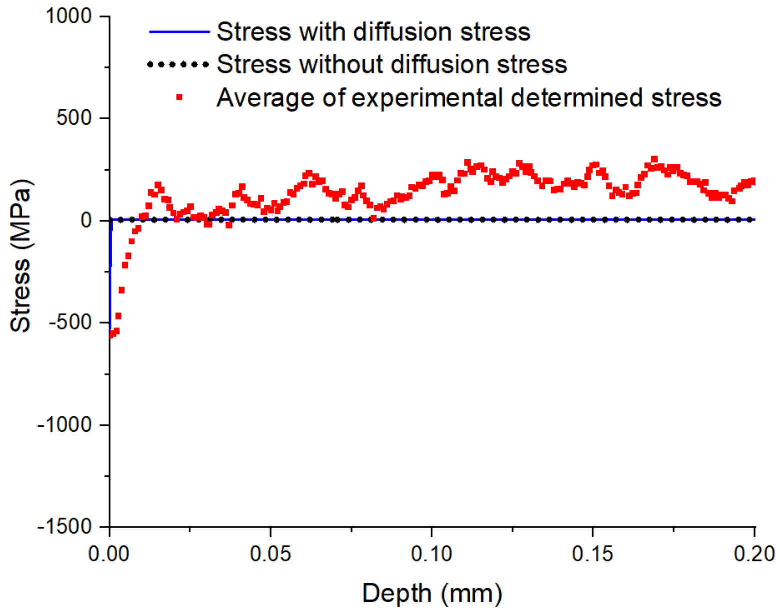

Figure 4.18.c Stress distribution in sample Rec_T800_10h

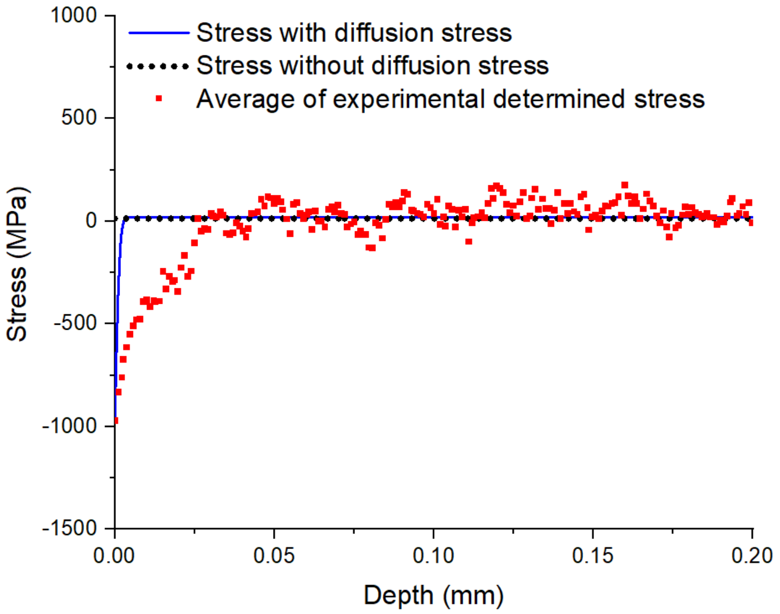

Figure 4.18.d Stress distribution in sample Rec_T900_10h

The results of Fig. 4.18.a-d are compared in Table 4.11.

Table 4.11. Comparison of the four samples

| | Experimental results | | With diffusion stress | | Without diffusion stress |
|---|---|---|---|---|---|
| | Depth for 0 MPa | Average stress after depth for 0 MPa | Depth for 0 MPa | Average stress after depth for 0 MPa | Average stress |
| Cyl_T1000_1h | 7 µm | 452.3 MPa | 4 µm | 8.4 MPa | 6.6 MPa |

| | | | | | |
|---|---|---|---|---|---|
| Cyl_T1000_5h | 14 µm | 388.8 MPa | 4 µm | 18.3 MPa | 14.6 MPa |
| Rec_T800_10h | 10 µm | 151.5 MPa | 1 µm | 8.52 MPa | 7.8 MPa |
| Rec_T900_10h | 26 µm | 41.7 MPa | 3 µm | 18.60 MPa | 14.0 MPa |

Fig. 4.18.a-d show that the stress in metal far from the interface zone is a positive value for the model with and without the diffusion stress. After adding the diffusion stress, a stress gradient is systematically predicted for the near interface zone. The focus on the evolution of stress gradient is presented in Fig. 4.19

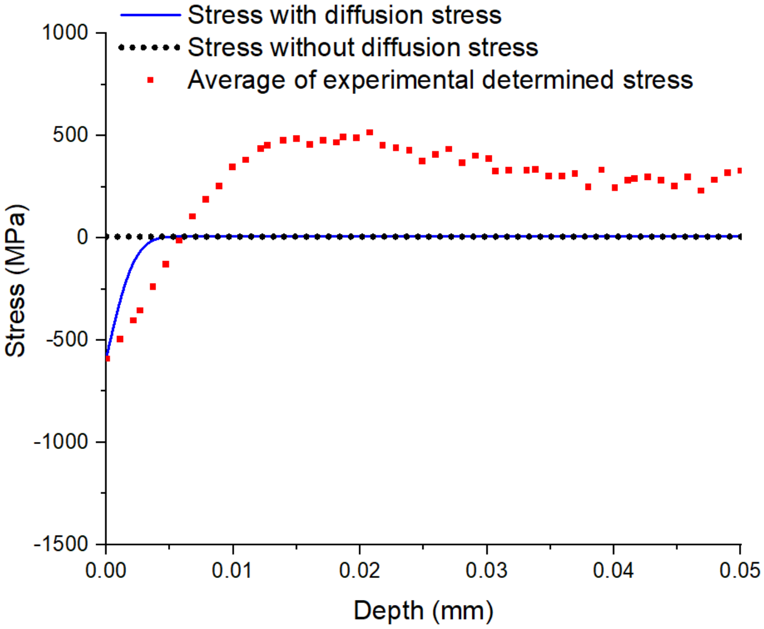

Figure 4.19.a Stress distribution in sample Cyl_T1000_1h

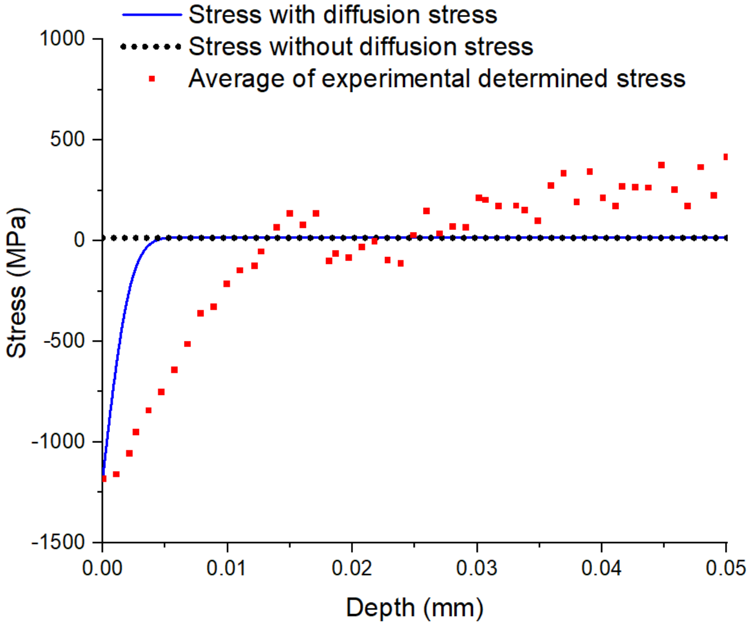

Figure 4.19.b Stress distribution in sample Cyl_T1000_5h

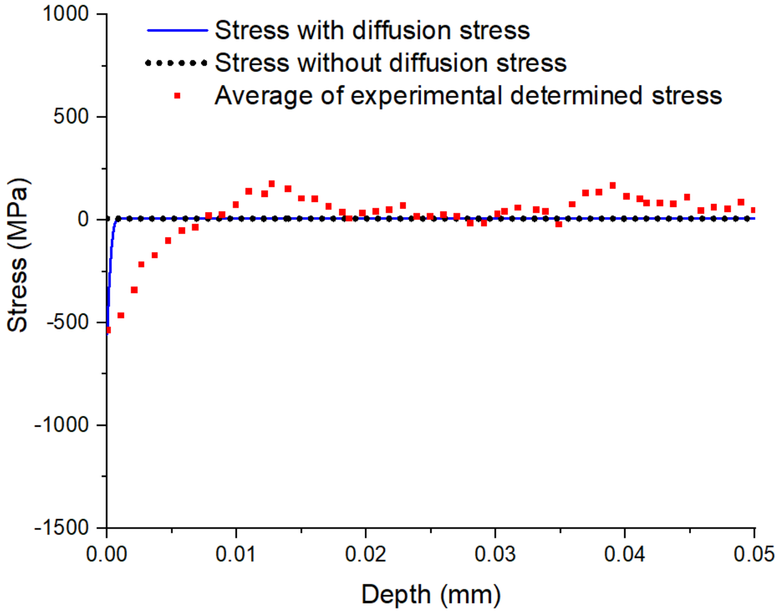

Figure 4.19.c Stress distribution in sample Rec_T800_10h

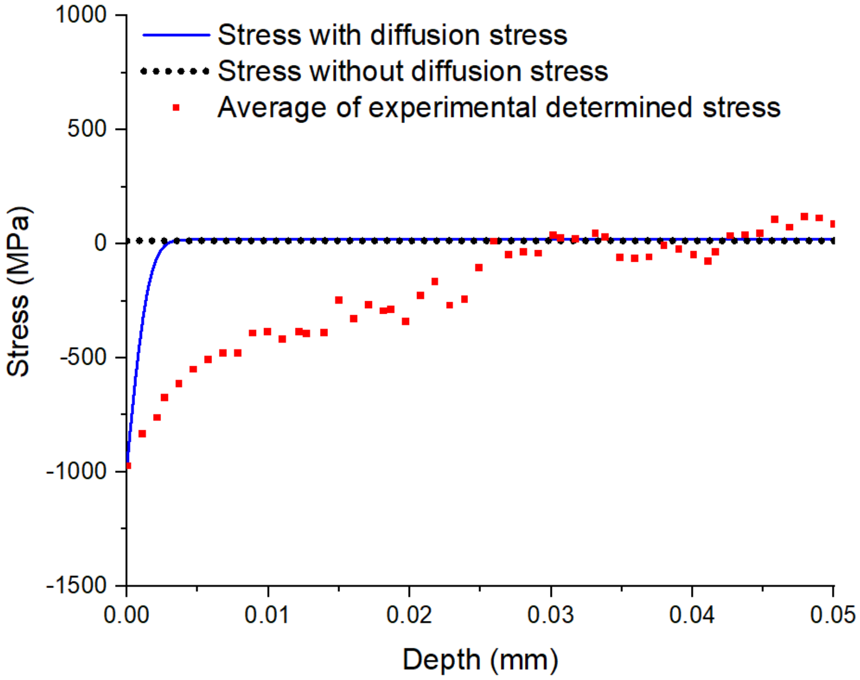

Figure 4.19.d Stress distribution in sample Rec_T900_10h

For sample Cyl_T1000_1h and Cyl_T1000_5h, the stress gradient in the near interface zone with diffusion stress is similar to the experimental results, shown in Fig.4.19.a and Fig. 4.19.b. The gradient depths have also the same order of magnitude. However, the average stress after depth for 0 MPa of experimental results is different from the results with (or without) diffusion stress. By comparing these two samples, it shows that with a longer oxidation time, the stress should be lower in the bulk metal, whereas the predicted model values are opposite (with or without diffusion stress). This can be related to the stress-free values of characteristic diffraction pattern ($2\theta_0$) or the experimental uncertainties that are quite important in the metal as well as the standard deviation that corresponds to the effect of different rotations on each sample.

For sample Rec_T800_10h and Rec_T900_10h, the stress gradient in the near interface zone is present for all the simulations with diffusion stress, but the gradient depths are ten times smaller than the experimental ones, shown in Fig.4.19.c and Fig. 4.19.d. Nevertheless, the average stress after depth for 0 MPa is more consistent to the experimental results especially for Rec_T900_10h (see Fig 4.18.b). The same reason as previously can be invoked to explain the differences. This may also be caused by a thinner thickness of metal layer or the specific shape of samples, which would require further investigations.

For the second group experiments, for the same temperature, as the Zr doping fluence is increasing, the minimal stress increases and the constant stress decreases. Therefore, the difference between minimal stress and the constant stress decreases. Moreover, the difference between minimal stress and the average stress for near surface zone and the stress spatial gradient evolution for near surface zone decreases. However, the influence about the reactive elements on the stress spatial distribution will be studied in future works.

**References of chapter 4**

[1] B. Panicaud, J.-L. Grosseau-Poussard, Z. Tao, F. Rakotovao, G. Geandier, P.-O. Renault, P. Goudeau, N. Boudet, N. Blanc, Acta Mech 2017, 228, 3595.

[2] Z. J. Tao, F. Rakotovao, J. L. Grosseau-Poussard, B. Panicaud, AMR 2014, 996, 896.

[3] Z. Wang, J.-L. Grosseau-Poussard, B. Panicaud, G. Geandier, P.-O. Renault, P. Goudeau, N. Boudet, N. Blanc, F. Rakotovao, Z. Tao, Computational Materials Science 2020, 180, 109689.

[4] W. Przybilla, M. Schutze, Role of Growth Stresses on the Structure of Oxide Scales on Nickel at 800 and 900°C, (n.d.) 43.

[5] C. Liu, A.-M. Huntz, J.-L. Lebrun, Materials Science and Engineering: A 1993, 160, 113.

[6] J.G. Goedjen, J.H. Stout, Q. Guo, D.A. Shores, Materials Science and Engineering, 1994, 117, 115

[7] C. Li, S. D. M. Jacques, Y. Chen, P. Xiao, A. M. Beale, M. di Michiel, N. Markossan, P. Nylen, R. J. Cernik, Scripta Materialia 2016, 113, 122.

[8] L. Le, D.W. Ming, B. Sutter, 2015. Transmission x-ray diffraction (xrd) patterns relevant to the msl chemin 2.

[9] R. Delhez, S. J. Van der Gaast, A. Wielders, J. L. de Boer, R. B. Helmholdt, J. van Mechelen, C. Reiss, L. Woning, H. Schenk, Waikoloa, Hawai'i, United States, , 87.

[10] B.B. He, U. Preckwinkel, K.L. Smith, 2003. Comparison between conventional and two-dimensional xrd 46, 6.

[11] S. Petrovic, N. Bundaleski, M. Radovic, Z. Ristic, G. Gligoric, D. Perusko, S. Zec, Sci Sintering 2006, 38, 155.

[12] Z. Wang, J.-L. Grosseau-Poussard, B. Panicaud, G. Geandier, P.-O. Renault, P. Goudeau, N. Boudet, N. Blanc, F. Rakotovao, Z. Tao, Metals 2018, 8, 913.

[13] B. Panicaud, Contraintes « de croissance » et cinétiques d'oxydation dans des couches d'oxydes thermiques de Fer et de Nickel ; Etude in-situ par Diffraction des Rayons X et modélisation, PhD Thesis, Université de La Rochelle, La Rochelle, France, 2004.
[14] B. Panicaud, J.-L. Grosseau-Poussard, M. Kemdehoundja, J.-F. Dinhut, Computational Materials Science. 2009, 46, 42–48.
[15] D.P Whittle, D.J Evans, D.B Scully, G.C Wood, Acta Metallurgica, 1967, 15, 1421.
[16] J. Růžičková, B. Million, Materials Science and Engineering. 1981, 50, 59–64.
[17] K. Monma, H. Suto, H. Oikawa. J. Jpn, inst, Met, 28(1964) 188-192.
[18] A. Milton, S. Irene, Abramowitz and Stegun, U.S., 1964.
[19] D.Fettre, Aspects mécaniques de l'oxydation haute température du zirconium: modélisation des champs de contrainte et suivi expérimental multi technique des endommagements, PhD Thesis, Université de Compiègne, Compiègne, France, 2017.
[20] Z.J. Tao, Etude expérimentale et modélisation des caractéristiques mécaniques d'une couche d'oxyde sous charges thermiques. PhD thesis, Université de Technologie de Troyes, Troyes, 2018.
[21] S. Daghigh, Evolution des contraintes dans le système Ni70Cr30/Cr2O3 en fonction de la température. Etude in situ par diffraction des rayons X et modélisation = Evolution of stresses in Ni70Cr30/Cr2O3 system as a function of the temperature. In situ experiments with. PhD thesis, Paris XI Orsay University, 1996.
[22] F.N. Rakotovao, Relaxation des contraintes dans les couches de chromine développées sur alliages modèles (NiCr et Fe47Cr). Apport de la diffraction in situ à haute température sur rayonnement Synchrotron à l'étude du comportement viscoplastique. Effets d'éléments réactifs, PhD thesis, Université de La Rochelle, 2016.
[23] M. Guerain, Contribution à l'étude des mécanismes de relaxation de contraintes dans les films de chromine formés sur Ni-30Cr et Fe-47Cr : approche multi-échelle par spectroscopie Raman et microdiffraction Synchrotron, PhD Thesis, Université de La Rochelle, La Rochelle, France, 2012.
[24] Y. Wang, H. Fang, C.l. Zacherl, Z. Mei, S. Shang, L.-q. Chen, P.d. Jablonski, Z.-k. Liu, Surface Science 2012, 606.
[25] J.-L. Grosseau-Poussard, B. Panicaud, S. Ben Afia, Computational Materials Science 2013, 71, 47.
[26] B. Panicaud, Contraintes « de croissance » et cinétiques d'oxydation dans des couches d'oxydes thermiques de Fer et de Nickel ; Etude in-situ par Diffraction des Rayons X et modélisation, PhD Thesis, Université de La Rochelle, La Rochelle, France, 2004.

# Chapter 5: Finite Element Simulations

# 5.1 Introduction to Finite Element method

## 5.1.1 Finite Element method

### 5.1.1.1 Development of finite element method

For the recent years, a large number of articles about finite element method have been published, especially some successful comparison with experimental studies, and papers, which have theoretically contributed to the development of finite elements. For example, there are works that are specialized in nonlinear finite element analysis, in which the more influential ones include the work of Kikuchi and Oden [1] and Crisfield [2]. Kikuchi and Oden's books are pioneering works on nonlinear finite element analysis of solids and structures. For nonlinear finite element analysis, these books provide a useful tutorial. Meanwhile, the most complete treatment of linear finite element analysis is the work of Hughes [3].

Over the past 30 years, the speed, the decreasing cost, and the increasing power of computation programs have led to a revolution in computer simulation, and finite element analysis has become a fundamental part of computer-aided engineering. The first and most valuable application area was automotive crashing simulations, which has expanded rapidly. In a large number of industries, finite element simulation is replacing prototype testing with faster and less costly ways to evaluate the design. Product design relies on simulations of normal operating conditions and other extreme loading situations. Fabrication processes can be also simulated using finite elements, such as forging, thin sheet metal forming, extrusion etc [4].

The explicit and implicit solutions are two different methods to solve the ordinary differential equations. An explicit solution is any solution that is given in the form y=y(x), where y(x) is explicitly defined as an explicit function of x, and x is the only independent variable. An implicit solution is any solution that is given in the form f(x, y)=0. The solution of an equation can always be found in implicit form, but it cannot always be expressed in explicit form, especially for differential equations. The explicit and implicit solutions are used depending on the situation. As industrial problems and scientific research subjects continue to develop, there is a need for more development of both methods [4].

There is a general problem of stability in simulation process, as explained in [4]. In our case, the stability of the simulation is to avoid disordered elements in the calculation steps and to allow the simulation to function properly. In numerical simulations, it is possible to obtain physically unstable results, and therefore the corresponding simulation is relatively meaningless. Most of the solutions are sensitive to material and loading parameters. Choosing incorrect parameters can cause unreliable strain and stress when dealing with mechanical simulation. In some cases, the results are even sensitive to the mesh used, which is absolutely not consistent from a physical point of view. Users of finite element software must be aware of these properties and estimate the potential traps that may be faced. Otherwise, the results produced by computer simulation may be incorrect.

Smoothness of the calculation is also a common problem in finite element analysis [4]. The smoothness discussed here refers to the convergence of calculations, and depends on the size of mesh elements, the calculation step, among the main parameters. Lack of smoothness may introduce unexpected variations in the results and stop the simulation. In the software ABAQUS, they have developed a technique to improve response smoothness, called the adjustment process, which is automatically applied to adjust the calculation step time. For a given calculation step time, if the calculation does not converge, the software will reduce the calculation step time until convergence or the set value given in input file. However, the adjustment process is often not based on physical phenomena. We can impose the parameters associated with this adjustment by modifying the set value of the calculation step time given in input file.

#### 5.1.1.2 Implicit solution

The first step in any finite element simulation is to discretize the actual geometry of the structure with a collection of finite elements. Each element representing a discretized part of this actual structure. Shared nodes connect these elements together. The assembly of nodes and elements is called a mesh. The number of elements in a given mesh is called mesh density. In stress analysis, the displacement of each node is the basic degree of freedom of the calculation. Once the displacement of a node is known, the stress and strain of each element can be therefore calculated.

A simple example of a truss is shown in Fig. 5.1 using 1D bar element, with one side constrained and the other side loaded by a force Fc.

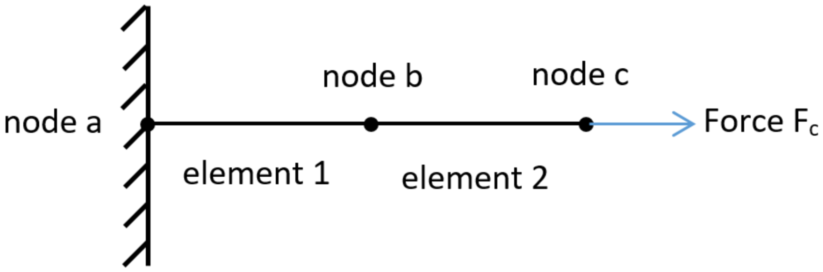

Figure 5.1 The discretized model for a 1D truss problem

As shown in Fig. 5.1, the simple truss problem is discretized into a model with 3 nodes and 2 elements. The external load is applied at node c. In general, each node in the model will be under external loads

$F$ and internal loads $I$. The internal loads $I$ is caused by the stresses in the elements connected to the nodes. For a model in static balance, the combined forces at each node must be zero, i.e., the external and internal loads at each node must be balanced as shown in Fig. 5.2.

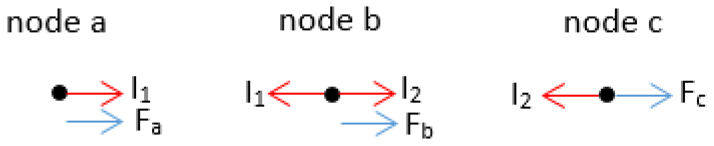

Figure 5.2 The loads at each node

For node a, the strain can be calculated as:

$$\varepsilon_{11} = \frac{u_b - u_a}{L} \tag{5.1}$$

where $\varepsilon_{11}$ is the strain of element 1; $u_b$ and $u_a$ represent the displacement of node a and node b; L is the initial length of element 1. Assuming that the materiel is elastic, the stress for 1D geometry can be calculated as:

$$\sigma_{11} = E\varepsilon_{11} \tag{5.2}$$

with the Young's modulus E. The force applied at node c is equal to the stress multiplied by the section A, which gives the relation between internal load, stress, materiel property and displacement:

$$I_1 = \sigma_{11}A = E\varepsilon_{11}A = \frac{EA}{L}(u_b - u_a) \tag{5.3}$$

Therefore, the balance equation at node a is established as:

$$F_a + \frac{EA}{L}(u_b - u_a) = 0 \tag{5.4}$$

The mechanical balance at node b must consider the internal loads of the two connected elements, which leads to:

$$F_b - \frac{EA}{L}(u_b - u_a) + \frac{EA}{L}(u_c - u_b) = 0 \tag{5.5}$$

The mechanical balance at node c is:

$$F_c - \frac{EA}{L}(u_c - u_b) = 0 \tag{5.6}$$

For the implicit solution, these balance equations need to be solved at the same time to obtain simultaneously the displacement of each node. The matrix formalism is preferred for the above equations. Therefore, the contributions of the internal and external loads are written in a matrix form. If the properties and dimensions of the two elements are the same, the balance equations can be simplified into the following form:

$$\begin{Bmatrix} F_a \\ F_b \\ F_c \end{Bmatrix} - \frac{EA}{L}\begin{bmatrix} 1 & -1 & 0 \\ -1 & 2 & -1 \\ 0 & -1 & 1 \end{bmatrix}\begin{Bmatrix} u_a \\ u_b \\ u_c \end{Bmatrix} = 0 \tag{5.7}$$

In the implicit solution, the system of equations can be solved for the values of the three unknown variables $u_b, u_c$ and $F_a$ (in this problem, $u_a$ has been given as 0). Once the displacements are obtained, the stresses in the element can be calculated by applying the Hooke's law as shown in Eq 5.2. At the end of each solving increment step, the implicit finite element solution requires solving a set of equations.

## 5.1.2 Software and subroutine

### 5.1.2.1 Software ABAQUS

ABAQUS is a powerful finite element method-based engineering simulation software that can solve a wide range of problems from relatively simple linear analysis to extremely nonlinear simulations. ABAQUS has a very large library of elements that can simulate almost any real shape. It also has an extensive library of material models that can simulate the properties of most typical engineering materials, including metals, rubbers, polymers, composites materials etc.

As a universal simulation tool, ABAQUS can be applied not only to solve mechanical or structural analysis (stress/displacement), but also to simulate and study problems in a wide range of areas with multiphysics applications, such as heat transfer, mass diffusion, chemical applications...

ABAQUS provides to users a wide range of functions that are easy to use and make it easy to create models for complex problems. For the majority of simulations, including highly nonlinear problems, the user only needs to provide data such as:

- structural geometry,
- material properties,
- boundary conditions,
- and loading conditions.

In addition, the mesh generation and the element type selection should be provided according to the possibilities offered by ABAQUS. In nonlinear analysis, ABAQUS automatically selects the appropriate load increments and convergence criteria. ABAQUS not only automatically selects the values of these parameters, but also continuously optimizes them during the analysis to ensure an accurate solution. The solver presently used in ABAQUS is ABAQUS/Standard, which is an implicit solver.

#### 5.1.2.2 User subroutine UMAT

Although ABAQUS provides users a large library of elements and solution models that allow them to use these models for the majority of problems, the actual situations in engineering are so complex that it is impossible for ABAQUS to simulate all possible physical situations. Therefore, ABAQUS provides a user material subroutine (UMAT) that allows users to define their own models to fit their problems if they cannot find a suitable model.

The user material subroutine (UMAT) enables data exchange with ABAQUS through an interface with the main ABAQUS solver. In the input file, the keyword * USER MATERIAL * is used to indicate the definition of user material subroutine [5].

The UMAT has powerful capabilities:

- It is possible to define the intrinsic relationships of materials.
- It is possible to calculate with materials that are not included in the ABAQUS material library.
- It can be used for almost any procedure of mechanical behavior.

The Jacobian matrix of the material intrinsic model must be provided in UMAT, i.e., the rate of change of stress increments to strain increments. By using the given guide of UMAT, we have implemented:

- Definition and separation of oxide and metal layers.
- Material properties of oxide and metal layers that has to be defined.
- Simulation of the full process of oxidation, including temperature increase, isothermal conditions and decrease.
- Addition of different strains such as elastic stain, thermal strain, viscoplastic strain, growth strain for the oxide, and elastic stain, thermal strain, viscoplastic strain, in addition to diffusion strain for the metal.

These aspects will be further detailed.

## 5.2 The numerical modeling construction

In this section, the objective is to establish a numerical modeling based on the full thermomechanical modeling proposed in section 4.3.1. The whole process of numerical modeling construction is shown in this section, which includes design of the simulation geometry, determination of simulation step, comparison of different meshes and discussion about the influence of different components and parameters.

In order to have preliminary results, the input parameters related to the materials given in Table 5.1 are used, which corresponds to the oxidation of NiCr at 900 °C for 10 h. These parameters can be found in [6, 7] or are obtained by experimental results, which may be different from the parameters used for the final simulation. However, as the preliminary simulation, it is sufficient to draw some conclusions about the simulation and guide the further advanced simulations.

Table 5.1. Input parameters for tests

| $Ap$ $(mm\,s^{-1/2})$ | $E_{ox}$ $(MPa)$ | $\nu_{ox}$ | $K_{ox}$ $(MPa\,s^{1/Nox})$ | $N_{ox}$ | $\alpha_{ox}$ $(K^{-1})$ | $[Cr]_0$ | $D$ $(mm^2 s^{-1})$ |
|---|---|---|---|---|---|---|---|
| 1.76E-4 | 215000 | 0.29 | 1.67E10 | 1 | 7.11E-5 | 0.345 | 4.09E-11 |
| $D_{ox}$ $(mm^{-1})$ | $E_m$ $(MPa)$ | $\nu_m$ | $K_m$ $(MPa\,s^{1/Nm})$ | $N_m$ | $\alpha_m$ $(K^{-1})$ | Η | |
| 0.54576 | 165000 | 0.3 | 1.5E3 | 4.1 | 1.96E-4 | -1.18E-02 | |

In this table, $Ap$ is the kinetics coefficient of the global chemical oxidation reaction; $E_{ox}$ corresponds to the Young's modulus of oxide layer; $\nu_{ox}$ is the Poisson's ratio of oxide layer; $K_{ox}$ and $N_{ox}$ correspond to the viscoplastic parameters of oxide layer; $\alpha_{ox}$ is the thermal expansion coefficient of oxide layer; $D_{ox}$ corresponds to the growth strain parameter; $E_m$ and $\nu_m$ are the Young's modulus and the Poisson's ratio of metal layer; $K_m$ and $N_m$ are the viscoplastic parameters of metal layer; $\alpha_m$ corresponds to thermal expansion coefficient of metal layer; $[Cr]_0$ is the initial weight percentages concentration of element Cr; η corresponds to a constant coefficient coupling the chromium concentration profiles to the diffusion strain and $D$ is the diffusion coefficient of chromium in NiCr.

## 5.2.1 System geometry and mesh

### 5.2.1.1 System geometry

The geometry established is a three layers model, which contains an air layer, an oxide layer and a metal layer as shown in Fig. 5.3.

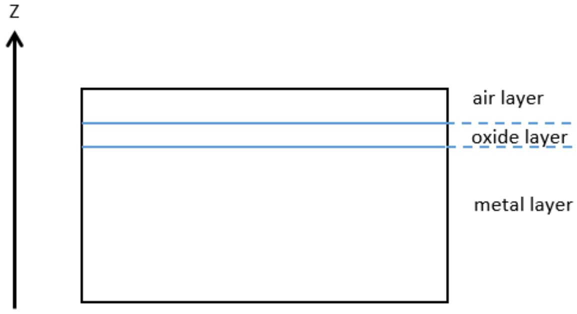

Figure 5.3 Illustration of geometry for the simulations

As discussed in section 1.2.3.2, the oxide/metal geometry is supposed to have symmetrical oxidation of the two metallic sides. By applying a symmetry boundary condition at neutral plane, the simulation geometry is advantageously simplified. Therefore, only half of the system is considered for simulation, from top surface to the neutral plane. Moreover, an air layer is added, because of the outward growth of oxide layer. It is necessary to add because if not, there will be no predefined space for the growth of the oxide layer, which could not be simulated otherwise. The quantities are set to be zero for the air layer, which will not affect the stress calculation for the oxide and metal layers. The simulation geometry is determine at the beginning of the process, including the mesh type, the element number, the node number etc., which cannot be modified during the simulation. As previously written, the stresses and strains in the air layer will always be under control as 0 during the simulation. At the initial time of simulation, the thickness of oxide layer is 1 nm in order to start from a non-zero value. The layer distinction between the different chemical phases is eventually controlled by the coordinates (COORDS) of each element in order to attribute specific behaviour or properties to each chemical phase.

The chosen general geometry is a rectangular cuboid, which is 0.6x0.6x0.25 mm$^3$, as shown in Fig. 5.4. The depth that interests us is at the micro scale (less than 100 µm), especially to investigate the spatial heterogeneity. The simulation results will be especially compared to the experimental results obtained in section 4.1.2.2. Knowing that the sample shape is 6x6x0.4 mm, in order to avoid overmuch elements, a 160 times smaller model is considered. Moreover, the stress that interests us is along axis Z and the geometry is symmetrical with respect to neutral plane. Thus, the interesting thickness of simulation geometry is reduced to 0.25 mm.

- Boundary conditions

Free boundary conditions are applied to the top surface and lateral surfaces to this geometry and the XY plane symmetry boundary condition is applied to the bottom surface. An analytical path is created along axis Z at the center of this geometry, which will be used to plot the depth-dependent stress.

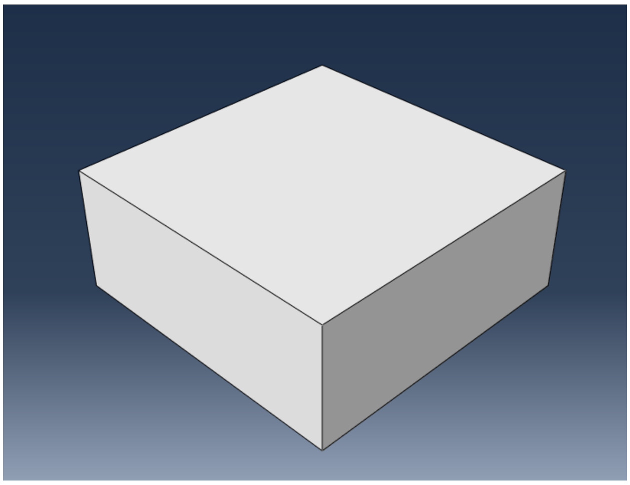

Figure 5.4 Simulation geometry

### 5.2.1.2 Thermal loading and evolution with three temperature phases

Phase means here for a time domain variation for temperature, which is a time period that corresponds to the different temperature conditions.

To have more realistic conditions of high temperature oxidation of our samples, different temperature phases were defined and created in the UMAT, which are respectively temperature increase, isothermal oxidation and temperature decrease shown in Fig. 5.5.

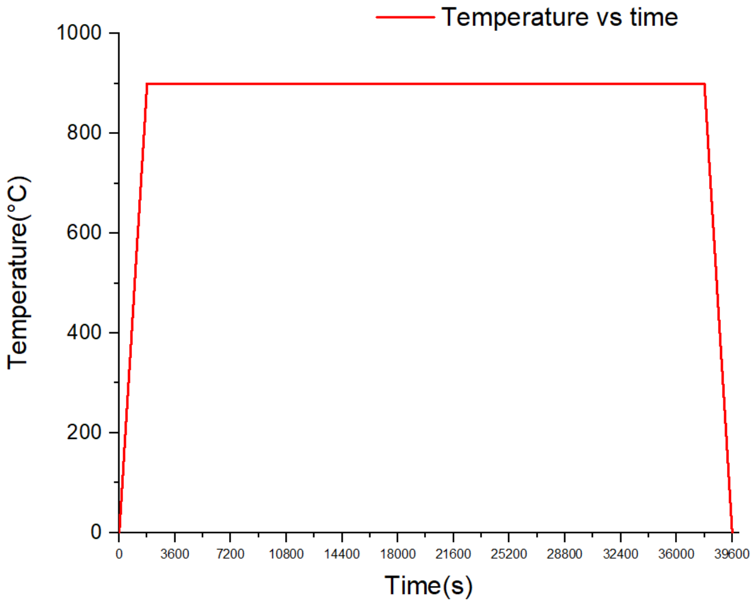

Figure 5.5 Temperature vs time

As shown in Fig. 5.5, there are three temperature phases for oxidation at 900°C for 10h. As proposed in section 4.3.1, the different strains in this system may include: ${\varepsilon^{elastic}}_{m}, {\varepsilon^{viscoplastic}}_{m}, {\varepsilon^{thermal}}_{m}, {\varepsilon^{diffusion}}_{m}, {\varepsilon^{elastic}}_{ox}, {\varepsilon^{viscoplastic}}_{ox}, {\varepsilon^{thermal}}_{ox}\ and\ {\varepsilon^{growth}}_{ox}$. The indices "ox" and "m" refer to the oxide layer and the metal layer respectively. The calculation requires considering systematically elastic strain to relate to the stress through Hooke’s model.

**Phase one - temperature increase**

The time period is from 0 to 1800 s, during which the temperature goes from 25 to 900 Celsius degrees during 30 minutes.

In the phase one, the thermal strain and elastic strain are mainly concerned and the other strains are not concerned.  We assumed that during this temperature increase phase, there are no viscoplastic strain, diffusion strain, and growth strain. Compared to the isothermal phase, these strains are negligible because duration of temperature increase phase is relatively short compared to the isothermal phase and the oxide growth is mainly developing during the isothermal phase. The viscoplastic strain is more significant at high temperature. Thus, for the temperature increase phase, these strains are not considered, which is the same for the temperature decrease phase.

This phase is divided into 10 time steps. Each time step is Δt = 180 s and temperature rises ΔT = 87.5 Celsius degrees per time step. The phase time, step time, Δt and ΔT are programmed in the input file for ABAQUS.

**Phase two - constant temperature at 900°C**

The time period is from 1800 s to 37800 s. The temperature is maintained at 900 Celsius degrees for 10h. During the simulation, the viscoplastic strain, diffusion strain, growth strain and elastic strain may be considered. The thermal strain is not considered because of the isothermal condition of phase two.

This phase is divided into 60 time steps. Each time step is Δt = 600 s and temperature remains at 900 Celsius degrees. In this phase, the growth of the oxide layer is concerned. As proposed in Eq. 1.10, it is calculated by means of the kinetics coefficient Ap and the oxidation time t. The kinetics coefficient Ap is given in UMAT file and the oxidation time t is related to the phase time and step time.

**Phase three - temperature decrease**

The period is from 37800 s to 39600 s. During which, the temperature goes from 900 to 25 Celsius degrees in 30 minutes. In phase three, the thermal strain and elastic strain are concerned and the other strains are not concerned. As the temperature decreases, there is no growth of oxide layer because of the protection of oxide layer. The decreasing of temperature also cause the lack of activation energy for viscoplastic and diffusion phenomena. We assume thus that during the temperature decrease phase, there are no viscoplastic strain, diffusion strain, and growth strain. It is divided in 20 time steps. Each step is Δt = 90 s and temperature rises ΔT = -43.75 Celsius degrees per time step.

The Flowchart of UMAT implementation can be found in APPENDICE 3.

### 5.2.1.3 Fine mesh and rough mesh

For the mesh, two kinds of mesh are tested (as shown in Fig. 5.6 and Fig. 5.7).

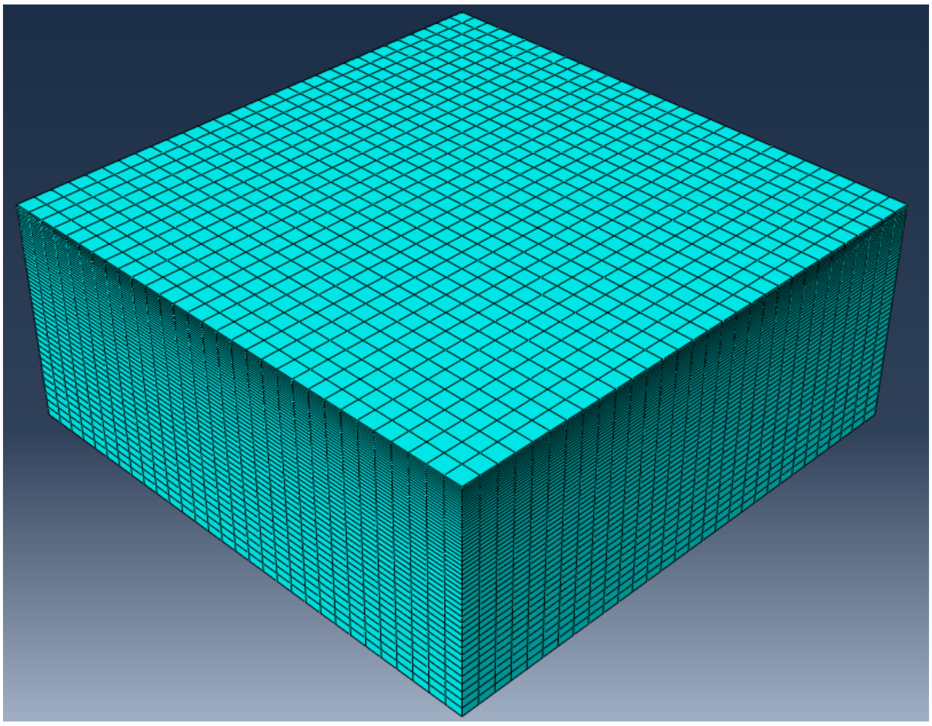

Figure 5.6 Rough mesh

As shown in Fig. 5.6, the element number is 30*30*50. The total number of elements is thus 45000. In addition, for the elements along z direction, the elements at bottom surface are 5 times thicker than the elements at top surface. Refinement of the mesh is required in order to adapt to the thickness of oxide layer (thickness of the metal is around 200 µm, whereas the oxide thickness is less than 2 µm). The total number of nodes is 49011. The element type is C3D8R, which is a 8-node hexahedral linear reduced integration element. Compared to the full integration element, the linear reduced integration element contains only one integration point at the center of the element. The linear reduced integration element has the following advantages [8]:

(1) The shear self-locking phenomenon is relatively difficult to occur under the bending load.

(2) The results of the displacement solution are more accurate.

(3) The accuracy of the analysis is not greatly affected when the mesh is deformed.

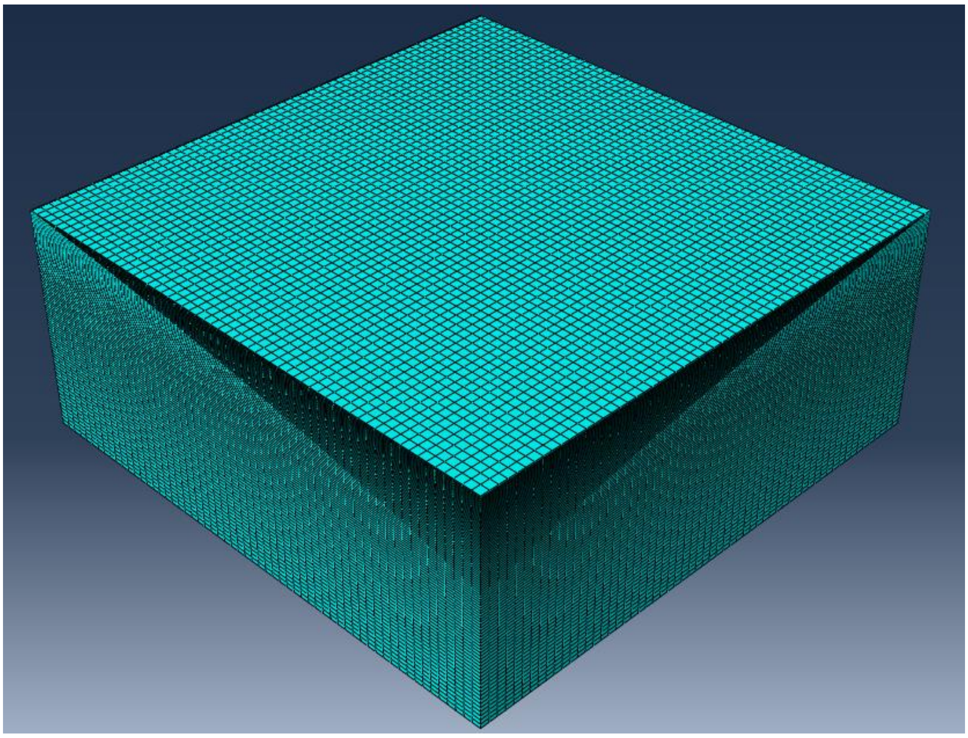

Figure 5.7 Fine mesh

As shown in Fig. 5.7, the elements number for the fine mesh is 8 times than the number for the rough mesh. The element number is 60*60*100. The total number of elements is thus 360000. Meanwhile, for the elements along z direction, the elements at bottom surface are 5 times thicker than the elements at top surface. The total number of nodes is 375821. The element type is also linear hexahedral elements C3D8R with the same kind of advantages as previously described.

In order to compare the effect of the 2 different meshes, all the other parameters are the same for the simulations in this section and all the strain contributions are considered to see the global influence of the mesh $\varepsilon^{elastic}{}_{m}, \varepsilon^{viscoplastic}{}_{m}, \varepsilon^{thermal}{}_{m}, \varepsilon^{diffusion}{}_{m}, \varepsilon^{elastic}{}_{ox}, \varepsilon^{viscoplastic}{}_{ox}, \varepsilon^{thermal}{}_{ox}$ $and\ \varepsilon^{growth}{}_{ox}$ .

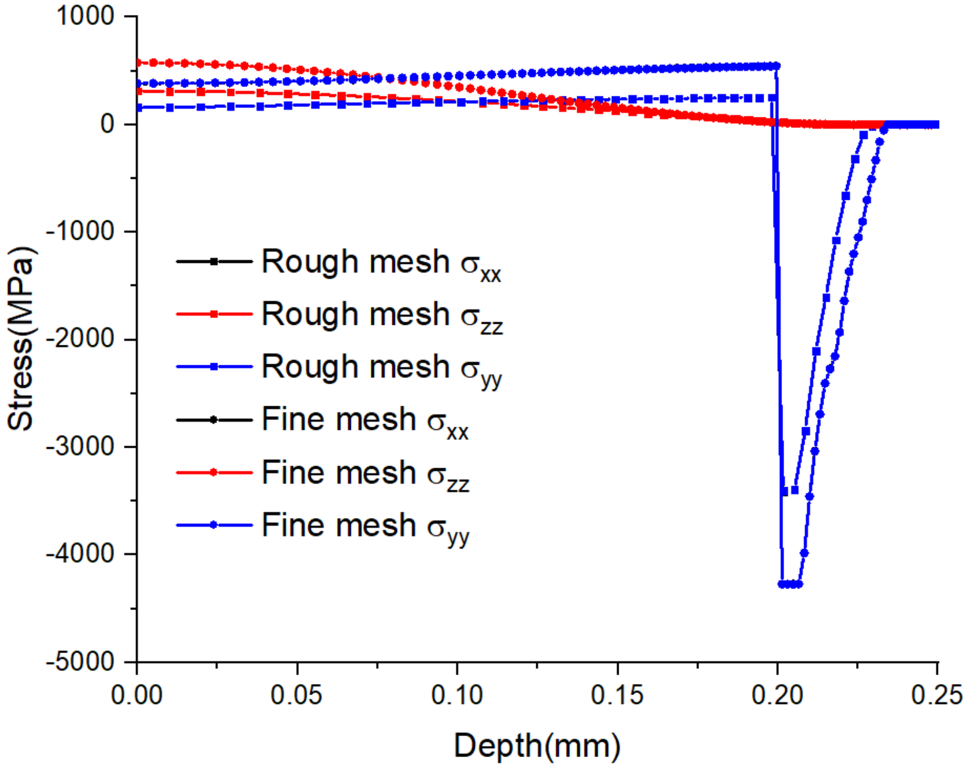

Figure 5.8 Stress distribution at the end of phase 2 for the different stress components for the 2 meshes ($\sigma_{xx}$ and $\sigma_{yy}$ are overlapped whatever the mesh is)

As shown in Fig. 5.8, the results of stress distribution at the end of phase 2 is chosen to compare the differences between the fine mesh and rough mesh. The metal layer is from 0 mm to 0.2 mm. The oxide layer and the air layer is from 0.2 mm to 0.25 mm. The results chosen to plot are along the center path as defined at page 9. In addition, there are 50 points along the center path for rough mesh and 100 points for fine mesh.

It is shown that the stress in the oxide layer is in compression and in the metal layer the stress is in tension. For both rough mesh and fine mesh, $\sigma_{xx}$ and $\sigma_{yy}$ are very close, which shows that the simulation leads to an isotropic mechanical state as expected for the considered parameters. Considering the absolute values of stress, the stress for fine mesh is higher than for rough mesh in both metal layer and oxide layer for all stress components. For the $\sigma_{xx}$ $and$ $\sigma_{yy}$, the discontinuity is obvious at the interface oxide/metal, whatever the mesh is. However, the $\sigma_{zz}$ does not have a jump at the interface metal/oxide, which shows a continuity stress at the interface for this component.

Table 5.2. The maximum stresses in the metal layer

| | Rough mesh | | Fine mesh | |
|---|---|---|---|---|
| | Value(MPa) | Location | Value(MPa) | Location |
| $\sigma_{xx}$ | 254 | Metal/oxide interface | 545 | Metal/oxide interface |
| $\sigma_{yy}$ | 254 | Metal/oxide interface | 543 | Metal/oxide interface |
| $\sigma_{zz}$ | 312 | Neutral plane of metal layer | 575 | Neutral plane of metal layer |

Table 5.3. The extremum stresses in the oxide layer

| | Rough mesh | | Fine mesh | |
|---|---|---|---|---|
| | Value(MPa) | Location | Value(MPa) | Location |
| $\sigma_{xx}$ | -3409 | Metal/oxide interface | -4273 | Metal/oxide interface |
| $\sigma_{yy}$ | -3398 | Metal/oxide interface | -4274 | Metal/oxide interface |
| $\sigma_{zz}$ | 22 | Metal/oxide interface | 18 | Metal/oxide interface |

According to the results presented in Table 5.2 and 5.3, the fine mesh improves 2 times the error precision for the 3 components, which causes a 115% increase of the maximum stress in the metal layer and a 25% increase of the extremum stress in the oxide layer for in-plane stresses. As expected, the quality of mesh has a significant influence on the stress values. However, it does not change the trend. Therefore, the geometry with fine mesh is now systematically chosen for the next simulations.

### 5.2.2 Contribution of the different strains

In this section, the objective is to ensure that in our simulation works for all the proposed strains and to try to understand the influence of the different contributions to the strain on the results.

#### 5.2.2.1 Elastic strain + thermal strain

In this simulation, the contributions of strain include: the elastic strain of metal layer ${\varepsilon^{elastic}}_{m}$, the elastic strain of oxide layer ${\varepsilon^{elastic}}_{ox}$, the thermal strain of metal layer ${\varepsilon^{thermal}}_{m}$, the thermal strain of oxide layer ${\varepsilon^{thermal}}_{ox}$. We basically starts with elastic and thermal contributions to see their influence, for a constant thickness layer. The other strain contributions are not considered, such as ${\varepsilon^{viscoplastic}}_{m}$, ${\varepsilon^{diffusion}}_{m}$, ${\varepsilon^{viscoplastic}}_{ox}$ $and$ ${\varepsilon^{growth}}_{ox}$

We focus on the results along the center path, as defined at page 9.

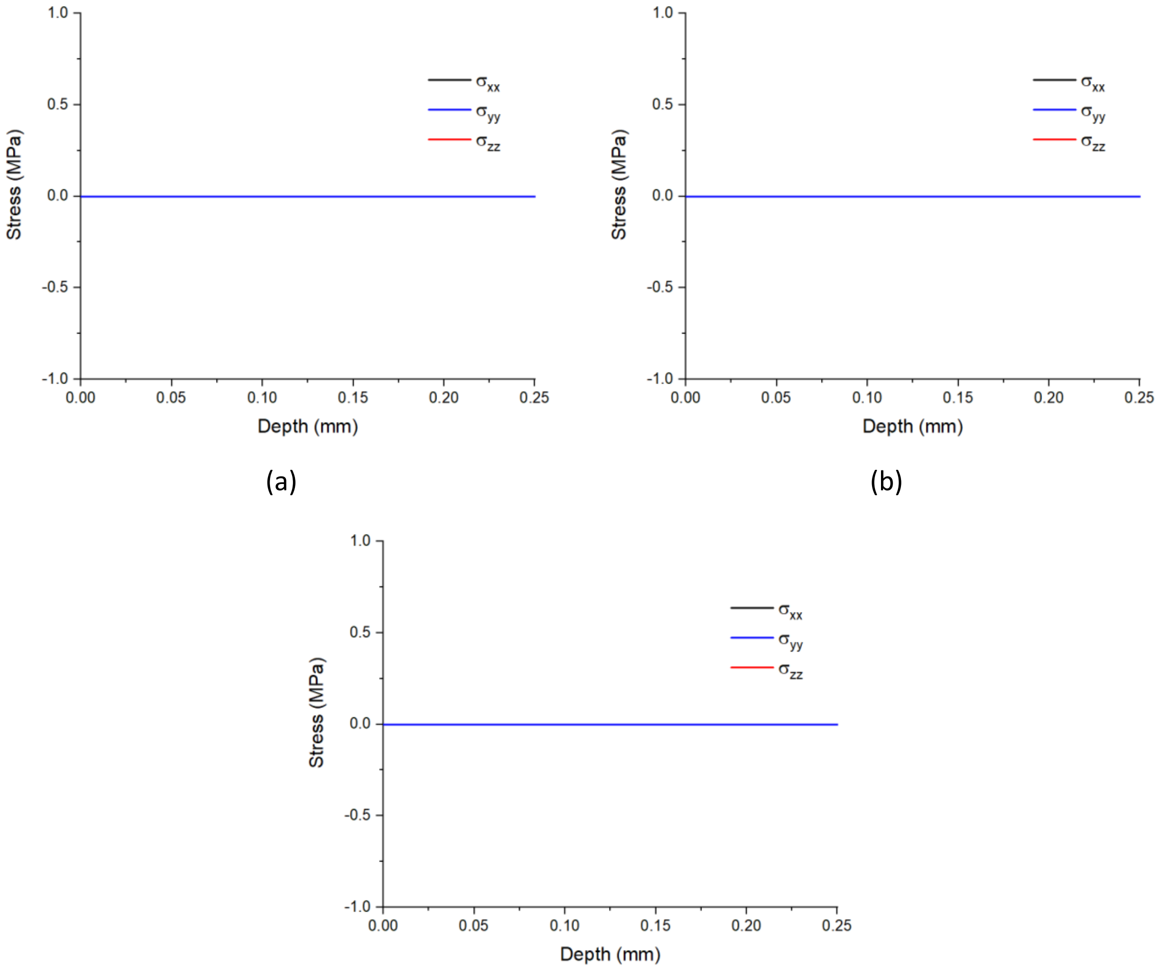

(a)

(b)

(c)

Figure 5.9 The distribution of stress components at the end of phase 1 (a), at the end of phase 2 (b), and at the end of phase 3 (c)

Fig. 5.9 shows that the stress in this system is 0 MPa whatever the phases are. Because in this simulation, the growth of the oxide layer is not considered, then the thickness of oxide layer is always 1 nm. As a consequence, the thickness of oxide layer is not sufficient to generate thermal strain and a corresponding stress. The thermal strain will be important only if the thickness of oxide layer is large enough. Moreover, the growth strain is not taken into account. Both drive stress contributions are absent or negligible that explains the so weak value for the stress.

### 5.2.2.2 Elastic strain + thermal strain + growth strain

In this simulation, the contributions of strain include: the elastic strain of metal layer ${\varepsilon^{elastic}}_{m}$, the elastic strain of oxide layer ${\varepsilon^{elastic}}_{ox}$, the thermal strain of metal layer ${\varepsilon^{thermal}}_{m}$, the thermal strain of oxide layer ${\varepsilon^{thermal}}_{ox}$, and now the growth strain in the oxide layer ${\varepsilon^{growth}}_{ox}$ to see its influence.

The stress-field nephogram is shown in Fig. 5.10.

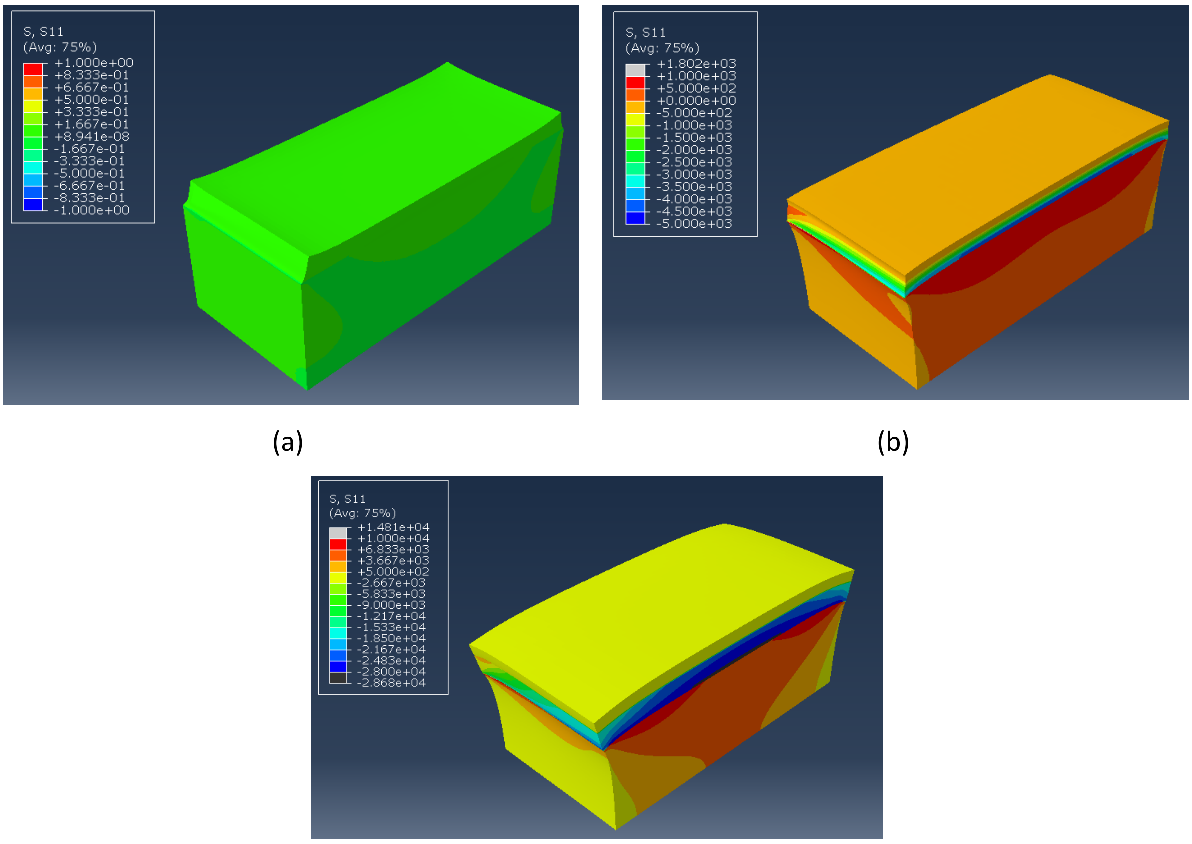

(a)

(b)

(c)

Figure 5.10 Stress-field nephogram at the end of phase 1 (a), at the end of phase 2 (b), and at the end of phase 3 (c)

Fig. 5.10 shows, at the end of phase 1, that the stress in the simulation is almost 0 MPa. At the end of phase 2, there is a stress variation along axis z. Generally, the stress is positive in the metal layer and the stress is negative in the oxide layer. At the end of phase 2 (Fig. 5.10 (b)) and phase 3 (Fig. 5.10(c)), the stress-field nephograms show that the color in the metal layer is manly orange and yellow, which means positive stresses and the color in the oxide layer is mainly blue and green, which means negative stresses. In addition, there is a deflection because of the stresses. However, there is no more oxide growth in phase 3 and the stress in air layer is 0 MPa. Therefore, in terms of stress values in the oxide layer and metal layer, the simulation seems to be quite accurate during the different temperature phases.

The stress vs. depth curve is plotted in Fig. 5.11 along the center path, as defined at page 9.

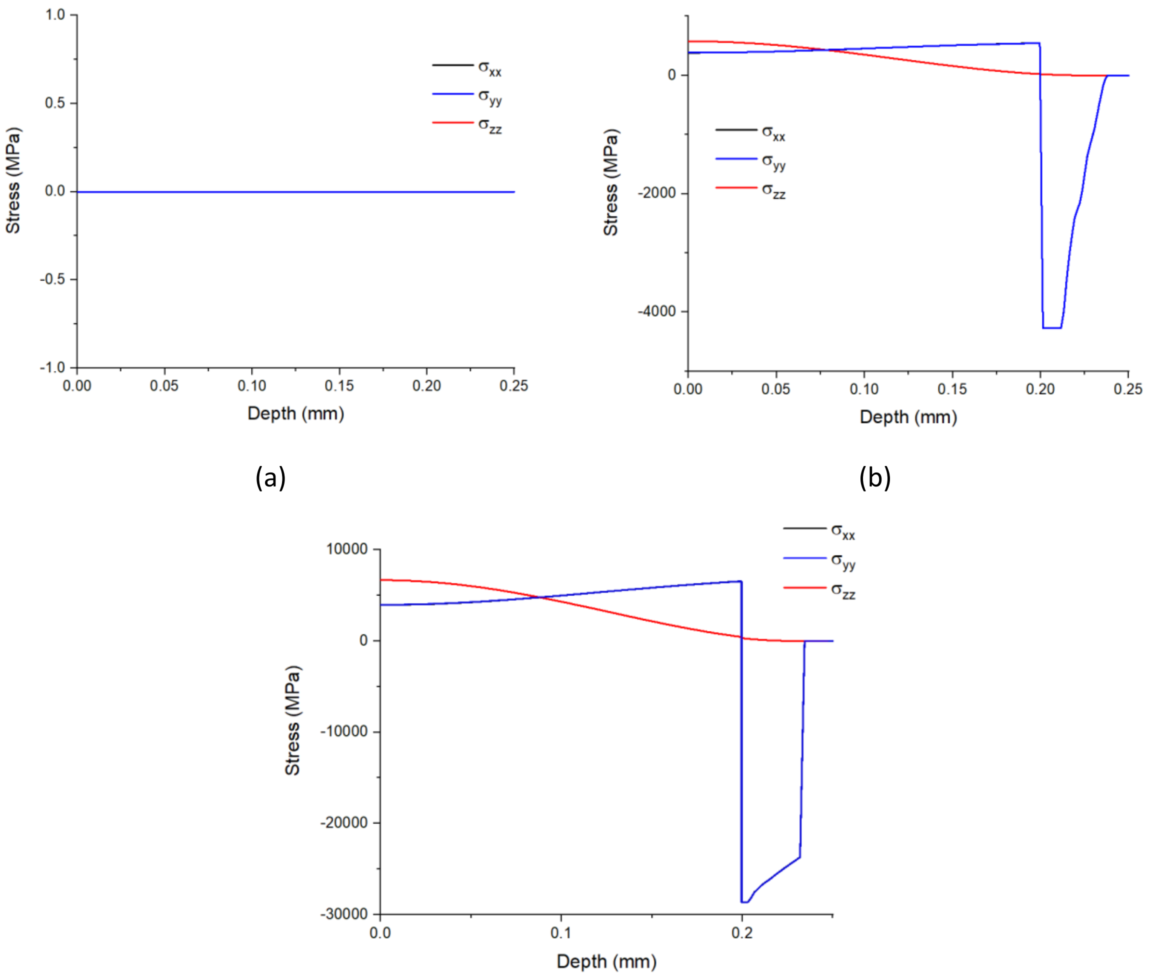

(a)

(b)

(c)

Figure 5.11 The distribution of stress components at the end of phase 1 (a), at the end of phase 2 (b), and at the end of phase 3 (c)

Fig. 5.11 confirms, at the end of phase 1, that the stress in the sample is almost 0 MPa, because for this first phase, the growth of the oxide layer is not considered. The given oxide thickness 1 nm is not sufficient to generate thermal strain and a corresponding stress. The $\sigma_{xx}$ and $\sigma_{yy}$ are very close for all the time, which is consistent with isotropy of the mechanical state. The stress distribution is mainly divided into 3 parts. The metal layer is from 0 mm to 0.2 mm, for which stress is positive. The stress distribution in the metal layer shows that the maximum value appears at the metal/oxide interface and it decrease via the neutral plan. The oxide layer is from 0.2 mm to the oxide/air surface, for which stress is negative. The third part is the stress in air layer, for which it is 0. The comparison of stress values is presented in Table 5.4 and Table 5.5.

Table 5.4. The maximum stress in the metal layer

| | At the end of phase 2 | | At the end of phase 3 | |
|---|---|---|---|---|
| | Value(MPa) | Location | Value(MPa) | Location |
| $\sigma_{xx}$ | 542 | Metal/oxide interface | 6539 | Metal/oxide interface |
| $\sigma_{yy}$ | 542 | Metal/oxide interface | 6539 | Metal/oxide interface |
| $\sigma_{zz}$ | 575 | Neutral plane of metal layer | 1516 | Neutral plane of metal layer |

Table 5.5. The extremum stress in the oxide layer

| | At the end of phase 2 | | At the end of phase 3 | |
|---|---|---|---|---|
| | Value(MPa) | Location | Value(MPa) | Location |
| $\sigma_{xx}$ | -4275 | Metal/oxide interface | -28682 | Metal/oxide interface |
| $\sigma_{yy}$ | -4275 | Metal/oxide interface | -28682 | Metal/oxide interface |
| $\sigma_{zz}$ | 18 | Metal/oxide interface | 397 | Metal/oxide interface |

Considering the absolute value of stress, the stresses for all components are much higher at the end of phase 3 than at the end of phase 2. For the $\sigma_{xx}$ and $\sigma_{yy}$, the maximum absolute values appear at the oxide/metal interface where it was expected. There are two main sources of driven stresses: growth stress due to the growth of the oxide; thermal stress due to mismatch between the different thermal expansion coefficients between the oxide and the metal substrate when the temperature changes. The mismatch occurs at the interface, which will theoretically cause a concentration of stress at the oxide/metal interface. The stress caused by thermal strain in phase 3 is well occurring in the results. Because of adding thermal strain in phase 3, the stress at the end of phase 3 is much higher than the stress at the end of phase 2. However, the value of stress is too high, which seems incorrect. In real systems, during the phase 2 and the beginning of phase 3 for high temperature values, there would still be viscoplastic strain. But in the simulation of this section, we proposed that there is no viscoplastic strain, which may cause this too important stress value. Another reason is the inappropriate value of $Ap$, which is the kinetics coefficient of the global chemical oxidation reaction. As shown in table 2.2, the value of $Ap$ is bigger than ours for some other studies for similar materials at the same temperature, for example in article [6], which causes a thicker oxide layer. Therefore, in phase 3, when we simulate the thermal stress during the cooling process, it gives us a much higher thermal stress. However, as the preliminary results, it shows that the thermal strain and growth strain mechanisms are well operated in UMAT.

### 5.2.2.3 Elastic strain + thermal strain + growth strain + viscoplastic strain

In this case, the viscoplastic strain for oxide layer $\varepsilon^{viscoplastic}{}_{ox}$ and metal layer $\varepsilon^{viscoplastic}{}_{m}$ are added, compared to the section 5.2.2.2. The idea is now to understand its influence on the results. We expect for relaxation of the stress through this mechanism. The stress-field nephogram is quite similar with the case before, and is not shown here. Along the center path, the stress distribution curve is plotted.

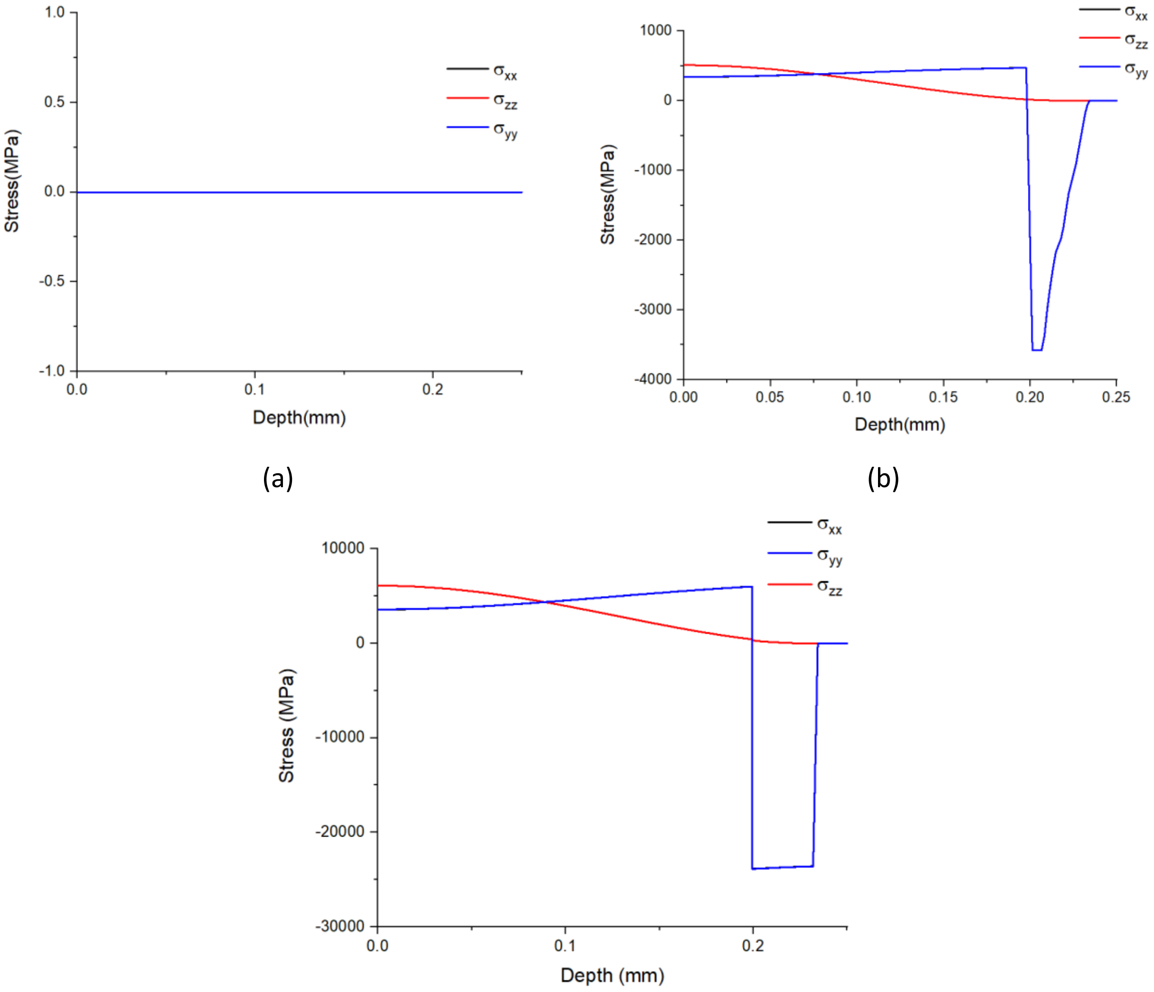

(a) (b)

(c)

Figure 5.12 The distribution of stress components at the end of phase 1 (a), at the end of phase 2 (b), and at the end of phase 3 (c)

The stress distribution as a function of depth is very similar to the case before adding viscoplastic strain. In order to investigate the effect of adding the viscoplastic strain, the stress values are shown in Table 5.6 and Table 5.7. The presented values in these tables are the results at end of phase 2 for comparison with or without viscoplastic strain.

Table 5.6. The maximum stress in the metal layer

| | Before adding viscoplastic strain | | After adding viscoplastic strain | |
|---|---|---|---|---|
| | Value(MPa) | Location | Value(MPa) | Location |
| $\sigma_{xx}$ | 542 | Metal/oxide interface | 473 | Metal/oxide interface |
| $\sigma_{yy}$ | 542 | Metal/oxide interface | 472 | Metal/oxide interface |
| $\sigma_{zz}$ | 575 | Neutral plane of metal layer | 512 | Neutral plane of metal layer |

Table 5.7. The extremum stress in the oxide layer

| | Before adding viscoplastic strain | | After adding viscoplastic strain | |
|---|---|---|---|---|
| | Value(MPa) | Location | Value(MPa) | Location |
| $\sigma_{xx}$ | -4275 | Metal/oxide interface | -3582 | Metal/oxide interface |
| $\sigma_{yy}$ | -4275 | Metal/oxide interface | -3583 | Metal/oxide interface |
| $\sigma_{zz}$ | 18 | Metal/oxide interface | 15 | Metal/oxide interface |

By adding viscoplastic strain, the maximum stress in the metal layer decrease of 13% and the maximum absolute stress in the oxide layer decrease of 16% for in-plane stresses, compared to the case without viscoplasticity. The stress is relaxed during the phase 2. The curve of stress vs. time can also be plotted.

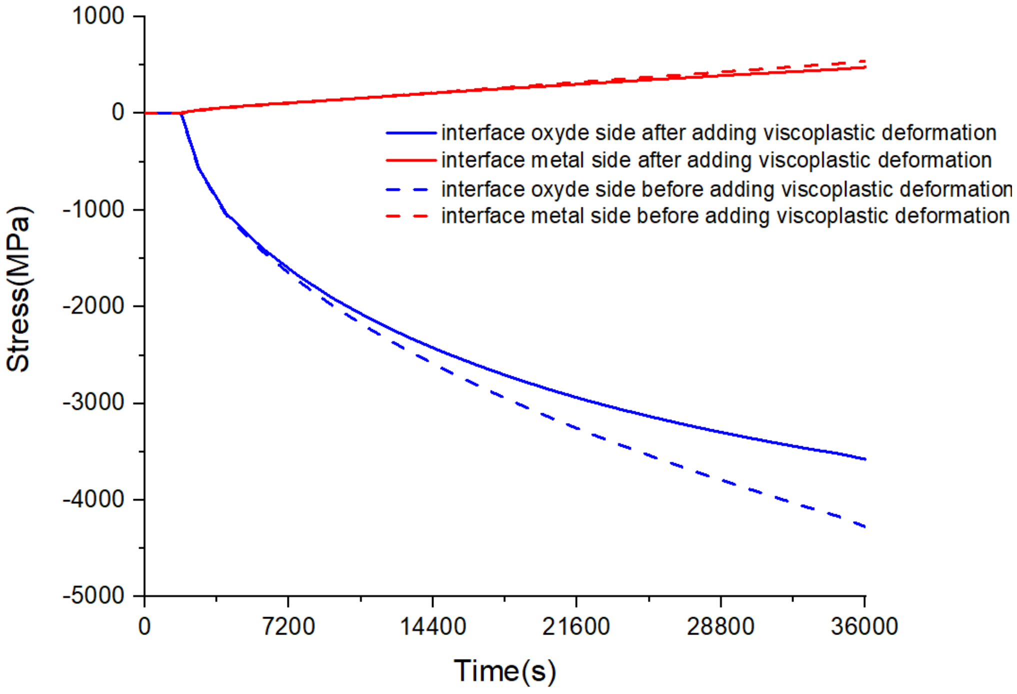

Figure 5.13 Stress $\sigma_{xx}$ vs. time curve during phase 2

Fig. 5.13 shows that the stress has a significant relaxation after adding the viscoplastic strain in phase 2, as expected. However, the stress relaxation does not a priori look like other existing studies [6, 7], because we ought to expect to have a decrease toward 0 (in absolute value) at the end of the oxidation. Consequently, we can question the values of the viscoplastic parameters. The $K_{ox}$ is equal to 16.7*10$^9$$Pa\ s^{1/N_{ox}}$ with $N_{ox}$= 1. By modifying the viscoplastic parameter $K_{ox}$ for oxide layer, the different stress vs. time curves are now plotted in Fig. 5.14 showing how it influences the calculation.

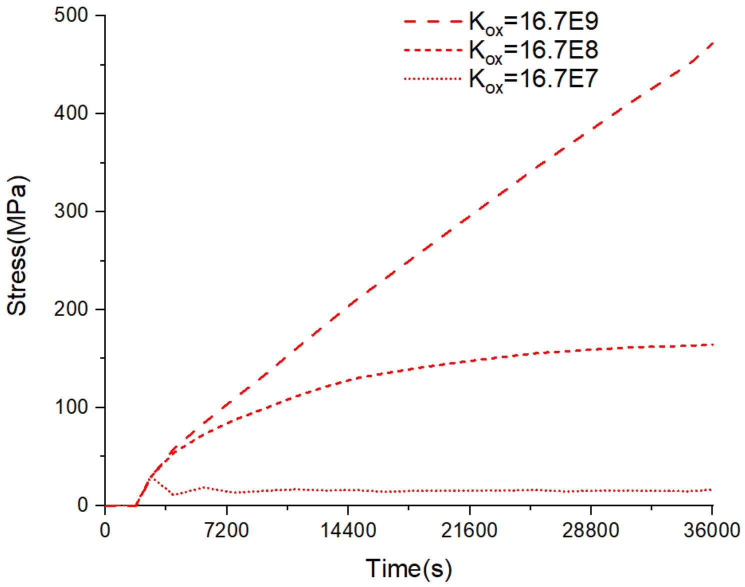

Figure 5.14 a Stress $\sigma_{xx}$ vs. time curve of metal layer during phase 2

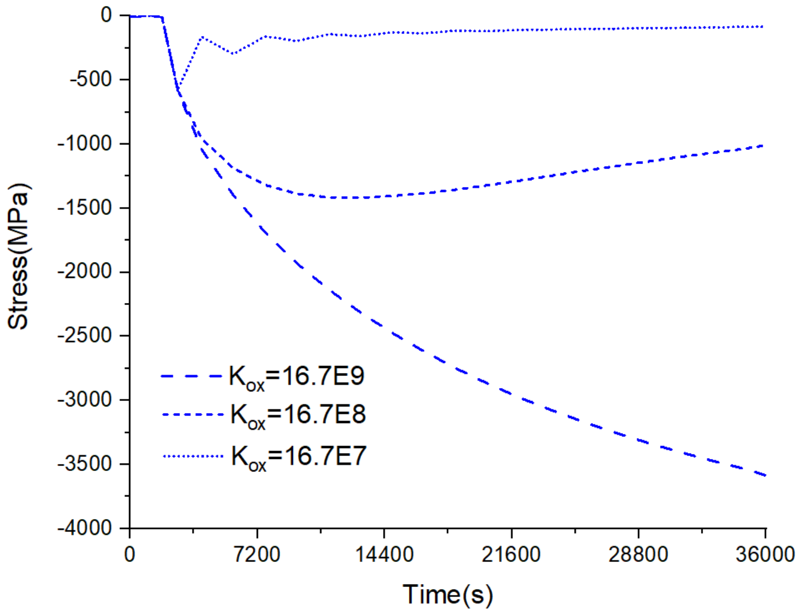

Figure 5.14 b Stress $\sigma_{xx}$ vs. time curve of oxide layer during phase 2

Fig. 5.14 shows that by modifying the value of the viscoplastic parameter $K_{ox}$ for oxide layer, the stress relaxation changes a lot during the phase 2. Knowing that the phase 2 is an isothermal phase, there is no thermal strain in this phase. The stresses shown in Fig. 5.17 and Fig. 5.18 are only the results of the combination effect of growth strain and viscoplastic strain. Growth strain leads to an increase of stress and viscoplastic strain leads to stress relaxation. It is clear for oxide layer and in very good agreement with the results of [6, 7].

For K = 16.7*$10^7$ $Pa\ s^{1/N_m}$ with $N_{ox}$= 1, it is well evidenced the combination and quick rebalance between the effect of growth strain and viscoplastic strain. However, these oscillations may be caused by the size of the time step, which may be  not reliable from a physical point of view.

### 5.2.2.4 Elastic strain + thermal strain + growth strain + viscoplastic strain + diffusion strain

In this case, the diffusion strain $\varepsilon^{diffusion}{}_{m}$ is added in order to improve the thermomechanical modelling according to the suggestions, which has been proposed in section 4.3.1. The stress-field nephogram is not shown here and only the stress spatial distribution curves are plotted.

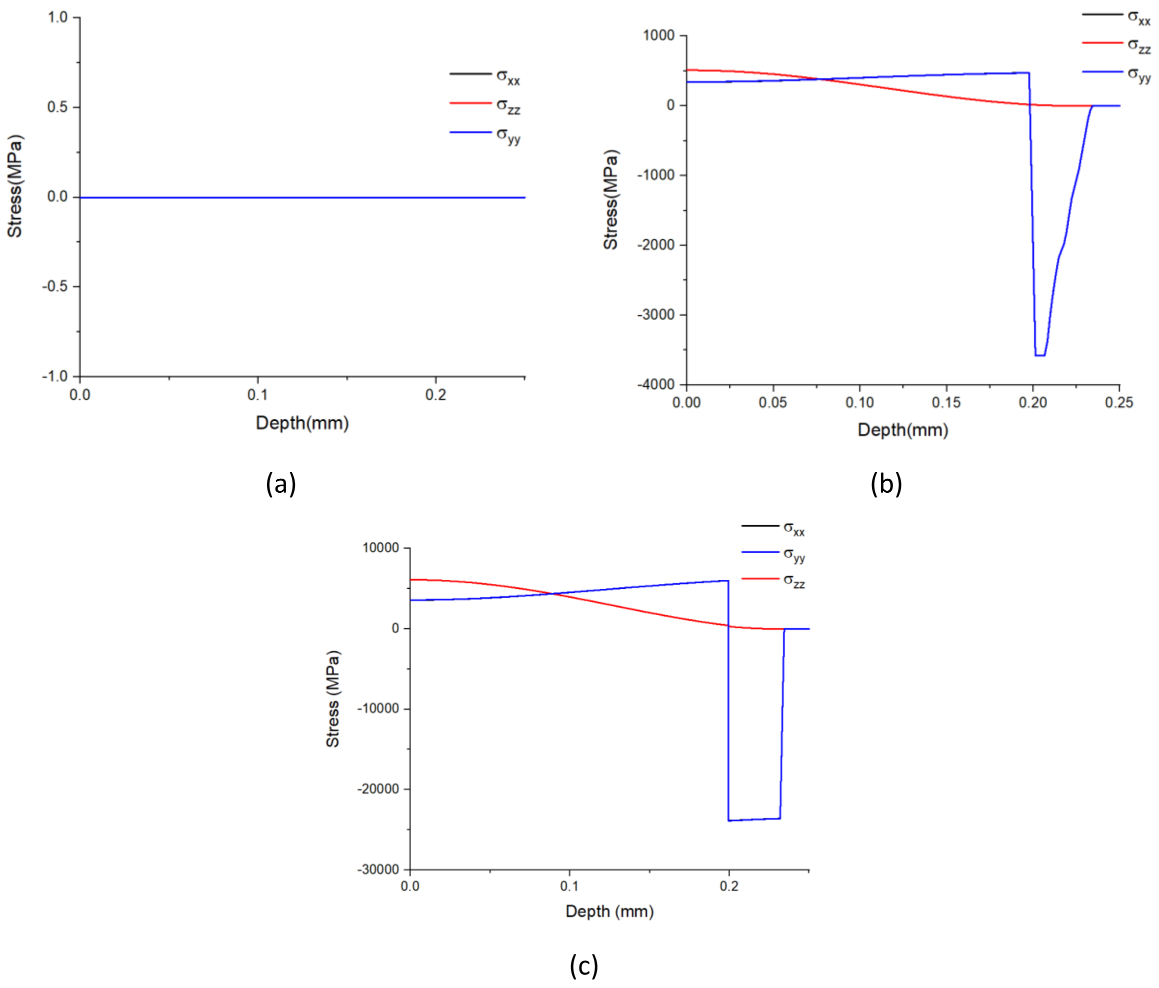

(a) (b)

(c)

Figure 5.15 The distribution of stress components at the end of phase 1 (a), at the end of phase 2 (b), and at the end of phase 3 (c)

As shown in Fig. 5.15 the tendency before adding diffusion strain and after adding diffusion strain are quite similar. To compare more deeply the influence of adding diffusion strain, the stress distribution for $\sigma_{xx}$ at the end of phase 2 is plotted along the axis Z at the center of the geometry.

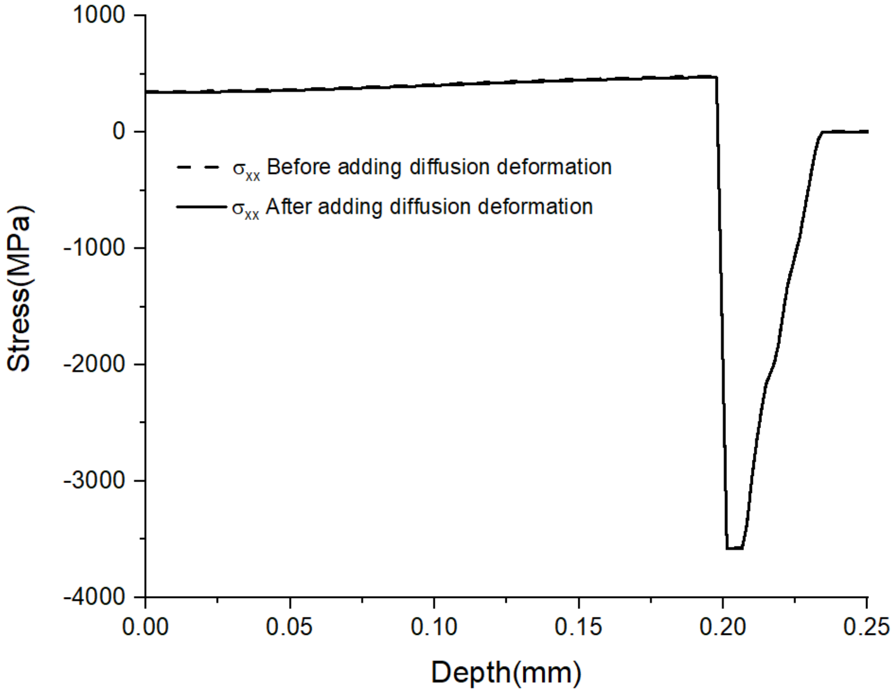

Figure 5.16 Stress distribution for $\sigma_{xx}$ at the end of phase 2

As shown in Fig. 5.16, the stress distribution for $\sigma_{xx}$ at the end of phase 2 of case before adding diffusion strain (corresponding to the calculation of section 5.2.2.3 and case after adding diffusion strain are very close. However, the diffusion stress is proposed and discussed in section 4.2, which is calculated by a Matlab program from analytic formula. Its influence in the Finite Element modelling may present some differences that require more investigation.

In order to investigate the influence of this diffusion strain $\varepsilon^{diffusion}{}_{m}$ in the metal layer, several tests have been done by using a smaller geometry 0.02*0.02*0.02 mm and finer mesh under an isothermal oxidation condition for the following behaviors:

- Only considering the diffusion strain $\varepsilon^{diffusion}{}_{m}$ in the metal layer
- Only considering the growth strain $\varepsilon^{growth}{}_{ox}$ in the oxide layer
- Considering both the diffusion strain $\varepsilon^{diffusion}{}_{m}$ in the metal layer and the growth strain $\varepsilon^{growth}{}_{ox}$ in the oxide layer

The material parameters used are the parameters given in Table 5.1. A smaller geometry may enhanced the effect of diffusion at local scale and the comparison between the different sources of strain should enables to know their relative influences.

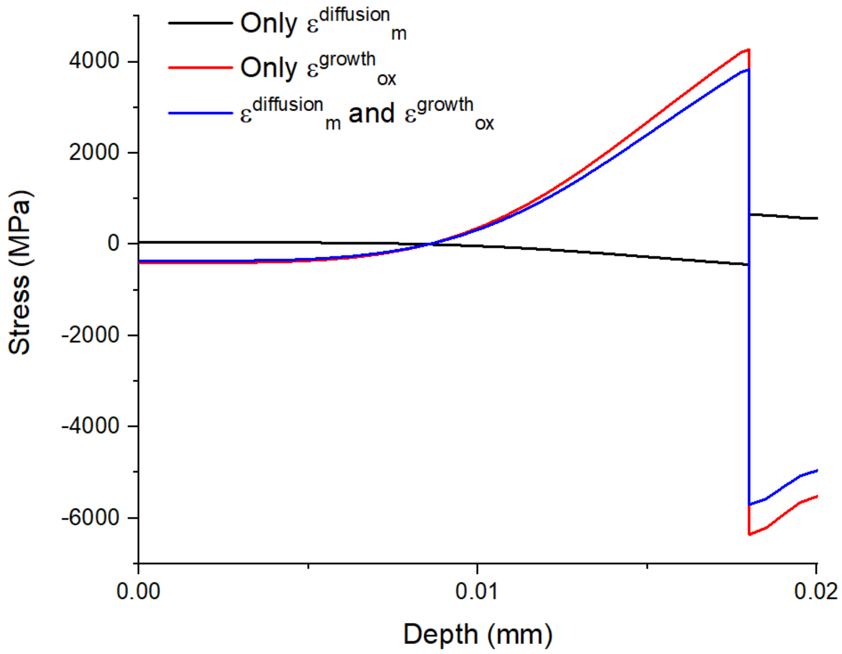

Figure 5.17 Investigation on the influence of the diffusion strain

The metal/oxide interface is at 0.018 mm. From 0 to 0.018 mm is now the metal layer and from 0.018 mm to 0.02 mm is the oxide layer. For the case considering only the diffusion strain $\varepsilon^{diffusion}{}_{m}$, Fig. 5.17 shows that there is indeed a spatial distribution of stresses, whatever the calculation is. In the metal layer, the stress is in compression -438 MPa and the stress is in tension 653 MPa in the oxide layer. The tension stress in the oxide layer is opposite to the stress in the metal, which is caused by the mechanical balance of the whole sample. The stress is discontinue at the metal/oxide interface. When only considering the diffusion strain, the stress spatial distribution can be seen from the simulation results, which is negative at the near surface zone and increases until a small positive value. This kind of stress spatial distribution is related to the diffusion strain, which has been discussed in chapter 4.

For the case considering only the growth strain $\varepsilon^{growth}{}_{ox}$, the stress in the metal layer is in tension 4268 MPa and the stress in the oxide layer is in compression -6360 MPa, which accords with the known stress in terms of sign [7, 9]. However, the stress value is too big, because the viscoplastic properties are not considered in this test.

For the case considering the diffusion strain $\varepsilon^{diffusion}{}_{m}$ and the growth strain $\varepsilon^{growth}{}_{ox}$, Fig. 5.17 shows that there is a difference with the case considering only the growth strain $\varepsilon^{growth}{}_{ox}$. The stress in the metal layer is smaller 3830 MPa and the stress in the oxide layer is -5707 MPa. By adding the diffusion strain, the stress value decreases, which corresponds to an addition of the distribution of the stress.

From these tests, we can conclude that it is hard to deconvolute the diffusion stresses directly in the metal layer. Comparing the red curve and blue curve, the difference is only about 500 MPa. Moreover, in this case, the viscoplastic strain is not considered. When the viscoplastic is considered, Fig. 5.16 has shown the overlap of stress curves with and without diffusion strain. The presence of viscoplasticity reinforces the difficulty to identify the diffusion stress from a numerical point of view. The diffusion coefficient has a strong the influence to the diffusion stress, which directly couples the diffusion strain and the diffusion stress. However, this parameter can only be determine by the experiments for now.

The spatial variations of stresses occur mainly in the near interface zone. However, this zone is deeply influenced by the mechanical balance for the whole sample, both for metal side and oxide side. From a numerical simulation point of view, when considering the full thermomechanical modeling, the diffusion strain decreases the stress in the metal layer in the near interface zone, but its effect is difficult to directly evidence numerically.

## 5.3 Simulation of isothermal oxidation conditions

In this section, the simulation will be compared to the time-depending stress results obtained in Zhaojun Tao's work [7] and also the results obtained in section 4.1.2.1. In work [7], it was shown the time-depending stresses for 800°C, 900°C, 1000°C oxidized for 7.4h. The parameters used correspond to Ni30Cr material, which represents 30% of the weight of Cr [7]. The samples have been introduced in sections 4.1.1.1, which are Ni28Cr and Ni35Cr with respectively 28% of the weight of Cr and 35% of the weight of Cr. We expect that the chosen parameters values with an in-between percentage of chromium may describe correctly both of the material. Knowing that the samples are oxidized at 800 °C, 900°C or 1000 °C, the input parameters for the three temperatures are shown in Table 5.8.

Table 5.8. The input parameters [7, 9, 10]

| Oxidation condition | $Ap$ $(mm\ s^{-1/2})$ | $E_{ox}$ $(MPa)$ | $\nu_{ox}$ | $K_{ox}$ $(MPa\ s^{1/Nox})$ | $N_{ox}$ | $\alpha_{ox}$ $(K^{-1})$ |
|---|---|---|---|---|---|---|
| 800 °C, 10 h | 2.83E-6 | 225000 | 0.29 | 2.65E8 | 1 | 6.99E-6 |
| 900 °C, 10 h | 4.73E-6 | 215000 | 0.29 | 1.83E8 | 1 | 7.11E-6 |
| 1000 °C, 1 h | 1.43E-5 | 205000 | 0.29 | 3.5E7 | 1 | 7.24E-6 |

|  | $D_{ox}$ $(mm^{-1})$ | $E_m$ $(MPa)$ | $\nu_m$ | $K_m$ $(MPa\ s^{1/Nm})$ | $N_m$ | $\alpha_m$ $(K^{-1})$ |
|---|---|---|---|---|---|---|
| 800 °C, 10 h | 51.4 | 170000 | 0.3 | 2.39E11 | 1 | 1.9E-5 |
| 900 °C, 10 h | 56.6 | 165000 | 0.3 | 1.05E13 | 1 | 1.96E-5 |
| 1000 °C, 1 h | 51.9 | 160000 | 0.3 | 1.88E15 | 1 | 2.02E-5 |
|  | $[Cr]_0$ | η | $D$ $(mm^2 s^{-1})$ |  |  |  |
| 800 °C, 10 h | 0.345 | -6.57E-03 | 2.59E-12 |  |  |  |
| 900 °C, 10 h | 0.345 | -1.18E-02 | 4.09E-11 |  |  |  |
| 1000 °C, 1 h | 0.2828 | -8.98E-03 | 4.19E-10 |  |  |  |

In this table, $Ap$ is the kinetics coefficient of the global chemical oxidation reaction; $E_{ox}$ corresponds to the Young's modulus of oxide layer; $\nu_{ox}$ is the Poisson's ratio of oxide layer; $K_{ox}$ and $N_{ox}$ correspond to the viscoplastic parameters of oxide layer; $\alpha_{ox}$ is the thermal expansion coefficient of oxide layer; $D_{ox}$ corresponds to the growth strain parameter; $E_m$ and $\nu_m$ are the Young's modulus and the Poisson's ratio of metal layer; $K_m$ and $N_m$ are the viscoplastic parameters of metal layer; $\alpha_m$ corresponds to thermal expansion coefficient of metal layer; $[Cr]_0$ is the initial weight percentages concentration of element Cr; η corresponds to a constant coefficient coupling the chromium concentration profiles to the diffusion strain and $D$ is the diffusion coefficient of chromium in NiCr.

In order to solve the problem presented before, a smaller geometry and a finer mesh is applied.

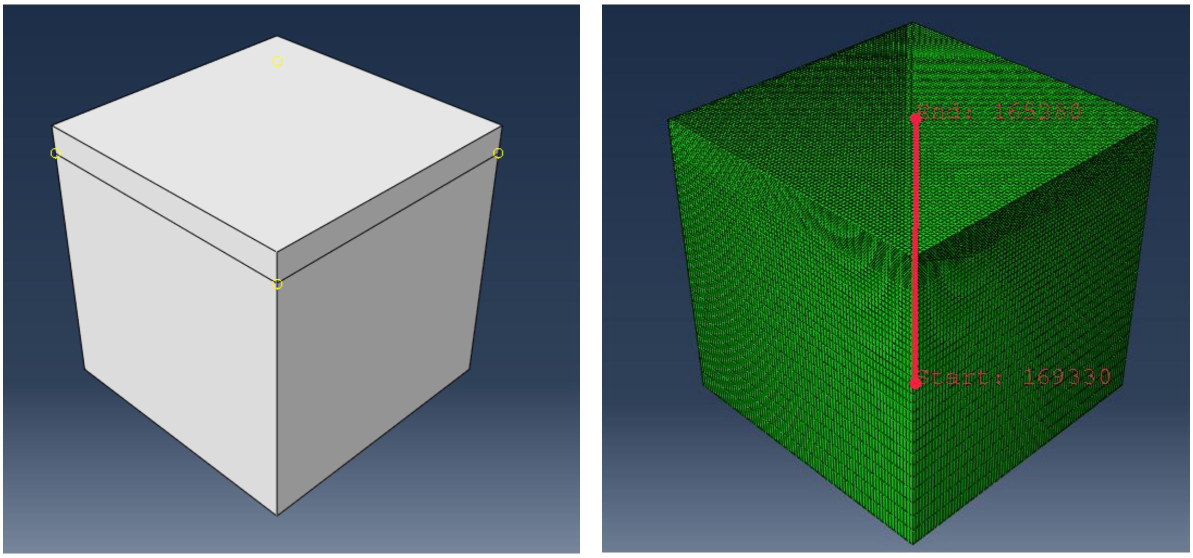

(a) (b)

Figure 5.18 The local geometry (a) and mesh (b)

As shown in Fig. 5.18, in order to adapt to the oxide layer thickness, the simulation is applied to a smaller geometry, which is 0.02*0.02*0.02 mm. Along axis z, from 0 to 0.018 mm is the metal layer and from 0.018 mm to 0.02 mm is the the oxide + air layer (a). For the different layers, a different mesh is considered (b). Refinement of the mesh is required to obtain a correct accuracy. For oxide + air layer, there are 20 nodes, which means that the thickness of one element is 0.0001 mm that is more suitable for the simulation of oxide layer. For the metal layer, there are 30 nodes and for the elements that are close to the interface, they are smaller. The element type is C3D8R. The simulations discussed further in this section are using the geometry and mesh shown in Fig.5.18.

## 5.3.1 Oxidation at 800°C for 10h

The stress-field nephograms are similar for all the three samples, which is shown in APPENDICE 4. By using the parameters in Table 5.8, the mesh and geometry of Figure 5.18, the simulation results are obtained and the stress distribution curves along the center path are plotted.

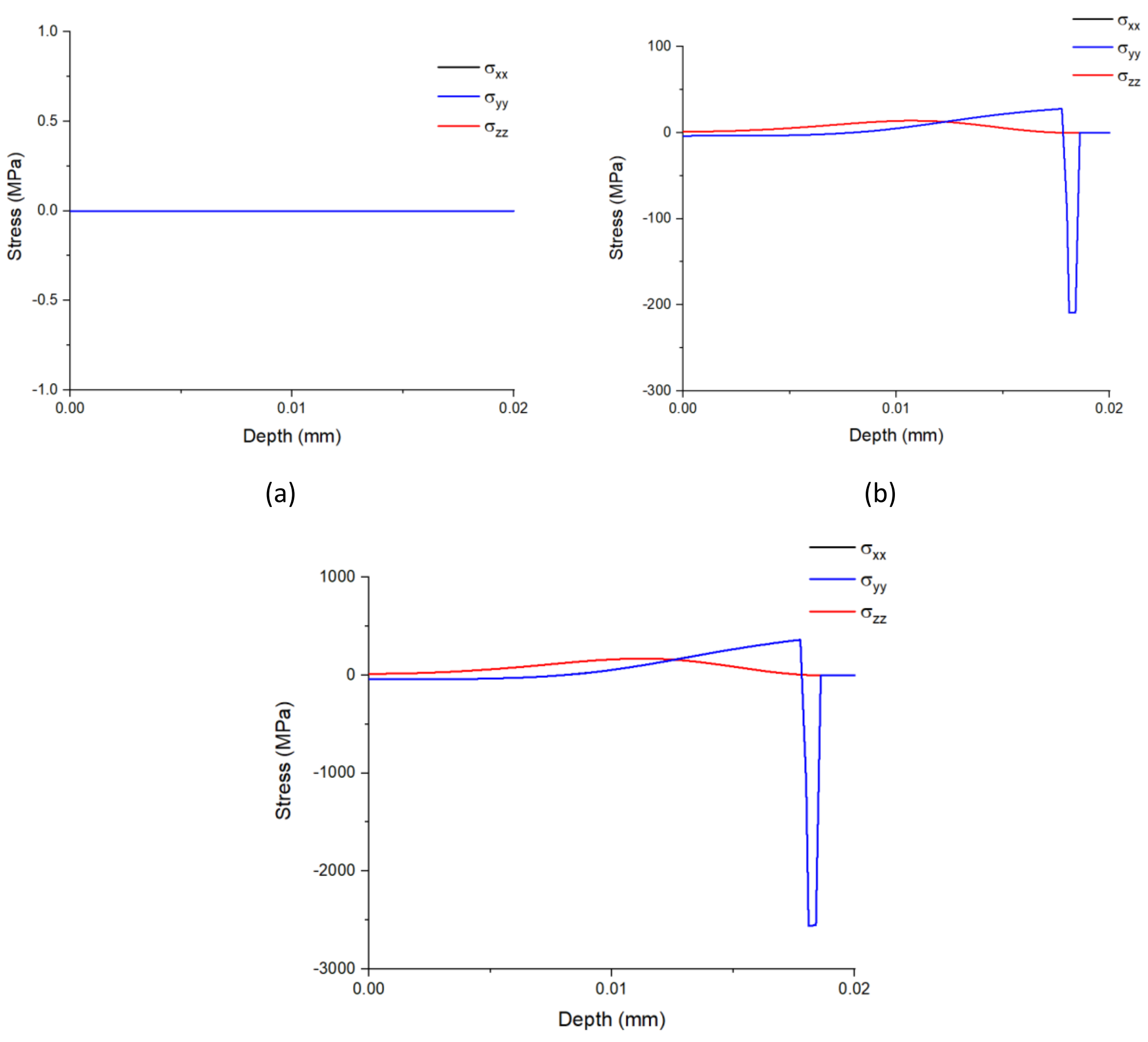

(a) (b)

(c)

Figure 5.19 The distribution of stress components at the end of phase 1 (a), at the end of phase 2 (b), and at the end of phase 3 (c)

For Fig. 5.19 (a)-(c), the interface of metal/oxide is at depth 0.018 mm. As shown in Figure 5.19, the $\sigma_{xx}$ and $\sigma_{yy}$ are very close for all phases, which indicates that the simulation leads to an isotropic mechanical state. At the end of phase 2, the isothermal phase, the maximum absolute value for stress in the oxide layer is 209 MPa and in the metal layer is 28 MPa. At the end of phase 3, room temperature, the maximum absolute value for stress in the oxide layer is 2561 MPa and in the metal layer is 362 MPa. For phase 2 and phase 3, the maximum stress appears near the oxide/metal interface. The maximum absolute value for stress in the oxide layer at the room temperature corresponds to the values obtained in other works, which is around 2-2.5 GPa [7, 9, 10]. The stresses at the interface are shown in Table 5.9.

Table 5.9. The stress at the interface at the end of phase 3 for the metal side

| | Stress (MPa) |
|---|---|
| Experimental results | -557 ± 148 |
| Simulation results | -1098 |

The stress at interface for the metal side of experimental results and simulation results are both measured at room temperature. The simulation results is two times higher than the experimental results. As mentioned in section 5.2.2.4, the experimental stress at interface for the metal side is deeply related to the growth strain, viscoplastic strain, thermal strain and the mechanical balance. However, it is shown that the stress is in compression at the interface, for which order of magnitudes is -1 GPa.

The time-dependent stress can also be plotted, which can be compared with the results obtained in the work of Tao [7], for materiel Ni30Cr and oxidized at 800°C for 7.4h. In figure 5.20 is presented the time-dependent stress of the first 7 hours for the experimental results and simulation results.

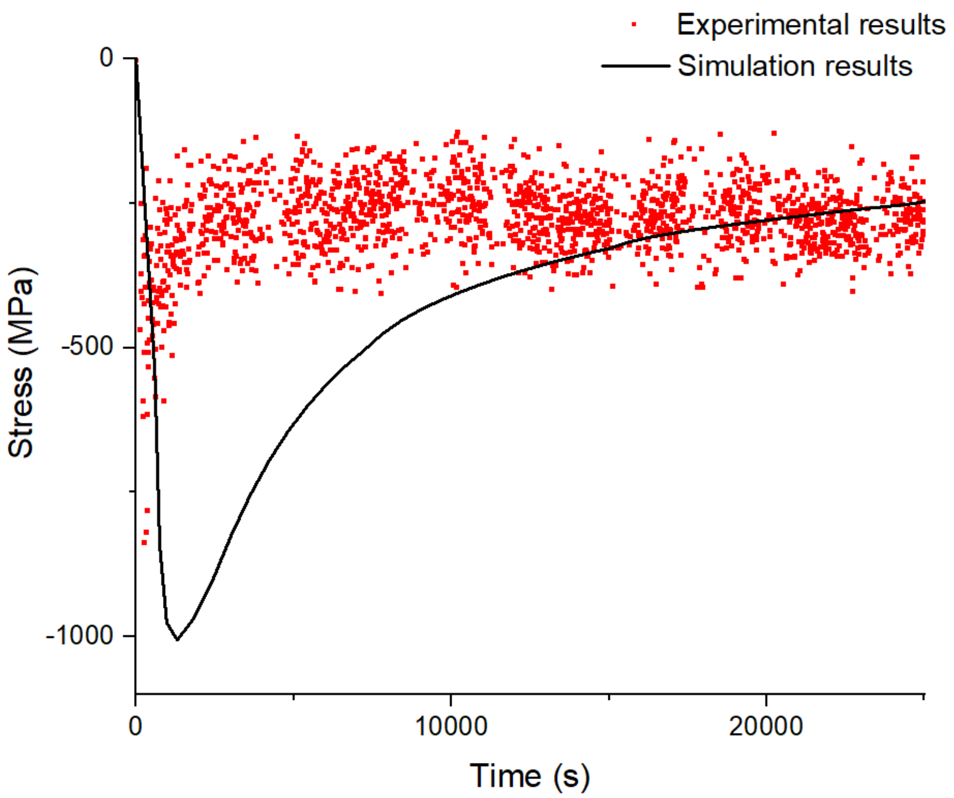

Figure 5.20 Time-dependent stress for isothermal condition 800 °C

Fig. 5.20 shows the comparison of the time-dependence of stress for oxide layer, which includes the experimental results and the simulation results for isothermal oxidation condition at 800 °C. The simulation results correspond quite well with the experimental results, especially at the end of the phase 2. For all time, the amplitude agrees well but evolution presents slight difference, especially in term of the time of the minimum. For numerical simulation, it is shown that at the beginning, the absolute stress increases in the oxide layer. At the same time, the viscoplasticity causes a relaxation of stress, which finally gets a balance between the increase and relaxation. Therefore, the minimum stress is affected by the parameters such as the viscoplastic parameters of oxide layer $K_{ox}$ and the growth strain parameter $D_{ox}$.

For the delay of the time inflection, it may be caused by the difference of condition for phase 1. As mentioned before, in the simulation, the viscoplastic strain, diffusion strain, and growth strain are not considered in this phase. However, in the experiment, these strains may exist, which will cause a residual stress for the isothermal phase. For the simulation, at the beginning of phase 2, the stress is 0 MPa, the stress increase and stress relaxation occur after delaying the time inflection.

## 5.3.2 Oxidation at 900°C for 10h

By using the parameters in Table 5.8, the mesh and geometry of Figure 5.18, the simulation results are obtained and the stress distribution curves along the center path are plotted.

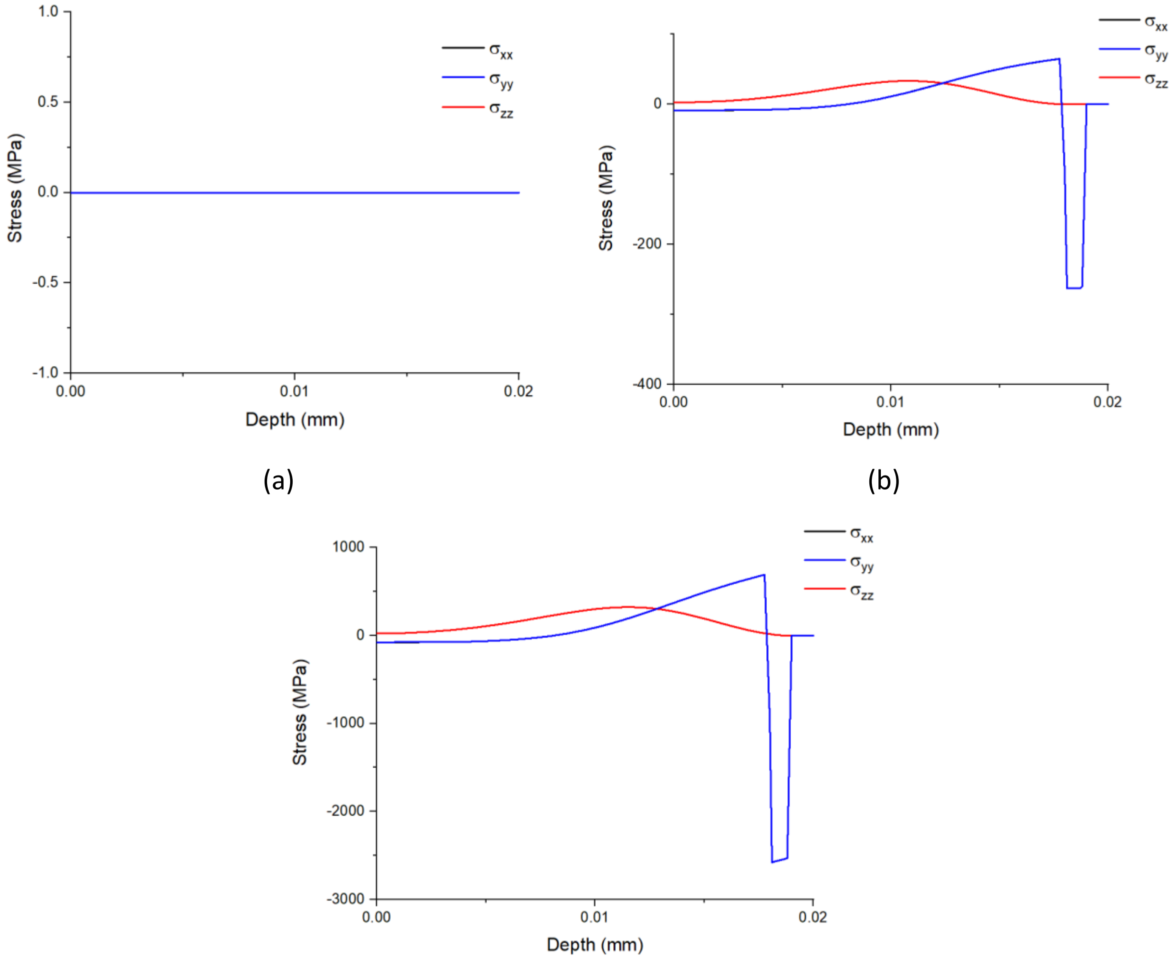

(a) (b)

(c)

Figure 5.21 The distribution of stress components at the end of phase 1 (a), at the end of phase 2 (b), and at the end of phase 3 (c)

Fig. 5.21 shows the stress distribution along axis z. For Fig. 5.21 (a)-(c), the interface of metal/oxide is at depth 0.018 mm. The results show that the stress in the metal layer is in tension and in the oxide layer is in compression. At the end of phase 2, the maximum absolute value for stress in the oxide layer is 262 MPa and in the metal layer is 65 MPa. At the end of phase 3, room temperature, the maximum absolute value for stress in the oxide layer is 2577 MPa and in the metal layer is 691 MPa. For phase 2 and phase 3, the maximum stress appears near the oxide/metal interface. The stress at the interface are shown in Table 5.10.

Table 5.10. The stress at the interface at the end of phase 3 for the metal side

| | Stress (MPa) |
|---|---|
| Experimental results | -970 ± 329 |
| Simulation results | -941 |

As shown in Table 5.10, the experimental results and simulation results are quite very close for the stress at the interface at the end of phase3 for the metal side. It indicates that the stress spatial distribution in the metal layer begins with a value around -1 GPa.

In order to be compared with the results obtained in the work of Tao [7], for materiel Ni30Cr and oxidized at 900 °C for 7.4h, the time-dependent stress is plotted. In figure 5.22 is shown the time-dependent stress of the first 7 hours for both the experimental and simulation results.

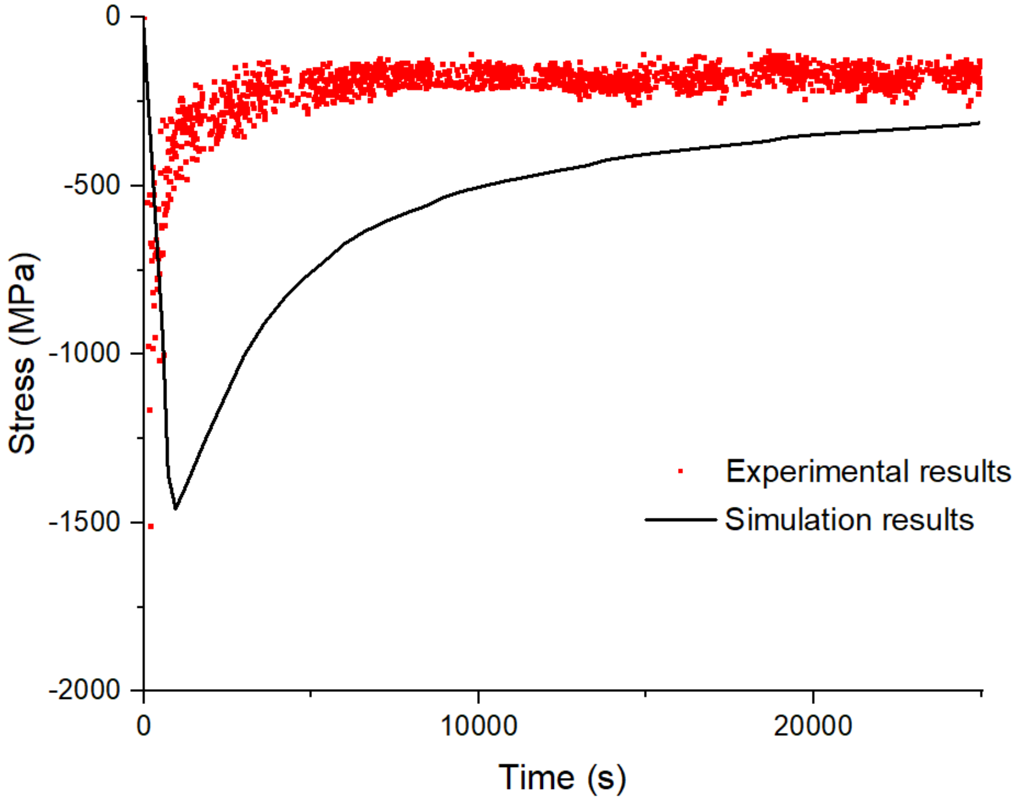

Figure 5.22 Time-dependent stress for isothermal condition 900 °C

By using the given parameters in Table 5.8, the simulation results is shown in Fig. 5.22. The performance of simulation is quite good, which means that the simulation results are similar to the experimental results. The minimum stress for simulation results is -1458 MPa, which is very close to the minimal experimental result -1508 MPa. As discussed before, the growth strain and the viscoplastic strain at high temperature play important roles in this system and this numerical model is suitable for simulating this kind of systems. Once again, the delay of the time inflection may be caused by the different conditions between the experiments and simulation for the temperature increase phase.

### 5.3.3 Oxidation at 1000°C for 1h

By using the parameters in Table 5.8, the mesh and geometry of Figure 5.18, the simulation results are obtained and the stress distribution curves along the center path are plotted.

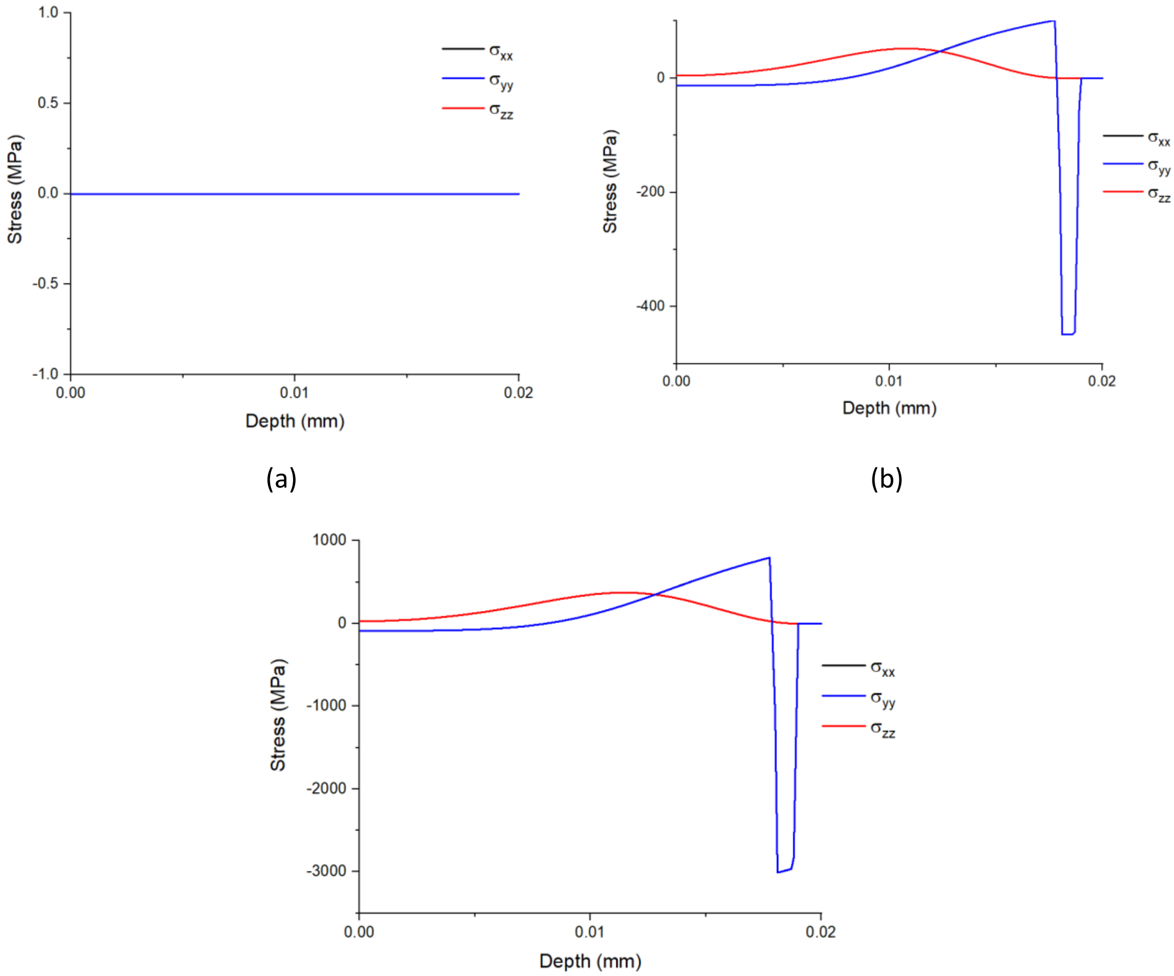

(a)

(b)

(c)

Figure 5.23 The distribution of stress components at the end of phase 1 (a), at the end of phase 2 (b), and at the end of phase 3 (c)

Fig. 5.23 indicates the stress distribution along axis z. For Fig. 5.23 (a)-(c), the interface of metal/oxide is at depth 0.018 mm. The results shows that the stress in the metal layer is in tension and in the oxide layer is in compression. At the end of phase 2, the maximum absolute value for stress in the oxide layer is 449 MPa and in the metal layer is 101 MPa. At the end of phase 3, room temperature, the maximum absolute value for stress in the oxide layer is 3009 MPa and in the metal layer is 795 MPa. The stresses at the interface are shown in Table 5.11.

Table 5.11. The stress at the interface at the end of phase 3 for the metal side

| | Stress (MPa) |
|---|---|
| Experimental results | -588 ± 128 |
| Simulation results | -1104 |

The experimental results and simulation results show that the stress spatial distribution begins with compression. The simulation results is two times higher than the experimental results. The experimental stress at interface for the metal side is deeply related to the growth strain, viscoplastic strain, thermal strain and the mechanical balance, which needs more studies for the simulation.

In order to be compared with the results obtained in the work of Tao [7], for materiel Ni30Cr and oxidized at 1000 °C for 7.4h, the time-dependent stress is plotted. It is shown the time-dependent stress of the first one hour for the experimental results and simulation results.

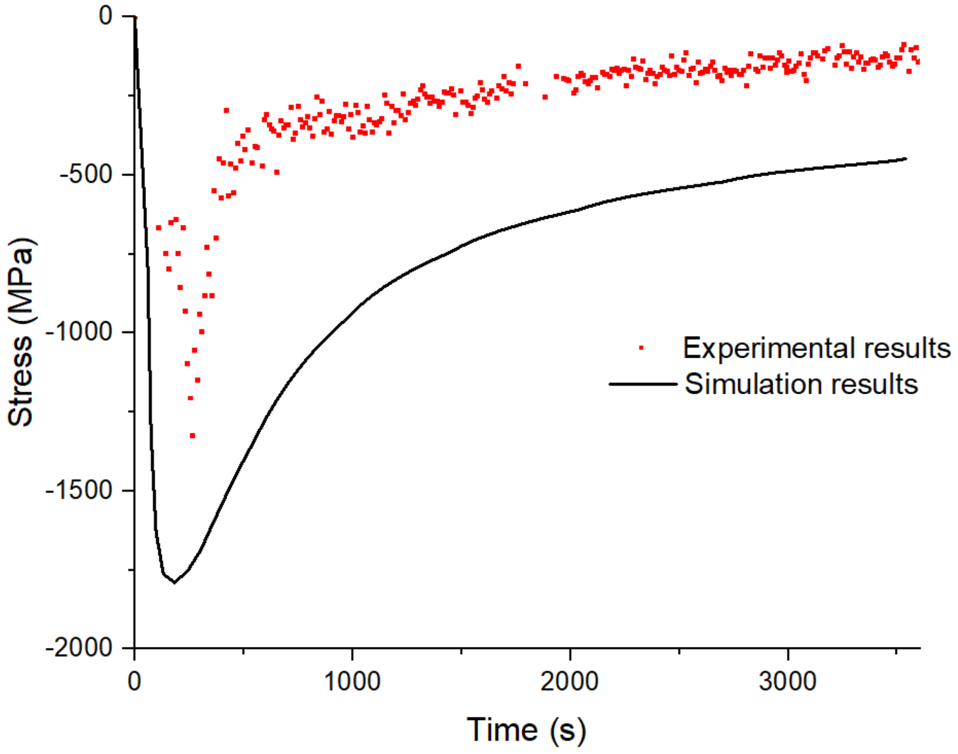

Figure 5.24 Time-dependent stress for isothermal condition 1000 °C

Fig. 5.24 shows that the simulation results have the same trend with the experimental results. However the simulation results is lower that the experimental results. For the minimum stress, it is -1788 MPa for the simulation results and -1324 MPa for the experimental results. Overall, this simulation proved its suitability for calculating stresses at isothermal loading.

**References of chapter 5**

[1] N Kikuchi, JT Oden, Contact problems in elasticity: a study of variational inequalities and finite element methods, 1988

[2] M. A. Crisfield, G. F. Moita, International Journal of Solids and Structures 1996, 33, 2969.

[3] Thomas J. R. Hughes, The Finite Element Method: Linear Static and Dynamic Finite Element Analysis, 2012

[4] Z. Zhuang, ABAQUS finite element based analysis and application (Chinese), Tsinghua University, 2009.

[5] http://130.149.89.49:2080/v2016/books/sub/default.htm?startat=ch01s01asb44.html#sub-rtn-uumat

[6] J.-L. Grosseau-Poussard, B. Panicaud, S. Ben Afia, Computational Materials Science 2013, 71, 47.

[7] Z. Tao, Etude expérimentale et modélisation des caractéristiques mécaniques d’une couche d'oxyde sous charges thermiques. PhD thesis, Université de Technologie de Troyes, Troyes, 2018.

[8] http://web.mit.edu/calculix_v2.7/CalculiX/ccx_2.7/doc/ccx/node27.html

[9] M. Guerain, Contribution à l’étude des mécanismes de relaxation de contraintes dans les films de chromine formés sur Ni-30Cr et Fe-47Cr : approche multi-échelle par spectroscopie Raman et microdiffraction Synchrotron, PhD Thesis, Université de La Rochelle, La Rochelle, France, 2012.

[10] F.N. Rakotovao, Relaxation des contraintes dans les couches de chromine développées sur alliages modèles (NiCr et Fe47Cr). Apport de la diffraction in situ à haute température sur rayonnement Synchrotron à l’étude du comportement viscoplastique. Effets d’éléments réactifs, PhD thesis, Université de La Rochelle, 2016.

# Conclusion

Residual stresses have been determined both in metal and oxide in different oxide/metal systems. Measurements and analyses of stress in the oxide layer have been especially performed in-situ during thermal loadings at high temperature thanks to synchrotron X-ray diffraction in reflection mode. Moreover, complementary measurements of stress in substrate at room temperature have been realized by synchrotron X-ray diffraction in transmission mode. A thermomechanical model has been developed, with additional terms to the existing ones with different possible sources for stresses: growth strain, thermal strain and diffusion/chemical strain. For this “full” thermomechanical model, it has been also proposed to perform simulations with a numerical approach using ABAQUS.

The first part of the work was based on the time–dependent stresses evolution that are obtained by treating the results of in-situ high temperature synchrotron diffraction measurements (in reflection mode) obtained at European Synchrotron Radiation Facility. To identify the unknown or unsure parameters of the modelling, it has been required to investigate a numerical solution of the full thermomechanical modelling, which includes the known strain components, such as elastic strain, viscoplastic strain, thermal strain and growth strain for oxide layer. Therefore, an adapted method has been improved then applied to process the experimental results. By comparing the time–dependent stresses and the numerical solution at least-squares sense, the creep parameter for oxide ($J_{ox}$) and the growth stress parameter for oxide ($D_{ox}$) have been optimized for several samples. Such parameters have been investigated to determine the activation energy associated to the mechanisms and have been favorably compared to the existing ones in bibliography.

Indeed, the residual stresses have been determined in oxide phase in a {$Cr_2O_3$+Ni28Cr} system. Thanks to synchrotron X-ray diffraction in reflection mode, it allows in situ measurements during high temperature thermal loadings. We found the best simulations of peak profiles by use of Pearson 7 distribution simultaneously with background fitting. For each sample, over 13,000 pictures were processed by applying the $\sin^2\psi$ method to obtain the time-dependent stresses and 7 samples corresponding to different materials were treated.

Considering the isothermal oxidation condition and a homogeneous stress in the metal, for all the materials, including the yttria-coated samples and zirconium-doped samples, the evolution of stress is mainly the result of mechanical balance between two phenomena. It is confirmed that there is an increase of stress in magnitude mainly caused by the growth of oxide layer and a relaxation of stress mainly caused by viscoplastic behavior related to creep mechanisms. The thermomechanical modelling of these {oxide + metal} systems has been successfully implemented. Using Matlab software and a classical Runge-Kutta method, the creep parameter for oxide ($J_{ox}$) and the growth stress parameter for oxide ($D_{ox}$) have been thus identified for all the considered materials.

The aims of introducing reactive elements is to improve the protective properties of the thermally grown chromia layer under high temperature oxidation. By increasing the quantity of yttria coated or zirconium doped, the viscoplastic strain is proved to be smaller with a large quantity of coated yttria or doped zirconium at the same temperature than without those elements, which is associated to the fact that the reactive element $Y_2O_3$ and Zr are effective for slowing down the cationic diffusion.

By increasing the quantity of yttria coated or zirconium doped, the growth strain parameter $D_{ox}$ decreases. In addition, the activation energy for growth $Q_D$ is calculated, which decreases as the exposure time increases or the doping fluence increases. The $D_{ox}$ parameter may also be related to the ratio of the cationic/anionic flux occurring within the grain boundaries as the oxide layer grows. An interpretation of this effect has been proposed.

With such an approach, we now better understand the underlying physical mechanisms, and especially those responsible for the creep behavior. With the presence of reactive elements, the surface properties and creep behavior are significantly modified.

The second part of work is dedicated to investigate the stress-depth evolution in the metallic substrate that has been obtained by treating the results of synchrotron in transmission mode measurements obtained at room temperature at DESY Synchrotron in Germany. To investigate the residual stress distribution in the metallic substrate after oxidation, a $\sin^2\varphi$ method, variant of $\sin^2\psi$ method, is developed.

The largest part of the stress distribution is ranged from 0 MPa to 500 MPa and presents a gradient distribution, which is in the near interface zone (up to 15μm before roughly constant values) between metal and oxide. The stress varies towards the surface in a non-linear way. With a lower oxidation temperature or lower oxidation time, the absolute value of stress at oxide/metal interface is smaller and the depth of stress gradient is thinner.

Moreover, we have proposed adding a diffusion stress in existing thermomechanical model to explain this stress gradient in the near interface zone. Due to the rapid variation of chromium depletion in the near-surface zone, this diffusion stress changes as a function of depth. After adding this diffusion stress in the modelling, the stress distribution agrees quite well with the measured stress compared to the modeling without diffusion stress. However, the correspondence of the gradient stress distribution between experiments and modelling still requires further improvement. Numerical values for the coupling of chromium concentration with diffusion/chemical stress have also been obtained. These values have been identified to strongly influence the level of calculated stress. However, these values are related to the experimental results and thus may present some uncertainties that requires further additional investigations.

The present study fills a gap in the literature by using high energy X-ray in transmission mode to measure the stress distribution in depth metal layer and by proposing a model to calculate the stress spatial distribution for comparison. From an experimental point of view, the oxidation conditions, even the shape of samples can influence the stress distribution. From a modelling point of view, the input parameters and the different mechanisms can influence the results. The comparison is thus difficult because of the numerous uncertainties and errors origins. However, the observation of spatial gradient and its prediction, by adding the diffusion stress component in the thermomechanical modeling, leads to a better explanation for the stress distribution in the metal layer.

Finally, the last part of the present study is focused on the development of a spacetime numerical model for the prediction of the stress generated in high temperature oxidation. The numerical simulation results are both compared to the time–dependent stresses for oxide layer, and to the spatial-dependence stresses for metal layer near the metal/oxide interface.

The oxide layer is subjected to high compressive stresses of the order of 2-2.5 GPa at room temperature after the cooling process. Their maximum absolute values are at the metal-oxide interface. The stress in the metal substrate remains low, which is of the order of a few MPa and their maximum absolute values are also at the metal-oxide interface.

The results of these simulations are compared with experimental observations that quite shows a good agreement with the time–dependent stresses for oxide layer. The absolute value of stress increases at the beginning of oxidation and it decreases because of the creep phenomena at high temperature. After the cooling process, the stress increases largely, which is due to the different thermal expansion coefficient between the oxide and metal layer of the present suited system.

The spatial distribution stress comparison between the simulation results and the experimental results at the interface does not show a clear agreement. However, by testing the different strain contributions, such as with and without the diffusion strain, it is shown that after adding the diffusion strain, the stress changes at the interface for both oxide side and metal side. However, the influence of the viscoplastic strain and growth strain in the oxide layer is much bigger than the diffusion strain in the metal layer, which affects significantly the stress spatial distribution only in few microns near the interface. These conclusions lead us to consider that there may be other phenomena in the near interface zone for the metal layer.

# Future prospects

At the end of this work, there are some perspectives that are interesting to investigate for further works.

Firstly, more investigations can be done in order to determine the stress in the oxide layer and metal layer for the system NiCr/$Cr_2O_3$. Except the XRD measurement, there exists also Raman spectroscopy, deflection experiments etc. As discussed in Section 2.2, the deflection method could be more deeply investigated to obtain a more accurate measurement of stress and the numerical simulation can be used to predict and compare with the experimental results. By comparing the results obtained from different experiments, it is possible to have a more accurate determination of the stress in the oxide layer and metal layer. These measurements are the analysis from macroscopic scale. We can also analyze the stresses from microscopic scale, the grains size scale, by numerical simulation. The investigations from microscopic scale should give a new angle of view for stress evolution and distribution.

Secondly, more studies about the reactive elements effect should be done. The influence of the reactive elements on the activation energy of the viscoplastic phenomena and the oxide growth phenomena is not fully clear. A larger number of different reactive elements should be tested with different quantities, which can help us to better understand the viscoplastic phenomena and the oxide growth phenomena.

The transmission mode may be used to detect the spatial distribution of stresses with these reactive elements, which can help us better to understand how the presence of those reactive elements changes the stress distribution in the metal and how they affect the diffusion coefficient. Especially, the adding of reactive elements changes the parameters like the kinetics coefficient, the viscoplastic parameters for oxide and metal, the oxide growth strain parameter etc., which should be optimized and verified with the existing thermomechanical modelling.

Thirdly, the stress spatial distribution is also more specially interesting. By using the high-energy XRD with transmission mode, the stress spatial distribution is observed in the metal layer. However, the mechanism that causes this phenomenon has not been deeply studied before. In this work, we have proposed a possibility to explain the stress spatial distribution. In order to better understand the possible other mechanisms, more experiments with different oxidation condition are required, such as different oxidation temperature, different oxidation time etc. In addition, other experiments that helps us investigate the stress spatial distribution are also important to consider, such as the stress spatial distribution calculation with the deflection experiments.

Finally, the numerical simulation is quite suitable for the thermomechanical modelling, which can solve situations that are more complicated, especially concerning geometry or nonlinear contributions of stress-strain behaviors. With the correct parameters, the simulation results is quite close to the experimental results. The numerical simulation can go further. By adding phases in the UMAT, it would be now possible to simulate oxidation for a complicated thermal solicitation, such as cyclic loadings, step loadings and isothermal conditions. It could also be used for simulating other types of materials as long as the material parameters are known. In addition, it can even be extended by adding other types of strains, for example the epitaxial strains. Moreover, different intrinsic equations for the strains can be tested in the UMAT, such as other equations describing the growth strain, the viscoplastic strain etc.

# APPENDICE 1

Unlike the implicit solution, the explicit solution does not require solving a group of equations or calculating the global stiffness matrix at the same time. The solution is obtained by a dynamic process that extrapolates from one incremental step to the next.

In this example, a three elements 1D truss problem is considered as shown in Fig 1:

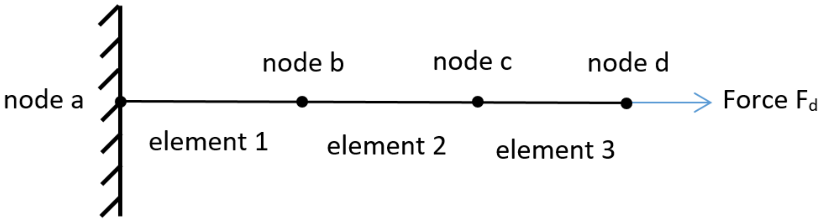

Figure 1 The discretized model at initial for a 1D truss problem

At the first time increment, the concentrated force $F_d$ applied to node d causes an acceleration $\ddot{u}_d$ at node d.

$$\ddot{u}_d = \frac{F_d}{M_3} \tag{1}$$

This acceleration generates a speed $\dot{u}_d$ at node d, which causes a strain rate $\dot{\varepsilon}_{11}$ in element 3. The strain increment $d\varepsilon_{11}$of element 3 is obtained by integrating the strain rate in the first time increment.

$$\dot{u}_d = \int \ddot{u}_d dt \tag{2}$$

$$\dot{\varepsilon}_{11} = \frac{\dot{u}_d}{L} \tag{3}$$

$$d\varepsilon_{11} = \int \dot{\varepsilon}_{11} dt \tag{4}$$

The total strain $\varepsilon_{11}$ is the sum of the initial strain $\varepsilon_0$ and the strain increment $d\varepsilon_{11}$. In this problem the initial strain is zero because of constraint node a.

$$\varepsilon_{11} = \varepsilon_0 + d\varepsilon_{11} \tag{5}$$

Once the element strain is obtained, the stress $\sigma_{11}$ of the element can be calculated. For elastic materiel, the stress is equal to the total strain multiplied by Young's modulus.

$$\sigma_{11} = E\varepsilon_{11} \tag{6}$$

This process is shown in Fig. 2. In the first time increment, nodes b and c do not move because there is no force applied to them.

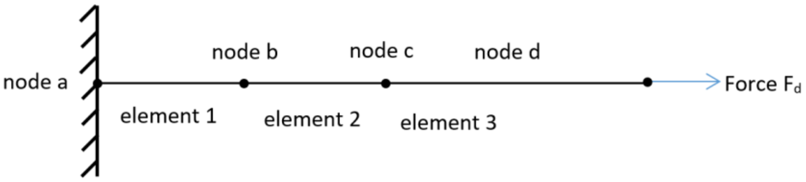

Figure 2 The discretized model at end of first time increment

In the second time increment, the internal load is applied at the node connected to element 3, which is node c, as shown in  Fig. 3.

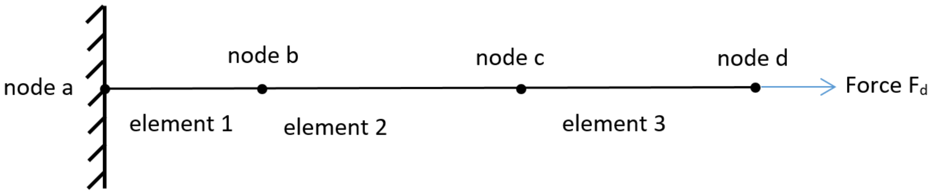

Figure 3 The discretized model at end of second time increment

The dynamic balance equations are:

$$\ddot{u}_d = \frac{F_d - I_3}{M_3} \Rightarrow \dot{u}_d = \dot{u}_d{}^{old} + \int \ddot{u}_d dt \tag{7}$$

$$\ddot{u}_c = \frac{I_3}{M_2} \Rightarrow \dot{u}_c = \int \ddot{u}_c dt \tag{8}$$

$$\dot{\varepsilon}_{11} = \frac{\dot{u}_c - \dot{u}_d}{L} \Rightarrow d\varepsilon_{11} = \int \dot{\varepsilon}_{11} dt \tag{9}$$

$$\varepsilon_{11} = \varepsilon_{11}{}^{old} + d\varepsilon_{11} \Rightarrow \sigma_{11} = E\varepsilon_{11} \tag{10}$$

The process continues and by the beginning of the third time increment, stresses are present in elements 2 and 3, while forces are present in nodes b, c and d. This process will continue until the end of the total analysis time.

# APPENDICE 2

The variables commonly used in UMAT are defined at the beginning of the file, usually in the following format:

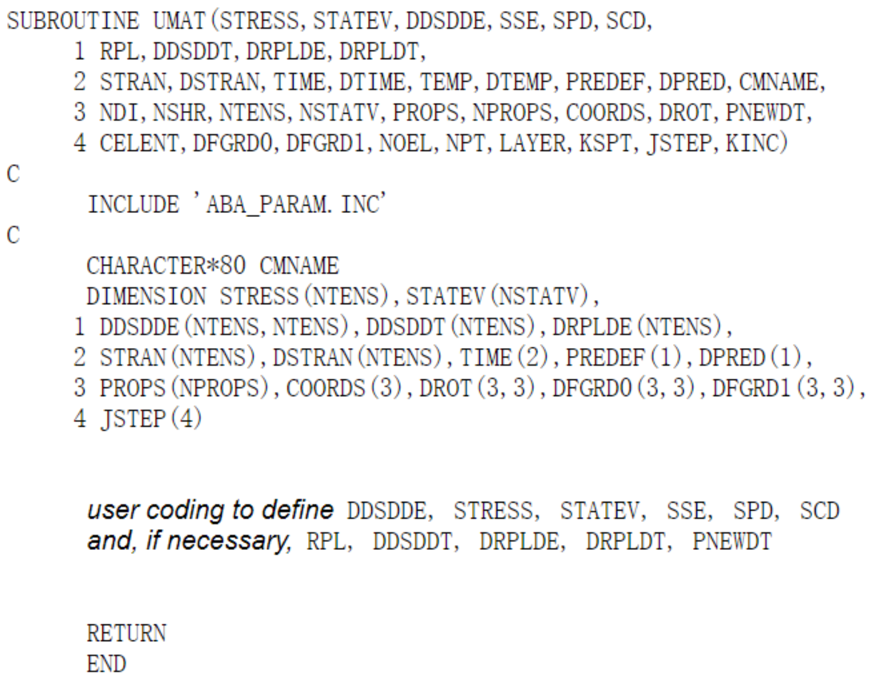

```
SUBROUTINE UMAT(STRESS,STATEV,DDSDDE,SSE,SPD,SCD,
     1 RPL,DDSDDT,DRPLDE,DRPLDT,
     2 STRAN,DSTRAN,TIME,DTIME,TEMP,DTEMP,PREDEF,DPRED,CMNAME,
     3 NDI,NSHR,NTENS,NSTATV,PROPS,NPROPS,COORDS,DROT,PNEWDT,
     4 CELENT,DFGRD0,DFGRD1,NOEL,NPT,LAYER,KSPT,JSTEP,KINC)
C
      INCLUDE 'ABA_PARAM.INC'
C
      CHARACTER*80 CMNAME
      DIMENSION STRESS(NTENS),STATEV(NSTATV),
     1 DDSDDE(NTENS,NTENS),DDSDDT(NTENS),DRPLDE(NTENS),
     2 STRAN(NTENS),DSTRAN(NTENS),TIME(2),PREDEF(1),DPRED(1),
     3 PROPS(NPROPS),COORDS(3),DROT(3,3),DFGRD0(3,3),DFGRD1(3,3),
     4 JSTEP(4)


      user coding to define DDSDDE, STRESS, STATEV, SSE, SPD, SCD
      and, if necessary, RPL, DDSDDT, DRPLDE, DRPLDT, PNEWDT


      RETURN
      END
```

Figure 4 User subroutine interface

This user subroutine interface is given in Abaqus User Subroutines Reference Guide. The parameters used in UMAT includes (not only):

1. DDSDDE(NTENS,NTENS)

This is a NTENS degrees square matrix called a Jacobi matrix, which is $\partial\Delta\sigma/\ \partial\Delta\varepsilon$, where $\Delta\sigma$ is the increment of stress and $2\Delta\varepsilon$ is the increment of strain. DDSDDE(I ,J) represents  the change in the Ith stress component at the end of the time increment caused by an infinitesimal perturbation of the Jth component of the strain increment array. Usually, Jacobi matrix is a symmetric matrix.

2. STRESS(NTENS)

This is the stress tensor matrix with NTENS degrees. At the beginning of the incremental step, the values in the stress tensor matrix are transferred to UMAT through the interface between UMAT and the main program. At the end of the incremental step, UMAT updates the stress tensor matrix. The stress tensor is calculated as the true stress in UMAT.

3. STATEV(NSTATV)

An array containing the solution-dependent state variables. These are passed in as the values at the beginning of the increment unless they are updated in user subroutines USDFLD or UEXPAN, in which case the updated values are passed in. In all cases STATEV must be returned as the values at the end of the increment.

4. TIME(1)

Value of step time at the beginning of the current increment or frequency.

5. TIME(2)

Value of total time at the beginning of the current increment.

6. COORDS

An array containing the coordinates of this point. These are the current coordinates if geometric nonlinearity is accounted for during the step.

# APPENDICE 3

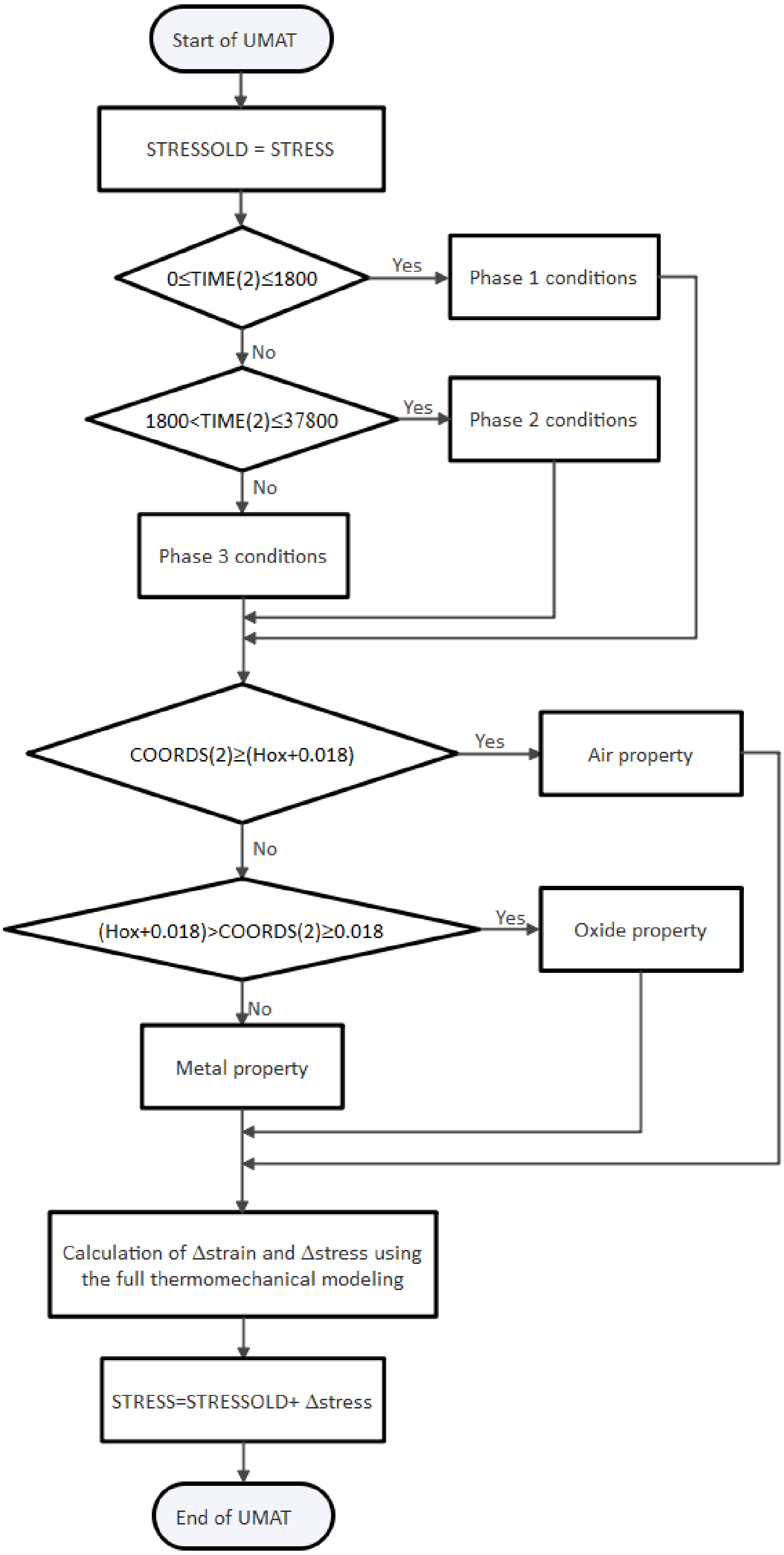

Figure 5 Flowchart of UMAT implementation

As shown in Fig. 5, in the UMAT, the stresses of the previous increment step are saved in the matrix STRESSOLD. There are two choices in the UMAT: the first one distinguishes the phase conditions and the second one gives us the different material property. The most important part is the calculation of the difference of strain and stress by using the full thermomechanical model, which has been introduced in section 2. We have elastic strain, viscoplastic strain, thermal strain, growth strain and diffusion strain. The calculation of difference elastic strain to difference stress is performed using the Hooke model with a Jacobian matrix. The elastic strain is obtained by the total strain minus the other strains, including the viscoplastic strain, where the total strain is obtained by the last step increment and the viscoplastic deformation plays a role of relaxation. At the end of this increment step, the stresses are obtained by adding the STRESSOLD and difference of stresses together.

# APPENDICE 4

The stress-field nephograms are shown in Fig. 6.

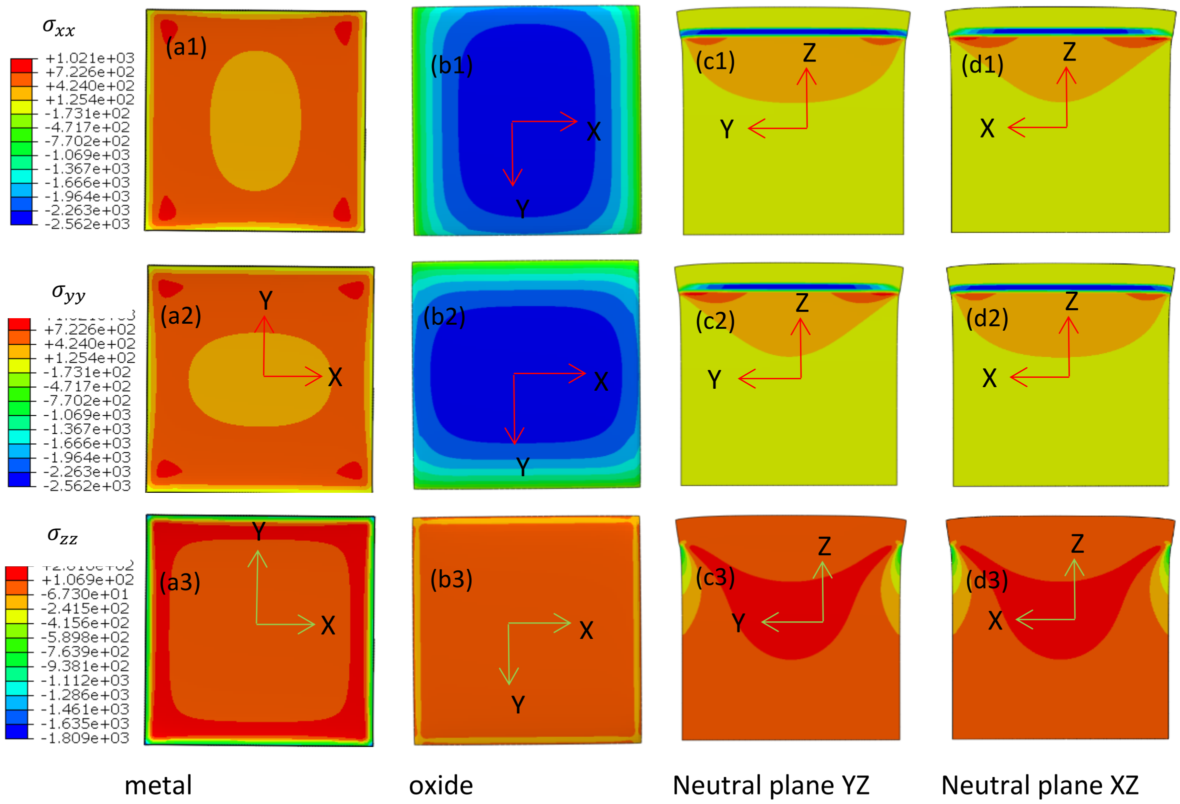

Figure 6. The stress-field nephograms

# French summary

# Introduction

Lorsqu'un métal ou un alliage métallique est oxydé à haute température, un film d'oxyde se forme généralement et la contrainte causée par la croissance de l'oxyde peut affecter le métal. Cependant, la durabilité des matériaux métalliques est une préoccupation majeure. Pour les applications à haute température, des alliages à base de chrome ont été développés afin de former des films d'oxyde de chrome dans des atmosphères oxydantes, qui protègent généralement bien contre une oxydation future. Pendant l'oxydation, une contrainte de croissance de compression se produit généralement dans l'oxyde formé thermiquement, alors que les cations et anions diffusants se rencontrent et réagissent, en particulier le long des joints de grains verticaux. Le problème est que de telles contraintes de croissance, lorsqu'elles sont combinées aux contraintes thermiques qui se développent pendant le refroidissement, peuvent provoquer et entraîner une failure de la couche d'oxyde (i. e., fissuration ou écaillage) avec des conséquences mécaniques et chimiques, ce qui limite la durée de vie des alliages dans un environnement aussi sévère.

La déformation plastique ou viscoplastique (fluage) du substrat et de l'oxyde contribue à la relaxation de la contrainte. Concernant la relaxation des contraintes, d’après les cartes d'Ashby, il s'agit généralement d'un fluage de l'oxyde plutôt que d'un délaminage, pour la chromine sollicitée à des températures suffisamment élevées et avec des grains fins. A partir de travaux antérieurs concernant les alliages NiCr, il a été montré que les contraintes sont relaxées par fluage dans le film de chromine pour des tailles de grain généralement comprises entre 0,2 et 0,8 µm. Les études de relaxation de la contrainte dans les couches de chromine ont été réalisées in-situ, après avoir imposé un changement brutal de température introduisant une source de contrainte supplémentaire liée à la différence entre les coefficients de dilatation thermique de l'oxyde et de l'alliage.

Pour améliorer les propriétés de protection de la couche d'oxyde de chrome obtenue par croissance thermique lors d'une oxydation à haute température, des éléments réactifs sont souvent introduits dans le matériau ou à la surface d'un alliage métallique, comme l'oxyde d'yttrium (Y2O3/yttria) et le zirconium (Zr). Il a été démontré que ces types d'éléments réactifs diminuent la cinétique d'oxydation et augmentent significativement l'adhésion de la couche d'oxyde de chrome au substrat métallique. Cependant, l'influence de l'ajout d'éléments réactifs sur les paramètres du fluage ou de la croissance de l'oxyde a été insuffisamment étudiée, ce qui sera notamment discuté dans ce travail.

Des modèles analytiques ont été établis pour prédire l'évolution des contraintes, mais à notre connaissance, la majorité d'entre eux considèrent généralement un état mécanique homogène par morceau dans la couche d'oxyde et dans le substrat. Cependant, dans des situations réelles, la distribution des contraintes est liée à l'hétérogénéité du système, en particulier pour le substrat métallique. Dans les travaux précédents, ce type de modèle homogène par morceau a été appliqué pour optimiser les paramètres thermomécaniques. Cependant, ce modèle analytique existant est adapté pour analyser les résultats obtenus à partir d'expériences en mode réflexion par diffraction des rayons X synchrotron à haute énergie, notamment réalisées à l'ESRF. Pour améliorer notre compréhension de la distribution spatiale des contraintes dans le substrat pour un système duplex oxyde-substrat métallique, une méthode spécifique en mode transmission par diffraction des rayons X synchrotron de haute énergie a été développée, qui nécessite une comparaison avec des modèles plus avancées tenant compte de l’hétérogénéité du système.

L'objectif principal de ce travail est donc d'étudier finement l’état mécanique dans les systèmes métal + oxyde thermique dans un environnement à haute température (typiquement au-dessus de 600°C) et de permettre d'étudier l'hétérogénéité de cet état mécanique. Pour cela, une approche expérimentale et numérique a été développée. Dans cette thèse, une liste de questions sera répondue :

1. Comment mettre en place un modèle thermomécanique adapté pour décrire le comportement mécanique des systèmes métal + oxyde thermique à haute température ?

2. Comment déterminer la distribution contrainte pendant l'oxydation à haute température ou à la température ambiante en utilisant différents modes d'équipement XRD à haute énergie ?

3. Comment optimiser les paramètres mécaniques des échantillons avec des éléments réactifs et expliquer les mécanismes associés ?

4. Comment établir un modèle pour expliquer la distribution spatiale des contraintes liée à l'hétérogénéité de l’état mécanique du système ?

5. Comment développer un modèle numérique et l'implémenter dans Abaqus pour simuler l'état mécanique de ces systèmes ?

Ce manuscrit de thèse de doctorat est composé de 5 chapitres :

Le premier chapitre fournit une présentation du modèle thermomécanique avec une revue générale de la bibliographie, qui présente les phénomènes se produisant pendant l'oxydation à haute température et le processus de refroidissement. Il comprend la cinétique de croissance et d'oxydation, les sources de contrainte et la relaxation de la contrainte mécanique.

Le deuxième chapitre contient la procédure expérimentale et les résultats préliminaires. Les substrats matériels étudiés dans cette thèse sont également présentés. Deux méthodes spécifiques sont proposées pour traiter les résultats obtenus par différents modes d'équipement XRD à haute énergie (réalisés au sein des grands instruments ESRF et DESY).

Le troisième chapitre présente l'optimisation des paramètres mécaniques des échantillons avec et sans éléments réactifs. Les données sont obtenues en mode réflexion par XRD en utilisant la procédure de détermination des contraintes présentée dans le chapitre deux. En appliquant le modèle thermomécanique proposé dans le premier chapitre, les paramètres mécaniques sont ainsi obtenus et les mécanismes associés sont discutés.

Le quatrième chapitre traite de l'hétérogénéité de l'état mécanique et de la distribution spatiale des contraintes. Les données sont obtenues par XRD en transmission en utilisant la procédure de détermination des contraintes présentée dans le chapitre 2. Pendant l'oxydation, l'appauvrissement du chrome dans le substrat ne peut être ignoré, ce qui introduit des cavités dans la zone proche de l'interface du substrat. Ces cavités provoquent une déformation dite chimique. Si l'on considère l'équilibre mécanique, il s'agira d'une source de contrainte supplémentaire importante dans le substrat. La concentration du profil de chrome fournit une hétérogénéité du phénomène, qui est considérée comme étant liée à la distribution spatiale de la contrainte.

Le cinquième chapitre présente un modèle numérique dans Abaqus, qui peut être utilisé pour simuler l'état mécanique de ces systèmes. La procédure d'établissement du modèle numérique est présentée en détail. En comparant les résultats de la simulation et les résultats expérimentaux, les paramètres mécaniques peuvent être vérifiés et cela nous aide à mieux comprendre les phénomènes associés au modèle proposé pour valider leur pertinence ou proposer de possibles améliorations.

# 1. Développement et relaxation des contraintes dans la couche d'oxyde et la couche métallique

## 1.1 Sources de contraintes

### 1.1.1 Partie élastique

La déformation élastique est la pierre angulaire de toutes les discussions à l'échelle macro et à l'échelle micro, qui fournit une relation entre la déformation et les contraintes. Le modèle classique de Hooke est utilisé pour la déformation élastique $\varepsilon^{\mathrm{elastic}}$ dans le métal et dans l'oxyde [1], pour une contrainte dans le plan :

$$\varepsilon^{elastic} = \left(\frac{1-\nu}{E}\right)\sigma \tag{1.1}$$

Dans un formalisme en vitesse de déformation [2], par l'utilisation de la dérivée temporelle de l'équation 1.1, cela conduit à :

$$\frac{d\varepsilon^{elastic}}{dt} = \frac{d}{dT}\left(\frac{1-\nu}{E}\right)\frac{dT}{dt}\sigma + \left(\frac{1-\nu}{E}\right)\frac{d\sigma}{dt} \tag{1.2}$$

Dans cette équation, le coefficient de Poisson ν est supposé être indépendant de la température et le module de Young E est supposé aussi être dépendant de la température.

### 1.1.2 Partie thermomécanique

Des contraintes thermiques sont générées lors des variations temporelles de température en raison des différents coefficients de dilatation thermique entre l'oxyde et le substrat métallique, notamment pendant la période de refroidissement après oxydation. En général, le coefficient de dilatation thermique du métal est supérieur à celui de l'oxyde, ce qui signifie $\alpha_m > \alpha_{ox}$. Par conséquent, lors du refroidissement, la couche d'oxyde est en compression et le métal en tension. Plus la différence entre ces coefficients est grande, plus les contraintes thermiques sont importantes. Pour la contrainte thermique $\varepsilon^{\mathrm{thermal}}$ dans le métal et dans l'oxyde, on considère la dilatation thermique classique [1] :

$$\frac{d\varepsilon^{thermal}}{dt} = \alpha(T)\frac{dT}{dt} \tag{1.3}$$

### 1.1.3 Partie déformation de croissance pour l'oxyde

L'approche de Clarke a été vérifiée et généralisée par Panicaud et al [3]. La vitesse de déformation de la croissance est proportionnelle à la cinétique de la couche d'oxyde :

$$\frac{d\varepsilon^{growth}}{dt} = D_{ox}(T)\frac{dh_{ox}}{dt} \tag{1.4}$$

Pour le paramètre de déformation de croissance $D_{ox}$, il est plus difficile d'expliciter l'expression car les mécanismes dépendent du système considéré. Nous savons que le paramètre $D_{ox}(T)$ dépend des caractéristiques microstructurales et peut également dépendre de la température [4].

L'épaisseur d'oxyde $h_{ox}$ suit une évolution parabolique avec le temps d'oxydation t qui a déjà été mise en évidence expérimentalement pour le présent matériau avec une caractérisation expérimentale par analyse thermogravimétrique [4, 5]. $h_{ox}$ est l'épaisseur de la couche d'oxyde évoluant avec le temps :

$$\frac{dh_{ox}}{dt} = \frac{Ap}{2\sqrt{t}} + \frac{dAp}{dT}\frac{dT}{dt}\sqrt{t} \tag{1.5}$$

avec Ap le paramètre de la cinétique parabolique qui varie avec la température T, dans la gamme de température étudiée.

## 1.2 Relaxation des contraintes

A haute température, le comportement viscoplastique d'un matériau est déterminé par l'évolution de la vitesse de déformation correspondant au deuxième stade [6, 7]. Une loi de puissance de Norton-Hoff est souvent utilisée pour simuler la déformation viscoplastique $\varepsilon^{viscoplastic}$, telle que généralement considérée dans le métal et dans l'oxyde [1], pour une contrainte dans le plan :

$$\frac{d\varepsilon^{viscoplastic}}{dt} = sign(\sigma)J|\sigma|^N = \frac{1}{2}sign(\sigma)\left(\frac{|\sigma|}{K}\right)^N \quad and\ N \in R \tag{1.6}$$

où J et K sont les paramètres de fluage ($\mathrm{J} = \frac{1}{2}\left(\frac{1}{\mathrm{K}}\right)^{\mathrm{N}}$) et N est l'exposant de Norton. Il s'agit déjà d'une forme en vitesse de déformation. Nous supposons que la relaxation des contraintes est causée principalement par la diffusion du fluage dans la couche d'oxyde, qui est régulée par le transport d'espèces chimiques le long des joints de grains. La même approche que celle décrite dans [6-8] a été appliquée, avec une valeur d'exposant de contrainte égale à l'unité dans le modèle de flux de Norton. Le coefficient de Norton J pour l'oxyde est donné par :

$$J_{ox} = \frac{AD_0\delta\Omega}{k_BT}\left(\frac{1}{L}\right)^3 exp\left(-\frac{Q}{RT}\right) \tag{1.7}$$

Où A est la constante de Coble sans dimension, $\mathrm{D_0}$ est le coefficient de diffusion, δ est l'épaisseur moyenne du joint de grain, Ω est le volume molaire, $\mathrm{k_B}$ est la constante de Boltzmann, L est la taille de grain moyenne et Q est l'énergie d'activation du mécanisme.

## 1.3 Modélisation thermomécanique

### 1.3.1 Condition de continuité

Pour assurer systématiquement la condition de continuité pendant tout le temps d'oxydation du métal, les hypothèses les plus importantes sont :

- Les effets bidimensionnels tels que le froissement (rumpling) ne sont pas considérés.

- Les phénomènes mécaniques non linéaires (flambage, fissuration, écaillage) ne sont pas pris en compte.

De plus, la température peut évoluer avec le temps, mais aucun gradient spatial de température n'est considéré. En raison de l'adhérence entre la couche d'oxyde et le substrat métallique, après les calculs, l'équation de continuité peut être exprimée comme suit, quel que soit le temps :

$$\varepsilon_m = \varepsilon_{ox} \tag{1.8}$$

Les indices "ox" et "m" désignent respectivement la couche d'oxyde et la couche métallique. Avec la décomposition de la déformation proposée, on obtient :

$$\left(\varepsilon^{elastic} + \varepsilon^{viscoplastic} + \varepsilon^{thermal}\right)_m = \left(\varepsilon^{elastic} + \varepsilon^{viscoplastic} + \varepsilon^{thermal} + \varepsilon^{growth}\right)_{ox} \tag{1.9}$$

### 1.3.2 Équilibre mécanique global

Pour calculer l'évolution des contraintes pendant l'oxydation d'un métal, les hypothèses les plus importantes sont les suivantes :

- Le système a un comportement isotrope et présente un état de contrainte biaxial.

- La déformation chimique n'est pas prise en compte, à ce stade des modèles développés par notre équipe.

- L'oxydation symétrique des deux faces métalliques est considérée.

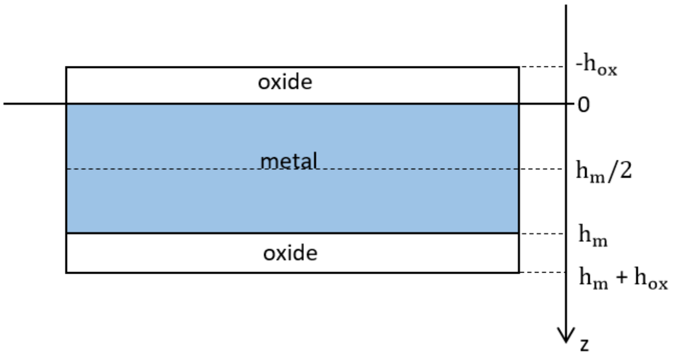

Figure 1.1 Géométrie de l'oxyde croissant sur un métal

La Fig.1.1 présente la géométrie de la croissance de l'oxyde sur un métal. Ainsi, l'équation de l'équilibre mécanique peut être exprimée comme suit :

$$\int_{0}^{h_m} \sigma_m(z)dz + \int_{-h_{ox}}^{0} \sigma_{ox}\, dz + \int_{h_m}^{h_m+h_{ox}} \sigma_{ox}\, dz = 0 \tag{1.10}$$

Où $\sigma_{ox}$ est la contrainte dans l'oxyde, $h_{ox}$ est l'épaisseur de l'oxyde qui dépend du temps t, $\sigma_m(z)$ est la contrainte dans le substrat qui dépend de z, et $h_m$ est l'épaisseur du substrat [10]. L'influence de l'oxyde sur les surfaces supérieure et inférieure est l'effet principal, provoquant l'apparition de contraintes résiduelles parallèles à l'interface oxyde-métal dans le métal. En considérant une distribution homogène des contraintes ($\sigma_m$) dans le métal et l'oxyde, l'équation d'équilibre mécanique globale du métal et de l'oxyde peut être exprimée comme :

$$\sigma_m h_m + 2\sigma_{ox} h_{ox} = 0 \tag{1.11}$$

On considère une oxydation symétrique, grâce au coefficient 2 dans le bilan mécanique de l'équation 1.11. Sous forme de taux de déformation, il correspond à :

$$\dot{\sigma}_m h_m + 2\dot{\sigma}_{ox} h_{ox} + 2\sigma_{ox}\dot{h}_{ox} = 0 \tag{1.12}$$

### 1.3.3 Vers des solutions analytiques

Pour une application ultérieure, nous proposons de résoudre ce problème en condition isotherme. Les équations 1.1 à 1.12 sont simplifiées pour obtenir l'équation décrivant l'évolution de la contrainte d'oxyde avec le temps. Elle conduit à une équation différentielle ordinaire :

$$\dot{\sigma}_{ox} = \frac{\frac{\sigma_{ox}}{t}\frac{1-\nu_m}{E_m} - signe(\sigma_{ox})\left(\frac{h_m}{Ap\sqrt{t}}\right)^{1-N_m} J_m|\sigma_{ox}|^{N_m} + signe(\sigma_{ox})J_{ox}|\sigma_{ox}|^{N_{ox}}\frac{h_m}{Ap\sqrt{t}} + \frac{D_{ox}h_m}{2t}}{\left(\frac{1-\nu_{ox}}{E_{ox}}\frac{h_m}{Ap\sqrt{t}} + 2\frac{1-\nu_m}{E_m}\right)} \tag{1.13}$$

Il y a 1 paramètre géométrique et 10 paramètres matériaux à identifier : $\mathrm{h_m}, \mathrm{\nu_m}, \mathrm{E_m}, \mathrm{\nu_{ox}}, \mathrm{E_{ox}},\ \mathrm{Ap},\ \mathrm{J_m}, \mathrm{N_m}, \mathrm{J_{ox}}, \mathrm{N_{ox}}\ et\ \mathrm{D_{ox}}$. $\mathrm{h_m}$ est l'épaisseur de la pièce métallique, qui peut être facilement mesurée et qui est supposée être constante. Les valeurs numériques du module de Young de l'oxyde $Cr_2O_3$ ($\mathrm{E_{ox}}$) et du coefficient de Poisson de l'oxyde $Cr_2O_3$ ($\mathrm{\nu_{ox}}$) peuvent être trouvées dans la littérature [11]. Des valeurs numériques des autres paramètres peuvent également être trouvées dans la littérature [12] pour différentes températures, comme le module de Young du métal ($\mathrm{E_m}$), le coefficient de Poisson du métal ($\mathrm{\nu_m}$), le paramètre de cinétique parabolique (Ap), le paramètre de fluage de l'oxyde $Cr_2O_3$ ($\mathrm{J_{ox}}$), l'exposant de Norton de l'oxyde $Cr_2O_3$ ($\mathrm{N_{ox}}$), le paramètre de fluage du métal ($\mathrm{J_m}$), l'exposant de Norton du métal ($\mathrm{N_m}$) et le paramètre de déformation de croissance de l'oxyde $Cr_2O_3$ ($\mathrm{D_{ox}}$).

# 2. Introduction à la diffraction des rayons X

## 2.1 Mode en réflexion

### 2.1.1 Montage expérimental

Les expériences, utilisant le mode réflexion, ont été réalisées in-situ à haute température sur la ligne de faisceau BM02 de l'ESRF (Européen Synchrotron Radiation Facility) à Grenoble. Le faisceau de rayons X arrivant sur l'échantillon est monochromatique, avec une longueur d'onde de 0,062 nm (énergie de 20 keV).

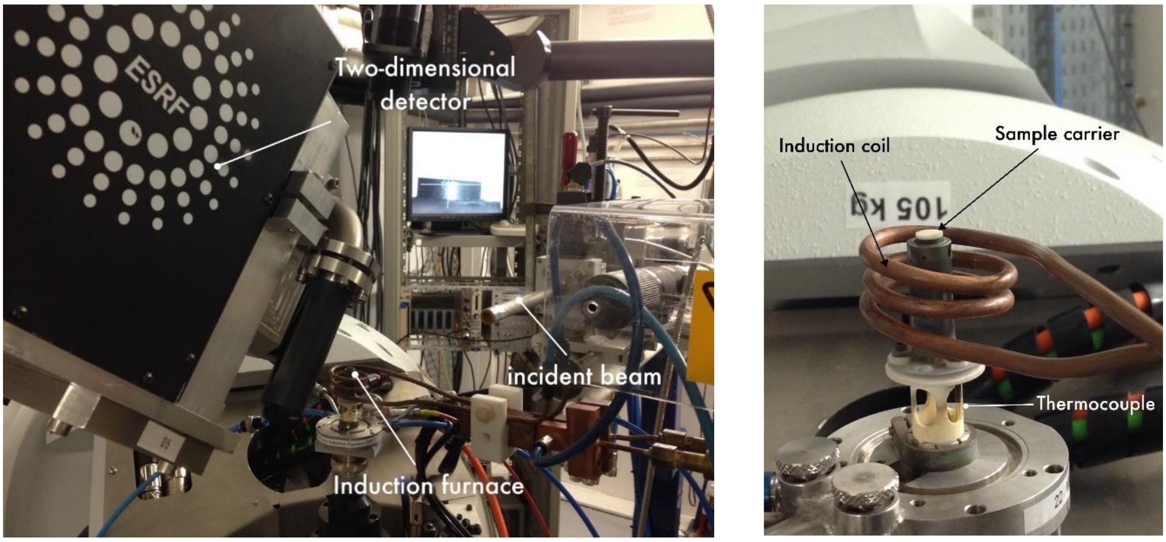

(a) (b)

Figure 2.1 L'équipement de faisceau BM02 de l'ESRF (a) et le four (b) [13].

La ligne de faisceau comprend un goniomètre, un porte-échantillon, un détecteur bidimensionnel et deux photodiodes. Le goniomètre nous permet de connaître les angles utilisés dans les calculs suivants. Le porte-échantillon est entouré d'une bobine d'induction de 7 mm de diamètre et de 4 mm de profondeur avec un générateur de haute puissance (maximum 3kW). La température maximume pouvant être atteinte est de 1600 °C. Le détecteur bidimensionnel reçoit le signal de réflexion des rayons X, qui sera analysé.

### 2.1.2 Traitement des données

Les données brutes non traitées (voir un exemple à la Fig. 2.2) sont des images des anneaux diffractés. Il faut une analyse plus poussée pour obtenir la contrainte dans les couches d'oxyde. Pour un matériau sans contrainte, les données devraient dessiner des cercles parfaits. La Fig. 2.2 montre un exemple enregistré pour le système Ni28Cr + $Cr_2O_3$.

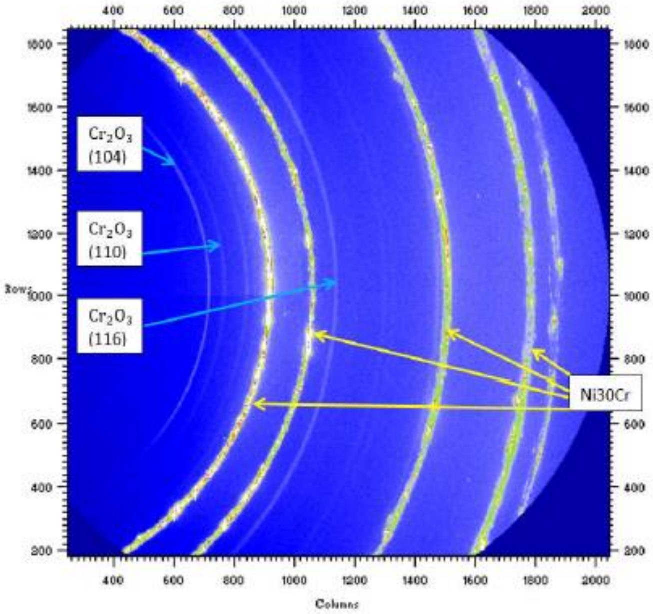

Figure 2.2 Anneaux diffractés pour le système Ni28Cr + $Cr_2O_3$

Afin d'analyser les données brutes, les anneaux ont été subdivisés en 128 secteurs γ dont les valeurs sont comprises entre {-61,5 ° et + 65,5 °} avec un pas de 1°. A partir de ces données, il est possible de tracer les intensités de chaque secteur γ en fonction de 2θ, ce qui donne un diagramme de diffraction 1D. Les pics à étudier pour l'oxyde de chrome sont (104), (110), (116), qui sont les plus intenses et les mieux définis. La position théorique de 2θ est liée à l'énergie des rayons X, où E=20 keV en mode réflexion.

Afin de choisir la meilleure simulation pour chaque diagramme de diffraction, quatre fonctions de distribution principales ont été testées pour simuler le profil des pics, à savoir Gauss, Lorentz, Pearson 7 et Pseudo-Voigt (Fig. 2.3). En outre, il est nécessaire de minimiser l'influence du fond. La relation polynomiale pour le fond est testée. Nous pouvons simuler la distribution des pics et le bruit de fond simultanément ou séparément.

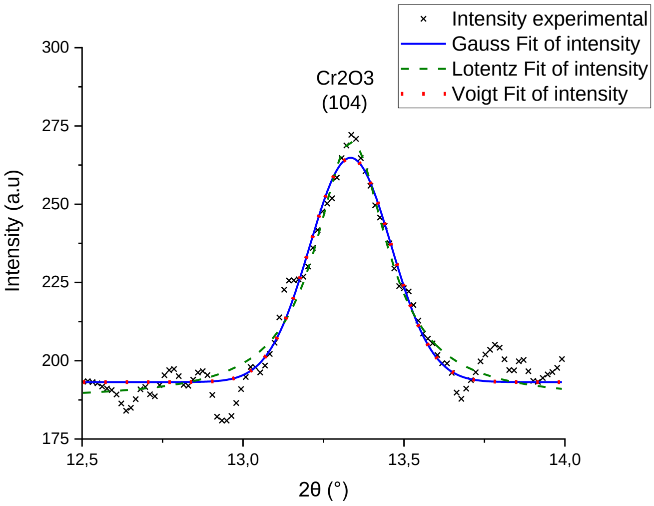

Figure 2.3 Modélisation de différents profils de pic

### 2.1.3 Méthode des $\mathrm{Sin}^2\psi$

Lorsqu'un matériau est déformé, la distance entre les plans cristallographiques $d_{hkl}$ s'allonge ou se contracte, ce qui entraîne un décalage de la position des anneaux dans le diagramme de diffraction. En retour, les changements de distance entre les plans cristallographiques peuvent être évalués par la mesure du décalage angulaire par rapport à la configuration non déformée, de sorte que la déformation élastique peut être déterminée.

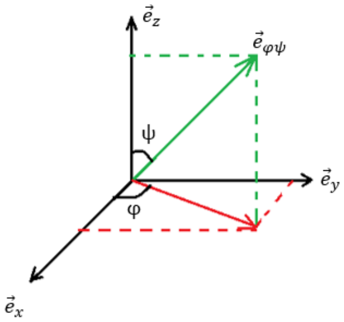

Figure 2.4 Directions et axes de mesure

La référence (x, y, z) est un système de coordonnées orthonormé lié à l'échantillon. La direction $\vec{e}_{\varphi\psi}$ est la normale aux plans de diffraction comme le montre la figure 2.4. La contrainte sur la direction $\vec{e}_{\varphi\psi}$ est :

$$\varepsilon_{\psi\varphi} = \vec{e}_{\varphi\psi}\overline{\overline{\varepsilon}}\vec{e}_{\varphi\psi} \tag{2.1}$$

Avec

$$\vec{e}_{\varphi\psi} = \sin\psi\cos\varphi\vec{e}_x + \sin\psi\sin\varphi\vec{e}_y + \cos\psi\vec{e}_z \tag{2.2}$$

et $\bar{\bar{\varepsilon}}$ est le tenseur de déformation élastique :

$$\bar{\bar{\varepsilon}} = \begin{pmatrix} \varepsilon_{xx} & \varepsilon_{xy} & \varepsilon_{xz} \\ \varepsilon_{xy} & \varepsilon_{yy} & \varepsilon_{yz} \\ \varepsilon_{xz} & \varepsilon_{yz} & \varepsilon_{zz} \end{pmatrix} \tag{2.3}$$

La déformation le long de la direction $\vec{e}_{\varphi\psi}$ peut être développée comme :

$$\varepsilon_{\psi\varphi} = \left(\varepsilon_{xx}\cos^2\varphi + \varepsilon_{yy}\sin^2\varphi + \varepsilon_{xy}\sin2\varphi - \varepsilon_{zz}\right)\sin^2\psi + \left(\varepsilon_{xz}\cos\varphi + \varepsilon_{yz}\sin\varphi\right)\sin(2\psi) + \varepsilon_{zz} \tag{2.4}$$

La déformation vraie le long de la direction $\vec{e}_{\varphi\psi}$ peut également être obtenue en comparant la distance non déformée $d_0$ entre les plans cristallographiques avec la distance déformée d.

$$\varepsilon_{\psi\varphi} = \ln\left(\frac{d}{d_0}\right) = \ln\left(\frac{\sin\theta_0}{\sin\theta}\right) \tag{2.5}$$

Si nous supposons que l'élasticité du matériau est linéaire, homogène et isotrope, la conversion de la déformation élastique en contrainte peut se faire en utilisant le modèle de Hooke selon :

$$\bar{\bar{\varepsilon}} = \frac{1+\nu}{E}\bar{\bar{\sigma}} - \frac{\nu}{E}\operatorname{trace}(\bar{\bar{\sigma}})\bar{\bar{I}} \tag{2.6}$$

avec trace $\bar{\bar{\sigma}}$ est le premier invariant du tenseur des contraintes et $\bar{\bar{I}}$ est le tenseur identité tridimensionnel (3D). Avec l'hypothèse de l'isotropie transversale pour un état de contrainte dans le plan comme prévu dans l'oxyde, nous pouvons simplifier l’expression du tenseur des contraintes. De plus, nous considérons qu'il n'y a pas de contrainte de cisaillement et nous supposons l'absence de gradient de contrainte. Finalement, on écrira :

$$\bar{\bar{\sigma}} = \begin{pmatrix} \sigma & 0 & 0 \\ 0 & \sigma & 0 \\ 0 & 0 & 0 \end{pmatrix} \tag{2.7}$$

La relation de contrainte $\sin^2\psi$ est obtenue en simplifiant les équations 2.4 à 2.7, qui indiquent le lien entre le décalage angulaire, correspondant à la différence entre $\theta_0$ et $\theta$, et la contrainte.

$$\ln\left(\frac{\sin\theta_0}{\sin\theta}\right) = \frac{1+\nu}{E}\sigma\sin^2\psi - \frac{\nu}{E}2\sigma \tag{2.8}$$

En utilisant les coefficients élastiques radio-cristallographiques Sij, la relation $\sin^2\psi$ devient :

$$\ln\left(\frac{1}{\sin\theta}\right) = \frac{1}{2}S_{2(hkl)}\sigma\sin^2\psi + 2S_{1(hkl)}\sigma - \ln(\sin\theta_0) \tag{2.9}$$

La pente de cette droite correspond à $\frac{1}{2}S_{2(hkl)}\sigma$ et l'ordonnée à l'origine correspond à $2S_{1(hkl)}\sigma - \ln(\sin\theta_0)$.

## 2.2 Mode en transmission

### 2.2.1 Montage expérimental

Les expériences ont été menées sur la ligne de faisceau PETRA P07-EH2 (DESY-Petra III, Hambourg, Allemagne). Un faisceau à haute énergie (E=103.4 keV) de forme rectangulaire et de petite dimension le long de l'axe vertical (300x2 microns²) a été utilisé couplé à une translation verticale à 10 microns/s et à un détecteur Perkin-Elemer 2D rapide avec une fréquence d'images de 10 Hz. Ceci permet d'obtenir une image 2D (2048x2048 pixels) contenant les anneaux complets de Debye-Scherrer, chaque pas de 2 micron correspondant à un volume de diffraction de 300x(taille de l'échantillon)x3 microns. Le détecteur a été placé à 1,5 m de l'échantillon. La surface supérieure de l'échantillon a été alignée avec le faisceau en utilisant des courbes de balancement et des scans d'absorption pour différentes orientations autour de l'axe vertical.

### 2.2.2 Traitement des données

Les données brutes (voir un exemple à la Fig. 2.5) correspondent à une image de l'anneau de diffraction. D'autres traitements sont nécessaires pour obtenir la contrainte.

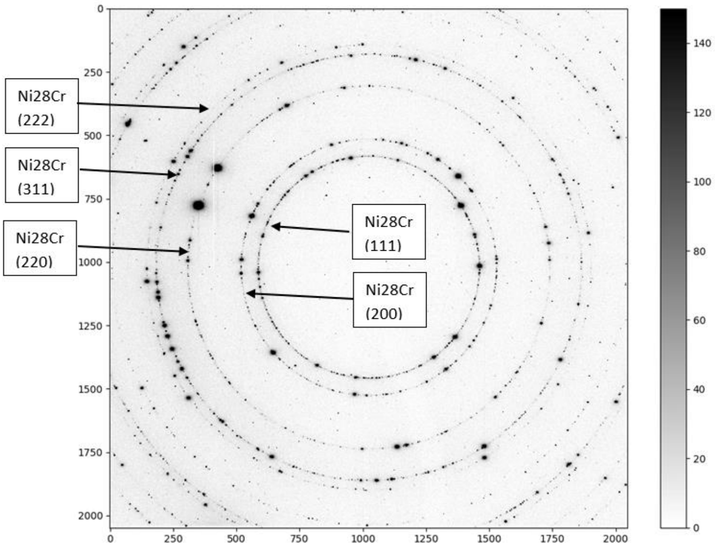

Figure 2.5 Anneaux diffractés pour le substrat Ni28Cr

Le processus de traitement des données est assez similaire à celui de la XRD en mode réflexion, qui a été abordé dans la section 2.1.2.

### 2.2.3 Méthode des Sin²ϕ

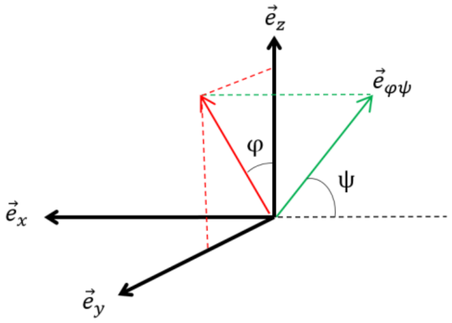

Figure 2.6 Directions et axes de mesure

Comme montré sur la figure 2.6, la référence (x, y, z) est un système de coordonnées orthonormé lié à l'échantillon. La contrainte sur la direction $\vec{e}_{\varphi\psi}$ est :

$$\varepsilon_{\psi\varphi} = \vec{e}_{\varphi\psi}\bar{\bar{\varepsilon}}\vec{e}_{\varphi\psi} \tag{2.10}$$

Avec

$$\vec{e}_{\varphi\psi} = -cos\psi\vec{e}_x + sin\psi sin\varphi\vec{e}_y + sin\psi cos\varphi\vec{e}_z \tag{2.11}$$

et $\bar{\bar{\varepsilon}}$ est le tenseur de déformation élastique en supposant qu'il n'y a pas de déformation de cisaillement :

$$\bar{\bar{\varepsilon}} = \begin{pmatrix} \varepsilon_{xx} & 0 & 0 \\ 0 & \varepsilon_{yy} & 0 \\ 0 & 0 & \varepsilon_{zz} \end{pmatrix} \tag{2.12}$$

La déformation le long de la direction $\vec{e}_{\varphi\psi}$ peut être développée comme :

$$\varepsilon_{\psi\varphi} = cos^2\psi\varepsilon_{xx} + sin^2\psi sin^2\varphi\varepsilon_{yy} + sin^2\psi cos^2\varphi\varepsilon_{zz} \tag{2.13}$$

La déformation vraie le long de la direction $\vec{e}_{\varphi\psi}$ peut également être calculée en comparant la distance non déformée $d_0$ entre les plans cristallographiques avec la distance déformée d.

$$\varepsilon_{\psi\varphi} = ln\left(\frac{d}{d_0}\right) = ln\left(\frac{sin\theta_0}{sin\theta}\right) \tag{2.14}$$

En supposant que l'élasticité du matériau est linéaire, homogène et isotrope, la conversion de la déformation élastique en contrainte peut être effectuée en utilisant le modèle de Hooke selon :

$$\bar{\bar{\varepsilon}} = \frac{1+\nu}{E}\bar{\bar{\sigma}} - \frac{\nu}{E}\mathrm{trace}(\bar{\bar{\sigma}})\bar{\bar{I}} \tag{2.15}$$

La contrainte de cisaillement n'est pas considérée comme dans les travaux précédents [10, 14]. De plus, une contrainte normale $\sigma_N$ le long de l'axe z est considéré. Le tenseur $\overline{\overline{\sigma}}$ doit être :

$$\overline{\overline{\sigma}} = \begin{pmatrix} \sigma & 0 & 0 \\ 0 & \sigma & 0 \\ 0 & 0 & \sigma_N \end{pmatrix} \tag{2.16}$$

En appliquant les coefficients élastiques radio-cristallographiques Sij, la relation sin²ϕ devient :

$$\begin{aligned} ln\left(\frac{1}{sin\theta}\right) = \frac{1}{2}S_{2(hkl)}(\sigma - \sigma_N)cos^2\theta_0 sin^2\varphi + \frac{1}{2}S_{2(hkl)}\sigma + S_{1(hkl)}(2\sigma + \sigma_N) \\ + \frac{1}{2}S_{2(hkl)}(\sigma_N - \sigma)cos^2\theta_0 - ln(sin\theta_0) \end{aligned} \tag{2.17}$$

# 3. Optimisation des paramètres thermomécaniques

## 3.1 Processus d'optimisation

### 3.1.1 Matériaux

Le matériau de base étudié est un alliage NiCr. L'alliage qui a été utilisé dans ces expériences réalisées à l'ERSF et présentées dans ce chapitre, contient un pourcentage massique de 28,28% de Cr, symbolisé par Ni28Cr. Dans le but d'étudier l'influence des éléments réactifs sur les propriétés mécaniques des couches de chrome, plusieurs groupes d'expériences ont été réalisés avec les éléments réactifs $Y_2O_3$ ou Zr. Afin d'appeler plus facilement l'échantillon, nous avons donné des noms de code aux échantillons Ni28Cr avec différents temps d'exposition correspondant à différentes quantités de $Y_2O_3$ dans l'alliage, comme indiqué dans le tableau 3.1, et aux échantillons Ni28Cr avec différentes fluences de dopage correspondant à différentes quantités de Zr dans l'alliage, comme indiqué dans le tableau 3.2 :

Table3.1. Noms de code pour l'échantillon Ni28Cr avec différents temps d'exposition

| Noms de code | temps d'exposition |
|---|---|
| $Y_2O_3$_t10 | t = 10s |
| $Y_2O_3$_t50 | t = 50s |
| $Y_2O_3$_t100 | t = 100s |

Table 3.2. Noms de code pour l'échantillon Ni28Cr avec différentes fluences de dopage

| Noms de code | fluences de dopage |
|---|---|
| Zr_1E15 | 1*$10^{15}$ ions.$cm^{-2}$ |
| Zr_5E15 | 5*$10^{15}$ ions.$cm^{-2}$ |
| Zr_1E16 | 1*$10^{16}$ ions.$cm^{-2}$ |

### 3.1.2 Principe de l'optimisation

La sollicitation thermique appliquée à l'échantillon Ni28Cr sans prétraitement est présentée à la Fig. 3.1 :

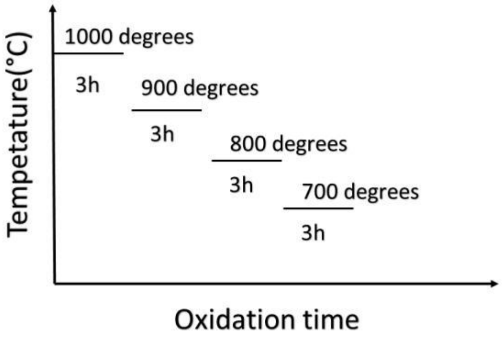

Figure 3.1. Sollicitation thermique pour l'échantillon Ni28Cr

La méthode d'optimisation des paramètres est basée sur la comparaison des contraintes en fonction du temps et de la solution numérique. En faisant varier les paramètres (le paramètre de déformation de croissance pour l'oxyde ($\mathrm{D_{ox}}$) et le paramètre de fluage pour l'oxyde ($\mathrm{J_{ox}}$)), la solution numérique peut être rendue aussi similaire que possible aux contraintes expérimentales en fonction du temps. La manière de trouver la meilleure solution numérique par rapport aux contraintes dépendant du temps est appelée optimisation des paramètres et correspond à un fitting plateau par plateau.

En raison de la protection induite par la couche d'oxyde de chrome formée à 1273K, il n'y a plus de croissance significative de la couche d'oxyde à un plateau de température inférieur. Ceci a été vérifié par l'ATG par l'évolution de la masse dans la phase d'oxyde. De plus, il est montré dans [15] que l'évolution des intensités de diffraction ne change plus après le plateau de température le plus élevé. Par conséquent, $\mathrm{D_{ox}}$ peut être choisi égal à zéro à 973K, 1073K et 1173K avec une bonne confiance, lorsqu'un plateau précédent à une température plus élevée est réalisé [8]. En outre, le paramètre de la cinétique parabolique (Ap) est égal à zéro, en raison de l'absence de croissance significative de l'oxyde sur les plateaux de température inférieure. Ainsi, le seul paramètre à identifier pour ces plateaux à basse température est $\mathrm{J_{ox}}$.

De plus, une condition pour un fitting correct est que $\mathrm{J_{ox}(T)}$ ait également une signification physique. Le paramètre $\mathrm{J_{ox}(T)}$ peut être décrit comme suit :

$$J_{ox} = \frac{Cste}{k_B T} \exp\left(-\frac{Q}{RT}\right) \tag{3.1}$$

où Cste est une constante, $k_B$ est la constante de Boltzmann et Q est l'énergie d'activation associée au mécanisme de fluage considéré. Cette équation peut être transformée en :

$$Ln(J_{ox} k_B T) = Ln(Cste) - \frac{Q}{R} \times \frac{1}{T} \tag{3.2}$$

Si nous traçons la courbe de $Ln(J_{ox} k_B T)$ en fonction de 1/T pour différentes températures, nous devrions obtenir une ligne droite et l'énergie d'activation Q peut être déduite de la pente de cette ligne. En traçant la courbe $Ln(J_{ox} k_B T)$ en fonction de 1/T avec $J_{ox}$ pour les plateaux de température à 973K, 1073K et 1173K, on peut extrapoler la valeur théorique de $J_{ox}$ pour 1273K. En utilisant cette valeur théorique de $J_{ox}$ pour 1273K à la première itération, nous pouvons fitter le premier plateau de température à 1273K et optimiser les valeurs de $J_{ox}$ et $D_{ox}$ en même temps.

### 3.1.3 Exemples de l'optimisation réalisée

Pour les échantillons implantés d'yttria, il n'y a pas de plateau de chargement thermique à 973K. La simulation des données expérimentales de l'échantillon $Y_2O_3\_t10$ et la procédure d'optimisation pour les plateaux 1073K, 1173K et 1273K sont présentées dans les Figs. 3.2 a.b.c.

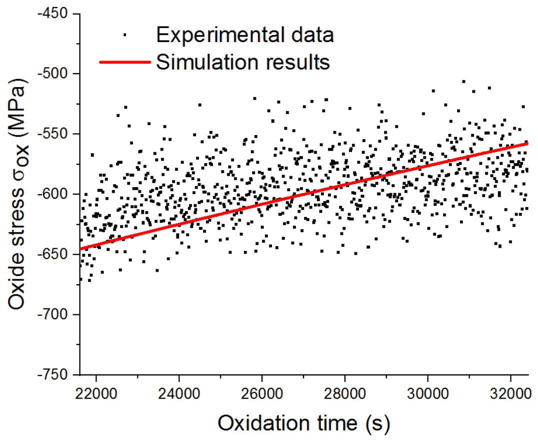

(a)

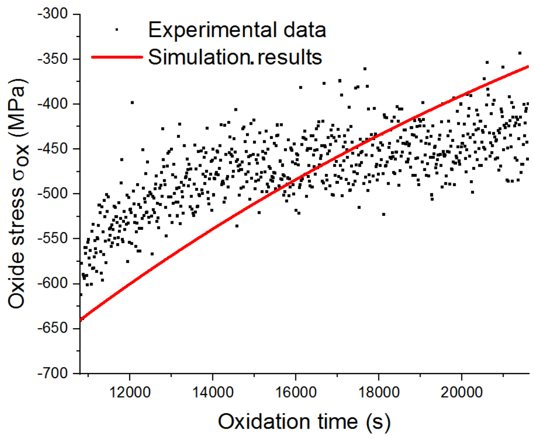

(b)

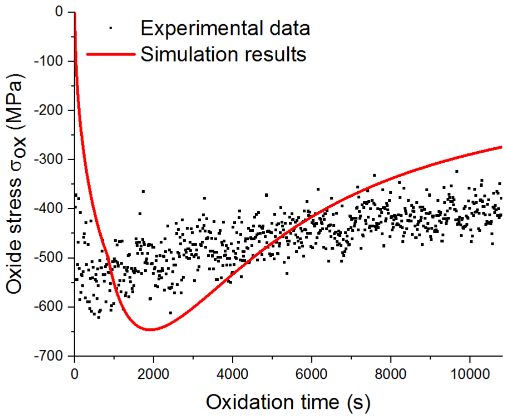

(c)

Figure 3.2 Fitting pour le paramètre $J_{ox}$ à 1073K (a), pour le paramètre $J_{ox}$ à 1173K (b), pour les paramètres $J_{ox}$ et $D_{ox}$ à 1273K (c)

Les figures 3.2.a.b.c montrent les simulations de $J_{ox}$ pour l'échantillon $Y_2O_3\_t10$ avec Nox = 1, qui correspondent à la plus faible quantité d'oxyde d'yttrium déposée. La Fig 3.2.c indique que l'évolution de la contrainte est le résultat d'un équilibre entre deux phénomènes, qui sont l'augmentation de la contrainte en valeur absolue principalement causée par la croissance de la couche d'oxyde et la relaxation de la contrainte principalement causée par le comportement de fluage. Au début du plateau 1273K, l'augmentation de la contrainte tient une position dominante, jusqu'à environ 714s quand la contrainte atteint -646MPa. Après cela, la relaxation de la contrainte occupe principalement la position dominante dans l'équilibre mécanique. Les figures 3.2.a et 3.2.b indiquent qu'il n'y a pas d'augmentation de la contrainte, en relation avec la protection de la couche d'oxyde formée à 1273K. Cela indique également que la couche d'oxyde formée à haute température empêche la formation de la couche d'oxyde à des températures plus basses. Ce phénomène a été discuté dans des travaux précédents avec un modèle simple [13]. Dans le présent travail, un modèle thermomécanique plus complet est appliqué qui obtient la même conclusion, ce qui confirme également que l'épaisseur de la couche d'oxyde n'augmente pas lorsque des sauts de température ont été appliqués vers des valeurs inférieures. La contrainte a été relaxée durant 2 périodes isothermes pendant 6h (3h pour 1173K et 3h pour 1073K). La contrainte relaxée durant ces plateaux de température est de 280 MPa à 1173 K et de 90 MPa à 1073 K.

## 3.2 Résultats pour les différents matériaux

### 3.2.1 Résultats pour les matériaux implantés avec de l'oxyde d'yttrium

Les valeurs de $J_{ox}$ en fonction de la température sont présentées à la Fig. 3.3(a) et les régressions linéaires de $\mathrm{Ln}(\mathrm{J_{ox}k_BT})$ en fonction de 1/T sont présentées à la Fig. 3.3(b):

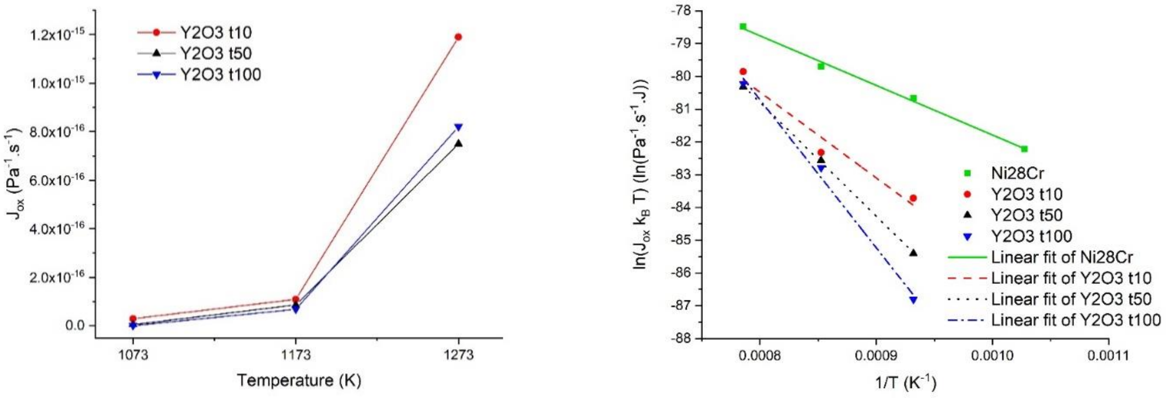

Figure 3.3. $J_{ox}$ en fonction de la température pour les différents échantillons implantés d'yttria (a), régression linéaire de $\mathrm{Ln}(\mathrm{J_{ox}k_BT})$ en fonction de 1/T (b).

La figure 3.3 indique que pour le matériau brut et pour tous les matériaux implantés d'oxyde d'yttrium, le paramètre de fluage $J_{ox}$ diminue avec une température plus basse, ce qui prouve l'activation thermique du mécanisme de fluage suivant un modèle d'Arrhenius. De plus, ce comportement est observé indépendamment de la quantité d'yttrium introduite. Pour ces systèmes {Ni28Cr + yttria-implanté + Cr2O3}, lorsque la quantité d'yttria augmente, la pente devient plus élevée ce qui correspond à une augmentation de l'énergie d'activation. Les énergies d'activation ont été déduites pour tous les différents matériaux. L'énergie d'activation pour les dépôts d'yttrium de 10s et 50s est respectivement de 2.25eV et 2.99eV, ce qui est beaucoup plus élevé que l'énergie d'activation pour la matière brute sans dépôt qui vaut 1.42eV.

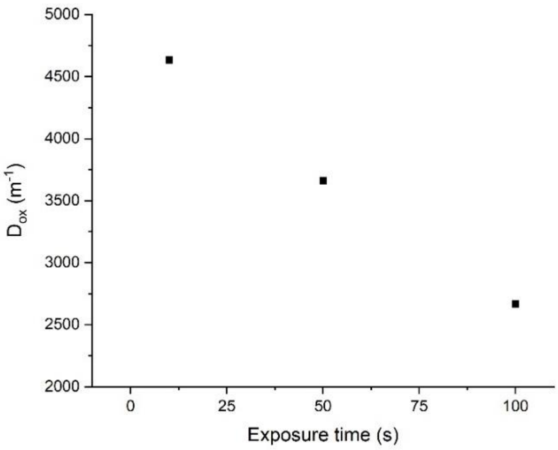

Figure 3.4. Paramètre de la déformation de croissance en fonction du temps d'exposition à 1273K

La Fig. 3.4 donne l'évolution du paramètre $\mathrm{D_{ox}}$ en fonction du temps d'exposition ; ainsi, lorsque la quantité d'yttria augmente, les valeurs de $\mathrm{D_{ox}}$ diminuent. Sachant que $\mathrm{D_{ox}}$ est le paramètre de croissance de l'oxyde, avec un $\mathrm{D_{ox}}$ plus faible, la contrainte de croissance diminue.

# 4. Distribution spatiale des contraintes

## 4.1 Résultats expérimentaux

### 4.1.1 Matériaux

Les matériaux étudiés sont différents alliages NiCr. Dans le but de mieux comprendre la distribution des contraintes dans le substrat, plusieurs échantillons ont été élaborés.

Tableau 4.1. Noms de code pour les échantillons de différentes formes et conditions d'oxydation

| Nom de code | Composition chimique | Forme | Taille | Température d'oxydation | Temps d'oxydation |
|---|---|---|---|---|---|
| Cyl_T1000_1h | Ni28Cr | cylindre | Ø6x0.9 mm | 1000 °C | 1 h |
| Cyl_T1000_5h | Ni28Cr | cylindre | Ø6x0.9 mm | 1000 °C | 5 h |
| Rec_T900_10h | Ni35Cr | rectangulaire | 6x6x0.4 mm | 900 °C | 10 h |
| Rec_T800_10h | Ni35Cr | rectangulaire | 6x6x0.4 mm | 800 °C | 10 h |

### 4.1.2 Résultats des échantillons avec différentes formes et conditions d'oxydation

La DRX en mode transmission peut être utilisée pour déterminer la distribution des contraintes résiduelles dans le substrat en fonction de la profondeur. Pour les échantillons ayant des formes et des conditions d'oxydation différentes, trois directions de pénétration ont été systématiquement appliquées : 0°, 90° et -90°, qui sont liées à la rotation propre de la position de l'échantillon autour de l'axe z. Afin d'étudier la distribution des contraintes en fonction de la profondeur, la contrainte moyenne sur les trois directions de rotation a été calculée. Simultanément, les écarts standards de l'échantillon sont également obtenus.

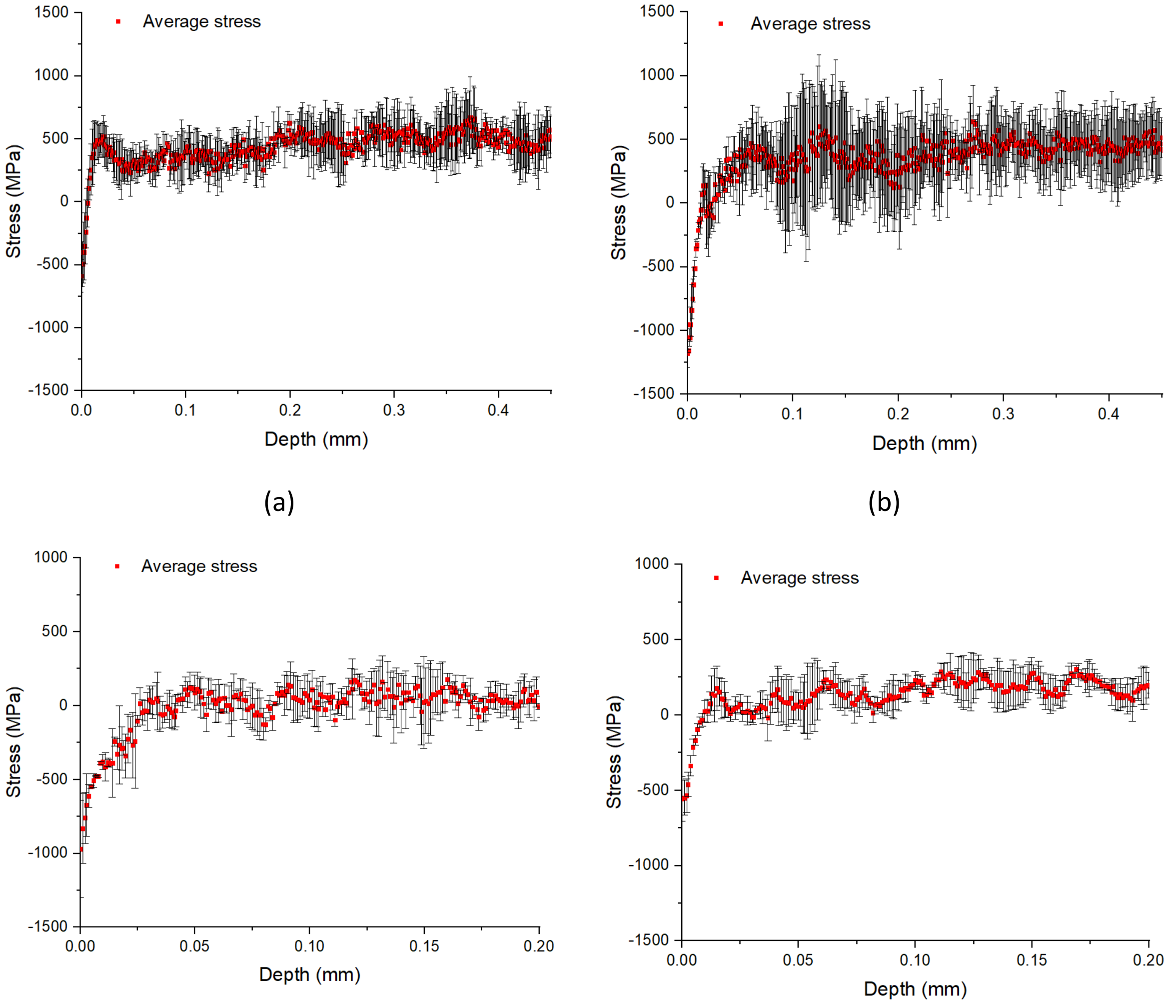

(a) (b)

(c) (d)

Figure 4.1. Contrainte moyenne sur les trois directions de rotation en fonction de la profondeur de l'échantillon Cyl_T1000_1h (a), Cyl_T1000_5h (b), Rec_T900_10h (c), Rec_T800_10h (d).

Les Fig. 4.1 a-d indiquent que la contrainte minimale apparaît à l'interface oxyde/métal. Il montre qu'avec la même température d'oxydation, plus le temps d'oxydation est long, plus la contrainte minimale est faible ; et avec le même temps d'oxydation, plus la température d'oxydation est élevée, plus la contrainte minimale est faible. Pour tous les échantillons, il y a un gradient de contrainte dans la zone proche de la surface sur une profondeur d'environ 20 µm.

## 4.2 Proposition de la source de contrainte

### 4.2.1 Profils de concentration en chrome

Afin d'analyser la distribution des contraintes dans le substrat métallique, une contrainte chimique/de diffusion est introduite et proposée dans la modélisation, car les résultats expérimentaux montrent qu'un gradient de contrainte apparaît près de l'interface du métal et de la couche d'oxyde. En effet, dans de tels matériaux, le profil de concentration indique que la concentration de chrome change près de l'interface du métal et de la couche d'oxyde dans un tel système [16-18], ce qui a été prouvé comme ayant un effet sur l'espacement de réseau (distance interréticulaire d) entre les plans cristallographiques dans le matériau. La variation de Cr crée une déformation chimique, qui est une source de contrainte. Le gradient de cette concentration conduit à un gradient de déformation donc à un gradient de contrainte. Cette variation de concentration peut être observée à travers la variation de la position angulaire d'un pic de diffraction (loi de Végard). Ainsi, une déformation chimique reliée à la diffusion est proposée.

Pour calculer le profil de concentration du chrome, on utilise la diffusion 1D de la loi de Fick :

$$D\frac{\partial^2[Cr](z,t)}{\partial z^2}-\frac{\partial[Cr](z,t)}{\partial t}=0 \tag{4.1}$$

où D est le coefficient de diffusion du chrome dans l'alliage ; [Cr] est la concentration en pourcentage massique de l'élément Cr, et z est la profondeur. Le coefficient de diffusion D de l'élément Cr dans le système des alliages Nickel-Chrome a été étudié dans [17, 18]. Dans le travail de Ruzickova, J et al. [17], l'alliage utilisé est Ni29.4Cr et l'alliage est Ni30Cr dans le travail de Monma, K et al. [18], qui sont assez similaires aux alliages étudiés dans notre présent travail. Une loi d'Arrhenius est par ailleurs proposée pour décrire la dépendance à la température :

$$D=D_0exp\left(\frac{-Q}{RT}\right) \tag{4.2}$$

où $D_0$ est le facteur pré-exponentiel, Q l'énergie d'activation, R la constante du gaz idéal et T la température. Le coefficient de diffusion à 800°C, 900°C et 1000°C peut être calculé (Tableau 4.2) à partir de l'équation 4.2 en utilisant les données de la littérature [17, 18].

Tableau 4.2. Coefficient de diffusion avec $D_0$=297.5 $mm^2/s$ et Q=288.8kJ

| T (K) | D ($mm^2/s$) |
|---|---|
| 1073 | $2.59038*10^{-12}$ |
| 1173 | $4.09273*10^{-11}$ |
| 1273 | $4.19124*10^{-10}$ |

Pour analyser la concentration du chrome dans notre système, les conditions initiales (IC) et les conditions limites (BC) sont considérées comme suit :

$$\begin{cases} IC: \quad [Cr]_i=[Cr](z,0)=28.28\% \text{ or } 34.5\% \\ BC1: \quad \frac{\partial[Cr](z,t)}{\partial z}=0, z=\frac{h_m}{2}, 0<t<\infty \\ BC2: \quad [Cr](0,t)=\alpha[Cr]_i, 0<t<\infty \end{cases} \tag{4.3}$$

La condition initiale indique qu'au moment initial, la concentration du chrome est de 28,28% pour toutes les profondeurs des échantillons cylindriques et de 34,5% pour les échantillons rectangulaires. La première condition aux limites (BC1) indique qu'à tout moment, le taux de concentration de Cr au niveau du plan central est égal à 0 en raison de la symétrie supposée du système. Au contraire, dans la zone proche de l'interface, l'appauvrissement du Cr ne peut être ignoré. La deuxième condition aux limites (BC2) indique qu'à l'interface oxyde/métal, la concentration de chrome est liée à la valeur initiale de 28,28% ou 34,5%. La concentration à l'interface de cation est étudiée dans [16], ce qui montre que pendant les dernières étapes de l'oxydation, la concentration à l'interface de cation augmente jusqu'à une valeur presque constante.

Les conditions données dans l'équation 4.3 sont des conditions aux limites de Neumann-Dirichlet dans notre cas. L'Eq.4.1 peut être résolue en considérant la solution générale suivante :

$$[Cr](z,t) = (1-\alpha)[Cr]_i erf(q) + \alpha[Cr]_i \tag{4.4}$$

où $[Cr]_i$ est la concentration initiale de chrome ; et $q = \frac{z}{2\sqrt{Dt}}$. Les approximations numériques de la fonction erreur erf sont données dans [19]. En combinant l'approximation numérique et l'équation 4.4, une solution analytique est obtenue sous la forme suivante :

$$[Cr](z,t) = (1-\alpha)[Cr]_i\left(1 - (a_1 n + a_2 n^2 + a_3 n^3 + a_4 n^4 + a_5 n^5)e^{-q^2}\right) + \alpha[Cr]_i \tag{4.5}$$

Avec

$$\left\{\begin{array}{c} q = \dfrac{z}{2\sqrt{Dt}} \\ n = \dfrac{1}{1+pq} \\ p = 0.3275911, a_1 = 0.254829592, a_2 = -0.284496736, \\ a_3 = 1.421413741, a_4 = -1.453152027, a_5 = 1.061405429 \\ \alpha = 0.413 \\ |error(z)| \leq 1.5 * 10^{-7} \end{array}\right. \tag{4.6}$$

### 4.2.2 Proposition pour la contrainte de diffusion

En raison de l'importante variation spatiale de la concentration en chrome dans la zone proche de la surface, nous proposons d'associer une déformation directement liée aux profils de concentration en chrome [20].

$$\bar{\bar{\varepsilon}}^{diffusion}(z) = \eta([Cr](z,t) - [Cr]_i)\bar{\bar{I}} \tag{4.7}$$

où $\bar{\bar{\varepsilon}}^{diffusion}(z)$ est la déformation due à la diffusion de Cr, qui est fonction de z ; η est un coefficient constant couplant les profils de concentration en chrome à la déformation de diffusion ; $[Cr](z,t)$ est les profils de concentration en chrome en fonction de z ; $[Cr]_i$ est la concentration initiale en chrome.

Le tenseur de contrainte $\bar{\bar{\sigma}}$ (Eq. 4.11) et le tenseur de déformation élastique $\bar{\bar{\varepsilon}}^{elastic}$ sont considérés comme isotropes dans le plan.

$$\bar{\bar{\sigma}} = \begin{pmatrix} \sigma & 0 & 0 \\ 0 & \sigma & 0 \\ 0 & 0 & \sigma_N \end{pmatrix} \text{ and } \bar{\bar{\varepsilon}}^{elastic} = \begin{pmatrix} \varepsilon^{elastic} & 0 & 0 \\ 0 & \varepsilon^{elastic} & 0 \\ 0 & 0 & {\varepsilon^{elastic}}_N \end{pmatrix} \tag{4.8}$$

On suppose une relation proportionnelle entre la contrainte dans le plan σ et la contrainte normale $\sigma_N$ dans le métal :

$$\sigma_N = \beta\sigma \tag{4.9}$$

D'après les observations expérimentales, β = 1. On obtient la relation entre la déformation élastique dans le plan $\varepsilon^{elastic}$ et la déformation élastique normale ${\varepsilon^{elastic}}_N$ dans le métal :

$${\varepsilon^{elastic}}_N = \frac{\beta - 2\nu_m}{1 - \nu_m - \beta\nu_m}\varepsilon^{elastic} \tag{4.10}$$

La contrainte dans le plan σ dans le métal peut alors être calculée :

$$\sigma = \frac{E_m}{1 - \nu_m - \beta\nu_m}\varepsilon^{elastic} \tag{4.11}$$

La déformation dans la couche métallique comprend différentes composantes. Après l'avoir modifiée en ajoutant $\varepsilon^{diffusion}$, la déformation dans la couche métallique est maintenant :

$$\varepsilon^{total} = \varepsilon^{elastic} + \varepsilon^{viscoplastic} + \varepsilon^{thermal} + \varepsilon^{diffusion} \tag{4.12}$$

L'équation 4.12 peut être exprimée comme suit :

$$\sigma = \frac{E_m}{1 - \nu_m - \beta\nu_m}\left(\varepsilon^{total} - \varepsilon^{viscoplastic} - \varepsilon^{thermal} - \varepsilon^{diffusion}\right) \tag{4.13}$$

L'équation 4.13 peut être divisée en 2 termes : la contrainte de diffusion et un autre terme :

$$\sigma^{diffusion} = \frac{-E_m}{1 - \nu_m - \beta\nu_m}\varepsilon^{diffusion} \tag{4.14}$$

$$\sigma^{else} = \frac{E_m}{1 - \nu_m - \beta\nu_m}\left(\varepsilon^{total} - \varepsilon^{viscoplastic} - \varepsilon^{thermal}\right) \tag{4.15}$$

Nous supposons pour simplifier que $\sigma^{else}$ ne dépend pas de z. L'équation de l'équilibre mécanique devient :

$$\int_0^{h_m/2}\left(\sigma(0)+\frac{E_m}{1-\nu_m-\beta\nu_m}\eta([Cr](0,t)-[Cr]_i)-\frac{E_m}{1-\nu_m-\beta\nu_m}\eta([Cr](z,t)-[Cr]_i)\right)dz + \int_{-h_{ox}}^{0}\sigma_{ox}\,dz=0 \qquad (4.16)$$

Dans l'équation 4.7, η est un coefficient constant. L'équation 4.16 peut être transformée en :

$$\eta=\frac{-\int_{-h_{ox}}^{0}\sigma_{ox}\,dz-\int_0^{h_m/2}\sigma(0)dz}{\int_0^{h_m/2}\frac{E_m}{1-2\nu_m}\big([Cr](0,t)-[Cr](z,t)\big)dz} \qquad (4.17)$$

## 4.3 Modélisation thermomécanique complète avec ajout de la contrainte de diffusion

### 4.3.1 Modélisation thermomécanique + diffusion

Après avoir ajouté la déformation de diffusion dans l'équation 1.9, le modèle thermomécanique devient :

$$\left(\varepsilon^{elastic}+\varepsilon^{viscoplastic}+\varepsilon^{thermal}+\varepsilon^{diffusion}\right)_m = \left(\varepsilon^{elastic}+\varepsilon^{viscoplastic}+\varepsilon^{thermal}+\varepsilon^{growth}\right)_{ox} \qquad (4.18)$$

En considérant l’équilibre mécanique, la solution analytique deviennent :

$$\dot{\sigma}_{ox}=\frac{\frac{\sigma_{ox}}{t}\frac{1-\nu_m}{E_m}-signe(\sigma_{ox})\left(\frac{h_m}{Ap\sqrt{t}}\right)^{1-N_m}J_m|\sigma_{ox}|^{N_m}+signe(\sigma_{ox})J_{ox}|\sigma_{ox}|^{N_{ox}}\frac{h_m}{Ap\sqrt{t}}+\frac{D_{ox}h_m}{2t}-\frac{\eta[\dot{Cr}](z,t)h_m}{Ap\sqrt{t}}}{\left(\frac{1-\nu_{ox}}{E_{ox}}\frac{h_m}{Ap\sqrt{t}}+2\frac{1-\nu_m}{E_m}\right)} \qquad (4.19)$$

Par rapport à l'équation 1.13, il y a deux nouveaux paramètres à identifier, le coefficient η qui lie les profils de concentration de chrome à la contrainte de diffusion et le taux de concentration de chrome $[\dot{Cr}]$.

### 4.3.2 Comparaison entre modélisation et résultats expérimentaux

Pour observer l'effet de l'ajout de la contrainte de diffusion dans la modélisation, plusieurs résultats sont tracés dans la même figure, qui inclut la contrainte sans la contrainte de diffusion, la contrainte dans la couche métallique avec la contrainte de diffusion et les résultats expérimentaux.

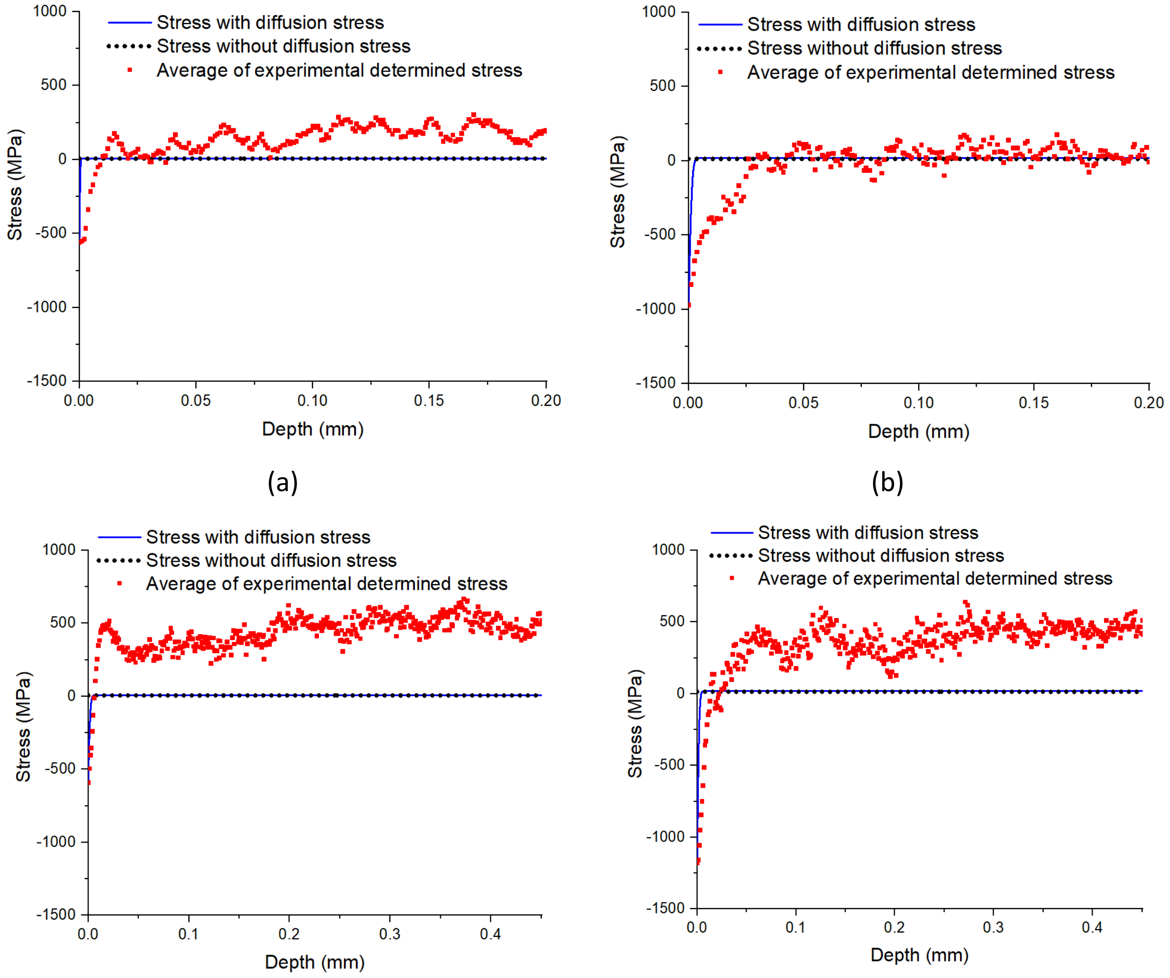

(a) (b)

(c) (d)

Figure 4.2 Distributions spatiales des contraintes dans les l'échantillon Rec_T800_10h (a), Rec_T900_10h (b), Cyl_T1000_1h (c), Cyl_T1000_5h (d)

Les figures 4.2.a-d montrent que la contrainte dans le métal loin de la zone d'interface est une valeur positive pour le modèle avec ou sans la contrainte de diffusion. Après avoir ajouté la contrainte de diffusion, un gradient de contrainte est systématiquement prédit pour la zone proche de l'interface. Pour les échantillons Cyl_T1000_1h et Cyl_T1000_5h, le gradient de contrainte dans la zone de proche interface avec la contrainte de diffusion est très similaire aux résultats expérimentaux. Les profondeurs de gradient ont également le même ordre de grandeur. Pour l'échantillon Rec_T800_10h et Rec_T900_10h, le gradient de contrainte dans la zone proche de l'interface est présent pour toutes les simulations avec contrainte de diffusion, mais les profondeurs de gradient sont dix fois plus petites que celles observées expérimentalement. Cela peut être dû à l'épaisseur plus faible de la couche métallique ou à la forme spécifique des échantillons, ce qui nécessiterait des études supplémentaires.

# 5. Simulations par éléments finis

## 5.1 La démarche de la modélisation numérique par EF

Dans cette section, la simulation sera comparée aux résultats des contraintes dépendant du temps obtenus dans le travail de Zhaojun Tao [13]. Dans ce travail [13], il a été montré les contraintes dépendant du temps pour 800°C, 900°C, 1000°C oxydés pendant 7.4h. Les paramètres utilisés sont pour un matériau Ni30Cr, qui représente 30% du poids du Cr. Sachant que les échantillons sont oxydés à 800 °C, 900 °C ou 1000 °C, les paramètres d'entrée pour les trois températures sont indiqués dans le tableau 5.1.

Table 5.1. Les paramètres d'entrée des simulations [12, 13, 21]

| Condition d'oxydation | $Ap$ $(mm\, s^{-1/2})$ | $E_{ox}$ $(MPa)$ | $\nu_{ox}$ | $K_{ox}$ $(MPa\, s^{1/Nox})$ | $N_{ox}$ | $\alpha_{ox}$ $(K^{-1})$ |
|---|---|---|---|---|---|---|
| 800 °C, 10 h | 2.83E-6 | 225000 | 0.29 | 2.65E8 | 1 | 6.99E-6 |
| 900 °C, 10 h | 4.73E-6 | 215000 | 0.29 | 1.83E8 | 1 | 7.11E-6 |
| 1000 °C, 1 h | 1.43E-5 | 205000 | 0.29 | 3.5E7 | 1 | 7.24E-6 |
| | $D_{ox}$ $(mm^{-1})$ | $E_m$ $(MPa)$ | $\nu_m$ | $K_m$ $(MPa\, s^{1/Nm})$ | $N_m$ | $\alpha_m$ $(K^{-1})$ |
| 800 °C, 10 h | 51.4 | 170000 | 0.3 | 2.39E11 | 1 | 1.9E-5 |
| 900 °C, 10 h | 56.6 | 165000 | 0.3 | 1.05E13 | 1 | 1.96E-5 |
| 1000 °C, 1 h | 51.9 | 160000 | 0.3 | 1.88E15 | 1 | 2.02E-5 |
| | $[Cr]_0$ | η | $D$ $(mm^2 s^{-1})$ | | | |
| 800 °C, 10 h | 0.345 | -6.57E-03 | 2.59E-12 | | | |
| 900 °C, 10 h | 0.345 | -1.18E-02 | 4.09E-11 | | | |
| 1000 °C, 1 h | 0.2828 | -8.98E-03 | 4.19E-10 | | | |

Dans ce tableau, Ap est le coefficient cinétique de la réaction d'oxydation chimique globale ; $E_{ox}$ correspond au module d'Young de la couche d'oxyde ; $\nu_{ox}$ est le coefficient de Poisson de la couche d'oxyde ; $K_{ox}$ et $N_{ox}$ correspondent aux paramètres viscoplastiques de la couche d'oxyde ; $\alpha_{ox}$ est le coefficient de dilatation thermique de la couche d'oxyde ; $D_{ox}$ correspond au paramètre de déformation de croissance ; $E_m$ et $\nu_m$ sont le module de Young et le coefficient de Poisson de la couche métallique ; $K_m$ et $N_m$ sont les paramètres viscoplastiques de la couche métallique ; $\alpha_m$ correspond au coefficient de dilatation thermique de la couche métallique ; $[Cr]_0$ est la concentration initiale en pourcentage massique de l'élément Cr ; η correspond à un coefficient constant couplant les profils de concentration en chrome à la déformation de diffusion et D est le coefficient de diffusion de Cr dans NiCr.

Pour la simulation, le logiciel ABAQUS est utilisé [22]. La géométrie et le maillage sont présentés à la Fig.5.1.

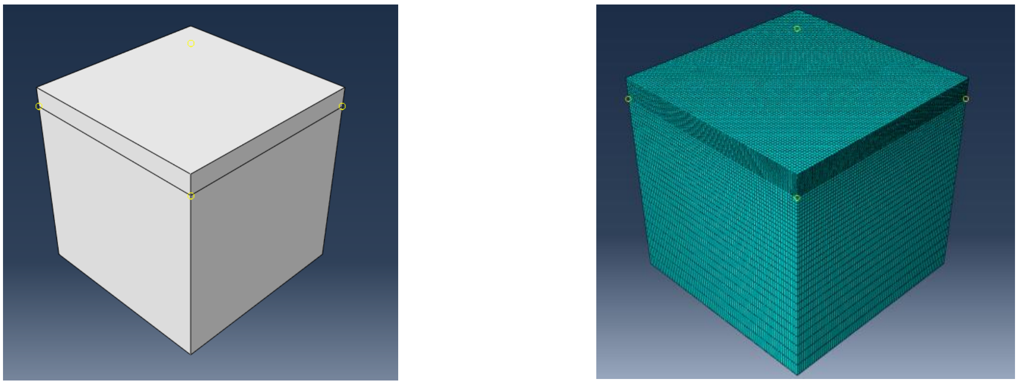
(a) (b)

Figure 5.1 La géométrie (a) et le maillage (b)

Comme le montre la Fig. 5.1, afin de s'adapter à l'épaisseur de la couche d'oxyde, la simulation est appliquée à une géométrie plus petite, qui est de 0,02*0,02*0,02 mm. Le long de l'axe z, de 0 à 0,018 mm se trouve la couche métallique et de 0,018 mm à 0,02 mm se trouve la couche d'oxyde + air (a). Pour les différentes couches, un maillage différent est donné (b). Pour la couche d'oxyde + air, il y a 20 nœuds, ce qui signifie que l'épaisseur d'un élément est de 0,0001 mm, ce qui est plus approprié pour la simulation de la couche d'oxyde en termes de précision. Pour la couche de métal, il y a 30 nœuds et pour les éléments qui sont proches de l'interface, ils sont plus petits. Le maillage y a été raffiné. Le type d'élément est C3D8R. Les simulations discutées plus loin dans cette section utilisent la géométrie montrée sur la Fig.5.1.

Une condition aux limites libre est appliquée à la surface supérieure et aux surfaces latérales de cette géométrie et une condition de symétrie du plan XY est appliquée à la surface inférieure. Un chemin est créé le long de l'axe Z au centre de cette géométrie, qui sera utilisé pour tracer la contrainte en fonction de la profondeur.

Pour obtenir des conditions plus réalistes, différentes phases de température ont été définies et créées dans l'UMAT, qui sont respectivement l'augmentation de la température, l'oxydation isotherme et la diminution de la température.

Dans la première phase, la déformation thermique et la déformation élastique sont principalement concernées et les autres déformations ne le sont pas. Nous avons supposé que pendant cette phase d'augmentation de la température, il n'y a pas de déformation viscoplastique, de déformation de diffusion et de déformation de croissance. Par rapport à la phase isotherme, ces déformations sont négligeables car le temps de la phase d'augmentation de la température est relativement court par rapport à la phase isotherme et la croissance de l'oxyde se produit principalement pendant la phase isotherme. Quant à la déformation viscoplastique, elle est plus significative à haute température. Ainsi, pour la phase d'augmentation de la température, ces déformations ne sont pas prises en compte, et il en est de même pour la phase de diminution de la température.

Pour la phase deux, la température est maintenue à 900 degrés Celsius pendant 10h. Pendant la simulation, la déformation viscoplastique, la déformation de diffusion, la déformation de croissance et la déformation élastique peuvent également être prises en compte. La déformation thermique n'est pas prise en compte en raison de la transformation isotherme lors de cette phase deux.

Pour la phase trois, la température passe de 900 à 25 degrés Celsius en 30 minutes. Dans la phase trois, la déformation thermique et la déformation élastique sont concernées et les autres déformations ne sont pas concernées. Lorsque la température diminue, il n'y a pas de croissance de la couche d'oxyde en raison de la protection de la couche d'oxyde. La diminution de la température entraîne également un manque d'énergie pour les phénomènes viscoplastiques et de diffusion. Nous supposons donc que pendant la phase de diminution de la température, il n'y a pas de déformation viscoplastique, de déformation de diffusion et de déformation de croissance.

## 5.2 Résultats et discussion

### 5.2.1 Oxydation à 800°C pendant 10h

En utilisant les paramètres du tableau 5.1, le maillage et la géométrie de la figure 5.1, les résultats de la simulation sont obtenus et les courbes de distribution spatiale des contraintes le long du chemin centrale sont tracées.

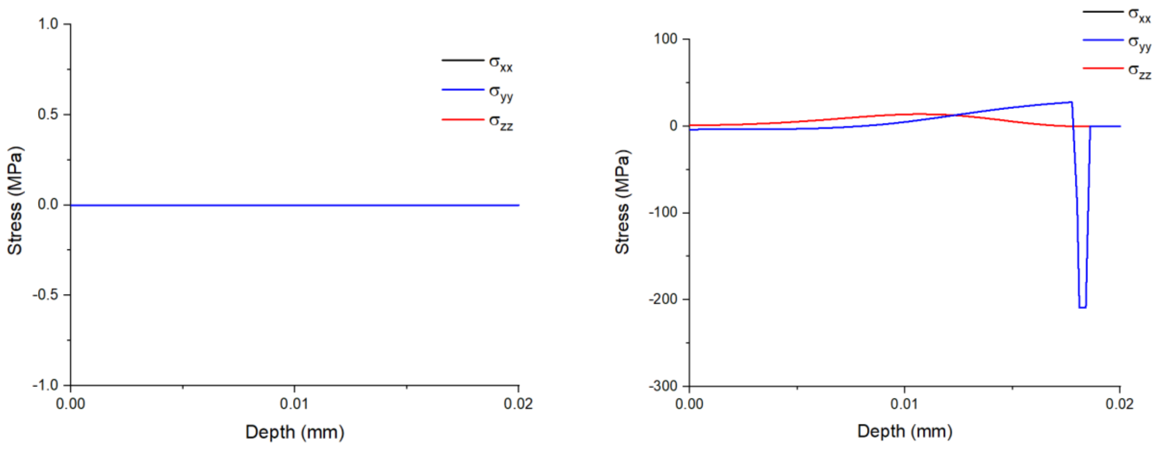

(a) (b)

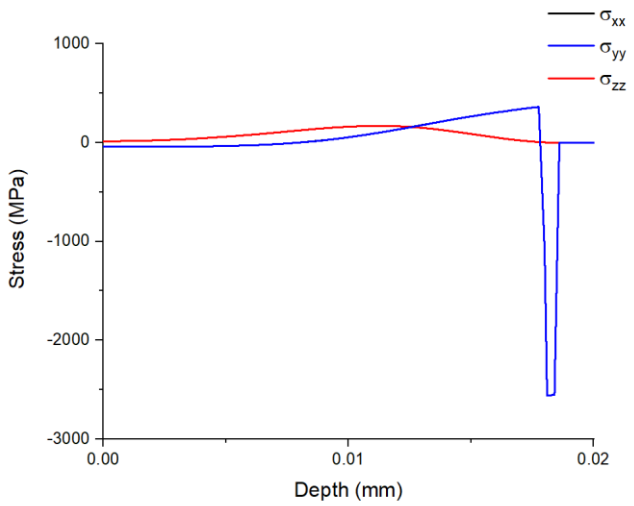

(c)

Figure 5.2 Distribution des composantes de la contrainte à la fin de la phase 1 (a), à la fin de la phase 2 (b), et à la fin de la phase 3 (c)

Pour les figures 5.2 (a)-(c), l'interface métal/oxyde est à une profondeur de 0,018 mm. Comme le montre la figure 5.2, les valeurs de $\sigma_{xx}$ et $\sigma_{yy}$ sont très proches pour toutes les phases, ce qui indique que la simulation conduit à un état mécanique isotrope. À la fin de la phase 2, la phase isotherme, la valeur absolue maximume de la contrainte dans la couche d'oxyde est de 209 MPa et dans la couche métallique de 28 MPa. A la fin de la phase 3, à température ambiante, la valeur absolue maximume de la contrainte dans la couche d'oxyde est de 2561 MPa et dans la couche métallique de 362 MPa. Pour la phase 2 et la phase 3, la contrainte maximume apparaît près de l'interface oxyde/métal. La valeur absolue maximume de la contrainte dans la couche d'oxyde à la température ambiante correspond aux valeurs obtenues lors d'autres travaux, qui sont de 2-2.5 GPa [15].

La contrainte en fonction du temps peut également être tracée, ce qui peut être comparé aux résultats obtenus dans un travail précédent [13], pour le matériau Ni30Cr et oxydé à 800°C pendant 7.4h.

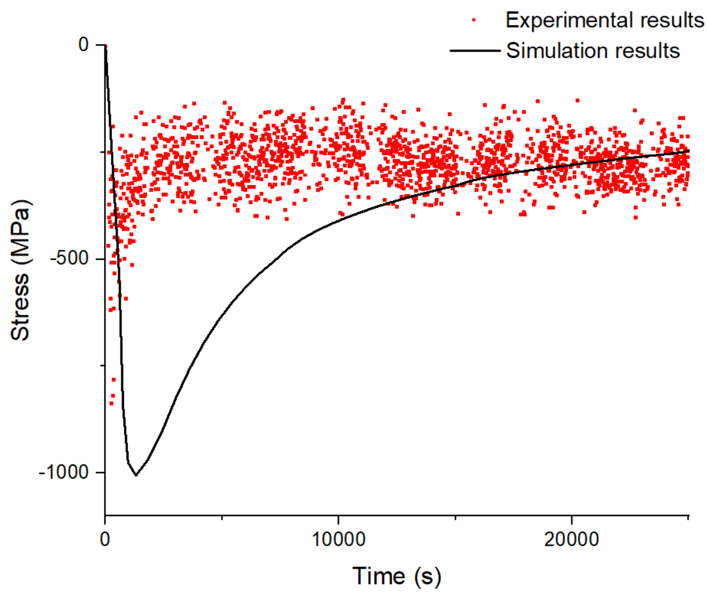

Figure 5.3 Contrainte en fonction du temps pour une condition isotherme 800 °C

La figure 5.3 montre la comparaison de la contrainte en fonction du temps pour la couche d'oxyde, qui inclut les résultats expérimentaux et les résultats de la simulation pour une condition d'oxydation isotherme à 800 °C. Les résultats de la simulation correspondent assez bien aux résultats expérimentaux au début et à la fin de la phase 2. Il est montré qu'au début, la contrainte absolue augmente dans la couche d'oxyde. En même temps, la viscoplasticité provoque une relaxation de la contrainte, qui obtient finalement un équilibre entre l'augmentation et la relaxation. Par conséquent, la contrainte minimale est affectée par des paramètres tels que les paramètres viscoplastiques de la couche d'oxyde $K_{ox}$ et le paramètre de déformation de croissance $D_{ox}$.

### 5.2.2 Oxydation à 900°C pendant 10h

Afin d'être comparé avec les résultats obtenus dans le travail [13], pour le matériel Ni30Cr et oxydé à 900 °C pendant 7.4h, la contrainte en fonction du temps est tracée. La figure 5.4 montre la contrainte en fonction du temps des 7 premières heures pour les résultats expérimentaux et les résultats de simulation.

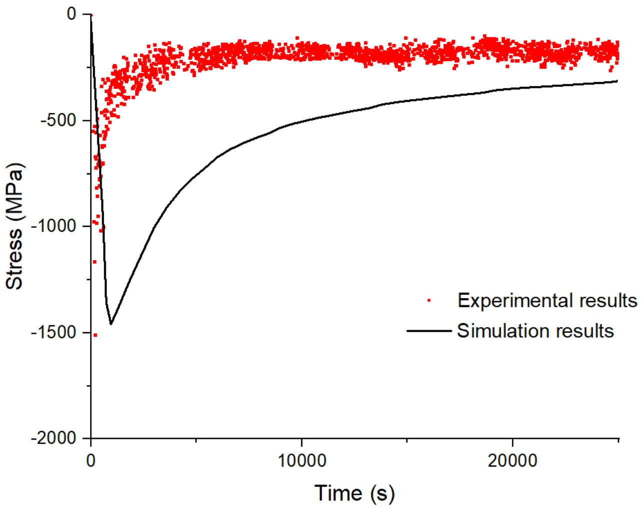

Figure 5.4 Contrainte en fonction du temps pour une condition isotherme 900 °C

En utilisant les paramètres donnés dans le tableau 5.1, les résultats de la simulation sont présentés à la figure 5.4. La performance de la simulation est assez bonne, ce qui signifie que les résultats de la simulation sont relativement similaires aux résultats expérimentaux. La contrainte minimale pour les résultats de simulation est de -1458 MPa, ce qui est proche du résultat expérimental minimal -1508 MPa. Comme nous l'avons vu précédemment, la déformation de croissance et la déformation viscoplastique à haute température jouent un rôle très important dans ce système et ce modèle numérique est adapté à la simulation de ce type de systèmes.

Le retard de l'inflexion du temps peut être causé par les différentes conditions entre les expériences et la simulation pour la phase d'augmentation de la température. Dans la simulation, la déformation viscoplastique, la déformation de diffusion et la déformation de croissance ne sont pas prises en compte. Alors, Dans la simulation, au début de la phase 2, la contrainte est de 0 MPa. Cependant, dans l'expérience, ces déformations peuvent exister, ce qui provoque une contrainte résiduelle à la fin de la phase d'augmentation de la température. Pour la simulation, l'augmentation de la contrainte et la relaxation de la contrainte sont bien visibles, et en même temps, il y a un retard dans l'inflexion du temps.

### 5.2.3 Oxydation à 1000°C pendant 1h

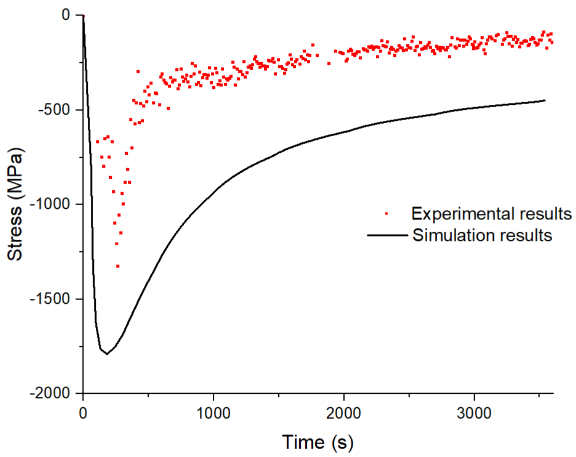

Figure 5.5 Contrainte en fonction du temps pour une condition isotherme 1000 °C

La figure 5.5 montre que les résultats de la simulation ont la même tendance que les résultats expérimentaux. Cependant, les résultats de la simulation sont légèrement inférieurs aux résultats expérimentaux. Pour la contrainte minimale, elle est de -1788 MPa pour les résultats de simulation, et de -1324 MPa pour les résultats expérimentaux.

# Conclusions

Les contraintes résiduelles ont été déterminées dans le métal et l'oxyde pour différents systèmes oxyde/métal. La détermination expérimentale des contraintes dans la couche d'oxyde a été réalisée in-situ lors de chargements thermiques à haute température grâce à la diffraction de rayons X synchrotron en mode réflexion. Les mesures de contraintes dans le substrat à température ambiante ont été réalisées par diffraction de rayons X synchrotron en mode transmission. Pour le modèle thermomécanique complet, il a été proposé de simuler par modélisation numérique dans ABAQUS.

La première partie du travail est basée sur l'évolution des contraintes en fonction du temps qui sont obtenues en traitant les résultats des mesures de diffraction synchrotron in-situ à haute température (en mode réflexion) obtenues à l'Européen Synchrotron Radiation Facility. Pour identifier les paramètres inconnus ou incertains, il a été nécessaire d'étudier la solution numérique d'un modèle thermomécanique complet, qui inclut les composantes de déformation pertinentes, telles que la déformation élastique, la déformation viscoplastique, la déformation thermique et la déformation de croissance pour la couche d'oxyde. Par conséquent, la méthode usuellement utilisée a été améliorée puis appliquée pour traiter les résultats expérimentaux. En comparant les contraintes en fonction du temps avec la solution numérique, au sens des moindres carrés, le paramètre de fluage pour l'oxyde ($J_{ox}$) et le paramètre de contrainte de croissance pour l'oxyde ($D_{ox}$) ont été optimisés. Ces paramètres ont été étudiés pour déterminer l'énergie d'activation associée aux mécanismes et ont été favorablement comparés aux paramètres existants dans la bibliographie.

Notamment, en considérant la condition d'oxydation isotherme et la contrainte homogène dans la couche métallique, pour tous les échantillons, y compris les échantillons implantés d'oxyde d'yttrium et les échantillons dopés au zirconium, l'évolution de la contrainte est le résultat de l'équilibre mécanique entre deux phénomènes, à savoir l'augmentation de la contrainte principalement causée par la croissance de la couche d'oxyde et la relaxation de la contrainte principalement causée par le phénomène viscoplastique lié aux mécanismes de fluage. La modélisation thermomécanique de ces systèmes oxyde/métal a été mise en œuvre avec succès. En utilisant le logiciel Matlab et une méthode classique de Runge-Kutta, le paramètre de fluage pour l'oxyde ($J_{ox}$) et le paramètre de contrainte de croissance pour l'oxyde ($D_{ox}$) ont été identifiés pour tous les échantillons considérés.

L'introduction d'éléments réactifs permet d'améliorer les propriétés protectrices de la couche d'oxyde de chrome obtenue par croissance thermique lors d'une oxydation à haute température. En augmentant la quantité d'oxyde d'yttrium ou de zirconium dopé, la déformation viscoplastique s'avère plus faible avec une grande quantité d'oxyde d'yttrium ou de zirconium dopé à la même température, ce qui signifie que les éléments réactifs $Y_2O_3$ et Zr sont efficaces pour ralentir la diffusion cationique.

En augmentant la quantité d'yttria ou zirconium, le paramètre de déformation de croissance $D_{ox}$ diminue. En plus, on calcule l'énergie d'activation pour la croissance $Q_D$, qui diminue lorsque le temps d'exposition augmente ou que la fluence de dopage augmente. Le paramètre $D_{ox}$ peut également être lié au rapport du flux cationique/anionique se produisant à l'intérieur des joints de grains lors de la croissance de la couche d'oxyde. Une interprétation de cet effet a été proposée.

La deuxième partie du travail est basée sur l'évolution de la contrainte en profondeur qui a été obtenue en traitant les résultats des mesures synchrotron en mode transmission obtenues à température ambiante au synchrotron DESY. Pour étudier la distribution des contraintes résiduelles dans le substrat métallique après oxydation, une méthode particulière des $\sin^2\phi$ a été développée puis appliquée.

La plus grande partie de la distribution des contraintes est comprise entre 0 MPa et 500 MPa et elle montre un gradient de distribution, qui se trouve dans la zone proche de l'interface (jusqu'à 15µm avant les valeurs approximativement constantes au cœur de l’alliage) entre le métal et l'oxyde. La contrainte varie vers la surface d'une manière non linéaire. Avec une température d'oxydation plus faible ou un temps d'oxydation plus faible, la contrainte à l'interface oxyde/métal est plus faible.

De plus, nous avons proposé d'ajouter la contrainte de diffusion dans le modèle thermomécanique existant pour expliquer le gradient de contrainte dans la zone proche de l'interface. En raison de la variation spatiale rapide de l'appauvrissement en chrome dans la zone proche de la surface, la contrainte de diffusion change en fonction de z. Après l'ajout de cette contrainte de diffusion dans la modélisation, la distribution des contraintes correspond mieux à la moyenne des contraintes mesurées par rapport à la modélisation sans contrainte de diffusion. Cependant, la correspondance de la distribution de la contrainte de diffusion entre les expériences et la modélisation doit encore être améliorée, notamment pour les températures étudiées les plus basses. Des valeurs numériques pour le couplage de la concentration de chrome avec la contrainte de diffusion/chimique ont également été obtenues. Ces valeurs ont été identifiées pour influencer au mieux le niveau de contrainte calculé.

Cette étude comble un vide dans la littérature en utilisant les rayons X à haute énergie en mode transmission pour mesurer la distribution des contraintes dans la couche métallique profonde et en proposant un modèle de calcul de la distribution spatiale des contraintes pour comparaison. D'un point de vue expérimental, les conditions d'oxydation et même la forme des échantillons peuvent influencer la distribution des contraintes. Du point de vue de la modélisation, les paramètres d'entrée et les différents mécanismes peuvent influencer les résultats. La comparaison est donc difficile en raison des nombreuses incertitudes et sources d’erreurs. Cependant, l'observation du gradient et sa prédiction, en ajoutant la composante de la contrainte de diffusion dans la modélisation thermomécanique, conduit à une meilleure explication de la distribution spatiale de la contrainte dans la couche métallique.

Enfin, la dernière partie de l'étude est consacrée au développement d'un modèle numérique spatio-temporel pour la prédiction des contraintes générées lors de l'oxydation à haute température, en tenant compte de l'hétérogénéité. Les résultats de la simulation numérique sont comparés aux contraintes en fonction du temps pour la couche d'oxyde, mais aussi aux distributions spatiales obtenues dans le métal.

La couche d'oxyde est soumise à des contraintes de compression élevées de l'ordre de 2-2,5 GPa à température ambiante après le refroidissement. Leurs valeurs absolues maximumes se situent à l'interface métal-oxyde. La contrainte dans le substrat métallique reste faible, de l'ordre de quelques MPa.

Le résultat de ces simulations est comparé aux observations expérimentales, ce qui montre une bonne concordance pour les contraintes notamment en fonction du temps pour la couche d'oxyde. La contrainte absolue augmente au début de l'oxydation et elle diminue à cause des phénomènes de fluage à haute température. Après le processus de refroidissement, la contrainte augmente largement, ce qui est dû à la différence de coefficient de dilatation thermique entre la couche d'oxyde et de métal.

## Références du résumé en français

[1] J. Lemaitre, J. l. Chaboche, Mécanique des matériaux solides, Paris, 2001.

[2] B. Panicaud, J.-L. Grosseau-Poussard, Z. Tao, F. Rakotovao, G. Geandier, P.-O. Renault, P. Goudeau, N. Boudet, N. Blanc, Acta Mechanica 2017, 228, 3595.

[3] B. Panicaud, J. L. Grosseau-Poussard, J. F. Dinhut, Computational Materials Science 2008, 42, 286.

[4] B. Panicaud, J.-L. Grosseau-Poussard, M. Kemdehoundja, J.-F. Dinhut, Computational Materials Science 2009, 46, 42.

[5] Z. J. Tao, F. Rakotovao, J. L. Grosseau-Poussard, B. Panicaud, Advanced Materials Research 2014, 996, 896.

[6] D. J. Baxter and K. Natesan, Reviews on high temperature materials, 1983, 5, 149.

[7] J. P. Poirier, Creep of crystals: high-temperature deformation processes metals, ceramics, and minerals, Cambridge University Press, New York, 1985.

[8] F. Rakotovao, B. Panicaud, J. L. Grosseau-Poussard, Z. Tao, G. Geandier, P. O. Renault, P. Girault, P. Goudeau, N. Blanc, N. Boudet, G. Bonnet, Acta Materialia 2018, 159, 276.

[10] Z. Wang, J.-L. Grosseau-Poussard, B. Panicaud, G. Geandier, P.-O. Renault, P. Goudeau, N. Boudet, N. Blanc, F. Rakotovao, Z. Tao, Metals 2018, 8, 913.

[11] Y. Wang, H. Fang, C.l. Zacherl, Z. Mei, S. Shang, L.-q. Chen, P.d. Jablonski, Z.-k. Liu, Surface Science 2012, 606.

[12] J.-L. Grosseau-Poussard, B. Panicaud, S. Ben Afia, Computational Materials Science 2013, 71, 47.

[13] Z.J. Tao, Experimental study and modelling of mechanical features in an oxide layer under thermal loadings, PhD Thesis, Université de technologie de Troyes, Troyes, France, 2018.

[14] Z. Wang, J.-L. Grosseau-Poussard, B. Panicaud, G. Geandier, P.-O. Renault, P. Goudeau, N. Boudet, N. Blanc, F. Rakotovao, Z. Tao, Computational Materials Science 2020, 180, 109689.

[15] F. Rakotovao, Relaxation des contraintes dans les couches de chromine développées sur alliages modèles (NiCr et Fe47Cr): apport de la diffraction in-situ à haute température sur rayonnement Synchrotron à l'étude du comportement viscoplastique: effets d'éléments réactifs, PhD Thesis, Université de La Rochelle, La Rochelle, France, 2016.

[16] D.P Whittle, D.J Evans, D.B Scully, G.C Wood, Acta Metallurgica, 1967, 15, 421-1430.

[17] J. Růžičková, B. Million, Materials Science and Engineering. 1981, 50, 59–64.

[18] K. Monma, H. Suto, H. Oikawa. J. Jpn, inst, Met, 28(1964) 188-192.

[19] A. Milton, S. Irene, Abramowitz and Stegun, U.S., 1964.

[20] D.Fettre, Aspects mécaniques de l'oxydation haute température du zirconium: modélisation des champs de contrainte et suivi expérimental multi technique des endommagements, PhD Thesis, Université de Compiègne, Compiègne, France, 2017.

[21] M. Guerain, Contribution à l'étude des mécanismes de relaxation de contraintes dans les films de chromine formés sur Ni-30Cr et Fe-47Cr : approche multi-échelle par spectroscopie Raman et microdiffraction Synchrotron, PhD Thesis, Université de La Rochelle, La Rochelle, France, 2012.

[22] http://130.149.89.49:2080/v2016/books/sub/default.htm?startat=ch01s01asb44.html#sub-rtn-uumat

**Zhimao WANG**

**Doctorat : Matériaux, Mécanique, Optique, Nanotechnologie**

**Année 2021**

## Étude expérimentale et modélisation des propriétés thermomécaniques et hétérogénéité des systèmes Cr2O3-NiCr

Les contraintes résiduelles ont été déterminées dans le métal et l'oxyde pour différents systèmes oxyde/métal. La détermination expérimentale des contraintes dans la couche d'oxyde a été réalisée in-situ lors de chargements thermiques à haute température grâce à la diffraction de rayons X synchrotron en mode réflexion. En comparant les contraintes en fonction du temps avec la solution numérique, au sens des moindres carrés, le paramètre de fluage pour l'oxyde (Jox) et le paramètre de contrainte de croissance pour l'oxyde (Dox) ont été optimisés. Les mesures de contraintes dans le substrat à température ambiante ont été réalisées par diffraction de rayons X synchrotron en mode transmission. La plus grande partie de la distribution des contraintes est comprise entre 0 MPa et 500 MPa et elle montre un gradient de distribution, qui se trouve dans la zone proche de l'interface. Pour le modèle thermomécanique complet, il a été proposé de simuler par modélisation numérique dans ABAQUS. Le résultat de ces simulations est comparé aux observations expérimentales, ce qui montre une bonne concordance pour les contraintes notamment en fonction du temps pour la couche d'oxyde.

Mots clés : contraintes (mécanique) – rayons X, diffraction – propriétés thermomécaniques – simulation par ordinateur.

## Experimental Study and Modelling of Thermomechanical Features and Heterogeneity of the Cr2O3-NiCr Systems

Residual stresses have been determined both in metal and oxide in different oxide/metal systems. Measurements and analyses of stress in the oxide layer have been especially performed in-situ during thermal loadings at high temperature thanks to synchrotron X-ray diffraction in reflexion mode. By comparing the stresses as a function of time with the numerical solution, in the least squares sense, the creep parameter for the oxide (Jox) and the growth stress parameter for the oxide (Dox) were optimized. Stress measurements in the substrate at room temperature were performed by synchrotron X-ray diffraction in transmission mode. Most of the stress distribution is between 0 MPa and 500 MPa and it shows a gradient distribution, which is in the area near the interface. For this “full” thermomechanical model, it has been also proposed to perform simulations with a numerical approach using ABAQUS. The result of these simulations is compared to the experimental observations, which shows a good agreement for the stresses especially as a function of time for the oxide layer.

Keywords: strains and stresses – X-rays, diffraction – thermomechanical properties – computer simulation.

**Thèse réalisée en partenariat entre :**

**Ecole Doctorale** "Sciences pour l'Ingénieur"